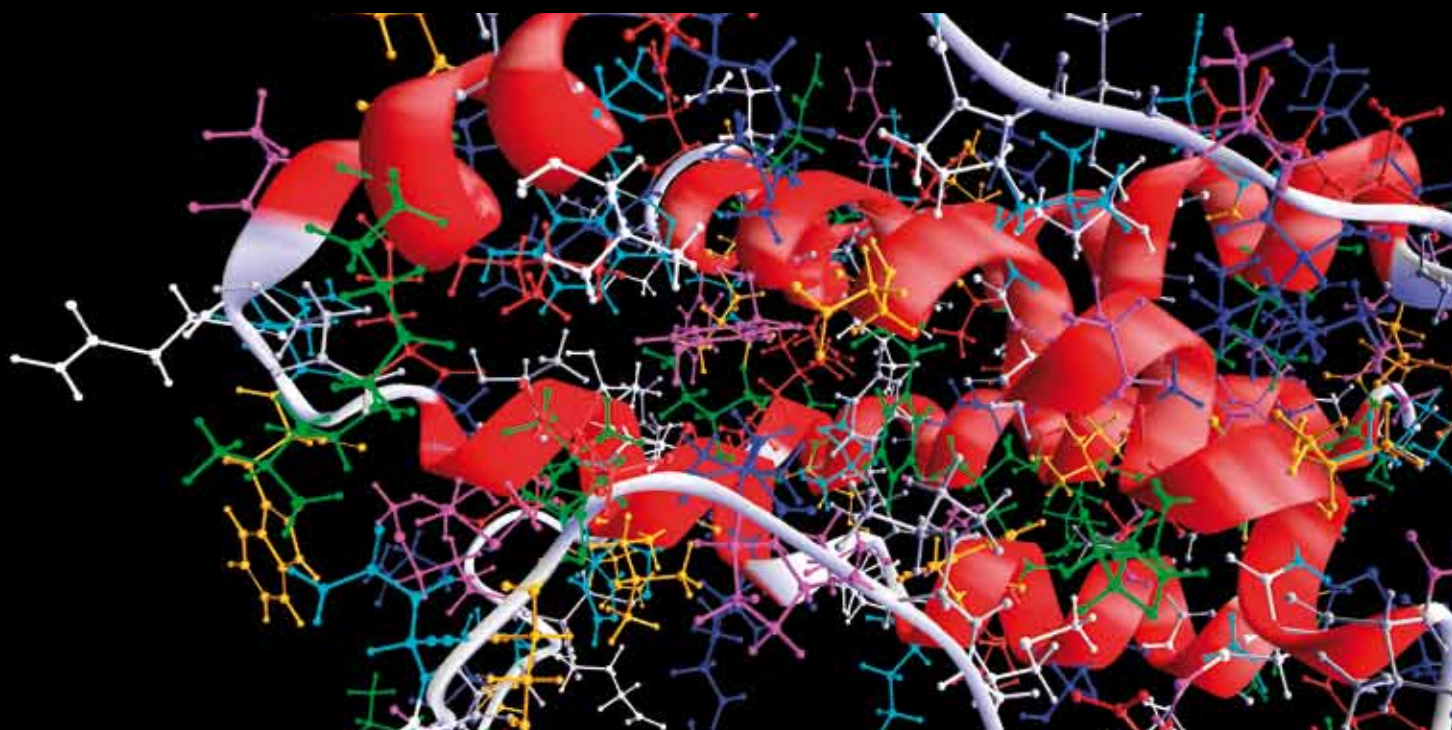


# GRAPH THEORETICAL APPROACHES IN BRAIN NETWORKS

GUEST EDITORS: FABRIZIO DE VICO FALLANI, DANIELLE BASSETT, AND TIANZI JIANG





---

# **Graph Theoretical Approaches in Brain Networks**

Computational and Mathematical Methods in Medicine

---

## **Graph Theoretical Approaches in Brain Networks**

Guest Editors: Fabrizio De Vico Fallani, Danielle Bassett,  
and Tianzi Jiang



---

Copyright © 2012 Hindawi Publishing Corporation. All rights reserved.

This is a special issue published in “Computational and Mathematical Methods in Medicine.” All articles are open access articles distributed under the Creative Commons Attribution License, which permits unrestricted use, distribution, and reproduction in any medium, provided the original work is properly cited.

## Editorial Board

Zvia Agur, Israel  
Emil Alexov, USA  
Gary C. An, USA  
Georgios Archontis, Cyprus  
Pascal Auffinger, France  
Facundo Ballester, Spain  
Dimos Baltas, Germany  
Chris Bauch, Canada  
Maxim Bazhenov, USA  
Niko Beerenwinkel, Switzerland  
Philip Biggin, UK  
Michael Breakspear, Australia  
Thierry Busso, France  
Carlo Cattani, Italy  
Bill Crum, UK  
Timothy David, New Zealand  
Gustavo Deco, Spain  
Carmen Domene, UK  
Wim Van Drongelen, USA  
Frank Emmert-Streib, UK  
Ricardo Femat, Mexico  
Alfonso T. García-Sosa, Estonia  
Kannan Gunasekaran, USA

Damien R. Hall, Japan  
William F. Harris, South Africa  
Vassily Hatzimanikatis, USA  
Tasawar Hayat, Pakistan  
Volkhard Helms, Germany  
J.-H. S. Hofmeyr, South Africa  
Seiya Imoto, Japan  
Bleddyn Jones, UK  
Lawrence A. Kelley, UK  
Lev Klebanov, Czech Republic  
Ina Koch, Germany  
David Liley, Australia  
Quan Long, UK  
Yoram Louzoun, Israel  
Jianpeng Ma, USA  
C.-M. C. Ma, USA  
Reinoud Maex, France  
Francois Major, Canada  
Simeone Marino, USA  
Ali Masoudi-Nejad, Iran  
Seth Michelson, USA  
Michele Migliore, Italy  
Karol Miller, Australia

Ernst Niebur, USA  
Kazuhisa Nishizawa, Japan  
Martin Nowak, USA  
Markus Owen, UK  
Hugo Palmans, UK  
Lech S. Papiez, USA  
Jean Pierre Rospars, France  
David James Sherman, France  
Sivabal Sivaloganathan, Canada  
Elisabeth Tillier, Canada  
Nestor V. Torres, Spain  
Anna Tramontano, Italy  
Nelson J. Trujillo-Barreto, Cuba  
Kutlu O. Ulgen, Turkey  
Nagarajan Vaidehi, USA  
Edelmira Valero, Spain  
Jinliang Wang, UK  
Jacek Waniewski, Poland  
Guang Wu, China  
X. George Xu, USA  
Henggui Zhang, UK

# Contents

**Graph Theoretical Approaches in Brain Networks**, Fabrizio De Vico Fallani, Danielle Bassett, and Tianzi Jiang  
Volume 2012, Article ID 590483, 2 pages

**A Computationally Efficient, Exploratory Approach to Brain Connectivity Incorporating False Discovery Rate Control, A Priori Knowledge, and Group Inference**, Aiping Liu, Junning Li, Z. Jane Wang, and Martin J. McKeown  
Volume 2012, Article ID 967380, 14 pages

**Redundancy as a Graph-Based Index of Frequency Specific MEG Functional Connectivity**, Claudia Di Lanzo, Laura Marzetti, Filippo Zappasodi, Fabrizio De Vico Fallani, and Vittorio Pizzella  
Volume 2012, Article ID 207305, 9 pages

**Source Space Analysis of Event-Related Dynamic Reorganization of Brain Networks**, Andreas A. Ioannides, Stavros I. Dimitriadis, George A. Saridis, Marotesa Voultzidou, Vahe Poghosyan, Lichan Liu, and Nikolaos A. Laskaris  
Volume 2012, Article ID 452503, 15 pages

**Weighted Phase Lag Index and Graph Analysis: Preliminary Investigation of Functional Connectivity during Resting State in Children**, Erick Ortiz, Krunoslav Stingl, Jana Münßinger, Christoph Braun, Hubert Preissl, and Paolo Belardinelli  
Volume 2012, Article ID 186353, 8 pages

**How the Statistical Validation of Functional Connectivity Patterns Can Prevent Erroneous Definition of Small-World Properties of a Brain Connectivity Network**, J. Toppi, F. De Vico Fallani, G. Vecchiato, A. G. Maglione, F. Cincotti, D. Mattia, S. Salinari, F. Babiloni, and L. Astolfi  
Volume 2012, Article ID 130985, 13 pages

**A Signal-Processing-Based Approach to Time-Varying Graph Analysis for Dynamic Brain Network Identification**, Ali Yener Mutlu, Edward Bernat, and Selin Aviyente  
Volume 2012, Article ID 451516, 10 pages

**Voxel Scale Complex Networks of Functional Connectivity in the Rat Brain: Neurochemical State Dependence of Global and Local Topological Properties**, Adam J. Schwarz, Alessandro Gozzi, Alessandro Chessa, and Angelo Bifone  
Volume 2012, Article ID 615709, 15 pages

## Editorial

# Graph Theoretical Approaches in Brain Networks

**Fabrizio De Vico Fallani,<sup>1,2</sup> Danielle Bassett,<sup>3</sup> and Tianzi Jiang<sup>4</sup>**

<sup>1</sup> *Research Centre of the Brain and Spinal Cord Institute, INSERM/UPMC/CNRS, 75005 Paris, France*

<sup>2</sup> *Department of Physiology and Pharmacology, Sapienza University of Rome, 00185 Rome, Italy*

<sup>3</sup> *Department of Physics and Sage Center for the Study of the Mind, University of California, Santa Barbara, CA 93106, USA*

<sup>4</sup> *National Laboratory of Pattern Recognition, Institute of Automation, Chinese Academy of Sciences, Beijing 100190, China*

Correspondence should be addressed to Fabrizio De Vico Fallani, [fabrizio.devicofallani@uniroma1.it](mailto:fabrizio.devicofallani@uniroma1.it)

Received 4 December 2012; Accepted 4 December 2012

Copyright © 2012 Fabrizio De Vico Fallani et al. This is an open access article distributed under the Creative Commons Attribution License, which permits unrestricted use, distribution, and reproduction in any medium, provided the original work is properly cited.

In the last decade network theory has proved an effective tool for modeling and describing the complex topology emerging either from anatomical or functional brain connectivity patterns. From a graph theoretical perspective, the brain can be conceived as a networked system composed of nodes coincident with different brain sites and links which in the current view can either represent anatomical tracts between brain regions or measures of statistical dependencies between their electrical activity. One of the most intriguing, and now well known, examples of the application of network theory to neuroimaging data unveiled that the way brain regions are connected is typically neither regular nor random. Instead brain networks, like other real networked systems, tend to exhibit a complex structure theoretically consistent with the capability of processing information within regional clusters and avoiding excessive connections between clusters. While the simplest instantiation of this configuration showed similar characteristics to mathematically defined “small-world” networks, it has become clear that additional topological structures including hierarchical modularity can nuance our expectations of the brain’s underlying architecture and dynamics. An important goal in these research endeavors is to identify how brain network organization can inform our understanding of the brain’s intuitive need to balance the two competing principles of integration and segregation and how alterations in brain structure and dynamics can lead to alterations in human behavior and cognitive function. The present special issue collects a series of selected contributions related to the methodological and practical applications

of network theory to anatomical and functional brain connectivity patterns.

The contribution entitled “*Voxel scale complex networks of functional connectivity in the rat brain: neurochemical state dependence of global and local topological properties*” addresses the dependence of the functional connectivity estimated from the fMRI signals of the rat brain in response to alterations of the neurotransmitter system as induced by the administration of specific pharmaceutical drugs such as d-amphetamine, fluoxetine, and nicotine.

The contribution entitled “*A signal-processing-based approach to time-varying graph analysis for dynamic brain network identification*” proposes a dynamic network summarization approach to describe the time-varying evolution of connectivity patterns in functional brain activity. The proposed method is evaluated on event-related potential (ERP) data, which demonstrates the dynamic nature of functional connectivity.

The contribution entitled “*how the statistical validation of functional connectivity patterns can prevent erroneous definition of small-world properties of a brain connectivity network*” addresses important methodological choices that are often made in the construction of functional brain network from EEG data, including the choice of statistical thresholds to determine the presence or absence of network links and the role of spatial correlations in determining graph properties.

The contribution entitled “*weighted phase lag index and graph analysis: preliminary investigation of functional*

*connectivity during resting state in children*” presents original results concerning the application of small-world parameters and betweenness centrality measures to characterize the topological structure of the functional network in the children’s brain from noninvasive MEG recordings.

The contribution entitled “*source space analysis of event-related dynamic reorganization of brain networks*” conducts a quantitative study of the dynamic reconfiguration of connectivity for event-related experiments at source space level, which provides a global and complete view of the stages of processing associated with the regional changes in activity.

The contribution entitled “*Redundancy as a Graph-Based Index of Frequency Specific MEG Functional Connectivity*” focuses on quantifying the differential role that paths of different lengths potentially play in brain connectivity and demonstrates that a redundancy-based measure captures unique information not accessible via approaches that only examine the shortest paths through a network.

The contribution entitled “*A computationally efficient, exploratory approach to brain connectivity incorporating false discovery rate control, a priori knowledge, and group inference*” proposes a multisubject, exploratory brain connectivity modeling approach. The proposed method allows for the incorporation of prior knowledge of connectivity and the determination of the dominant brain connectivity pattern among a group of subjects.

*Fabrizio De Vico Fallani  
Danielle Bassett  
Tianzi Jiang*

## Research Article

# A Computationally Efficient, Exploratory Approach to Brain Connectivity Incorporating False Discovery Rate Control, *A Priori* Knowledge, and Group Inference

Aiping Liu,<sup>1</sup> Junning Li,<sup>2</sup> Z. Jane Wang,<sup>1</sup> and Martin J. McKeown<sup>1,3</sup>

<sup>1</sup>Department of Electrical and Computer Engineering, University of British Columbia, Vancouver, BC, Canada V6T 1Z4

<sup>2</sup>Laboratory of Neuro Imaging, Department of Neurology, UCLA School of Medicine, Los Angeles, CA 90095, USA

<sup>3</sup>Division of Neurology, Department of Medicine and Pacific Parkinson's Research Centre, University of British Columbia, Vancouver, BC, Canada V5Z 1M9

Correspondence should be addressed to Z. Jane Wang, zjanew@ece.ubc.ca

Received 18 March 2012; Revised 6 July 2012; Accepted 10 July 2012

Academic Editor: Tianzi Jiang

Copyright © 2012 Aiping Liu et al. This is an open access article distributed under the Creative Commons Attribution License, which permits unrestricted use, distribution, and reproduction in any medium, provided the original work is properly cited.

Graphical models appear well suited for inferring brain connectivity from fMRI data, as they can distinguish between direct and indirect brain connectivity. Nevertheless, biological interpretation requires not only that the multivariate time series are adequately modeled, but also that there is accurate error-control of the inferred edges. The  $PC_{fdr}$  algorithm, which was developed by Li and Wang, was to provide a computationally efficient means to control the false discovery rate (FDR) of computed edges asymptotically. The original  $PC_{fdr}$  algorithm was unable to accommodate *a priori* information about connectivity and was designed to infer connectivity from a single subject rather than a group of subjects. Here we extend the original  $PC_{fdr}$  algorithm and propose a multisubject, error-rate-controlled brain connectivity modeling approach that allows incorporation of prior knowledge of connectivity. In simulations, we show that the two proposed extensions can still control the FDR around or below a specified threshold. When the proposed approach is applied to fMRI data in a Parkinson's disease study, we find robust group evidence of the disease-related changes, the compensatory changes, and the normalizing effect of L-dopa medication. The proposed method provides a robust, accurate, and practical method for the assessment of brain connectivity patterns from functional neuroimaging data.

## 1. Introduction

The interaction between macroscopic brain regions has been increasingly recognized as being vital for understanding the normal brain function and the pathophysiology of many neuropsychiatric diseases. Brain connectivity patterns derived from neuroimaging methods are therefore of great interest, and several recently published reviews have described different modeling methods for inferring brain connectivity from fMRI data [1, 2]. Specifically, graphical models which represent statistical dependence relationships between time series derived from brain regions, such as structural equation models [3], dynamic causal models [4], and Bayesian networks [5], appear to be well suited for assessing connectivity between brain regions.

Graphical models, when applied to functional neuroimaging data, represent brain regions of interest (ROIs) as nodes and the stochastic interactions between ROIs as edges. However, in most nonbrain imaging graphical model applications, the primary goal is to create a model that fits the overall multivariate data well, does not necessarily accurately reflect the particular connections between nodes. Yet in the applications of graphical models to brain connectivity, the neuroscientific interpretation is largely based on the pattern of connections inferred by the model. This places a premium on accurately determining the "inner workings" of the model such as accounting for the error rate of the edges in the model.

The false discovery rate (FDR) [6, 7], defined as the expected ratio of spurious connections to all learned

connections, has been suggested as a suitable error-rate control criterion when inferring brain connectivity. Compared with traditional type I and type II statistical error rates, the FDR is more informative in bioinformatics and neuroimaging, since it is directly related with the uncertainty of the reported positive results. When selecting candidate genes for genetic research, for example, researchers may want 70% of selected genes to be truly associated with the disease, that is, an FDR of 30%.

Naively controlling traditional type I and type II error rates at specified levels may not necessarily result in reasonable FDR rates, especially in the case of large, sparse networks. For example, consider an undirected network with 40 nodes, with each node interacting, on average, with 3 other nodes; that is, there are 60 edges in the network. An algorithm with the *realized* type I error rate of 5% and the *realized* power of 90% (i.e., the *realized* type II error rate = 10%) will recover a network with  $60 \times 90\% = 54$  correct connections and  $[40 \times (40 - 1)/2 - 60] \times 5\% = 36$  false connections, which means that  $36/(36 + 54) = 40\%$  of the claimed connections actually would not exist in the true network! This example, while relatively trivial, demonstrates that the FDR may not be kept suitably low by simply controlling traditional type I and type II error rates.

Recent work in the machine learning field has started to investigate controlling the FDR in network structures using a generic Bayesian approach and classical FDR assessment [8]. This work was subsequently extended to look specifically at graphical models where the FDR was assessed locally at each node [9].

Li and Wang proposed a network-learning method that allows asymptotically control of the FDR globally. They based their approach on the PC algorithm (named after Peter Spirtes and Clark Glymour), a computationally efficient and asymptotically reliable Bayesian network-learning algorithm. The PC algorithm assesses the (non)existence of an edge in a graph by determining the conditional dependence/independence relationships between nodes [10]. However, different from the original PC algorithm, which controls the type I error rate individually for each edge during conditional independence testing, the Li and Wang algorithm, referred as the  $PC_{fdr}$  algorithm, is capable of asymptotically controlling the FDR under prespecified levels [11]. The  $PC_{fdr}$  algorithm does this by interpreting the learning of a network as testing the existence of edges, and thus the FDR control of edges becomes a multiple-testing problem, which has a strong theoretical basis and has been extensively studied by statisticians [11].

Beside giving an introduction of these recent advancements, this paper will present two extensions to the original  $PC_{fdr}$  algorithm, the combination of which leads to a multi-subject brain connectivity modeling approach incorporating FDR control, *a priori* knowledge and group inference. One extension is an adaptation of *a priori* knowledge, allowing users to specify which edges must appear in the network, which cannot and which are to be learned from data. The resulting algorithm is referred to as  $PC_{fdr}^+$  algorithm in this paper. Many applications require imposing prior knowledge into network learning. For example, analyzing

causal relationship in time series may forbid backward connections from time  $t + 1$  to  $t$ , such as that in dynamic Bayesian networks. In some situations, researchers may want to exclude some impossible connections based on anatomical knowledge. Incorporating *a priori* knowledge into  $PC_{fdr}$  algorithm allows for more flexibility in using the method and potentially leads to greater sensitivity in accurately discovering the true brain connectivity.

The second extension to  $PC_{fdr}$  algorithm is a combination of the  $PC_{fdr}$  algorithm and a mixed-effect model to robustly deal with intersubject variability. As neuroimaging research typically involves a group of subjects rather than focusing on an individual subject, group analysis plays an important role in final biological interpretations. However, compared with the extensive group-level methods available for analysis of amplitude changes in blood-oxygen-level-dependent (BOLD) signals (e.g., Worsley et al. [12], Friston et al. [13]), the problem of group-level brain connectivity analysis is less well studied. This is likely due to the fact that it requires not only accommodating the variances and the correlations across subjects, but also accounting for the potentially different structures of subject-specific brain connectivity networks. The proposed group-level exploratory approach for brain connectivity inference combines the  $PC_{fdr}$  algorithm (or the extended  $PC_{fdr}^+$  algorithm if *a priori* knowledge is available) and a mixed-effect model, a widely used method for handling intersubject variability.

Several methods have been proposed to infer group connectivity in neuroimaging. Bayesian model selection [14] handles intersubject variability and error control; however, its current proposed implementation does not scale well, making it more suitable for confirmatory, rather than an exploratory research. Varoquaux et al. [15] propose a data-driven method to estimate large-scale brain connectivity using Gaussian modeling and deals with the variability between subjects by using optimal regularization schemes. Ramsey et al. [16] describe and evaluate a combination of a multisubject search algorithm and the orientation algorithm.

The major distinguishing feature of the proposed approach compared to these aforementioned approaches is that the current data-driven approach aims at controlling the FDR directly at the group-level network. We demonstrate that in simulations that, with a sufficiently large subject size, the proposed group-level algorithm is able to reliably recover network structures and still control the FDR around prespecified levels. When the proposed approach, referred as the  $gPC_{fdr}^+$  algorithm, is applied to real fMRI data with Parkinson's disease, we demonstrate evidence of direct and indirect (i.e., compensatory) disease-related connectivity changes, as well as evidence that L-dopa provides a "normalizing" effect on connectivity in Parkinson's disease, consistent with its dramatic clinical effect.

## 2. Materials and Methods

**2.1. Preliminaries.** Graphical models, such as Bayesian networks, encode conditional independence/dependence relationships among variables graphically with nodes and edges

according to the Markov properties [17]. The concept of conditional (in)dependence is very important for the inference of brain connectivity, as it assists in distinguishing between direct and indirect connectivity. For example, the activities in two brain regions are initially correlated, but become independent after all possible influences from other brain regions are removed, then this is an example of indirect connectivity, as the initial activity was actually induced by common input from another region(s). On the other hand, if the activities of two brain regions are correlated even after all possible influences from other regions are removed, then very likely there is a direct functional connection between them and hence is an example of direct connectivity. Conditional dependence is the real interest in learning brain connectivity because it implies that two brain regions are directly connected.

Since a graphical model is a graphical representation of conditional independence/dependence relationships, the nonadjacency between two nodes is tested by inspecting their conditional independence given all other nodes. As multiple edges are tested simultaneously, FDR-control procedures should be applied to correct the effect of multiple testing.

Given two among  $N$  random variables, there are  $2^{N-2}$  possible subsets of the other  $N - 2$  variables upon which the two variables could be conditionally independent. To avoid exhaustively testing such an exponential number of conditional independence relationships, the following proposition [10] can be employed [9, 11].

**Proposition 1.** *Given a multivariate probability distribution whose conditional independence relationships can be perfectly encoded as a Bayesian network according to the Markov property, two nodes  $a$  and  $b$  are nonadjacent if and only if there is a subset  $C$  of nodes either all in the neighbors of  $a$  or all in the neighbors of  $b$  such that  $a$  and  $b$  are conditionally independent on given  $C$ .*

Based on Proposition 1, nodes  $a$  and  $b$  can be disconnected once they are found conditionally independent upon a conditional node set  $C$ . As the tests of adjacency progress for every node pair, the neighborhood of nodes keeps shrinking, so an exhaustive search of the conditional node set  $C$  is avoided. This greatly reduces computation, especially for a sparse network.

## 2.2. Brain Connectivity Inference Incorporating False Discovery Rate Control and A Priori Knowledge

**2.2.1.  $PC_{\text{fdr}}^+$  Algorithm.** The initial version of Li and Wang's [11] method, called the  $PC_{\text{fdr}}$  algorithm, was proved to be capable of asymptotically controlling the FDR. Here we present an extension of the  $PC_{\text{fdr}}$  algorithm which can incorporate *a priori* knowledge, which was not specified in the original  $PC_{\text{fdr}}$  algorithm. We name the extension as the  $PC_{\text{fdr}}^+$  algorithm where the superscript “+” indicates that it is an extension. The pseudocode of the  $PC_{\text{fdr}}^+$  algorithm is given in Algorithm 1, and its Matlab implementation is downloadable at <http://www.junningli.org/software>. It

handles prior knowledge with two inputs:  $E_{\text{must}}$ , the set of edges assumed to appear in the true graph, and  $E_{\text{test}}$ , the set of edges to be tested from the data. The original  $PC_{\text{fdr}}$  algorithm can thus be regarded as a special case of the extended algorithm, by setting  $E_{\text{must}} = \emptyset$  and  $E_{\text{test}} = \{\text{all possible edges}\}$ .

**2.2.2. Asymptotic Performance.** Before we present theorems about the asymptotic performance of the  $PC_{\text{fdr}}^+$  algorithm and its heuristic modification, let us first introduce the assumptions related to the theorems.

- (A1) The multivariate probability distribution  $P$  is faithful to a directed acyclic graph (DAG) whose skeleton is  $G_{\text{true}}$ .
- (A2) The number of vertices is fixed.
- (A3) Given a fixed significance level of testing conditional independence, the power of detecting conditional dependence approaches 1 at the limit of large sample sizes.
- (A4) The union of  $E_{\text{must}}$ , the edges assumed to be true, and  $E_{\text{test}}$ , the edges to be tested, covers  $E_{\text{true}}$ , all the true edges; that is,  $E_{\text{test}} \cup E_{\text{must}} \supseteq E_{\text{true}}$ .

Assumption (A1) is generally assumed when graphical models are applied, and it restricts the probability distribution  $P$  to a certain class. Assumption (A2) is usually implicitly stated, but here we emphasize it because it simplifies the proof. Assumption (A3) may seem overly restrictive, but actually can be easily satisfied by standard statistical tests, such as the likelihood ratio test introduced by Neyman and Pearson [18] and the partial-correlation test by Fisher [19], if the data are identically and independently sampled. Assumption (A4) relates to prior knowledge, which interestingly does not require that the assumed “true” edges  $E_{\text{must}}$  be a subset of the true edges  $E_{\text{true}}$ , but just that all true edges are included in the union of the assumed “true” edges and the edges to be tested.

The detection power of the  $PC_{\text{fdr}}^+$  algorithm and its heuristic modification at the limit of large sample sizes is elucidated in Theorem 2.

**Theorem 2.** *Assuming (A1), (A2), and (A3), both the  $PC_{\text{fdr}}^+$  algorithm and its heuristic modification, the  $PC_{\text{fdr}}^{+*}$  algorithm, are able to recover all the true connections in  $E_{\text{test}}$  with probability one as the sample size approaches infinity:*

$$\lim_{m \rightarrow \infty} P(E'_{\text{true}} \subseteq E'_{\text{stop}}) = 1, \quad (1)$$

where  $E'_{\text{true}}$  denotes the set of true edges in  $E_{\text{test}}$ ; that is,  $E'_{\text{true}} = E_{\text{true}} \cap E_{\text{test}}$ ;  $E'_{\text{stop}}$  denotes the set of edges inferred by the algorithm about  $E_{\text{test}}$ ; that is,  $E'_{\text{stop}} = E_{\text{stop}} \cap E_{\text{test}}$ , and  $m$  denotes the sample size.

It should be noted that Theorem 2 does not need Assumption (A4), which implies that the true edges in  $E_{\text{test}}$  are still able to be recovered by the algorithms with probability one at the limit of large sample sizes, even if

**Input:** the data  $D$ , the undirected edges  $E_{\text{must}}$  that are assumed to exist in the true undirected graph  $G_{\text{true}}$  according to prior knowledge, the undirected edges  $E_{\text{test}}$  ( $E_{\text{must}} \cap E_{\text{test}} = \emptyset$ ) to be tested from the data  $D$ , and the FDR level  $q$  for making inference about  $E_{\text{test}}$ .

**Output:** an undirected graph  $G_{\text{stop}}$ , that is, the value of  $G$  when the algorithm stops, or equivalently,  $E_{\text{stop}}$ , the edges in  $G_{\text{stop}}$ .

**Notations:**  $D$  denotes the multivariate input data.  $a, b$  denote the vertices.  $E, C$  denote the vertex sets.  $a \sim b$  denotes an undirected edge.  $\text{adj}(a, G)$  denotes vertices adjacent to  $a$  in graph  $G$ .  $a \perp b | C$  denotes the conditional independence between  $a$  and  $b$  given  $C$ .

- (1) Form an undirected graph  $G$  from  $E_{\text{test}} \cup E_{\text{must}}$ .
- (2) Initialize the maximum  $p$  values associated with the edges in  $E_{\text{test}}$  as  $P^{\text{max}} = \{p_{a \sim b}^{\text{max}} = -1 \mid a \sim b \in E_{\text{test}}\}$ .
- (3) Let depth  $d = 0$ .
- (4) **repeat**
- (5)   **for** each ordered pair of vertices  $a$  and  $b$  that  $a \sim b \in E \cap E_{\text{test}}$  and  $|\text{adj}(a, G) \setminus \{b\}| \geq d$  **do**
- (6)     **for** each subset  $C \subseteq \text{adj}(a, G) \setminus \{b\}$  and  $|C| = d$  **do**
- (7)       Test hypothesis  $a \perp b | C$  and calculate the  $p$  value  $p_{a \perp b | C}$ .
- (8)       **if**  $p_{a \perp b | C} > p_{a \sim b}^{\text{max}}$ , **then**
- (9)         Let  $p_{a \sim b}^{\text{max}} = p_{a \perp b | C}$ .
- (10)       **if** every element of  $P^{\text{max}}$  has been assigned a valid  $p$  value by step 9, **then**
- (11)         Run the FDR procedure, Algorithm 2, with  $P^{\text{max}}$  and  $q$  as the input.
- (12)         **if** the non-existence of certain edges are accepted, **then**
- (13)         Remove these edges from  $G$ .
- (14)         Update  $G$  and  $E$ .
- (15)         **if**  $a \sim b$  is removed, **then**
- (16)         **break** the **for** loop at line 6.
- (17)         **end if**
- (18)       **end if**
- (19)       **end if**
- (20)       **end if**
- (21)     **end for**
- (22) **end for**
- (23) Let  $d = d + 1$ .
- (24) **until**  $|\text{adj}(a, G) \setminus \{b\}| < d$  for every ordered pair of vertices  $a$  and  $b$  that  $a \sim b$  is in  $E \cap E_{\text{test}}$ .

A heuristic modification, named the  $\text{PC}_{\text{fdr}}^+$  algorithm, at step 14 removes  $p_{a \sim b}^{\text{max}}$  from  $P^{\text{max}}$  as well once  $a \sim b$  is removed from  $G$ .

ALGORITHM 1: The  $\text{PC}_{\text{fdr}}^+$  algorithm.

the edges assumed to be present by users are not completely correctly specified.

The FDR of the  $\text{PC}_{\text{fdr}}^+$  algorithm at the limit of large sample sizes is elucidated in Theorem 3.

**Theorem 3.** *Assuming (A1), (A2), (A3), and (A4), the FDR of the set of edges inferred by the  $\text{PC}_{\text{fdr}}^+$  algorithm about  $E_{\text{test}}$  approaches a value not larger than the user-specified level  $q$  as the sample size  $m$  approaches infinity:*

$$\limsup_{m \rightarrow \infty} \text{FDR}(E'_{\text{stop}}, E'_{\text{true}}) \leq q, \quad (2)$$

where  $\text{FDR}(E'_{\text{stop}}, E'_{\text{true}})$  is defined as

$$\text{FDR}(E'_{\text{stop}}, E'_{\text{true}}) = E \left[ \frac{|E'_{\text{stop}} \setminus E'_{\text{true}}|}{|E'_{\text{stop}}|} \right], \quad (3)$$

$$\text{Define } \frac{|E'_{\text{stop}} \setminus E'_{\text{true}}|}{|E'_{\text{stop}}|} = 0, \quad \text{if } E'_{\text{stop}} = \emptyset.$$

Theorem 3 concerns the  $\text{PC}_{\text{fdr}}^+$  algorithm, and it requires Assumption (A4). We are still not sure whether similar

FDR performance can be proved for the  $\text{PC}_{\text{fdr}}^+$  algorithm. Assumption (A4) does not require that the assumed “true” edges  $E_{\text{must}}$  is a subset of the true edges  $E_{\text{true}}$  but only that all true edges are included in the union of the assumed “true” edges and the edges to be tested. This is particularly useful in practice, since it does not require users’ prior knowledge to be absolutely correct, but allows some spurious edges to be involved in  $E_{\text{must}}$ , once all true edges have been included in either  $E_{\text{must}}$  or  $E_{\text{test}}$ . Assumption (A4) can be satisfied by making  $E_{\text{test}} \cup E_{\text{must}}$  large enough to cover all the true edges, but as shown in (4) this will increase the computational cost of the algorithm.

Theorems 2 and 3 address the performance of the  $\text{PC}_{\text{fdr}}^+$  algorithm and its heuristic modification at the limit of large sample sizes. Because the  $\text{PC}_{\text{fdr}}^+$  algorithm is derived from the  $\text{PC}_{\text{fdr}}$  algorithm, its performance should be very similar. The numerical examples of the  $\text{PC}_{\text{fdr}}$  algorithm in Li and Wang’s [11] work may provide helpful and intuitive understanding on the performance of the  $\text{PC}_{\text{fdr}}^+$  algorithm with moderate sample sizes.

The detailed proofs of Theorems 2 and 3 are provided in Appendix A.

**Input:** a set of  $p$  values  $\{p_i \mid i = 1, \dots, H\}$ , and the threshold of the FDR  $q$   
**Output:** the set of rejected null hypotheses  
(1) Sort the  $p$ -values of  $H$  hypothesis tests in the ascendant order as  $p_{(1)} \leq \dots \leq p_{(H)}$ .  
(2) Let  $i = H$ , and  $H^* = H$  (or  $H^* = H(1 + 1/2, \dots, +1/H)$ , depending on the assumption of the dependency among the test statistics).  
(3) **while**

$$\frac{H^*}{i} p_{(i)} > q \text{ and } i > 0, \quad (*)$$

**do**  
(4) Let  $i = i - 1$ .  
(5) **end while**  
(6) Reject the null hypotheses associated with  $p_{(1)}, \dots, p_{(i)}$ , and accept the null hypotheses associated with  $p_{(i+1)}, \dots, p_{(H)}$ .

ALGORITHM 2: FDR setup [6].

**2.2.3. Computational Complexity.** The majority of the computational effort in the  $\text{PC}_{\text{fdr}}^+$  is utilized in performing statistical tests of conditional independence at step 7 and the FDR at step 11. If the algorithm stops at the depth  $d = d_{\max}$ , then the number of conditional independence tests required is bounded by

$$T = 2|E_{\text{test}}| \sum_{d=0}^{d_{\max}} C_{\Delta-1}^d \leq |E_{\text{test}}| 2^\Delta, \quad (4)$$

where  $|E_{\text{test}}|$  is the number of edges to be tested,  $\Delta$  is the maximum degree of graph  $G_{\text{init}}$  (the graph formed at step 1) whose edges are  $E_{\text{must}} \cap E_{\text{test}}$ , and  $C_{\Delta-1}^d$  is the number of combinations of choosing  $d$  unordered and distinct elements from  $\Delta - 1$  elements. The bound usually is very loose, because it assumes that no edge has been removed until  $d = d_{\max}$ .

The computational complexity of the FDR procedure, Algorithm 2, invoked at step 11 of the  $\text{PC}_{\text{fdr}}^+$  algorithm is  $O(H \log(H))$  when it is invoked for the first time, where  $H = |E_{\text{test}}|$  is the number of input  $p$  values and is  $O(H)$  later, with the optimization suggested in Appendix B. In the worst case that  $p_{a \perp b | C}$  is always larger than  $p_{a \sim b}^{\max}$ , the complexity of the computation spent on the FDR control in total is bounded by  $O(|E_{\text{test}}| \log(|E_{\text{test}}|) + T|E_{\text{test}}|)$  where  $T$  is the number of performed conditional independence tests (see (4)). This is a very loose bound because it is rare that  $p_{a \perp b | C}$  is always larger than  $p_{a \sim b}^{\max}$ .

In practice, the  $\text{PC}_{\text{fdr}}^+$  algorithm runs very quickly, especially for sparse networks. In our experiments (see Section 3.1), it took about 10 seconds to infer the structure of a first-order dynamic network with 20 nodes from data of 1000 time points.

**2.2.4. Miscellaneous Discussions.** It should be noted that controlling the FDR locally is not equivalent to controlling it globally. For example, if it is known that there is only one connection to test for each node, then controlling the FDR locally in this case will degenerate to controlling the point-wise error rate, which cannot control the FDR globally.

Listgarten and Heckerman [8] proposed a permutation method to estimate the number of spurious connections in a graph learned from data. The basic idea is to repetitively

apply a structure learning algorithm to data simulated from the null hypotheses with permutation. This method is generally applicable to any structure learning method, but permutation may make the already time-consuming structure learning problem even more computationally cumbersome, limiting its use in practical situations.

**2.3. FDR-Controlled Group Brain Connectivity Inference with or without A Priori Knowledge.** In this section, we propose another extension to the  $\text{PC}_{\text{fdr}}$  algorithm: from the single subject level to the group level. Assessing group-level activity is done by considering a mixed-effect model (Step 7 of Algorithm 3), and we name it the  $\text{gPC}_{\text{fdr}}$  algorithm where “g” indicates that it is an extension at the group level. When also incorporating *a priori* knowledge, the resulting algorithm is named the  $\text{gPC}_{\text{fdr}}^+$  algorithm.

Suppose we have  $m$  subjects within a group. Then for subject  $i$ , the conditional independence between the activities of two brain regions  $a$  and  $b$  given other regions  $C$  can be measured by the partial correlation coefficient between  $X_a(i)$  and  $X_b(i)$  given  $X_C(i)$ , denoted as  $r_{ab|C}(i)$ . Here  $X_\bullet$  denotes variables associated with a vertex or a vertex set, and index  $i$  indicates that these variables are for subject  $i$ . By definition, the partial correlation coefficient  $r_{ab|C}(i)$  is the correlation coefficient between the residuals of projecting  $X_a(i)$  and  $X_b(i)$  onto  $X_C(i)$  and can be estimated by the sample correlation coefficient as

$$\hat{r}_{ab|C}(i) = \frac{\text{Cov}[Y_{a|C}(i), Y_{b|C}(i)]}{\sqrt{\text{Var}[Y_{a|C}(i)] \text{Var}[Y_{b|C}(i)]}}, \quad (5)$$

where

$$\beta_{a|C}(i) = \arg \min_{\beta} |X_a(i) - X_C(i)\beta|^2, \\ \beta_{b|C}(i) = \arg \min_{\beta} |X_b(i) - X_C(i)\beta|^2, \quad (6)$$

$$Y_{a|C}(i) = X_a(i) - X_C(i)\beta_{a|C}(i),$$

$$Y_{b|C}(i) = X_b(i) - X_C(i)\beta_{b|C}(i).$$

For clarity, in the following discussion we omit the subscript “ $ab \mid C$ ” and simply use index “ $i$ ” to emphasize that a variable is associated with subject  $i$ .

**Input:** the multisubject data  $D$ , undirected complete graph  $G$ , complete vertex set  $E$  and the FDR controlled level  $q$  for making inference about  $E$ .

**Output:** the recovered undirected graph  $G_{\text{stop}}$ .

**Notations:**  $a, b$  denote the vertices.  $E, C$  denote the vertex set.  $a \sim b$  denotes an undirected edge.  $\text{adj}(a, G)$  denotes vertices adjacent to  $a$  in graph.  $a \perp b \mid C$  denotes the conditional independence between  $a$  and  $b$  given  $C$ .

- (1) Form an undirected graph  $G$  on the vertex set  $E$ .
- (2) Initialize the maximum  $p$  values associated with the edges in  $E$  as  $P^{\max} = \{p_{a \sim b}^{\max} = -1 \mid a \sim b \in E\}$ .
- (3) Let depth  $d = 0$ .
- (4) **repeat**
- (5)   **for** each ordered pair of vertices  $a$  and  $b$  that  $a \sim b \in E \cap E$  and  $|\text{adj}(a, G) \setminus \{b\}| \geq d$  **do**
- (6)     **for** each subset  $C \subseteq \text{adj}(a, G) \setminus \{b\}$  and  $|C| = d$  **do**
- (7)       Test hypothesis  $a \perp b \mid C$  for each subject and calculate the  $p$  value  $p_{a \perp b \mid C}$  at the **group level**.
- (8)       **if**  $p_{a \perp b \mid C} > p_{a \sim b}^{\max}$ , **then**
- (9)         Let  $p_{a \sim b}^{\max} = p_{a \perp b \mid C}$ .
- (10)       **if** every element of  $P^{\max}$  has been assigned a valid  $p$  value by step 9, **then**
- (11)         Run the FDR procedure, Algorithm 2, with  $P^{\max}$  and  $q$  as the input.
- (12)       **if** the non-existence of certain edges are accepted, **then**
- (13)         Remove these edges from  $G$ .
- (14)         Update  $G$  and  $E$ .
- (15)       **if**  $a \sim b$  is removed, **then**
- (16)         **break** the **for** loop at line 6.
- (17)       **end if**
- (18)     **end if**
- (19)   **end if**
- (20)   **end if**
- (21)   **end for**
- (22) **end for**
- (23)   Let  $d = d + 1$ .
- (24) **until**  $|\text{adj}(a, G) \setminus \{b\}| < d$  for every ordered pair of vertices  $a$  and  $b$  that  $a \sim b$  is in  $E$ .

**Note:** When *a priori* knowledge is available, we can also incorporate the prior knowledge into the  $\text{gPC}_{\text{fdr}}$  algorithm to obtain the  $\text{gPC}_{\text{fdr}}^+$  algorithm, where the inputs are updated as follows: the multisubject data  $D$ , the undirected edges  $E_{\text{must}}$  that are assumed to appear in the true undirected graph  $G_{\text{true}}$  according to prior knowledge, the undirected edges  $E_{\text{test}}$  whose existences are to be tested from the data, and the FDR controlled level  $q$  for making inference about  $E_{\text{test}}$ .

ALGORITHM 3: The  $\text{gPC}_{\text{fdr}}$  algorithm.

To study the group-level conditional independence relationships, a group-level model should be introduced for  $r_i$ . Since partial correlation coefficients are bounded and their sample distributions are not Gaussian, we apply Fisher's  $z$ -transformation to convert (estimated) partial correlation coefficients  $r$  to a Gaussian-like distributed  $z$ -statistic  $z$ , which is defined as

$$z = Z(r) = \frac{1}{2} \ln \left( \frac{1+r}{1-r} \right), \quad (7)$$

where  $r$  is a (estimated) partial correlation coefficient and  $z$  is its  $z$ -statistic.

The group model we employ is

$$z_i = z_g + e_i, \quad (8)$$

where  $e_i$  follows a Gaussian distribution  $N(0, \sigma_g^2)$  with zero mean and  $\sigma_g^2$  variance. Consequently, the group-level testing of conditional independence is to be used to test the null hypothesis  $z_g = 0$ .

Because  $z_i$  is unknown and can only be estimated, the inference of  $z_g$  should be conducted with  $\hat{z}_i = Z(\hat{r}_i)$ . If

$X_a(i)$ ,  $X_b(i)$ , and  $X_C(i)$  jointly follow a multivariate Gaussian distribution, then  $\hat{z}_i$  asymptotically follows a Gaussian distribution  $N(z_i, \sigma_i^2)$  with  $\sigma_i^2 = 1/(N_i - p - 3)$ , where  $N_i$  is the sample size of subject  $i$ 's data and  $p$  represents the number of variables in  $X_C(i)$ . Therefore, based on (8), we have

$$\hat{z}_i = z_g + e_i + \epsilon_i, \quad (9)$$

where  $\epsilon_i$  follows  $N(0, \sigma_i^2)$  and  $e_i$  follows  $N(0, \sigma_g^2)$ . This is a mixed-effect model where  $\epsilon_i$  denotes the intrasubject randomness and  $e_i$  denotes the intersubject variability. At the group level,  $\hat{z}_i$  follows a Gaussian distribution  $N(z_g, \sigma_i^2 + \sigma_g^2)$ . Note that unlike regular mixed-effect models, the intrasubject variance  $\sigma_i^2$  in this model is known, because  $N_i$  and  $p$  are known given the data  $X(i)$  and  $C$ . In general,  $\sigma_i^2 = 1/(N_i - p - 3)$  is not necessarily equal to  $\sigma_j^2$  for  $i \neq j$ , and the inference of  $z_g$  should be conducted in the manner of mixed models, such as estimating  $\sigma_g^2$  with the restricted maximum likelihood (ReML) approach. However, if the sample size of each subject's data is the same, then  $\sigma_i^2$  equals  $\sigma_j^2$ . For this balanced case, which is typically true in fMRI applications

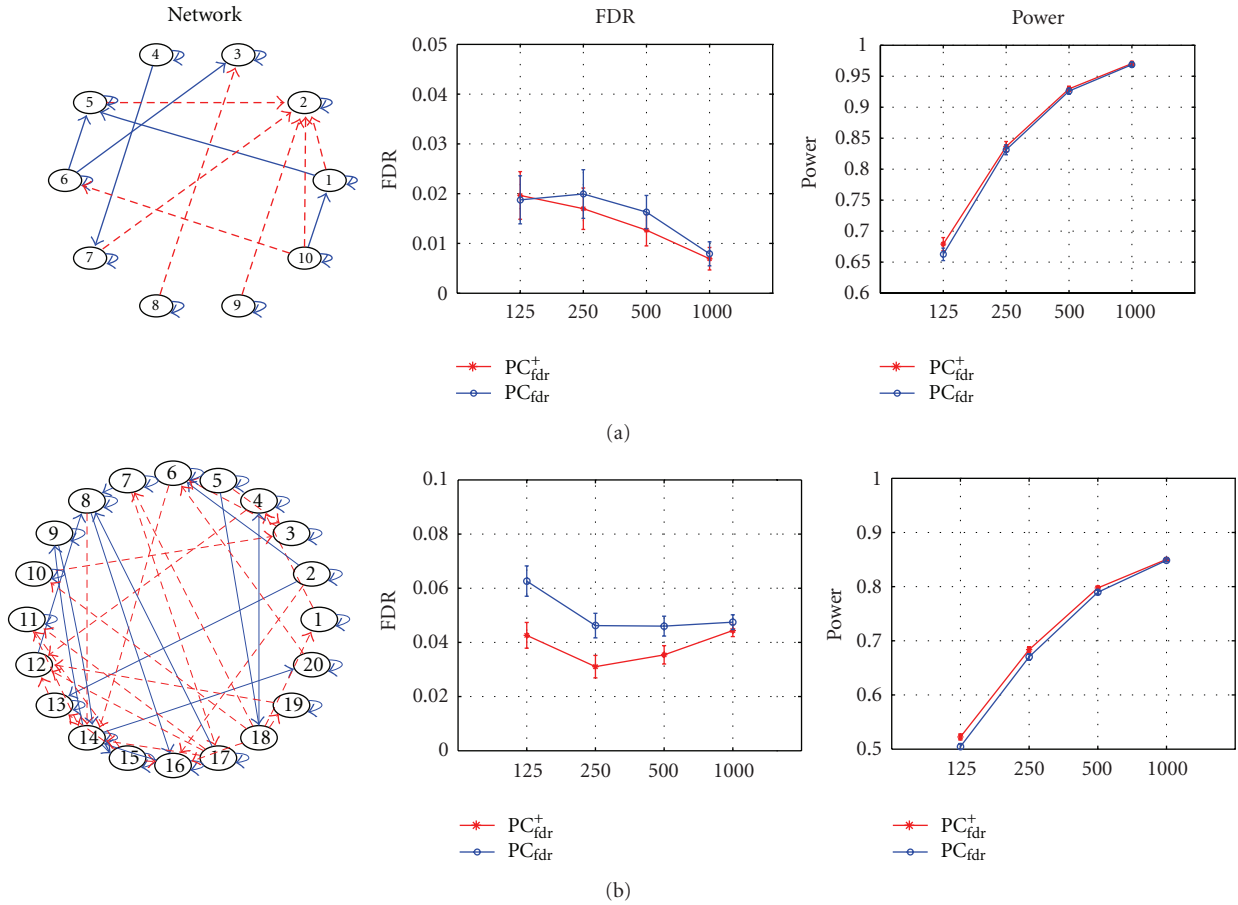


FIGURE 1: Simulation results for the  $PC_{fdr}^+$  algorithm. (a) Simulation results for the network with 10 nodes and 23 edges. (b) Simulation results for the network with 20 nodes and 56 edges. In the networks, solid arrows represent edges from time  $t$  to  $t+1$ , and dashed arrows represent edges with no time lag (i.e., from time  $t$  to  $t$ ). For the FDR and detection power curves, the blue solid lines represent the  $PC_{fdr}$  algorithm, the red solid lines represent the  $PC_{fdr}^+$  algorithm, the  $x$ -axis means the sample sizes, and the  $y$ -axis means the FDR or detection power.

and as well the case in this paper, we can simply apply a  $t$ -test to  $\hat{z}_i$ 's to test the null hypothesis  $z_g = 0$ .

Replacing Step 7 of the single-subject  $PC_{fdr}$  algorithm (i.e., the intrasubject hypothesis test) with the test of  $z_g = 0$ , we can extend the single-subject version of the algorithm to its group-level version. We will employ this  $t$ -test in our simulations and in the real fMRI data analysis presented later in this paper. Such a testing approach significantly simplifies the estimation process, and our simulation results presented later demonstrate that this method can still control the FDR at a user specified error rate level.

### 3. Experiments

**3.1. Simulations for the  $PC_{fdr}^+$  Algorithm.** Here we compare the performances of the proposed  $PC_{fdr}^+$  algorithm and the original  $PC_{fdr}$  algorithm, using time series generated from two dynamic Bayesian networks in Figure 1. One network has 20 nodes (10 channels) and 23 edges, and the other has 40 nodes (20 channels) and 56 edges. The dynamic Bayesian networks are assumed Gaussian, with connection coefficients

uniformly distributed in  $[0.2, 0.6]$  with Gaussian noise whose amplitudes are uniformly distributed in  $[0.5, 1.1]$ . We use partial correlation coefficients to test conditional independence relationships. The target FDR for both methods is set as 5%. For the  $PC_{fdr}^+$  algorithm, one-third of the nonexisting connections are excluded as prior knowledge.

Figure 1 shows the estimated FDR and detection power results, at sample sizes of 125, 250, 500, and 1000 time points and with 50 repetitive trials for each sample size. As shown in graphs (a) and (b), the  $PC_{fdr}^+$  and  $PC_{fdr}$  algorithms can both control the FDR under or around 5%. For both methods, the detection power increases as the sample size increases. However, we can see that the  $PC_{fdr}^+$  algorithm yields higher detection power and lower FDR than the original  $PC_{fdr}$  algorithm does. As mentioned earlier in the Introduction Section, the  $PC_{fdr}^+$  algorithm has the advantage of providing researchers more flexibility in using the method and higher accuracy in discovering brain connectivity.

**3.2. Simulations for the  $gPC_{fdr}$  Algorithm.** The simulations here serve two purposes: first, to verify whether the proposed  $gPC_{fdr}$  algorithm for modeling brain connectivity can control

the FDR at the group level, and second, to compare the  $gPC_{fdr}$  algorithm with the single-subject  $PC_{fdr}$  algorithm proposed in [11] and the state-of-art IMaGES algorithm investigated in Ramsey et al. [16] for inferring the structure of the group connectivity network.

The simulations were conducted as follows. First, a connectivity network is generated as the group-level model. Individual subject-level networks are then derived from the group-level model by randomly adding or deleting connections with a small probability, and subject-specific data are generated according to individual subject networks. Next, the network-learning methods, that is, the proposed  $gPC_{fdr}$  algorithm, the single-subject  $PC_{fdr}$  method with pooling together the data from all subjects, and the IMaGES algorithm, are applied to the simulated data. Finally, the outputs of the algorithms are compared with the true group-level network to evaluate their accuracy.

The data generation process is as follows.

- (1) Randomly generate a directed acyclic graph (DAG) as the group-level network and associate each connection with a coefficient. The DAG is generated by randomly connecting nodes with edges and then orienting the edges according to a random order of the nodes. The connection coefficients are assigned as random samples from the uniform distribution  $U(\beta_1, \beta_2)$ , where  $\beta_1$  and  $\beta_2$  characterize the coefficient strength.
- (2) For each subject, a subject-level network is derived from the group-level network by randomly adding and deleting connections. More specifically, for each of the existing connections, the connection is deleted with probability 0.05, and for each of the absent connections, a connection is added with probability 0.01. The corresponding connection coefficients are randomly sampled from the uniform distribution  $U(\beta_1, \beta_2)$ .
- (3) Given a subject-level network, the subject-specific data are generated from a Gaussian Bayesian network, with the additional Gaussian noise following the standard Gaussian distribution  $N(0, 1)$ .

In the first simulation, we compare the performances of the proposed  $gPC_{fdr}$  algorithm, the original  $PC_{fdr}$  algorithm, and the IMaGES algorithm [16], when using different connection coefficient strengths. In this example, the group-level network is the DAG in Figure 2(a). From this model, twenty subject-level models are derived, and for each subject, data with three hundred samples are simulated. To test the performances of the algorithms with a range of connection strengths, we vary the connection coefficient generating distribution  $U(\beta_1, \beta_2)$  gradually from  $U(0.2, 0.3)$  to  $U(0.7, 0.8)$ . At the network-learning stage, we set the target FDR to be 5% for the  $gPC_{fdr}$  algorithm. For reliable assessment, this procedure is repeated thirty times.

Figures 2(b), 2(c), and 2(d) show the FDR and the type I error rate, and the detection power results as a function of connection strength. We note that all methods are relatively invariant to connection strength. The proposed

$gPC_{fdr}$  algorithm steadily controls the FDR below or around the desired level and accurately makes the inference at the group level. The detection power of IMaGES algorithm is higher than that of  $gPC_{fdr}$  algorithm, but it fails to control the FDR under the specified 5% level. Its higher detection power is achieved by sacrificing FDR. This is reasonable, since IMaGES is not specifically designed to control the FDR error rate.

In the second simulation, we test the performances of the algorithms as a function of the number of subjects within the group. The group-level network is the DAG in Figure 3(a), and the number of subjects increases from eight to twenty-five. At the network-learning stage, we set the target FDR to be 5%. This procedure is repeated thirty times.

Figure 3(b) demonstrates the FDR results as a function of the number of subjects within the group. It is noted that the proposed  $gPC_{fdr}$  algorithm is able to keep the FDR below or around the specified level. The detection power gradually increases as the number of subjects increases. When there are more than 15 subjects, the  $gPC_{fdr}$  algorithm seems that it can achieve higher (better) detection power and lower (better) FDR and type I error rate than the IMaGES algorithm does. It suggests that when the number of subjects is large enough, the proposed  $gPC_{fdr}$  algorithm can jointly address efficiency, accuracy, and intersubject variability. The original  $PC_{fdr}$  algorithm of simply pooling the data together fails to control the FDR, and the resulting FDR does not decrease as the number of subject increases, probably due to the increasing heterogeneity within the group. In order to investigate the effects of the number of ROIs, we also investigate two networks with 15 and 25 nodes, respectively, and repeat the simulations (not shown here). The results are qualitatively similar to what we show here.

**3.3. fMRI Application.** In order to assess the real-world application performance of the proposed method, we apply the  $gPC_{fdr}^+$  algorithm for inferring group brain connectivity network to fMRI data collected from twenty subjects. All experiments were approved by the University of British Columbia Ethics Committee. Ten normal people and ten Parkinson's disease (PD) patients participated in the study. During the fMRI experiment, each subject was instructed to squeeze a bulb in their right hand to control an "inflatable" ring so that it smoothly passed through a vertically scrolling a tunnel. The normal controls performed only one trial, while Parkinson's subjects performed twice, once before L-dopa medication and the other approximately an hour later, after taking medication.

Three groups were categorized: group N for the normal controls, group  $P_{pre}$  for the PD patients before medication, and group  $P_{post}$  for the PD patients after taking L-dopa medication. For each subject, 100 observations were used in the network modeling. For details of the data acquisition and preprocessing, please refer to Palmer et al. [20]. 12 anatomically defined regions of interest (ROIs) were chosen based on prior knowledge of the brain regions associated with motor performance (Table 1).

We utilized the two extensions of the  $PC_{fdr}$  algorithm and learned the structures of first-order group dynamic Bayesian

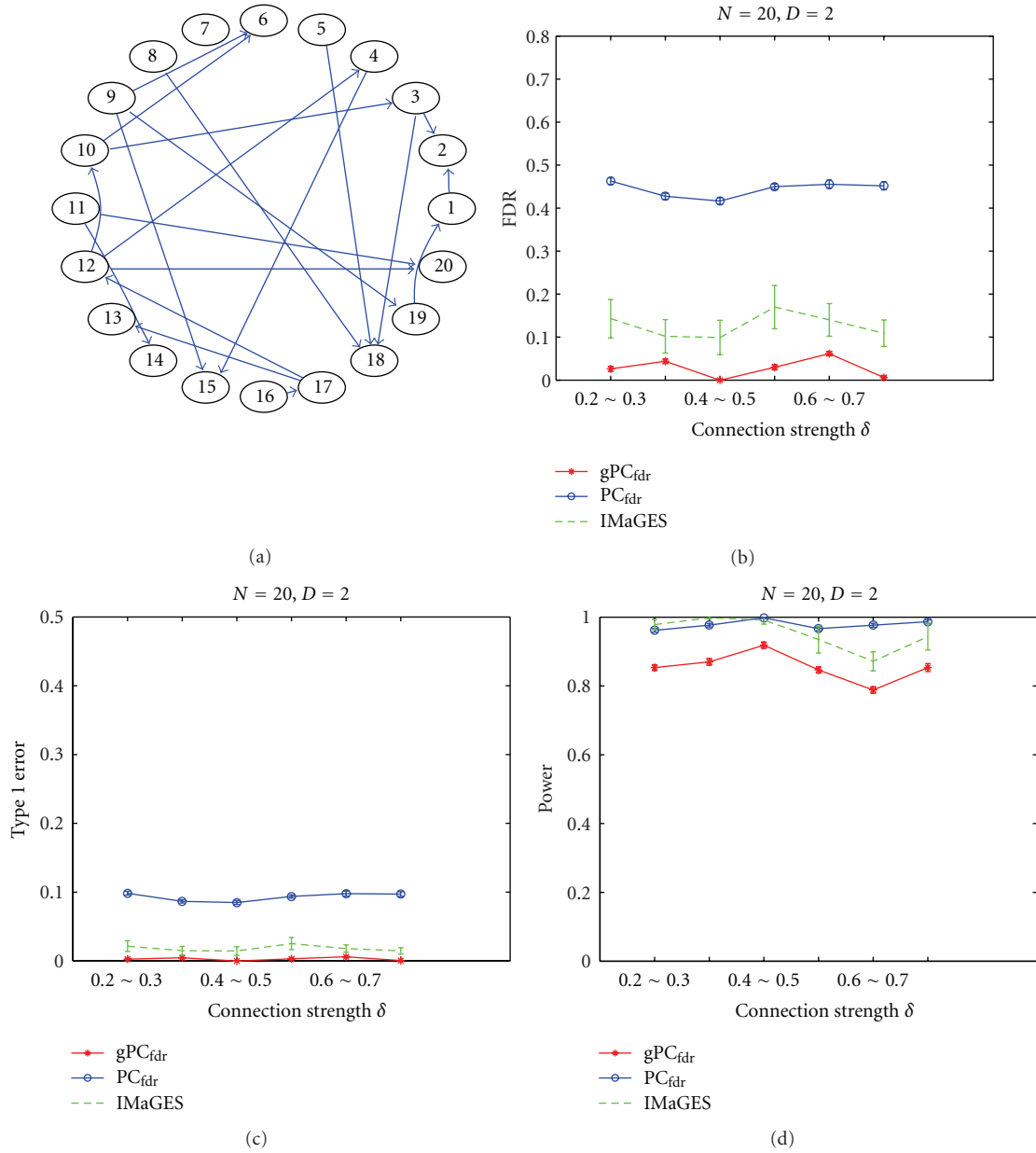


FIGURE 2: Simulation 1: assessing the effects of connection strength on the learned group networks. (a) The group-level network, with 20 nodes and an average of two connections per node. (b) The FDR curves (with standard deviation marked) of the gPC<sub>fdr</sub> algorithm, the original PC<sub>fdr</sub> algorithm by pooling all subject data together, and the IMaGES algorithm. (c) The type I error rate curves. (d) The detection power curves. The x-axis represents the generating distribution  $U(\beta_1, \beta_2)$  for sampling the connection coefficients.

networks from fMRI data. Because the fMRI BOLD signal can be considered as the convolution of underlying neural activity with a hemodynamic response function, we assumed that there must be a connection from each region at time  $t$  to its mirror at time  $t + 1$ . We also assumed that there must be a connection between each region and its homologous region in the contralateral hemisphere. The TR interval (i.e., sampling period) was a relatively long, 1.985 seconds; we restricted ourselves to learn only connections between ROIs without time lags. In total, there are  $12 + 6 = 18$  pre-defined connections and  $12 \times (12 - 1) \div 2 - 6 = 60$  candidate connections to be tested. The brain connectivity

networks (with the target FDR of 5%) learned for the normal (group N) and PD groups before (group P<sub>pre</sub>) and after (group P<sub>post</sub>) medication are compared in Figure 4. Note the connection between the cerebellar hemisphere and contralateral thalamus in the normal subjects and between the supplementary motor area (SMA) and the contralateral putamen, consistent with prior knowledge. Interestingly, in P<sub>pre</sub> subjects, the left cerebellum now connects with the right SMA, and the right SMA  $\leftrightarrow$  left putamen connection is lost. Also, there are now bilateral primary motor cortex (M1)  $\leftrightarrow$  putamen connections seen in the P<sub>pre</sub> group, presumably as a compensatory mechanism. After medication

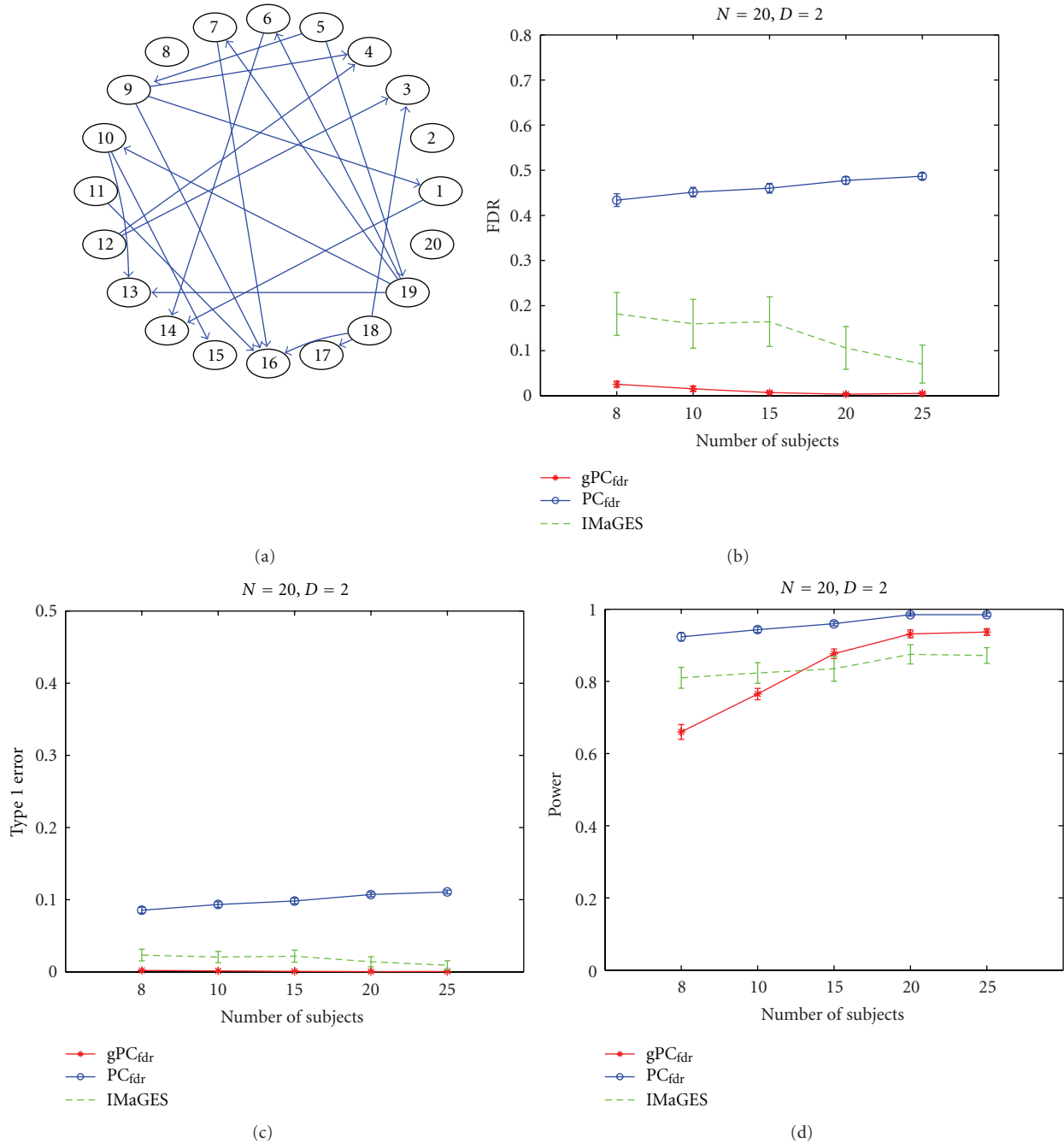


FIGURE 3: Simulation 2: assessing the effects of increasing the number of subjects on the learned group networks. (a) The group-level network, with 20 nodes and an average of two connections per node. (b) The FDR curves (with standard deviation marked) of the proposed  $gPC_{fdr}$  algorithm, the original  $PC_{fdr}$  algorithm by pooling all subject data together, and the IMaGES algorithm. (c) The type I error rate curves. (d) The detection power curves. The  $x$ -axis represents the number of subjects within the group.

( $P_{post}$ ), the left SMA  $\leftrightarrow$  left thalamus connection is restored back to be normal.

#### 4. Discussion

Up to now, graphical models to infer brain connectivity from fMRI data have implicitly relied on the unrealistic assumption that if a model accurately represented the

overall activity in several ROIs, the internal connections of such a model would accurately reflect underlying brain connectivity. The  $PC_{fdr}$  algorithm was designed to loosen this overly restrictive assumption and asymptotically control the FDR of network connections inferred from data.

In this paper, we first presented the  $PC_{fdr}^+$  algorithm, an extension of the  $PC_{fdr}$  algorithm, which allows for incorporation of prior knowledge of network structure into

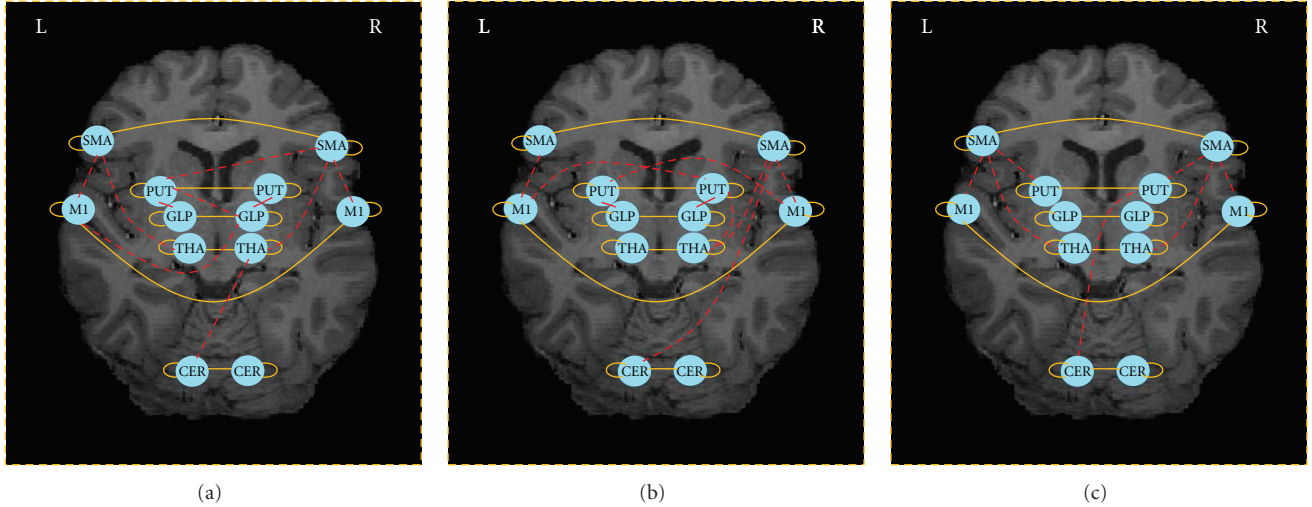


FIGURE 4: (a) Learned brain connectivity for the normal group (group N). (b) Learned brain connectivity for the PD group before medication (group  $P_{pre}$ ). (c) Learned brain connectivity for the PD group after medication (group  $P_{post}$ ). Here “L” and “R” refer to the left and right sides, respectively. The solid lines are predefined connectivity, and the dashed lines are learned connectivity.

TABLE 1: Brain regions of interest (ROIs).

Full name of brain region	Abbreviation
Left/right lateral cerebellar hemispheres	ICER, rCER
Left/right globus pallidus	IGLP, rGLP
Left/right putamen	IPUT, rPUT
Left/right supplementary motor cortex	ISMA, rSMA
Left/right thalamus	ITHA, rTHA
Left/right primary motor cortex	IMI, rM1

“l” or “r” in the abbreviations stands for “Left” or “Right,” respectively.

the learning process, greatly enhancing its flexibility in practice. The  $PC_{fdr}^+$  algorithm handles prior knowledge with two inputs:  $E_{must}$ , which is the set of edges that are assumed to appear in the true graph, and  $E_{test}$ , the set of edges that are to be tested from the observed data. We proved that, with mild assumptions and at the limit of large samples, the  $PC_{fdr}^+$  algorithm is able to recover all the true edges in  $E_{test}$  and also curb the FDR of the edges inferred about  $E_{test}$ .

It is interesting that the  $PC_{fdr}^+$  algorithm does not require the assumed “true” edges  $E_{must}$  to be a subset of the true edges  $E_{true}$ , but only that all true edges are included in the union of the assumed “true” edges and the edges to test. This is very useful in research practice, since it allows some spurious edges to be involved in  $E_{must}$ , as long as all the true edges have been included in either  $E_{must}$  or  $E_{test}$ . Users can satisfy this requirement by making  $E_{test} \cup E_{must}$  large enough to cover all the true edges.

When we compared the  $PC_{fdr}^+$  algorithm with the original  $PC_{fdr}$  algorithm, both of them successfully controlled the FDR under the target threshold in simulations, providing a practical tradeoff between computational complexity and accuracy. However, the  $PC_{fdr}^+$  algorithm achieved better detection power and better FDR than the original  $PC_{fdr}$  algorithm. Incorporating prior knowledge into  $PC_{fdr}$  algorithm

therefore enhances inference accuracy and improves the flexibility in using the method.

Another extension to  $PC_{fdr}$  algorithm we described here was the ability to infer brain connectivity patterns at the group level, with intersubject variance explicitly taken into consideration. As a combination of the  $PC_{fdr}$  algorithm and a mixed-effect model, the  $gPC_{fdr}$  algorithm takes advantage of the error control ability of the  $PC_{fdr}$  algorithm and the capability of handling intersubject variance. The simulation results suggest that the proposed method was able to accurately discover the underlying group network and steadily control the false discovery rate. Moreover, the  $gPC_{fdr}$  algorithm was shown to be much more reliable than simply pooling together the data from all subjects. This may be especially important in disease states and older subjects. Compared with the IMAges algorithm,  $gPC_{fdr}$  demonstrated better control of the FDR.

As with all group models, a limitation of the proposed  $gPC_{fdr}$  algorithm is the requirement of a sufficient number of subjects. While it is appreciated that in many biomedical applications data collection is resource intensive, and if the number of subjects is insufficient, the  $gPC_{fdr}$  algorithm may give unreliable results. Nevertheless, the group extension to the  $PC_{fdr}$  algorithm is one attempt to make brain connectivity inference using error-rate-controlled exploratory modeling.

When applying the proposed  $gPC_{fdr}^+$  to fMRI data collected from PD subjects performing a motor tracking task, we found group evidence of disease changes (e.g., loss of left cerebellar  $\leftrightarrow$  SMA connectivity), compensatory changes in PD (e.g., bilateral M1  $\leftrightarrow$  contralateral putamen connectivity), and evidence of restoration of connectivity after medication (left SMA  $\leftrightarrow$  left thalamus). The tremendous variability in clinical progression of PD is likely due to variability not only in disease rate progression, but also in variability in the magnitude of compensatory changes.

This highlights the importance of the proposed method, as it allows robust estimation of disease effects, compensatory effects, and effects of medication, all with a reasonable sample size, despite the enhanced intersubject variability seen in PD.

## Appendices

### A. Proof of Theorems

To assist the reading, we list below notations frequently used in the proof.

$V$ : all the nodes in a graph,

$G_{\text{true}}$ : the skeleton of the true underlying directed acyclic graph (DAG),

$\mathcal{A}_{a\sim b}$ : the event that edge  $a \sim b$  is in the graph recovered by the  $\text{PC}_{\text{fdr}}^+$  algorithm,

$\mathcal{A}_{E'_{\text{true}}}$ :  $\mathcal{A}_{E'_{\text{true}}} = \bigcap_{a\sim b \in E'_{\text{true}}} \mathcal{A}_{a\sim b}$ , the joint event that all the edges in  $E'_{\text{true}}$ , the true edges in  $E_{\text{test}}$ , are recovered by the  $\text{PC}_{\text{fdr}}^+$  algorithm,

$p_{a\sim b}$ : the value of  $p_{a\sim b}^{\max}$  when the  $\text{PC}_{\text{fdr}}^+$  algorithm stops,

$C_{a\sim b}^*$ : a certain vertex set that  $d$ -separates  $a$  and  $b$  in the true DAG and that is also a subset of either  $\text{adj}(a, G_{\text{true}}) \setminus \{b\}$  or  $\text{adj}(b, G_{\text{true}}) \setminus \{a\}$ , according to Proposition 1.  $C_{a\sim b}^*$  is defined only for vertex pairs that are not adjacent in  $G_{\text{true}}$ ,

$p_{a\sim b}^*$ : the  $p$  value of testing  $X_a \perp X_b \mid X_{C_{a\sim b}^*}$ . The conditional independence relationship may not be really tested during the process of the  $\text{PC}_{\text{fdr}}^+$  algorithm, but  $p_{a\sim b}^*$  can still denote the value as if the conditional independence relationship was tested,

$H^*$ : the value in  $(\star)$  in Algorithm 2 that is either  $H$  or  $H(1 + 1/2, \dots, +1/H)$ , depending on the assumption of the dependency of the  $p$  values.

**Lemma A.1.** *If  $\mathcal{A}_1(m), \dots, \mathcal{A}_K(m)$  are a finite number of events whose probabilities each approach 1 as  $m$  approaches infinity*

$$\lim_{m \rightarrow \infty} P(\mathcal{A}_i(m)) = 1, \quad (\text{A.1})$$

*then the probability of the joint of all these events approaches 1 as  $m$  approaches infinity:*

$$\lim_{m \rightarrow \infty} P\left(\bigcap_{i=1}^K \mathcal{A}_i(m)\right) = 1. \quad (\text{A.2})$$

For the proof of this lemma, please refer to Li and Wang's [11] work.

**Lemma A.2.** *If there are  $F$  ( $F \geq 1$ ) false hypotheses among  $H$  tested hypotheses and the  $p$  values of the all the false hypotheses are smaller than or equal to  $(F/H^*)q$ , where  $H^*$  is either  $H$  or  $H(1 + 1/2, \dots, +1/H)$  depending on the assumption of the dependency of the  $p$  values, then all the  $F$  false hypotheses will be rejected by the FDR procedure, Algorithm 2.*

For the proof of this lemma, please refer to Li and Wang's [11] work.

*Proof of Theorem 2.* If there is not any true edge in  $E'_{\text{true}}$ , that is,  $E'_{\text{true}} = \emptyset$ , then the proof is trivially  $E'_{\text{true}} = \emptyset \subseteq E'$ .

In the following part of the proof, we assume  $E'_{\text{true}} \neq \emptyset$ . For the  $\text{PC}_{\text{fdr}}^+$  algorithm and its heuristic modification, whenever the FDR procedure, Algorithm 2, is invoked,  $p_{a\sim b}^{\max}$  is always less than  $\max_{C \in V \setminus \{a,b\}} \{p_{a\sim b|C}\}$ , and the number of  $p$  values input to the FDR algorithm is always not more than  $|E_{\text{test}}|$ . Thus, according to Lemma 5, if

$$\max_{a\sim b \in E'_{\text{true}}} \left\{ \max_{C \in V \setminus \{a,b\}} \{p_{a\sim b|C}\} \right\} \leq \frac{|E'_{\text{true}}|}{|E_{\text{test}}| \sum_{i=1}^{|E_{\text{test}}|} (1/i)} q, \quad (\text{A.3})$$

then all the true connections will be recovered by the  $\text{PC}_{\text{fdr}}^+$  algorithm and its heuristic modification.

Let  $\mathcal{A}'_{a\sim b|C}$  denote the event

$$p_{a\sim b|C} \leq \frac{|E'_{\text{true}}|}{|E_{\text{test}}| \sum_{i=1}^{|E_{\text{test}}|} (1/i)} q, \quad (\text{A.4})$$

$\mathcal{A}'_{E'_{\text{true}}}$  denote the event of (A.3), and  $\mathcal{A}_{E'_{\text{true}}}$  denote the event that all the true connections in  $E_{\text{test}}$  are recovered by the  $\text{PC}_{\text{fdr}}^+$  algorithm and its heuristic modification.

$\therefore \mathcal{A}'_{E'_{\text{true}}}$  is a sufficient condition for  $\mathcal{A}_{E'_{\text{true}}}$ , according to Lemma 5.

$\therefore \mathcal{A}_{E'_{\text{true}}} \supseteq \mathcal{A}'_{E'_{\text{true}}}.$

$\therefore P(\mathcal{A}_{E'_{\text{true}}}) \geq P(\mathcal{A}'_{E'_{\text{true}}}).$

$\therefore \mathcal{A}'_{E'_{\text{true}}}$  is the joint of a limited number of events as

$$\mathcal{A}'_{E'_{\text{true}}} = \bigcap_{a\sim b \in E'_{\text{true}}} \bigcap_{C \in V \setminus \{a,b\}} \mathcal{A}'_{a\sim b|C}, \quad (\text{A.5})$$

and  $\lim_{m \rightarrow \infty} P(\mathcal{A}'_{a\sim b|C}) = 1$  according to Assumption (A3).

$\therefore$  According to Lemma 4,  $\lim_{m \rightarrow \infty} P(\mathcal{A}'_{E'_{\text{true}}}) = 1.$

$\therefore 1 \geq \lim_{m \rightarrow \infty} P(\mathcal{A}_{E'_{\text{true}}}) \geq \lim_{m \rightarrow \infty} P(\mathcal{A}'_{E'_{\text{true}}}) = 1.$

$\therefore \lim_{m \rightarrow \infty} P(\mathcal{A}_{E'_{\text{true}}}) = 1. \quad \square$

**Lemma A.3.** *Given any FDR level  $q > 0$ , if the  $p$  value vector  $P = [p_1, \dots, p_H]$  input to Algorithm 2 is replaced with  $P' = [p'_1, \dots, p'_H]$ , such that (1) for the those hypotheses that are rejected when  $P$  is the input,  $p'_i$  is equal to or less than  $p_i$ , and (2) for all the other hypotheses,  $p'_i$  can be any value between 0 and 1, then the set of rejected hypotheses when  $P'$  is the input is a superset of those rejected when  $P$  is the input.*

For the proof of this lemma, please refer to Li and Wang's [11] work.

**Corollary A.4.** *Given any FDR level  $q > 0$ , if the  $p$  value vector  $P = [p_1, \dots, p_H]$  input to Algorithm 2 is replaced with  $P' = [p'_1, \dots, p'_H]$  such that  $p'_i \leq p_i$  for all  $i = 1, \dots, H$ , then the set*

of rejected hypotheses when  $P'$  is the input is a superset of those rejected when  $P$  is the input.

The corollary can be easily derived from Lemma 6.

*Proof of Theorem 3.* Let  $P_{\text{stop}} = \{p_{a \sim b}\}$  denote the value of  $P^{\max}$  when the  $\text{PC}_{\text{fdr}}^+$ -skeleton algorithm stops.

$\therefore$  The FDR procedure is invoked whenever  $P^{\max}$  is updated, and  $P^{\max}$  keeps increasing as the algorithm progresses.

$\therefore$  According to Corollary 7,  $E'_{\text{stop}}$  is the same as the edges recovered by directly applying the FDR procedure to  $P_{\text{stop}}$ .

The theorem is proved through comparing the result of the  $\text{PC}_{\text{fdr}}^+$  algorithm with that of applying the FDR procedure to a virtual  $p$  value set constructed from  $P_{\text{stop}}$ . The virtual  $p$  value set  $P^*$  is defined as follows.

For a vertex pair  $a \sim b$  that is not adjacent in  $G_{\text{true}}$ , let  $C_{a \sim b}^*$  denote a certain vertex set that  $d$ -separates  $a$  and  $b$  in the true graph and that is also a subset of either  $\text{adj}(a, G_{\text{true}}) \setminus \{b\}$  or  $\text{adj}(b, G_{\text{true}}) \setminus \{a\}$ . Let us define  $P^* = \{p_{a \sim b}^* \mid a \sim b \in E_{\text{test}}\}$  as

$$p_{a \sim b}^* = \begin{cases} p_{a \perp b \mid C_{a \sim b}^*} & : a \sim b \notin E'_{\text{true}}, \\ p_{a \sim b} & : a \sim b \in E'_{\text{true}}. \end{cases} \quad (\text{A.6})$$

Though  $p_{a \perp b \mid C_{a \sim b}^*}$  may not be actually calculated during the process of the algorithm,  $p_{a \perp b \mid C_{a \sim b}^*}$  still can denote the value as if it was calculated.

Let us design a virtual algorithm, called *Algorithm\**, that infers true edges in  $E_{\text{test}}$  by just applying the FDR procedure to  $P^*$ , and let  $E^*$  denote the edges in  $E_{\text{test}}$  claimed to be true by this virtual algorithm. This algorithm is virtual and impracticable because the calculation of  $P^*$  depends on the unknown  $E'_{\text{true}}$ , but this algorithm exists because  $E'_{\text{true}}$  exists.

For any vertex pair  $a$  and  $b$  that is not adjacent in  $G_{\text{true}}$ , we have the following.

- $\therefore X_a$  and  $X_b$  are conditional independent given  $X_{C_{a \sim b}^*}$ .
- $\therefore p_{a \perp b \mid C_{a \sim b}^*}$  follows the uniform distribution on  $[0, 1]$ .
- $\therefore$  The FDR of *Algorithm\** is under  $q$ .

When all the true edges in the test set are recovered by the  $\text{PC}_{\text{fdr}}^+$  algorithm, that is,  $E'_{\text{true}} \subseteq E'_{\text{stop}}$ , all the edges in  $G_{\text{true}}$  are included in  $E_{\text{stop}}$  due to Assumption (A4). In this case, the conditional independence between  $X_a$  and  $X_b$  given  $X_{C_{a \sim b}^*}$  is tested for all the falsely recovered edges  $a \sim b \in E'_{\text{stop}} \setminus E'_{\text{true}}$ , because for these edges, subsets of  $\text{adj}(a, G_{\text{true}}) \setminus \{b\}$  and subsets of  $\text{adj}(b, G_{\text{true}}) \setminus \{a\}$  have been exhaustively searched and  $C_{a \sim b}^*$  is one of them. Therefore,  $p_{a \sim b} \geq p_{a \sim b}^*$  for all  $a \sim b \in E'_{\text{stop}}$  when event  $\mathcal{A}_{E'_{\text{true}}}$  happens. Consequently, according to Lemma 6,

$$\text{if event } \mathcal{A}_{E'_{\text{true}}} \text{ happens, } E'_{\text{stop}} \subseteq E^*. \quad (\text{A.7})$$

Let  $q(E')$  denote the *realized* FDR of reporting  $E'$  as the set of true edges in  $E_{\text{test}}$ :

$$q(E') = \begin{cases} \frac{|E' \setminus E'_{\text{true}}|}{|E'|} & : E' \neq \emptyset, \\ 0 & : E' = \emptyset. \end{cases} \quad (\text{A.8})$$

The FDRs of the  $\text{PC}_{\text{fdr}}^+$  algorithm and *Algorithm\** are  $E[q(E'_{\text{stop}})]$  and  $E[q(E^*)]$ , respectively. Here  $E[x]$  means the expected value of  $x$ .

$$\begin{aligned} \therefore E[q(E'_{\text{stop}})] &= E[q(E'_{\text{stop}}) \mid \mathcal{A}_{E'_{\text{true}}}]P(\mathcal{A}_{E'_{\text{true}}}) + \\ &E[q(E'_{\text{stop}}) \mid \overline{\mathcal{A}}_{E'_{\text{true}}}]P(\overline{\mathcal{A}}_{E'_{\text{true}}}) \leq Q + P(\overline{\mathcal{A}}_{E'_{\text{true}}}), \text{ where} \\ Q &= E[q(E'_{\text{stop}}) \mid \mathcal{A}_{E'_{\text{true}}}]P(\mathcal{A}_{E'_{\text{true}}}). \\ \therefore \limsup_{m \rightarrow \infty} E[q(E'_{\text{stop}})] &\leq \limsup_{m \rightarrow \infty} Q + \\ &\limsup_{m \rightarrow \infty} P(\overline{\mathcal{A}}_{E'_{\text{true}}}). \\ \therefore \lim_{m \rightarrow \infty} P(\mathcal{A}_{E'_{\text{true}}}) &= 1, \text{ according to Theorem 2.} \\ \therefore \limsup_{m \rightarrow \infty} P(\overline{\mathcal{A}}_{E'_{\text{true}}}) &= \lim_{m \rightarrow \infty} P(\overline{\mathcal{A}}_{E'_{\text{true}}}) = 0. \\ \therefore \limsup_{m \rightarrow \infty} E[q(E'_{\text{stop}})] &\leq \limsup_{m \rightarrow \infty} Q. \\ \therefore Q &\leq E[q(E'_{\text{stop}})]. \\ \therefore \limsup_{m \rightarrow \infty} Q &\leq \limsup_{m \rightarrow \infty} E[q(E'_{\text{stop}})]. \\ \therefore \limsup_{m \rightarrow \infty} E[q(E'_{\text{stop}})] &= \limsup_{m \rightarrow \infty} Q = \\ &\limsup_{m \rightarrow \infty} E[q(E'_{\text{stop}}) \mid \mathcal{A}_{E'_{\text{true}}}]P(\mathcal{A}_{E'_{\text{true}}}). \end{aligned}$$

Similarly,  $\limsup_{m \rightarrow \infty} E[q(E^*)] = \limsup_{m \rightarrow \infty} E[q(E^*) \mid \mathcal{A}_{E'_{\text{true}}}]P(\mathcal{A}_{E'_{\text{true}}})$ .

$\therefore$  Event  $\mathcal{A}_{E'_{\text{true}}}$  implies  $E'_{\text{true}} \subseteq E'_{\text{stop}} \subseteq E^*$ .

$\therefore$  Given event  $\mathcal{A}_{E'_{\text{true}}}$ ,

$$\begin{aligned} q(E'_{\text{stop}}) &= \frac{|E'_{\text{stop}}| - |E'_{\text{true}}|}{|E'_{\text{stop}}|} = 1 - \frac{|E'_{\text{true}}|}{|E'_{\text{stop}}|} \\ &\leq 1 - \frac{|E'_{\text{true}}|}{|E^*|} = \frac{|E^*| - |E'_{\text{true}}|}{|E^*|} = q(E^*). \end{aligned} \quad (\text{A.9})$$

- $\therefore \limsup_{m \rightarrow \infty} E[q(E'_{\text{stop}}) \mid \mathcal{A}_{E'_{\text{true}}}]P(\mathcal{A}_{E'_{\text{true}}}) \leq \limsup_{m \rightarrow \infty} E[q(E^*) \mid \mathcal{A}_{E'_{\text{true}}}]P(\mathcal{A}_{E'_{\text{true}}})$ .
- $\therefore \limsup_{m \rightarrow \infty} E[q(E'_{\text{stop}})] \leq \limsup_{m \rightarrow \infty} E[q(E^*)]$ .
- $\therefore$  *Algorithm\** controls the FDR under  $q$ .
- $\therefore E[q(E^*)] \leq q$ .
- $\therefore \limsup_{m \rightarrow \infty} E[q(E^*)] \leq q$ .
- $\therefore \limsup_{m \rightarrow \infty} E[q(E'_{\text{stop}})] \leq q$ . □

## B. Computational Complexity

The  $\text{PC}_{\text{fdr}}^+$  algorithm spends most of its computation on performing statistical tests of conditional independence at step 7 and controlling the FDR at step 11. If the algorithm stops at the depth  $d = d_{\max}$ , then the number of conditional independence tests required is bounded by

$$T = 2|E_{\text{test}}| \sum_{d=0}^{d_{\max}} C_{\Delta-1}^d, \quad (\text{B.1})$$

where  $|E_{\text{test}}|$  is the number of edges to test,  $\Delta$  is the maximum degree of graph  $G_{\text{init}}$  (the graph formed at step 1 of the  $\text{PC}_{\text{fdr}}^+$  algorithm) whose edges are  $E_{\text{must}} \cap E_{\text{test}}$ , and  $C_{\Delta-1}^d$  is the number of combinations of choosing  $d$  unordered and

distinct elements from  $\Delta - 1$  elements. In the worst case that  $d_{\max} = \Delta - 1$ , the complexity is bounded by  $2|E_{\text{test}}|2^{\Delta-1} = |E_{\text{test}}|2^{\Delta}$ . The bound usually is very loose, because it assumes that no edge has been removed until  $d = d_{\max}$ . In real-world applications, the algorithm is very fast for sparse networks.

The computational complexity of the FDR procedure, Algorithm 2, invoked at step 11 of the  $\text{PC}_{\text{fdr}}^+$  algorithm, in general is  $O(H \log(H) + H) = O(H \log(H))$  where  $H = |E_{\text{test}}|$  is the number of input  $p$  values. The main complexity  $H \log(H)$  is at the sorting (step 1). However, if it is recorded the sorted  $P^{\max}$  of the previous invocation of the FDR procedure, then the complexity of keeping the updated  $P^{\max}$  sorted is only  $O(H)$ . With this optimization, the complexity of the FDR-control procedure is  $O(H \log(H))$  at its first operation and is  $O(H)$  later. The FDR procedure is invoked only when  $p_{a \perp b|C} > p_{a \sim b}^{\max}$ . In the worst case that  $p_{a \perp b|C}$  is always larger than  $p_{a \sim b}^{\max}$ , the complexity of the computation spent on the FDR control in total is bounded by  $O(|E_{\text{test}}| \log(|E_{\text{test}}|) + T|E_{\text{test}}|)$  where  $T$  is the number of performed conditional independence tests. This is a very loose bound because it is rare that  $p_{a \perp b|C}$  is always larger than  $p_{a \sim b}^{\max}$ .

## Acknowledgment

This work was partially supported by the Canadian Institutes of Health Research (CIHR) Grant (CPN-80080 MJM) and the Canadian Natural Sciences and Engineering Research Council (NSERC) Grant (STPGP 365208-08).

## References

- [1] S. M. Smith, K. L. Miller, G. Salimi-Khorshidi et al., "Network modelling methods for fMRI," *NeuroImage*, vol. 54, no. 2, pp. 875–891, 2011.
- [2] K. J. Friston, "Functional and effective connectivity: a review," *Brain Connectivity*, vol. 1, no. 1, pp. 13–36, 2011.
- [3] A. R. McIntosh and F. Gonzalez-Lima, "Structural equation modeling and its application to network analysis in functional brain imaging," *Human Brain Mapping*, vol. 2, no. 1-2, pp. 2–22, 1994.
- [4] K. J. Friston, L. Harrison, and W. Penny, "Dynamic causal modelling," *NeuroImage*, vol. 19, no. 4, pp. 1273–1302, 2003.
- [5] J. Li, Z. J. Wang, J. J. Eng, and M. J. McKeown, "Bayesian network modeling for discovering "dependent synergies" among muscles in reaching movements," *IEEE Transactions on Biomedical Engineering*, vol. 55, no. 1, pp. 298–310, 2008.
- [6] Y. Benjamini and D. Yekutieli, "The control of the false discovery rate in multiple testing under dependency," *Annals of Statistics*, vol. 29, no. 4, pp. 1165–1188, 2001.
- [7] J. D. Storey, "A direct approach to false discovery rates," *Journal of the Royal Statistical Society B*, vol. 64, no. 3, pp. 479–498, 2002.
- [8] J. Listgarten and D. Heckerman, "Determining the number of non-spurious arcs in a learned DAG model: investigation of a Bayesian and a frequentist approach," in *Proceedings of the 23rd Conference on Uncertainty in Artificial Intelligence*, 2007.
- [9] I. Tsamardinos and L. E. Brown, "Bounding the false discovery rate in local bayesian network learning," in *Proceedings of the 23rd AAAI Conference on Artificial Intelligence (AAAI '08)*, pp. 1100–1105, July 2008.
- [10] P. Spirtes, C. Glymour, and R. Scheines, *Causation, Prediction, and Search*, The MIT Press, 2001.
- [11] J. Li and Z. J. Wang, "Controlling the false discovery rate of the association/causality structure learned with the pc algorithm," *Journal of Machine Learning Research*, vol. 10, pp. 475–514, 2009.
- [12] K. J. Worsley, C. H. Liao, J. Aston et al., "A general statistical analysis for fMRI data," *NeuroImage*, vol. 15, no. 1, pp. 1–15, 2002.
- [13] K. J. Friston, K. E. Stephan, T. E. Lund, A. Morcom, and S. Kiebel, "Mixed-effects and fMRI studies," *NeuroImage*, vol. 24, no. 1, pp. 244–252, 2005.
- [14] K. E. Stephan, W. D. Penny, J. Daunizeau, R. J. Moran, and K. J. Friston, "Bayesian model selection for group studies," *NeuroImage*, vol. 46, no. 4, pp. 1004–1017, 2009.
- [15] G. Varoquaux, A. Gramfort, J. B. Poline, and B. Thirion, "Brain covariance selection: better individual functional connectivity models using population prior," *Advances in Neural Information Processing Systems*, vol. 23, pp. 2334–2342, 2010.
- [16] J. D. Ramsey, S. J. Hanson, and C. Glymour, "Multi-subject search correctly identifies causal connections and most causal directions in the DCM models of the Smith et al. simulation study," *NeuroImage*, vol. 58, no. 3, pp. 838–848, 2011.
- [17] S. L. Lauritzen, *Graphical Models*, Oxford University Press, 1996.
- [18] J. Neyman and E. S. Pearson, "On the use and interpretation of certain test criteria for purposes of statistical inference: part I," *Biometrika*, vol. 20A, pp. 175–240, 1928.
- [19] R. A. Fisher, "Frequency distribution of the values of the correlation 40 coefficients in samples from an indefinitely large population," *Biometrika*, vol. 10, no. 4, pp. 507–521, 1915.
- [20] S. J. Palmer, B. Ng, R. Abugharbieh, L. Eigenraam, and M. J. McKeown, "Motor reserve and novel area recruitment: amplitude and spatial characteristics of compensation in Parkinson's disease," *European Journal of Neuroscience*, vol. 29, no. 11, pp. 2187–2196, 2009.

## Research Article

# Redundancy as a Graph-Based Index of Frequency Specific MEG Functional Connectivity

**Claudia Di Lanzo,<sup>1,2</sup> Laura Marzetti,<sup>1,2</sup> Filippo Zappasodi,<sup>1,2</sup>  
Fabrizio De Vico Fallani,<sup>3,4</sup> and Vittorio Pizzella<sup>1,2</sup>**

<sup>1</sup>Department of Neuroscience and Imaging, “G. d’Annunzio” University of Chieti-Pescara, Via dei Vestini 31, 66100 Chieti, Italy

<sup>2</sup>Institute of Advanced Biomedical Technologies, “G. d’Annunzio” University Foundation, Via dei Vestini 31, 66100 Chieti, Italy

<sup>3</sup>Neuroelectrical Imaging and BCI Lab, IRCCS Fondazione Santa Lucia, Via Ardeatina, 306, 00179 Rome, Italy

<sup>4</sup>Department of Physiology and Pharmacology, Sapienza University of Rome, Piazzale Aldo Moro 5, 00185 Rome, Italy

Correspondence should be addressed to Claudia Di Lanzo, claudia.dilanzo@unich.it

Received 30 March 2012; Revised 26 July 2012; Accepted 30 August 2012

Academic Editor: Danielle Bassett

Copyright © 2012 Claudia Di Lanzo et al. This is an open access article distributed under the Creative Commons Attribution License, which permits unrestricted use, distribution, and reproduction in any medium, provided the original work is properly cited.

We used a recently proposed graph index to investigate connectivity redundancy in resting state MEG recordings. Usually, brain network analyses consider indexes linked to the shortest paths between cerebral regions. However, important information might be lost about alternative trails by neglecting longer pathways. We measured the redundancy of the connectivity by considering the multiple paths at the global level (i.e., scalar redundancy), across different path lengths (i.e., vector redundancy), and between node pairs (i.e., matrix redundancy). We applied this approach to a robust frequency domain functional connectivity measure, the corrected imaginary part of coherence. The redundancy in the MEG networks, for each frequency band, was significantly ( $P < 0.05$ ) higher than in the random graphs, thus, confirming a natural tendency of the brain to present multiple interaction pathways between different specialized areas. Notably, this difference was more evident and localized among the channels covering the parietooccipital areas in the alpha range of MEG oscillations (7.5–13 Hz), as expected in the resting state conditions. Interestingly enough, the results obtained with the redundancy indexes were poorly correlated with those obtained using shortest paths only, and more sensitive with respect to those obtained by considering walk-based indexes.

## 1. Introduction

Over the last decade, there has been a growing interest in the detection of functional connectivity in the brain from different neuroelectromagnetic and hemodynamic signals recorded by several neuroimaging techniques. Many methods have been proposed and discussed in the literature with the aim of estimating the functional relationships among different cerebral structures [1, 2]. The recent application of graph theoretical analysis to human brain time series is a valuable approach to the study of functional brain architecture [3]. Graph theoretical properties of neural networks have been studied in healthy subjects [4–8] and in patients with brain pathologies such as Alzheimer’s disease (AD) [9, 10], schizophrenia [11, 12], and brain tumors [13]. These studies suggest that brain functional network parameters

might serve as useful biomarkers for neurocognitive disorders and to improve therapies [14].

Usually, graph-based studies consider indexes linked to the shortest path between two interacting cerebral regions. However, the consideration of the shortest pathway alone seems rather reductive, possibly providing incomplete information about the alternative longer pathways by which two cerebral regions could interact. In particular, in this work we considered *path*-based alternative longer pathways, that is, pathways in which nodes can be visited only once. Other strategies including nodes and links that can be revisited several times along the way (*walks*), as described in [15, 16] and named “communicability,” are possible although less biologically plausible.

The information about longer pathways appears strictly related to the concepts of “redundancy” and “robustness.”

These properties are critical for the survival of many biological systems as they allow for reliable functions despite the death of individual elements. Indeed, the number of different pathways between two areas, rather than the shortest one, could highlight the importance of the link between two regions. Even more importantly, in brain pathologies (Alzheimer, Parkinson, Stroke, etc.) the availability of alternative anatomical and functional pathways would allow the brain to reshape its physiologic mechanisms in order to compensate the critical consequences of the disease [17].

A graph-based index that includes robustness—taking inspiration from the recent findings on the evaluation of multiple paths between network elements [18–20]—has been defined and successfully applied in rest EEG [21]. In particular, three complementary indexes have been derived: (i) the scalar redundancy, a scalar number that characterizes the global level of redundancy in the network; (ii) the vector redundancy, a vector characterizing the overall redundancy for each path length; (iii) the matrix redundancy, a matrix describing the redundancy in each of the node pairs regardless of path length.

Indeed, De Vico Fallani and colleagues [21] showed that functional brain networks exhibit a high degree of redundancy, consistently with a natural tendency of the brain to establish multiple connections. However, EEG connectivity profiles are known to be strongly biased from volume conduction effect due to the low pass spatial filtering properties of the head and are influenced by the choice of the reference electrode [22, 23].

In this work, we calculate redundancy indexes from rest MEG data to avoid possible confounds from volume conduction and reference electrode effects. In fact, MEG does not require a reference channel and is intrinsically less influenced by volume conduction effect [24]. Moreover, the connectivity metric estimated from MEG data is a corrected version of the imaginary part of coherency [25] aimed at suppressing a spatial bias towards remote interactions. Finally, redundancy indexes from rest MEG data are compared to those identified using shortest path and walk-based pathways.

## 2. Materials and Methods

**2.1. MEG Recordings.** The present data were acquired in 7 healthy young adult subjects. The study was approved by the local ethical committee and all subjects gave their written informed consent. The subjects contributed one 5 min resting state MEG run during which they were instructed to maintain fixation on a visual crosshair. MEG was recorded using the 165-channel MEG system installed at the University of Chieti [26]. This system includes 153 dc SQUID integrated magnetometers arranged on a helmet covering the whole head plus 12 reference channels. Two electrical channels were simultaneously recorded (electrocardiogram and electrooculogram) to be used for artifact rejection. All signals were band-pass-filtered at 0.16–250 Hz and digitized at 1025 Hz. The position of the subject’s head with respect to the sensors was determined by five coils placed on the scalp recorded before and after each MEG run. The coil positions were digitized by means of a 3D digitizer (3Space Fastrak;

Polhemus), together with anatomical landmarks (left and right preauricular and nasion) defining the head coordinate system. After downsampling to 341 Hz, the recorded data were analyzed using Independent Components Analysis (ICA) by means of the fast ICA algorithm [27]. The ICs were automatically classified, the artefactual components were removed, and the nonartefactual ICs were then recombined thus providing cleaned time domain signals. In the present work, we considered only 61 evenly spaced MEG channels to compare the results with those reported with standard 64 ch EEG data [21].

**2.2. Functional Connectivity.** In the present study, we estimated a corrected version of the imaginary part of coherence, a robust measure of the linear relationship between two-time series in the frequency domain [25, 28].

Given two-time domain signals,  $x_i(t)$  and  $x_j(t)$ , and their fourier transforms,  $X_i(f)$  and  $X_j(f)$ , coherence is a complex valued measure of interaction defined as

$$C_{ij}(f) \equiv \frac{S_{ij}(f)}{\sqrt{S_{ii}(f)S_{jj}(f)}}, \quad (1)$$

where

$$S_{ij}(f) \equiv \langle X_i(f)X_j^*(f) \rangle \quad (2)$$

is the cross-spectrum between  $X_i(f)$ , and  $X_j(f)$ ,  $S_{ii}(f)$  is the power spectrum of  $X_i(f)$ , and  $S_{jj}(f)$  is the power spectrum of  $X_j(f)$ . The symbols  $*$  and  $\langle \rangle$  in (2) indicate complex conjugation and expectation value, respectively. In practice, expectation value is estimated as the average over signal epochs.

A nonvanishing imaginary component of complex coherence (ImCoh) can only indicate a phase-shifted relationship between  $X_i$  and  $X_j$ . As a consequence of this property, and assuming the quasistatic regime for Maxwell’s equations, ImCoh is robust to self-connectivity induced by volume conduction or crosstalk at the sensor level [25, 29]. Thus, ImCoh robustly measures functional connectivity [30–33] meaning that a significant deviation from zero cannot be generated by independent sources but rather by true brain interaction.

Since classical ImCoh might exhibit a spatial bias towards remote interactions, we rely on a corrected version of ImCoh (cImCoh) with the same properties introduced above and with the additional feature of compensating for preference for remote interactions [28]:

$$c\text{ImCoh}_{ij}(f) \equiv \frac{\text{Im}(C_{ij}(f))}{\sqrt{(1 - \text{Re}(C_{ij}(f)))^2}}. \quad (3)$$

The corrected ImCoh was estimated for each run as the average over signal epochs of 2-second duration. Therefore, a single complex coherence value for each frequency bin was generated for each possible channel pair combination. In order to study the level of synchronization in specific physiological frequency bands, we averaged the corrected imaginary

coherence values within specific ranges, thus, generating a single value for each frequency band of interest, namely: delta (1–3.5 Hz), theta (3.5–7.5 Hz), alpha (7.5–13 Hz), beta (13–24 Hz), and gamma (24–60 Hz). The frequency band specific values were thus, stored in a channel matrix. This matrix describes a functional network, where the particular combination of the  $i$ th row with the  $j$ th column indicates the synchronization value between the MEG signals of the  $i$ th and  $j$ th channels. At this stage, the functional brain connectivity is a fully connected and undirected network. To compute topological features, a network has to be converted into undirected and unweighted graph by considering a threshold, expressed as connection density, that represents the number of the most powerful connections to be considered. We choose an “optimal” connection density of 0.101, as this is the best statistical tradeoff to differentiate between the global and local structural properties of a network with 61 nodes. This highest separation would increase the independence between the two indexes when measuring the global and local properties of the network [34, 35]. This threshold retains the 370 highest values (in magnitude) for the MEG network by setting them equal 1 and by setting the remaining ones to 0.

**2.3. Network Redundancy.** A graph is defined as a set of vertices/nodes  $N$  and a set of links/connections representing some sort of interaction between the vertices. The adjacency matrix  $A$  of size  $N \times N$  contains the information about the graph connectivity structure. If a link connects the two nodes  $i$  and  $j$ , the corresponding entry of  $A$  is given by  $a_{ij} = 1$ ; otherwise,  $a_{ij} = 0$ . In a graph, a path is an alternating sequence of vertices and links, beginning and ending with a vertex, where each vertex is incident to both the preceding link and the following link in the sequence. Given such definition, it is clear that the shortest path is only one of the possible ways in which two nodes in a graph can interact. To account for all the possible ways, longer pathways should also be considered for characterizing functional brain connectivity [34, 35]. Our algorithm, implemented in Matlab (The MathWorks Inc., Natick, MA, USA), computes all the possible paths in a graph by counting the total number of links between the nodes excluding vertices already visited (self-connections). The main steps of this algorithm are highlighted in the flowchart of Figure 1. The algorithm output is a three-dimensional matrix  $P$  of size  $N \times N \times L$ , containing the number of all the possible paths of length  $l = 1, \dots, L$  in each node pair, where  $L \leq N - 1$ . Starting from this  $P$ -matrix, we evaluate the following characteristic measures.

**2.3.1. Scalar Redundancy.** The scalar redundancy  $R_s$  is the total sum of the number of paths, of any length  $l = 1, \dots, N - 1$ , found between all the nodes, that is,  $(N^2 - N)/2$ , excluding the self-connections:

$$R_s = \sum_{i=1}^N \sum_{j=1}^N \sum_{l=1}^L P(i, j, l). \quad (4)$$

It represents the global level of network redundancy by means of a scalar number. The higher is  $R_s$ , the higher is the tendency of the graph to exhibit multiple alternative pathways.

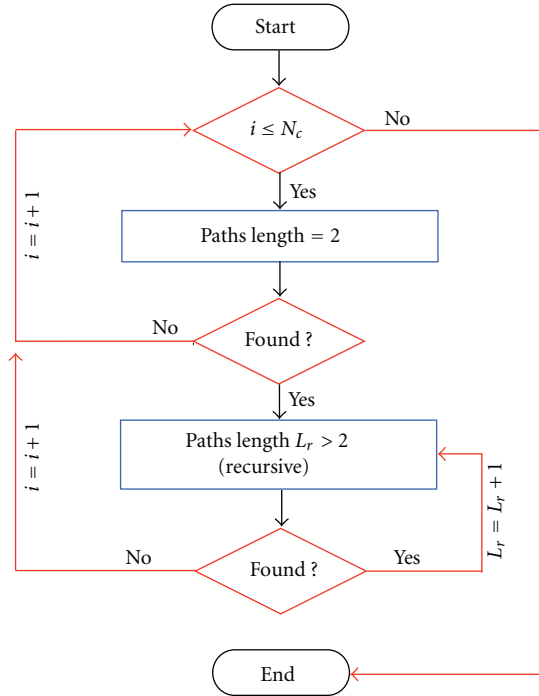


FIGURE 1: The main steps of this algorithm are highlighted in the flowchart that computes all the possible paths in a graph, able to count the total number of paths between the nodes excluding vertices already visited (self-connections).

**2.3.2. Vector Redundancy.** The vector redundancy  $R_v$  is the total sum of the number of paths found between all the nodes, that is,  $(N^2 - N)/2$ , excluding the self-connections, with respect to each path length  $l = 1, \dots, N - 1$ :

$$R_v(l) = \sum_{i=1}^N \sum_{j=1}^N P(i, j, l). \quad (5)$$

It represents the total level of network redundancy across different path lengths. The higher is  $R_v(l)$ , the higher is the tendency of the graph to exhibit multiple alternative pathways with a specific length  $l$ .

**2.3.3. Matrix Redundancy.** The matrix redundancy  $R_m$  is the total sum of the number of paths of any length  $l = 1, \dots, N - 1$  in each node pair:

$$R_m(i, j) = \sum_{l=1}^L P(i, j, l). \quad (6)$$

It represents the total level of redundancy between the nodes of the graph. The higher is  $R_m(i, j)$ , the higher is the tendency of the graph to exhibit many alternative pathways between the nodes  $i$  and  $j$ .

In the present study, the analysis of the network redundancy indexes was addressed by exploring paths of a maximal length of  $L = 5$ .

TABLE 1: Mean  $z$ -score values of scalar redundancy ( $R_s$ ) and vector redundancy ( $R_v$ ). Different rows correspond to different bands. In the  $R_v$  section, each column refers to a different path length  $l$ . Asterisks denote a significant ( $P < 0.05$ ) difference from random graphs.

	$R_s$	$R_v$				
		$l = 1$	$l = 2$	$l = 3$	$l = 4$	$l = 5$
Delta	38.32*	—	20.34*	23.74*	30.95*	39.60*
Theta	45.30*	—	19.86*	25.56*	34.41*	47.16*
Alpha	60.03*	—	24.77*	33.21*	45.76*	62.42*
Beta	39.40*	—	20.36*	24.62*	31.78*	40.72*
Gamma	54.54*	—	24.40*	31.41*	42.09*	56.68*

**2.3.4. Random Network Comparison.** The same redundancy indexes were computed in a set of reference graphs whose links were arranged in a random fashion. Indeed, random connections correspond to a scrambled situation, where no anatomical nor functional organization is implied, and are a baseline for the evaluation of all networks. In this work, 100 random graphs were generated by maintaining the same number of nodes and connections of the original MEG networks. Each time, links were randomly shuffled without preserving the node degree distribution [36]. This choice is motivated by the fact that the networks are rather small (61 MEG channels) and sparse (connection density  $\sim 0.1$ ), and preserving the degree distribution would generate very similar network topologies due to reduced number of different possible random combinations.

Finally, the statistical contrast with the random networks was addressed for the experimental subjects and for each frequency band by calculating the  $z$ -score of the obtained redundancy indexes.

**2.3.5. Comparison with Other Indexes.** Redundancy indexes were also compared with those found by using the shortest paths between all the node pairs. Starting from the three-dimensional matrix  $P$  of size  $N \times N \times L$  defined before, and containing the number of all the possible paths of length  $l$ , we calculated the matrix PS containing the number of shortest paths between the nodes (two-dimensional matrix of shortest path):

$$\begin{aligned} \text{PS}(i, j) &= P(i, j, k), \\ k &= \min(l) \quad \text{such that } P(i, j, k) > 0. \end{aligned} \quad (7)$$

Shortest path-based PS values were compared with the redundancy matrix index  $R_m$  (with  $L_{\max} = 5$ ). In order to reduce any effect related to the different range of values (i.e., the number of shortest paths could significantly deviate from the number of paths of any length), the original values were normalized by the mean values obtained from 100 random networks through a  $z$ -score. Then, the difference was assessed by computing the difference of the normalized matricial values, for each subject and frequency band.

Similarly, we implemented a matricial index using the number of alternative pathways (with  $L_{\max} = 5$ ) as revealed by walks, along the line of the communicability concept introduced in [16]. Starting from the adjacency matrix  $A$ , we evaluated the matrix communicability index  $G$  containing

the number of walks of length  $l = 1, \dots, L_{\max}$  that started at node  $i$  and finished at node  $j$ :

$$G(i, j) = \sum_{l=1}^{L_{\max}} A^l(i, j). \quad (8)$$

Again,  $G(i, j)$  was compared with the redundancy matrix index  $R_m$ . In order to reduce any effect related to the different range of values (i.e., the number of walks could significantly deviate from the number of paths of any length), the original values were normalized by the mean values obtained from 100 random networks through a  $z$ -score. Then, the difference was assessed by computing the difference of the normalized matricial values, for each subject and frequency band.

### 3. Results

The MEG network in the alpha frequency band relative to one subject is shown in Figure 2(a), whilst Figure 2(b) shows one random network obtained by randomizing the original links among the channels. As it can be observed, there is a clear difference between the two connectivity patterns. Notably, in the MEG network the nodes of the temporal, parietal, and occipital areas are strongly interconnected, while there is no particular structure in the random network.

Figure 3 shows the cumulative MEG graph in alpha frequency band relative to all of the 7 subjects.

Only values larger than 2 are shown. The cumulative MEG network resembles the functional structure shown in Figure 2(a), highlighting the consistency of temporal, parietal, and occipital interconnections in resting state MEG networks.

All three redundancy indexes— $R_s$ ,  $R_v$ ,  $R_m$ —computed for MEG data showed statistically significant difference ( $P < 0.05$ ) with respect to the random graph set for all frequency bands: delta, theta, alpha, beta, and gamma, as indicated by  $z$ -scores listed in Table 1.

Figure 4 details mean  $R_s$  values in the alpha frequency band calculated from single subject MEG networks as well as the mean  $R_s$  values from the random networks. The scalar redundancy in the MEG networks is significantly higher ( $P < 0.05$ ) with respect to random graphs. Figure 5 details mean  $R_v$  values in MEG and random networks in the alpha band. Although they have similar trends, showing a vector redundancy that increases with path length, the statistical comparison between their values is highly significant. In particular, the vector redundancy of the MEG network is

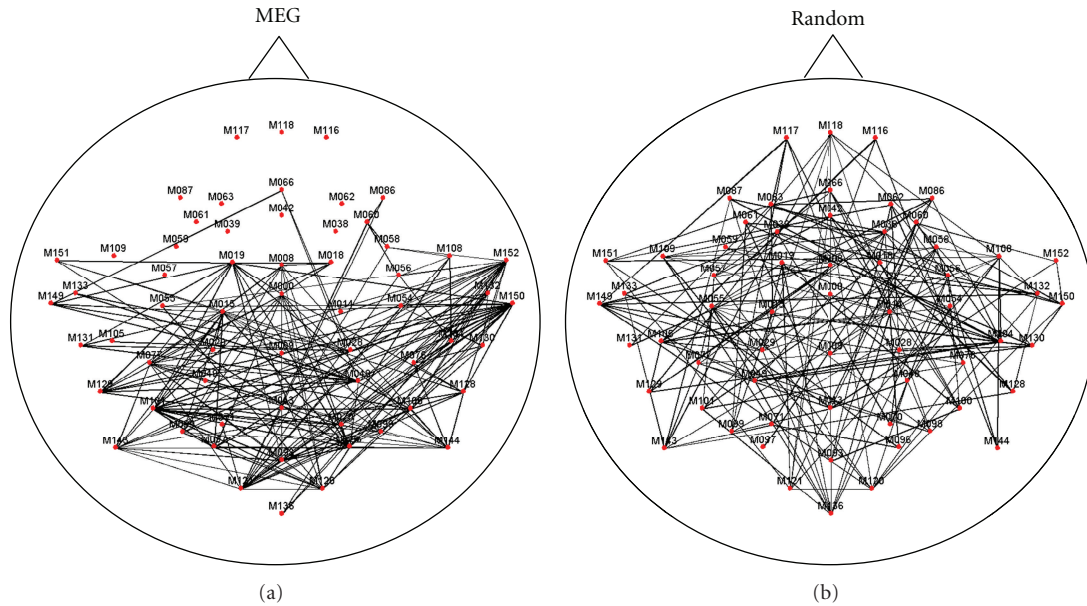


FIGURE 2: (a) Representation of the MEG network in alpha frequency band. Nodes represent MEG channels, while links indicate a significant synchronization in the frequency domain between the time series of all the MEG channels (1342 highest values of corrected imaginary coherence magnitude). (b) Representation of a simulated random network with same number of nodes and links of the MEG network.

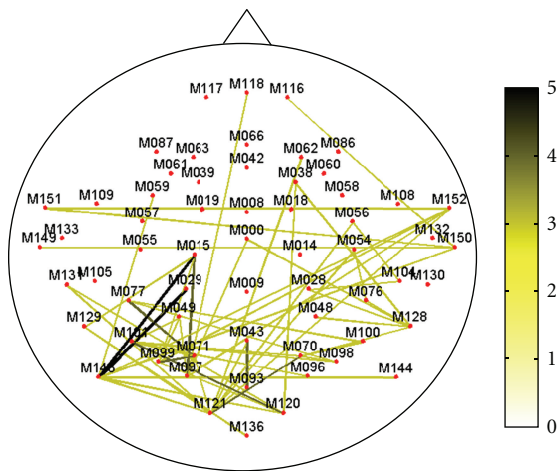


FIGURE 3: Representation of the MEG network in alpha frequency band for all subjects. Nodes represent MEG channels, while thickness and color line code the number of subjects who share that particular connection. Only values larger than 2 are shown. According to the color bar, connections common to many subjects are identified by green-black colors.

significantly higher ( $P < 0.05$ ) than that of random graphs for the path lengths  $l = 2, \dots, 5$ . Actually, the results for  $l = 1$  are identical due to the statistical threshold that made all the inspected networks having the same number of connections (see Functional connectivity paragraph in Section 2).

Figure 6 shows the mean  $z$ -score values of the matrix redundancy  $R_m$  for the representative alpha frequency band. Also in this case,  $R_m$  calculated for MEG networks is significantly different from that of random graphs. Similar results

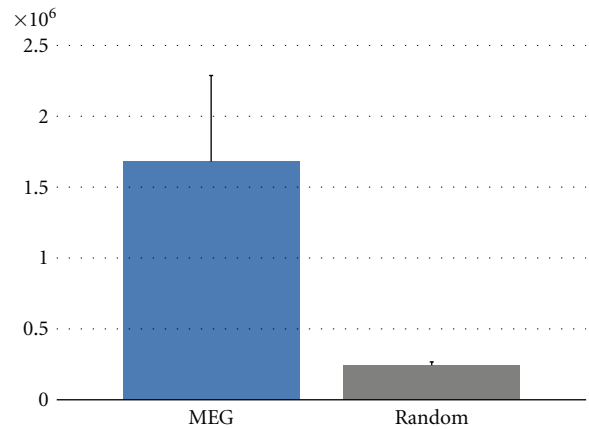


FIGURE 4: Mean scalar redundancy values for MEG network in the alpha frequency band and for random graphs. Vertical bars denote the standard deviation (of the values of 7 subjects for MEG graph and of the values of 100 random graph). A significant difference between the MEG and random values is found ( $P < 0.05$ ).

were also obtained in the other frequency bands. Furthermore, MEG networks show a clear topographical specificity as revealed by a very high redundancy between the nodes of the parietal and occipital areas.

Finally, Figure 7 summarizes the comparison of redundancy index with those obtained from shortest path and communicability in the alpha frequency band. In particular, we show in Figure 7(a) the mean  $z$ -score values related to shortest path-based matricial index, in Figure 7(c) the mean  $z$ -score values related to communicability-based matricial index. Figures 7(b) and 7(d) show the difference between

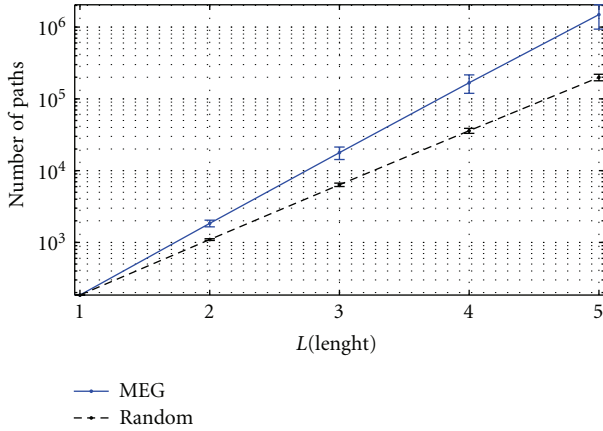


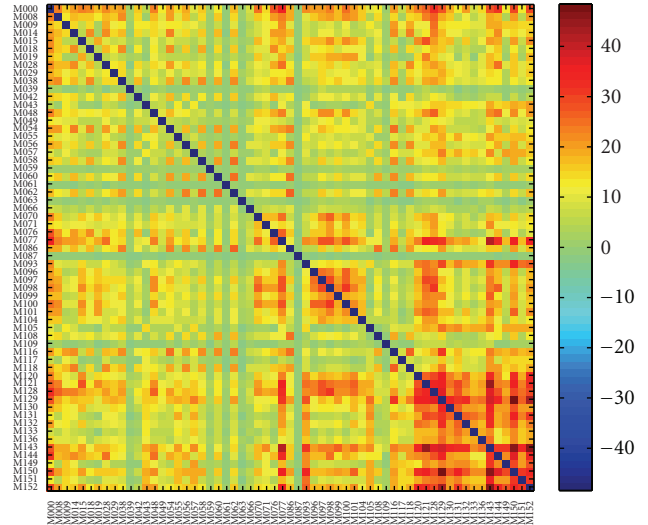
FIGURE 5: Mean vector redundancy values in logarithmic scale for MEG network in the alpha frequency band (solid blue line) and for random graphs (dashed black line). Vertical bars denote the standard deviations. A significant difference between the MEG and random values is found ( $P < 0.05$ ).

the mean  $z$ -score values for the matrix redundancy index (shown in Figure 6(a)) and the mean  $z$ -score for the shortest path and the communicability, respectively. Moreover, the number of nodes significantly correlated according to Spearman coefficient between redundancy index and shortest path-based index is 0.93% ( $P < 0.05$ , corrected for multiple comparisons through the rough false discovery rate [37]), while is much higher (56,12%) between the redundancy index and communicability-based index. Similar results were obtained in the other frequency bands.

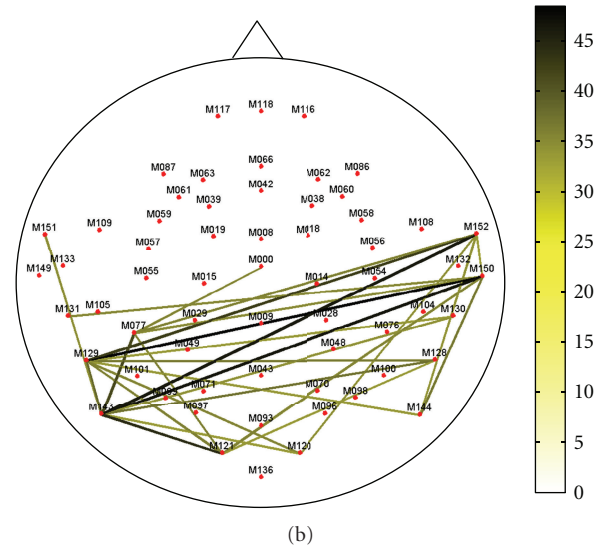
#### 4. Discussion

In this study, we derived graph theory parameters from a robust frequency domain functional connectivity measure, the corrected imaginary part of coherence estimated from MEG data. Indeed, MEG is immune to reference electrode effect and is less confounded by volume conduction effect [24]. The graph connectivity structure is represented as a binary quantity in the adjacency matrix and provides information about the links between vertices (i.e., MEG channels). Our data show that the MEG network features a less spread topology with respect to similar networks mapped by EEG [21]. In fact, the widespread topology found in EEG can possibly be ascribed to volume conduction effect and/or to the bias towards remote interactions.

In our study, we calculated three different indexes: scalar, vector, and matrix, to the aim of characterizing overall network redundancy, global network redundancy for a given path length, and redundancy of pairwise connections in the network. As a general rule, these indexes are related to the maximum path length ( $L_{\max}$ ) explored. The results presented here are obtained for  $L_{\max} = 5$ , which corresponds to a computationally reasonable amount of time and space (20 s per subject and per frequency band on a Intel i5-2400 CPU @ 3.10 GHz with 8 GB of RAM). The needed amount of time diverges for higher  $L_{\max}$  values. Nevertheless, as it can be seen



(a)



(b)

FIGURE 6:  $z$ -score values of matrix redundancy for MEG network in the alpha frequency band. (a) the degree of  $z$ -score redundancy for each channel pair is colour coded: highest values of redundancy, significantly different between MEG and random networks, are identified by yellow-red colours. (b) only values larger than 70% of the maximum value are shown. According to the colour bar, highest values of redundancy, significantly different between MEG and random networks, are identified by green-black colours.

from Figure 5, where the dependence of vector redundancy from  $L$  is shown, a linear trend (in semilogarithmic scale) rules such dependence. Thus, the vector redundancy for higher values of  $L_{\max}$  can be extrapolated. Moreover, the matrix redundancy obtained for  $L_{\max} = 5$  typically shows a high spatial correlation degree with respect to matrix redundancy obtained for higher  $L$  values (up to 10), meaning that topographical information is preserved also for lower  $L$  values. Graph theory parameters derived from adjacency matrices are usually calculated by considering the shortest possible pathway of interaction between two vertices. Nevertheless, shortest distances alone could provide an incomplete

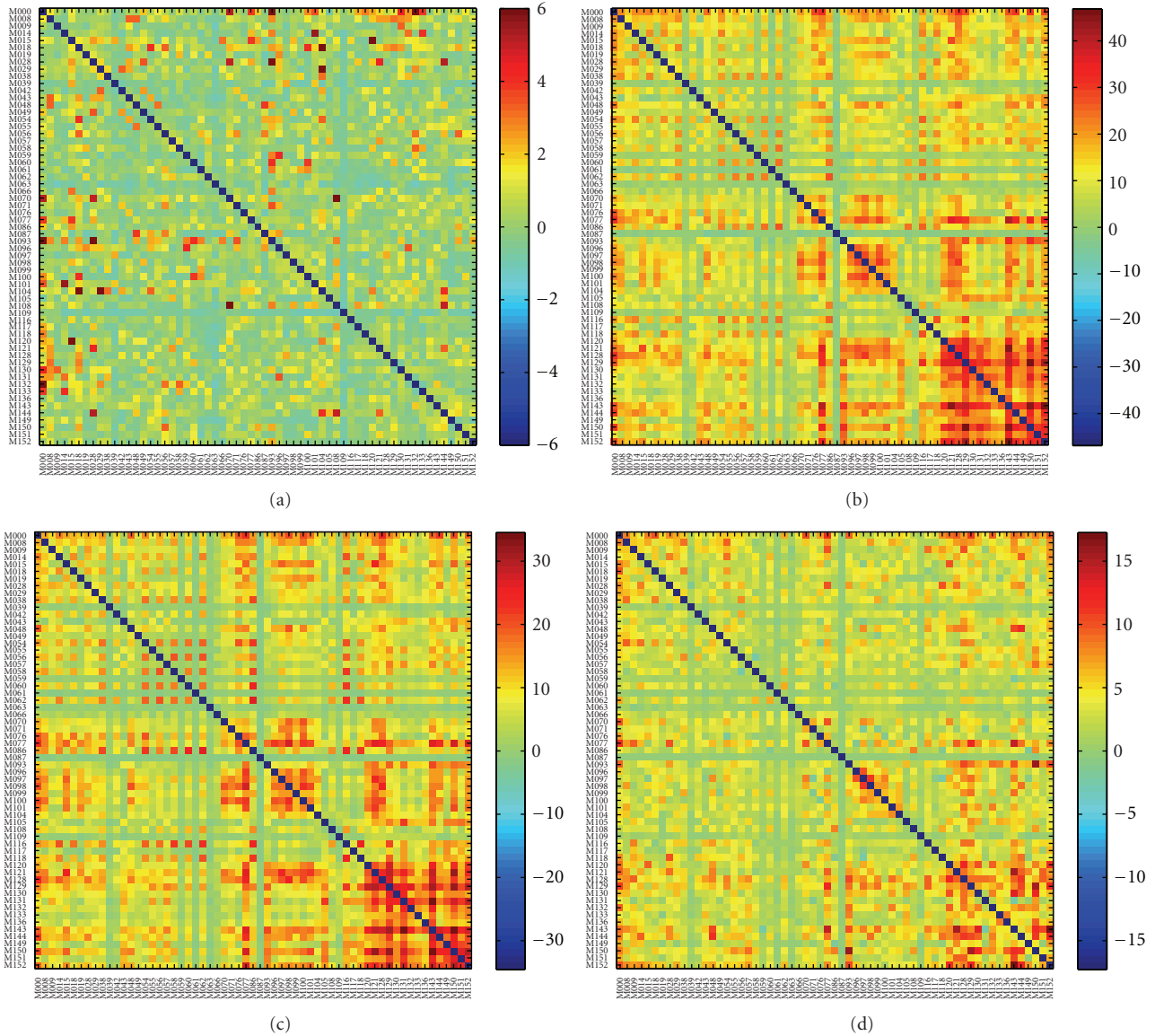


FIGURE 7: Comparison between redundancy, shortest path, and communicability for the alpha frequency band: (a) z-score values related to matrix containing the number of shortest paths between all the node pairs; (b) difference between mean z-score values of redundancy and mean z-score of shortest path; (c) z-score values of matrix of communicability, that is, redundancy indexes based on the computation of walks; (d) difference between mean z-score values of redundancy and mean z-score values of communicability.

characterization of a network, since connectivity in complex systems with similar shortest paths distribution can indeed, exhibit distinct structural and dynamical properties [34, 35]. In particular, by neglecting the longer pathways important information might be lost about the alternative trails that could connect two nodes in a network. The possibility to inspect multiple pathways within a system is strictly related to the concept of redundancy and robustness, which is supposed to be a natural mechanism of the brain for enhancing the resilience to neural damages and dysfunctions [38].

Scalar redundancy is related to overall network resilience. This index appeared significantly different than the corresponding value obtained from random networks in all the frequency bands.

Similar results were obtained with EEG recordings [21]. This difference suggests that scalar redundancy might be a functional correlate of brain connectivity disruption with a possible prognostic value.

Vector redundancy is related to global network redundancy for a given path length. Higher vector redundancy values for MEG graphs compared to random graphs indicate the network tendency to build a larger number of connections for a given path length  $L$ , regardless of specific node contribution. Analogous results were found for EEG [21]. Again, this parameter might serve as a prognostic index.

The matrix redundancy index informs us about the robustness of a given pairwise connection. Indeed, our data showed the most redundant interactions between the parietal

and occipital channels in the alpha frequency band, as expected in relation with the posterior alpha rhythm originating in occipito-parietal areas during rest [39]. Notably, our MEG results on the network topology show an improved spatial specificity with respect to its EEG counterpart [21], possibly thanks to the diminished bias from volume conduction and reference electrode effects.

*Methodological Considerations.* One of the main issues related to the used redundancy indexes is if they carry different information from other existing measures like for instance that related to the shortest paths or to walks.

As it can be noticed by comparing Figures 6 and 7(a), the connections characterized by high redundancy values differ from those obtained using shortest path-based values. A direct comparison between the  $z$ -scores (Figure 7(b)) shows that the redundancy values were generally higher than shortest path-based values, the difference being largely positive. Interestingly, the highest differences were located between the occipito-parietal regions. The significant correlation (Spearman) between the distribution of the shortest path-based and redundancy index gathered from the population observed in less than 1% of the connections strengthens the finding that the two indexes are not related and provide different information. Taken together these results indicate that the topological information carried by shortest paths is different from that obtained by redundancy. Furthermore, these two measures are generally not correlated, thus, justifying the additional time needed for redundancy computation.

When comparing communicability-based and redundancy matrix index, we observed a high degree of correlation. We would like to stress that the redundancy indexes are based on paths which never visit the same vertex twice, [40] thus, avoiding cycles that have a difficult interpretation in functional brain networks and that are generally neglected by the existing literature [41]. From a general point of view, this can be seen as the main difference between the present method and the communicability-based indexes. Indeed, pathways visiting a node more than once are fake alternatives to the possibly damaged link. To give an example, a link between two nodes (just suppose that this is the only way they can connect) is identified as a walk of distance equal to 3 and as a path of distance 1. In our view, there is no real redundant information between these two nodes, since they are directly connected as correctly identified by the path-based distance.

Nevertheless, Figure 7(d) shows that  $z$ -scores found from the redundancy values were generally higher than the ones obtained from communicability-based values. Thus, there exists a general tendency of the walk-based index to overestimate the number of actual interactions between nodes, and to generate lower  $z$ -scores with respect to redundancy values. This suggests that redundancy indexes are in general more sensible in identifying significant redundant interactions between nodes.

Overall, in the present work, we demonstrated that a natural high degree of redundancy, confidently ascribed to functional brain network behavior, is also exhibited by the MEG networks in a group of healthy subjects. Moreover, although we believe that it is not good practice to draw strong

conclusions about the underlying brain functioning from channel level information, our results may be attributed to the role of alpha band in mediating interactions in or between visual, attention, and default mode networks [42].

Finally, it would be interesting to investigate how different mental states or behavioral conditions, as well as alterations due to cerebral diseases, can affect this high natural redundancy of spontaneous functional brain networks.

## 5. Conclusion

This work has shown that functional brain networks as measured by MEG exhibit a natural high redundant degree of frequency specific interaction between different regions. The redundancy indexes used are defined to capture different information at the global level (scalar), at each path length (vector), and between any node pair (matrix). In our opinion, this information might integrate rather than substitute indexes based on the shortest path, thus, allowing for a more comprehensive understanding of network properties. In particular, the inclusion of redundancy metrics in a benchmark set of graph indexes might be particularly relevant for studying plasticity in connectivity pattern organization [17] such as those occurring during brain development in the first span and in healthy aging [6] in the last part of life, as well as brain injuries or diseases (e.g., Alzheimer's disease, brain tumors, etc.) [38].

## References

- [1] L. A. Baccalá and K. Sameshima, "Partial directed coherence: a new concept in neural structure determination," *Biological Cybernetics*, vol. 84, no. 6, pp. 463–474, 2001.
- [2] R. Kuś, M. Kamiński, and K. J. Blinowska, "Determination of EEG activity propagation: pair-wise versus multichannel estimate," *IEEE Transactions on Biomedical Engineering*, vol. 51, no. 9, pp. 1501–1510, 2004.
- [3] E. Bullmore and O. Sporns, "Complex brain networks: graph theoretical analysis of structural and functional systems," *Nature Reviews Neuroscience*, vol. 10, no. 3, pp. 186–198, 2009.
- [4] D. S. Bassett, A. Meyer-Lindenberg, S. Achard, T. Duke, and E. Bullmore, "Adaptive reconfiguration of fractal small-world human brain functional networks," *Proceedings of the National Academy of Sciences of the United States of America*, vol. 103, no. 51, pp. 19518–19523, 2006.
- [5] S. Micheloyannis, E. Pachou, C. J. Stam, M. Vourkas, S. Erimaki, and V. Tsirka, "Using graph theoretical analysis of multi channel EEG to evaluate the neural efficiency hypothesis," *Neuroscience Letters*, vol. 402, no. 3, pp. 273–277, 2006.
- [6] S. Micheloyannis, M. Vourkas, V. Tsirka, E. Karakonstantaki, K. Kanatsouli, and C. J. Stam, "The influence of ageing on complex brain networks: a graph theoretical analysis," *Human Brain Mapping*, vol. 30, no. 1, pp. 200–208, 2009.
- [7] D. J. A. Smit, C. J. Stam, D. Posthuma, D. I. Boomsma, and E. J. C. De Geus, "Heritability of "small-world" networks in the brain: a graph theoretical analysis of resting-state EEG functional connectivity," *Human Brain Mapping*, vol. 29, no. 12, pp. 1368–1378, 2008.
- [8] C. J. Stam, "Functional connectivity patterns of human magnetoencephalographic recordings: a "small-world" network?" *Neuroscience Letters*, vol. 355, no. 1-2, pp. 25–28, 2004.

- [9] C. J. Stam, B. F. Jones, G. Nolte, M. Breakspear, and P. Scheltens, "Small-world networks and functional connectivity in Alzheimer's disease," *Cerebral Cortex*, vol. 17, no. 1, pp. 92–99, 2007.
- [10] C. J. Stam, W. De Haan, A. Daffertshofer et al., "Graph theoretical analysis of magnetoencephalographic functional connectivity in Alzheimer's disease," *Brain*, vol. 132, no. 1, pp. 213–224, 2009.
- [11] S. Micheloyannis, E. Pachou, C. J. Stam et al., "Small-world networks and disturbed functional connectivity in schizophrenia," *Schizophrenia Research*, vol. 87, no. 1–3, pp. 60–66, 2006.
- [12] M. Rubinov, S. A. Knock, C. J. Stam et al., "Small-world properties of nonlinear brain activity in schizophrenia," *Human Brain Mapping*, vol. 30, no. 2, pp. 403–416, 2009.
- [13] F. Bartolomei, I. Bosma, M. Klein et al., "Disturbed functional connectivity in brain tumour patients: evaluation by graph analysis of synchronization matrices," *Clinical Neurophysiology*, vol. 117, no. 9, pp. 2039–2049, 2006.
- [14] L. Deuker, E. T. Bullmore, M. Smith et al., "Reproducibility of graph metrics of human brain functional networks," *NeuroImage*, vol. 47, no. 4, pp. 1460–1468, 2009.
- [15] J. J. Crofts, D. J. Higham, R. Bosnell et al., "Network analysis detects changes in the contralesional hemisphere following stroke," *NeuroImage*, vol. 54, no. 1, pp. 161–169, 2011.
- [16] E. Estrada and N. Hatano, "Communicability in complex networks," *Physical Review E*, vol. 77, no. 3, Article ID 036111, 12 pages, 2008.
- [17] H. Duffau, "Brain plasticity: from pathophysiological mechanisms to therapeutic applications," *Journal of Clinical Neuroscience*, vol. 13, no. 9, pp. 885–897, 2006.
- [18] L. F. Costa and F. A. Rodrigues, "Superedges: connecting structure and dynamics in complex networks," arXiv:0801.4068v2, 2008.
- [19] F. A. Rodrigues and L. da Fontoura Costa, "A structure-dynamic approach to cortical organization: number of paths and accessibility," *Journal of Neuroscience Methods*, vol. 183, no. 1, pp. 57–62, 2009.
- [20] F. A. Rodrigues and L. Da Fontoura Costa, "Generalized connectivity between any two nodes in a complex network," *Physical Review E*, vol. 81, no. 3, Article ID 036113, 10 pages, 2010.
- [21] F. De Vico Fallani, J. Toppi, C. Di Lanzo et al., "Redundancy in functional brain connectivity from eeg recordings," *International Journal of Bifurcation and Chaos*, vol. 22, no. 7, Article ID 1250158, 8 pages, 2012.
- [22] L. Marzetti, G. Nolte, M. G. Perrucci, G. L. Romani, and C. Del Gratta, "The use of standardized infinity reference in EEG coherency studies," *NeuroImage*, vol. 36, no. 1, pp. 48–63, 2007.
- [23] P. L. Nunez, R. Srinivasan, A. F. Westdorp et al., "EEG coherency I: statistics, reference electrode, volume conduction, Laplacians, cortical imaging, and interpretation at multiple scales," *Electroencephalography and Clinical Neurophysiology*, vol. 103, no. 5, pp. 499–515, 1997.
- [24] R. Srinivasan, W. R. Winter, J. Ding, and P. L. Nunez, "EEG and MEG coherence: measures of functional connectivity at distinct spatial scales of neocortical dynamics," *Journal of Neuroscience Methods*, vol. 166, no. 1, pp. 41–52, 2007.
- [25] G. Nolte, O. Bai, L. Wheaton, Z. Mari, S. Vorbach, and M. Hallett, "Identifying true brain interaction from EEG data using the imaginary part of coherency," *Clinical Neurophysiology*, vol. 115, no. 10, pp. 2292–2307, 2004.
- [26] S. Della Penna, C. Del Gratta, C. Granata et al., "Biomagnetic systems for clinical use," *Philosophical Magazine B*, vol. 80, no. 5, pp. 937–948, 2000.
- [27] A. Hyvarinen, J. Karhunen, and E. Oja, *Independent Component Analysis*, Wiley, New York, NY, USA, 2001.
- [28] A. Ewald, L. Marzetti, F. Zappasodi, F. C. Meinecke, and G. Nolte, "Estimating true brain connectivity from EEG/MEG data invariant to linear and static transformations in sensor space," *NeuroImage*, vol. 60, no. 1, pp. 476–488, 2012.
- [29] J. M. Schoffelen and J. Gross, "Source connectivity analysis with MEG and EEG," *Human Brain Mapping*, vol. 30, no. 6, pp. 1857–1865, 2009.
- [30] A. G. Guggisberg, S. M. Honma, A. M. Findlay et al., "Mapping functional connectivity in patients with brain lesions," *Annals of Neurology*, vol. 63, no. 2, pp. 193–203, 2008.
- [31] J. Martino, S. M. Honma, A. M. Findlay et al., "Resting functional connectivity in patients with brain tumors in eloquent areas," *Annals of Neurology*, vol. 69, no. 3, pp. 521–532, 2011.
- [32] L. Marzetti, C. Del Gratta, and G. Nolte, "Understanding brain connectivity from EEG data by identifying systems composed of interacting sources," *NeuroImage*, vol. 42, no. 1, pp. 87–98, 2008.
- [33] G. Nolte, L. Marzetti, and P. Valdes Sosa, "Minimum Overlap Component Analysis (MOCA) of EEG/MEG data for more than two sources," *Journal of Neuroscience Methods*, vol. 183, no. 1, pp. 72–76, 2009.
- [34] F. De Vico Fallani, F. Baluch, L. Astolfi, D. Subramanian, G. Zouridakis, and F. Babiloni, "Structural organization of functional networks from eeg signals during motor learning tasks," *International Journal of Bifurcation and Chaos*, vol. 20, no. 3, pp. 905–912, 2010.
- [35] F. De Vico Fallani, F. A. Rodrigues, L. Da Fontoura Costa et al., "Multiple pathways analysis of brain functional networks from eeg signals: an application to real data," *Brain Topography*, vol. 23, no. 4, pp. 344–354, 2011.
- [36] O. Sporns and J. D. Zwi, "The small world of the cerebral cortex," *Neuroinformatics*, vol. 2, no. 2, pp. 145–162, 2004.
- [37] Y. Benjamini and D. Yekutieli, "The control of the false discovery rate in multiple testing under dependency," *Annals of Statistics*, vol. 29, no. 4, pp. 1165–1188, 2001.
- [38] M. Hallett, "Brain redundancy: responsivity or plasticity?" *Annals of Neurology*, vol. 48, no. 1, pp. 128–130, 2000.
- [39] R. I. Goldman, J. M. Stern, J. Engel, and M. S. Cohen, "Simultaneous EEG and fMRI of the alpha rhythm," *NeuroReport*, vol. 13, no. 18, pp. 2487–2492, 2002.
- [40] B. Bollobas, *Modern Graph Theory*, vol. 184 of *Graduate Texts in Mathematics*, 1998.
- [41] M. Rubinov and O. Sporns, "Complex network measures of brain connectivity: uses and interpretations," *NeuroImage*, vol. 52, no. 3, pp. 1059–1069, 2010.
- [42] D. Mantini, M. G. Perrucci, C. Del Gratta, G. L. Romani, and M. Corbetta, "Electrophysiological signatures of resting state networks in the human brain," *Proceedings of the National Academy of Sciences of the United States of America*, vol. 104, no. 32, pp. 13170–13175, 2007.

## Research Article

# Source Space Analysis of Event-Related Dynamic Reorganization of Brain Networks

**Andreas A. Ioannides,<sup>1</sup> Stavros I. Dimitriadis,<sup>2</sup> George A. Saridis,<sup>1</sup> Marotesa Voultsidou,<sup>1</sup> Vahe Poghosyan,<sup>1</sup> Lichan Liu,<sup>1</sup> and Nikolaos A. Laskaris<sup>2</sup>**

<sup>1</sup>Laboratory for Human Brain Dynamics, AAI Scientific Cultural Services Ltd., Office 501 Galaxias Center, 33 Arch. Makarios III Avenue, 1065 Nicosia, Cyprus

<sup>2</sup>Artificial Intelligence & Information Analysis Laboratory, Department of Informatics, Aristotle University, 54124 Thessaloniki, Greece

Correspondence should be addressed to Andreas A. Ioannides, a.ioannides@aaiscs.com

Received 2 April 2012; Revised 5 June 2012; Accepted 10 August 2012

Academic Editor: Tianzi Jiang

Copyright © 2012 Andreas A. Ioannides et al. This is an open access article distributed under the Creative Commons Attribution License, which permits unrestricted use, distribution, and reproduction in any medium, provided the original work is properly cited.

How the brain works is nowadays synonymous with how different parts of the brain work together and the derivation of mathematical descriptions for the functional connectivity patterns that can be objectively derived from data of different neuroimaging techniques. In most cases static networks are studied, often relying on resting state recordings. Here, we present a quantitative study of dynamic reconfiguration of connectivity for event-related experiments. Our motivation is the development of a methodology that can be used for personalized monitoring of brain activity. In line with this motivation, we use data with visual stimuli from a typical subject that participated in different experiments that were previously analyzed with traditional methods. The earlier studies identified well-defined changes in specific brain areas at specific latencies related to attention, properties of stimuli, and tasks demands. Using a recently introduced methodology, we track the event-related changes in network organization, at source space level, thus providing a more global and complete view of the stages of processing associated with the regional changes in activity. The results suggest the time evolving modularity as an additional brain code that is accessible with noninvasive means and hence available for personalized monitoring and clinical applications.

## 1. Introduction

Even the simplest of tasks, be it purely cognitive, purely muscular, or a combination of the two involves coordinated activity in distinct brain areas distributed across the cortical mantle and deep brain nuclei. The coordination however is full of redundancy so that an identical goal, for example, a movement of a finger or an eye, the perception of a simple figure or a letter, can be accomplished in any of number of possible ways [1]; only in pathology the repetition of an identical task involves a rigid repetition of a fixed sequence of brain activations. The apparent orderly progression of activity that the averaged (over many trials and subjects) electroencephalography (EEG) and magnetoencephalography (MEG) data reveal is a mirage of a sandwich of histories [2]. There is however much useful information in this mirage, primarily the identification of key brain areas and

points in time. In terms of cortical networks the analysis of gross measures like the average signal elicited by a large number of identical stimuli can reveal key nodes in the network that play critical role in the task and points in time when stages of processing reach a climax or are completed. Careful experimental design can then help identify the stages of processing supporting the perception of a specific type of stimuli or how they are underpinning a specific task.

Here, we adapt a dynamic graph theoretical formalism [3, 4] to the study of real-time regional brain activations derived from tomographic source analysis of MEG signals [5]. In line with many recent studies we use phase coupling to describe quantitatively the stimulus- and task-related synchronization (as a putative mechanism for long-range integration) of brain responses. We use single trial tomographic estimates of brain activity to statistically identify the key individual brain regions and derive dynamic brain networks and their

graph theoretical properties. The methodology allows us to generalize the viewpoint of isolated regional changes in brain activity to the wider framework of quantifiable changes in network properties and organization. We are specifically interested in personalized monitoring of brain function and therefore apply the methodology to the single trial MEG data from individual subjects in two different sets of experiments. The first set of experiments was designed to examine the effect of attention on the earliest sensory processing stages in the brain. In our earlier study of regional time courses we found that spatial attention modulates the initial feedforward response in the primary visual cortex beginning at  $\sim 55$  ms [6]. The second set of experiments focuses on the use of letter and pseudoletters as elements for category selection. The earlier analysis of neural activity in individual brain regions revealed key roles of cuneus and fusiform gyrus (FG) in this task [7].

Using methodologies and algorithms from the well-established branch of graph theory, the multidisciplinary approach of *complex-network* analysis characterizes a wide range of naturally occurring systems by quantifying the topologies of their network representations [8–10]. A wide range of methods have been proposed to characterize the rich anatomical and functional connectivity patterns of the brain using signals from modern brain-imaging techniques, such as diffusion MRI, functional MRI (fMRI), and EEG/MEG [11–14]. In retrospect, the description of the anatomical and functional organization of the brain as complex networks seems almost unavoidable and the question is which of the many different ways is more appropriate. The vast majority of previous studies have relied on analyzing the topological properties of static graphs, where nodes correspond to distinct brain regions and link to pairwise associations among them. The links in these graphs remain unaltered over time. Whereas this approach is reasonable for anatomical connectivity, it fails to account for the labile and highly dynamic nature of brain activity, particularly when signals from fast-recording modalities of EEG/MEG are used [15]. It is widely accepted that perceptually and behaviorally relevant events are reflected in the changes of neural activity in large-scale distributed neuronal networks [16]. However, it is much less clear how these networks are organized dynamically. This is due to the inherent difficulty in extracting information, from multiple recording sites, about the various processes participating in a particular cognitive task. The situation is further complicated by the fact that not only the state of any particular cortical area, but also the relations between cortical areas can shift rapidly on a time scale of tens of milliseconds [17, 18].

Recently a few studies have appeared focusing on the evolution of connectivity pattern as this is estimated from multichannel recordings. These studies use a moving time-window to estimate distinct connectivity graphs from the enclosed signal-segments, and by employing a topological descriptor (i.e., network metric), they derive as output a timeseries reflecting the event-related network self-organization. In most network evolution studies the connectivity is computed from the analysis of the raw signals of individual EEG/MEG sensors [19, 20]. However, a sensor

based description of connectivity does not necessarily relate in an obvious way to the actual functional connectivity in the brain. For EEG, volume conduction effects and the high resistivity of the skull make the signal of each EEG electrode sensitive to a large number of brain areas. In the case of MEG, the signal of magnetometers and axial gradiometers are also influenced by a number of generators and in addition the same generator in the brain gives rise to strong contributions in different MEG sensors. The connectivity pattern computed directly over EEG/MEG sensors must therefore be interpreted with caution.

As a remedy, neuronal interactions can be studied based on signals resulting from source reconstruction [15, 21–23]. It is possible to compute the connectivity pattern from actual source activity estimates derived from the average signal of multichannel recordings of either EEG [24] or MEG [25]. To fully capture the dynamic changes in event-related connectivity, it is necessary to use single trial tomographic solutions, but this has so far been attempted for only a small number of areas [26, 27]. The results from studies using only a small fraction of the network nodes do not necessarily reflect large scale changes in network organization. Here, we combine the potential of time-varying network-analysis [3, 4] with the power of tomographic source reconstruction derived either from single trial MEG signals or many averages of few trials. The analysis allows us to examine visual response mechanisms under the innovative perspective of network reconfiguration dynamics.

## 2. Methods

### 2.1. Quantifying Functional Brain Connectivity

**2.1.1. Time-Varying Functional Connectivity.** Complex networks are characterized by recurring patterns, motifs, and abrupt changes in network organization that demand the refinement of existing methods and the development of new ones [10]. In an effort to accommodate the need for a dynamic description of functional brain connectivity, we have developed a network analysis framework for quasi-instantaneous estimates of connectivity patterns. In each step of the analysis, functional coupling measures capture a snapshot of connectivity within a window that encompasses only a small segment of the signals. The window is then moved forward by a fixed step to track the time evolution of the computed quantities. The method can be applied to broadband signals or to signals filtered within a predefined frequency band. The selection of window width must preserve the features in the signal, that is, it must correspond to the frequency band used. For narrow band signals the window is determined by the lower frequency limit since this defines what brain rhythm (synchronized oscillations) survive the filtering process. In the narrow band computations we will describe next the “cycle-criterion” (CC), as defined by Cohen [28]. According to this criterion the time-window width is  $CC = 2$  cycles of the lower frequency. For the time step we used 5 samples, moving forward by that amount the centre of the window and recomputing the various quantities

for the whole network connectivity based on the new signal segments.

**2.1.2. Functional Connectivity Graphs (FCG).** To detect and precisely characterize neural synchrony between distinct recording sites, one can employ various synchrony measures like the phase locking value (PLV) [29], phase lag index (PLI) [30], coherence, and mutual information over the corresponding signals. These measures are applied, using  $N$  signals filtered within a particular frequency band, to every possible pair of electrodes or regions of interests (ROIs). The derived quantities are tabulated in an  $[N \times N]$  matrix in which an entry conveys the strength of the functional connection between a particular pair. This matrix has a natural graph representation, called hereafter the “functional connectivity graph” (FCG), with the nodes being the recording sites and edges representing the in-between links weighted by the tabulated value. In this study we put emphasis on phase synchrony and decided to experiment with two different measures of phase coupling, namely, PLV and PLI. In our multitrial setting, both measures have been adapted so as to describe response related synchronization (as a putative mechanism for long-range integration) during information flow in visual cortex.

Phase synchrony measures have recently gained great popularity as tools for the study of brain network organization. Based on the theoretical argument that weak coupling first affects the phases of oscillators, the detection of phase synchronization is considered sufficient to reveal interactions between two weakly coupled (sub)systems [31]. In addition, brain signals and phase synchronization in specific frequency bands are thought to play a critical role in neuronal information processing [32]. Recent studies have demonstrated the pivotal role of phase synchronization in memory processes [33] and mental calculations [34].

PLV is the basic measure for frequency-specific synchronization between two signals. For every trial  $k$  ( $k = 1, \dots, N_{\text{trials}}$ ), and for every latency  $n$ , the instantaneous phase  $\varphi(n, k)$  is extracted using the signal segment enclosed within a window of  $W_L$  samples long. The window length is defined, independently for each frequency band under study, as  $W_L = (CC/f_{\text{low}}) * f_s + 1$ , where  $CC$  denotes the number of samples, which in our case corresponds to 2 cycles of a cosine with the lowest frequency  $f_{\text{low}}$  in the particular frequency band, and  $f_s$  is the sampling frequency. For a given pair  $(u, v)$  of ROIs, the following formula estimates the latency dependent phase synchronization according to PLV estimator:

$$\begin{aligned} & \text{PLV}^{(u,v)}(n)_{\text{across trials}} \\ &= \frac{1}{N_{\text{trials}}} \left| \sum_{k=1}^{N_{\text{trials}}} \frac{1}{W_L} \sum_{n'=n-W_L/2}^{n+W_L/2} \exp(i\Delta\varphi(n', k)) \right|, \end{aligned} \quad (1)$$

where  $\Delta\varphi(n, k)$  is the phase difference  $\varphi^u(n, k) - \varphi^v(n, k)$  between the corresponding signals (filtered within a particular frequency range). PLV quantifies the intertrial variability of this phase difference at latency  $n$ . If the phase difference varies little across the trials, PLV is close to 1; otherwise it

is close to 0 [29]. Usually, the above quantity is integrated over successive latencies (that correspond to the moving window) so as to achieve a more robust measurement. In our implementation, the reconstructed regional activations are filtered within known frequency bands (e.g.,  $\alpha$ -waves,  $\gamma$ -oscillations) and the estimated latency-dependent PLV values are used to derive the final weights for the FCGs with the statistical procedure described at the end of this section.

PLI has been introduced as an alternative phase synchronization measure, with the additional advantage of providing coupling measurements that are insensitive to the presence of common sources or volume conduction (and/or active reference electrodes in the case of EEG). The principal idea behind PLI is to quantify, only, the (relative) phase distribution’s *asymmetry*. In our latency-dependent implementation, this phase synchronization estimator takes the following form:

$$\begin{aligned} & \text{PLI}^{(u,v)}(n)_{\text{across trials}} \\ &= \frac{1}{N_{\text{trials}}} \left| \sum_{k=1}^{N_{\text{trials}}} \frac{1}{W_L} \sum_{n'=n-W_L/2}^{n+W_L/2} |\text{sign}[\sin \Delta\varphi(n')]| \right|. \end{aligned} \quad (2)$$

The PLI is bounded  $0 \leq \text{PLI} \leq 1$  and a PLI of zero indicates either no coupling or coupling with a phase difference centred on  $0 \bmod \pi$ . Since the neuroelectric recordings take place at the quasistatic range of frequencies, volume conduction introduces a zero lag phase, which is eliminated by PLI. Depending on what frequency is used, PLI will also eliminate contributions from synchronies with short delays.

It is a common practice to trim the initial estimates of functional connectivity so as to null out insignificant couplings that always appear due to random fluctuations in any time series. Based on a Rayleigh test for the uniformity of a synchronization measure (SM), we calculated the significance of each value (significance is calculated as  $p = \exp(-N_{\text{trials}} * \text{SM}^2)$  [35]; with SM denoting either PLV or PLI). To correct for multiple testing, the false discovery rate (FDR) method was adopted [36]. A threshold of significance was set such that the expected fraction of false positives was restricted to  $q \leq 0.001$ . The  $\text{PLV}^{(u,v)}$  (or  $\text{PLI}^{(u,v)}$ ) values surviving this threshold were used to fill the weighted adjacency matrix  $\mathbf{W}$  (the tabular counterpart of a given FCG).

**2.1.3. Characterizing FCGs via Network Metrics.** FCGs can be described [37], classified, and selected as representatives of a group [38] according to various network metrics. Here, we characterize FCGs using a popular topological metric established for weighted connectivity graphs known as local efficiency (LE) [39]. It is defined as

$$\text{LE} = \frac{1}{N} \sum_{i \in N} \frac{\sum_{j, h \in G_{i,j,h \neq i}} (d_{jh})^{-1}}{k_i(k_i - 1)} \quad (3)$$

with  $N$  representing the total number of nodes in the network (i.e., the number of selected ROIs),  $k_i$  corresponding to the total number of neighbors of the current node, while  $d$  denotes the shortest absolute path length between every possible pair in the neighborhood of the current node.

LE is understood as a measure of the fault tolerance of the network, indicative of how well subgraphs exchange information when the indexed node is eliminated [40]. Specifically, each node was assigned the shortest path length within the subgraph,  $G_i$ .

**2.1.4. Detecting Modules in the FCG.** A recently introduced graph-theoretic algorithm [38] is employed for identifying the most-cohesive group of vertices given the undirected weighted matrix  $\mathbf{W}$  of a graph. The algorithm is based on the identification of the dominant set of nodes and when repeatedly applied yields the effective clustering, in a sequential mode, of pairwise relational data. One of its main characteristics is the compact, elegant formulation. In our case takes the form of deriving the  $N$ -dimensional vector  $\mathbf{y}$  that maximizes the following objective function (i.e., the set-compactness):

$$\begin{aligned} \max F(\mathbf{y}) &= \mathbf{y}^T \mathbf{W} \mathbf{y}, \\ \mathbf{y} \in \Delta, \Delta^n &= \left\{ \mathbf{y} \in \mathbf{R}^N : y_i \geq 0 \forall i \cup \sum_{i=1}^n y_i = 1 \right\}. \end{aligned} \quad (4)$$

Following a random initialization (with  $N =$  (no. of sources) small positive numbers as the components of  $\mathbf{y}$ ), a simple recursive formula leads to the desired solution:

$$y_i^{[k+1]} = y_i^{[k]} \frac{(\mathbf{W} \mathbf{y}^{[k]})_i}{(\mathbf{y}^{[k]})^T \mathbf{W} \mathbf{y}^{[k]}}, \quad i = 1, 2, \dots, N. \quad (5)$$

After a fixed number of iterations, the support of  $\mathbf{y}$  (i.e., the set of indices corresponding to its nonzero components) is computed providing the set of nodes participating in the dominant graph-component. The full partition of a graph into disjoint sets of nodes is accomplished by repeating the following three steps: (i) finding the current dominant set, (ii) removing the vertices in that cluster, and (iii) iterating again on the rest of nodes.

With the above procedure, each single FCG is segmented into distinct graph-components. Provided that internode similarity is expressing functional coupling, the clustering result can be considered as detection of independent functional modules within the network of visual areas. The end output is a  $N$ -tuple  $\mathbf{c} = [c_1, \dots, c_N]$ ,  $c_i \in Z$  (e.g.,  $\mathbf{c} = [1 \ 3 \ 2 \ 3 \ \dots \ 2 \ 1 \ 1 \ 1 \ 2]$ ) summarizing the graph-partition. Each integer is associated with an ROI and coincides with the membership label in one of the sequentially formed groups: 1 for the most prominent functional group, 2 for the second, and so forth. We adopted as cohesive index (CI) of each cluster the objective function that is maximized by the graph clustering algorithm (4). CI is defined alternative to (4) as

$$CI_i = \frac{1}{N_c} \sum_{s=1}^{N_c} ICS(s), \quad (6)$$

where  $CI_i$  is the CI for each cluster  $i$ ,  $N_c$  is the number of nodes participated in the cluster, and ICS is the total weight of within cluster connections of each node (called intracluster strength).

**2.2. Experiments Used.** We applied the connectivity analysis methodology described above to two sets of data, both using visual stimuli presented to the lower left and right part of the visual field. The first experiment was designed to study the role of spatial attention and the main comparison of interest to us here was between responses elicited by identical stimuli in attended versus ignored conditions. The second experiment was designed to study how the nature of stimuli (letter versus pseudoletter) affected the categorization process in the brain. The categories were defined based on either shape or identity.

**2.2.1. Spatial Attention Experiment.** The full details of the experimental protocol, data preprocessing and source analysis are described elsewhere [6, 41]. Here we used the subset of the data where checkerboard stimuli were used to test the effect of spatial attention on visually evoked responses. Specifically, two sets of single trial data from two different experimental runs are presented here. In both sets of trials the same ellipse-shaped high-contrast checkerboard stimuli were presented in a random order, at  $10^\circ$  eccentricity along the  $45^\circ$  diagonals in lower left or right visual hemifield. Checkerboards had dimensions of  $8.5^\circ \times 6.5^\circ$ , a check size of  $0.85^\circ \times 0.85^\circ$ , and were oriented vertically, tilted at  $18^\circ$  or  $-18^\circ$  angles. All stimuli were 350 ms in duration with interstimulus interval varied randomly between 600 and 1200 ms. During a run, each stimulus exemplar (different orientations) in each hemifield was presented for six times, thus total of 36 trials are used here (3 orientations (exemplars)  $\times$  6 repetitions of each exemplar  $\times$  2 presentation sides, left and right).

Subjects were instructed to avoid any kind of eye or body movement, maintain fixation on a central cross, and respond to stimuli appearing in the target hemifield, as accurately and quickly as possible. In one run (18 trials) the target was the left hemifield, in another run the right hemifield. The effect of spatial attention is identified by comparing the brain activity elicited by same stimuli when the attention is directed to the stimulated versus opposite visual hemifield.

Two sets of ROIs are used in the current study for the connectivity analysis. The first set includes twelve visual cortical ROIs, bilaterally in: V1, V2, V4, V5, lateral occipital (LO) cortex and fusiform gyrus (FG). These ROIs were defined by statistically comparing visually evoked neural responses in the post- versus prestimulus periods, as described in [41]. The second set includes eight ROIs in: medial precuneus, paracentral lobule, middle frontal gyrus (MFG), right MFG, and bilateral inferior parietal lobule (IPL) and precentral gyrus (preCG). These are putative ROIs involved in the control of visual attention. They were identified by comparing the prestimulus periods of tomographic estimates from all the trials where attention was directed to visual versus auditory modality (for the details on all visual and auditory attention conditions see the full description of the experiment in [41]).

**2.2.2. Letters and Shapes Experiment.** In this, the letters and shapes experiment, subjects performed a two-alternative forced-choice categorization task. The task was a shape

(i.e., the two stimuli within a category had similar shape), an identity (i.e., the two stimuli differed in shape), or an arbitrary task. The stimuli were letters and pseudoletters presented with either a congruent or incongruent surround, and were presented to the center, lower left or lower right of the visual field. The experiment is a continuation of an earlier experiment where stimuli were presented in the left and right part of the visual field only [7]. We will report here results from the second experiment.

Before each run subjects memorized a pair of categories, consisting of four target items each. They were labeled 1 and 2 and were presented simultaneously on the left and right side of the screen. Next, subjects practiced the task in a training session. A trial started with a cue (fixation cross, “<” or “>”) at the center of the screen signaling to the subjects in which part of the visual field the stimuli will be presented (bottom left, centre or bottom right). We instructed subjects to fixate on this cue during the entire trial. The stimulus appeared in the cued part of the visual field after a random interval (600–1200 ms), at 8 degrees eccentricity from the center of the screen for the peripheral presentations. Cue and stimulus remained on screen until the subject responded “Category 1” (by lifting the left index finger), or “Category 2” (right index finger). During training visual performance feedback was provided, but during recording runs ( $n = 16$ ) no feedback was given. A recording run had 144 trials, that is, 6 repetitions of each of the 24 unique trials (2 letters and 2 pseudoletters, each occurring in 2 surround conditions and 3 visual field locations).

MEG signals were recorded while subjects performed the task. We first used standard preprocessing of the MEG signal to remove environmental noise and subject artifacts (heart beats and eye blinks). We then averaged the signals for the 6 repetitions of each unique trial condition in each run and each visual field location. Finally, we applied magnetic field tomography to the averaged signal to obtain independent tomographic reconstruction of activity throughout the brain for each timeslice of the signal (every 0.8 ms), from 200 ms before to 500 ms after stimulus onset. The analysis produces for each visual field location and for each latency (step 0.8 ms) a total of 48 tomographic estimates of activity for each stimulus type (letter or pseudoletter), and a total of 32 tomographic estimates of activity for each task condition (Arbitrary “A”, Identity “I” and Shape “S”). To define ROIs, we applied statistical parametric mapping. Factorial analysis (ANOVA) quantified how the activity in each identified ROI changed over factors of task, stimulus type, surround and visual field location.

We again use ROIs defined functionally for the connectivity analysis. For this case we include for V1 not only the ROIs defined for the stimuli we used, but also the ones defined for placements in the top part of the visual field. The key areas for the experiment are the LO and mid-FG areas and the Cuneus (Cu). In this and the previous study [7] the separate regional analysis identified the LO and FG areas to be most relevant for the processing of letters and sensitive to task demands and the Cu to play a role in anticipation of stimuli and coordinating the resource allocation for each task.

Our analysis of the letter and shape experiments explores how the network properties evolve in the left and right hemispheres for two distinct cases. In the first case we compare the network evolution for stimuli that are either over-learned symbols (letters) or similar in shape, that is, a pseudoletter, that has not yet acquired the letter identity; pseudoletters must be processed each time according to their shape. In the second case we compare the network evolution for three different tasks. In the first task the subject simply responds to any stimulus without the need to make any category distinction while in the other two a selection based on category membership must be made. In the second task (identity) the categories can be differentiated by identity of the members since the shapes are mixed in each category. In the last task (shape) the elements of each category can be distinguished by a prominent shape difference (e.g., members of one category have curved surface while that of the other are rectangular).

### 3. Results

**3.1. Spatial Attention.** PLV- and PLI-based FCGs were constructed for five frequency bands:  $\delta$  (1–4 Hz),  $\theta$  (4–8 Hz),  $\alpha$  (8–13 Hz),  $\beta$  (13–30 Hz), and  $\gamma$  (30–45 Hz). We used LE of FCGs in each of these bands to identify the effect of spatial attention on event-related connectivity. The clearest attention-related changes were found in  $\alpha$  and  $\beta$  bands for both PLV- and PLI-based FCGs (Figure 1). In  $\alpha$ -band there was a marked attention-related decrease of LE, while opposite effect was found in  $\beta$ -band. Interestingly, these effects are identified at the same early latencies as the key regional activity modulations found in our earlier studies [6, 41]. To determine the sources of attention-related changes in LE we examined the dynamics of  $\alpha$  and  $\beta$  band FCGs in attended and ignored conditions. Figure 2 shows the PLI-based  $\alpha$  (c, d) and  $\beta$  ((a, b)) band FCGs at  $\sim 70$  ms, for stimuli presented in the lower left visual quadrant, when attention was directed to the left (attended condition, (a, c)) and right (ignored condition, (b, d)) visual hemifields. In  $\beta$  band there is a strong phase coupling (increased connectivity) between early contralateral (right) visual cortical areas (V1, V2, V4, and LO) in the attended condition, which likely enables an efficient processing of attended stimuli. In the  $\alpha$  band, strong phase coupling is found in the ignored condition, between the contralateral (right) visual cortical areas and the right IPL. Such coupling between the IPL, which is involved in attentional control processes [42–44], and lower level visual areas likely reflects the top-down suppression of ignored stimuli.

### 3.2. Letters and Shapes

**3.2.1. Comparison between Letters and Pseudoletters.** We first used the cluster analysis described in Section 2.1.4 to study the connectivity patterns elicited by each stimulus category (letters and pseudoletters) presented in different parts of the visual field (center, lower left, and right quadrants). The adopted clustering algorithm was applied to PLV-based FCG computed from wide band data. Figure 3 shows the dynamics

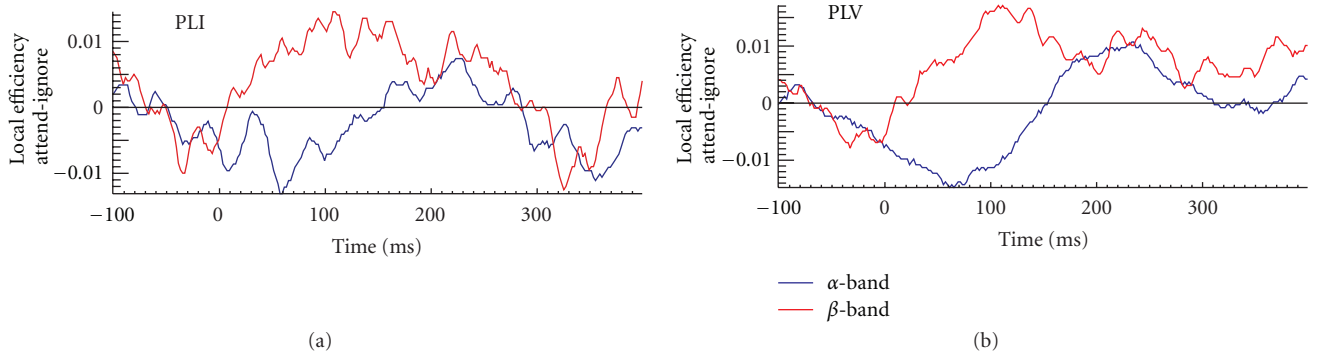


FIGURE 1: Local efficiency (LE) difference between the attended and ignored conditions as a function of latency in the  $\alpha$  (blue) and  $\beta$  (red) frequency bands. These results were computed after averaging the corresponding values for the occipital sensors and for stimuli presented to the left and right bottom parts of the visual field. The results are similar for the phase lag index (PLI; (a)) and for the phase locking value (PLV; (b)). In both cases the minimum reduction in  $\alpha$  band coincides with the peak of the early attentional effects in V1 ( $\sim 70$  ms).

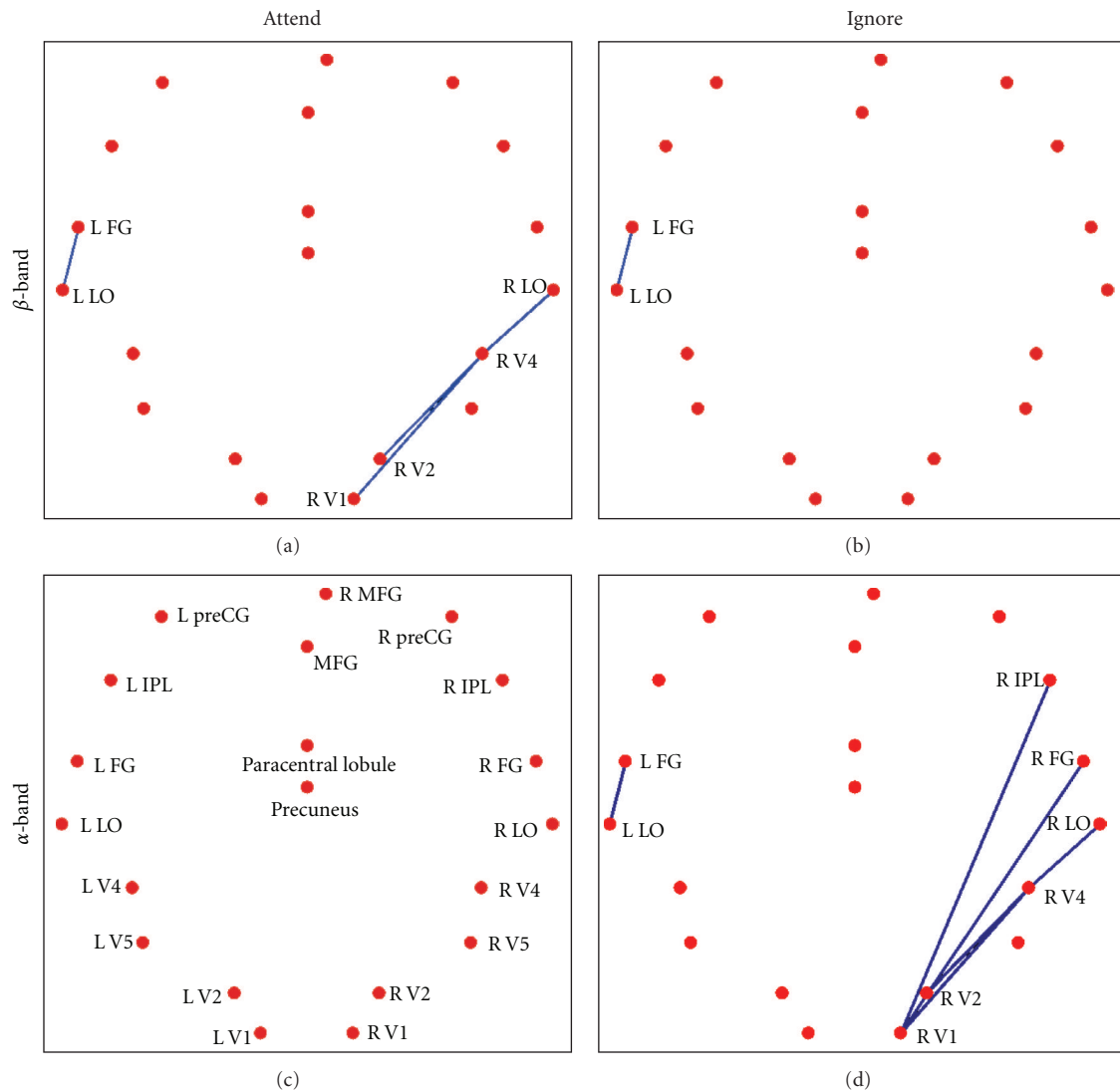


FIGURE 2: The strongest links  $\alpha$  (c, d) and  $\beta$  (a, b) frequency bands for stimuli presented in the bottom left part of the visual field at 70 ms. For the  $\beta$  band the strongest links that differentiate attend versus ignore conditions are in the contralateral (right) hemisphere and connect V1 and V2 to V4 and V4 to LO. For the  $\alpha$  band, the strongest links are in the ignore condition, again in the contralateral (right) hemisphere; they involve the same early visual areas, connecting V1 and V2 to V4 and V4 to LO, and in addition links between V1 and the FG and IPL.

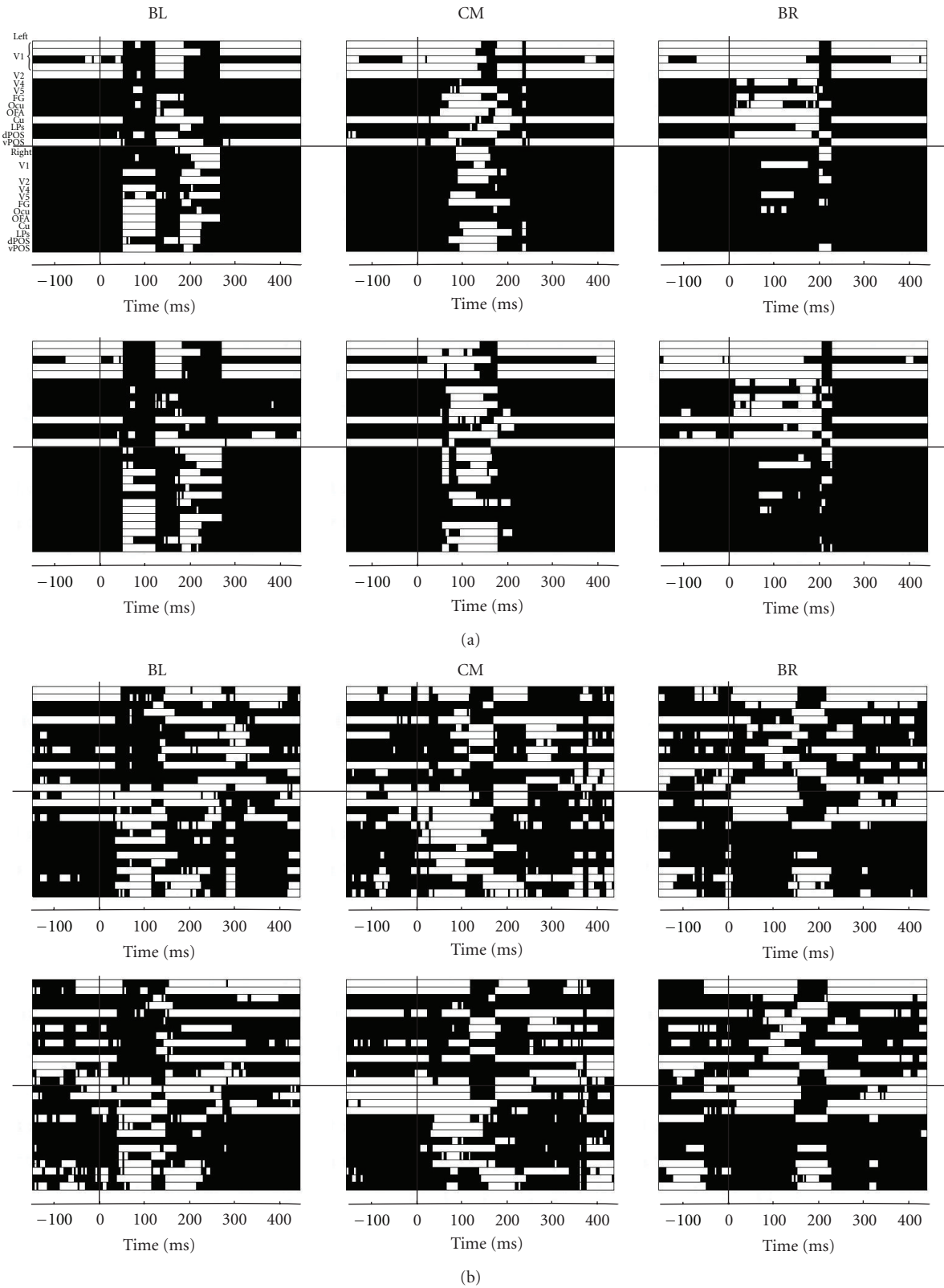


FIGURE 3: Global clustering patterns in the lower left (left column), centre (middle column), and lower right (right columns) visual fields for (a) subject 1 and (b) subject 2. Separate computations are shown for letters (upper rows in (a) and (b)) and pseudoletters (lower rows). Membership to the dominant cluster is represented by white and membership to any other cluster by black color. The computation for cluster membership was done from the wide band data pooling all three conditions (arbitrary, identity, and shape tasks).

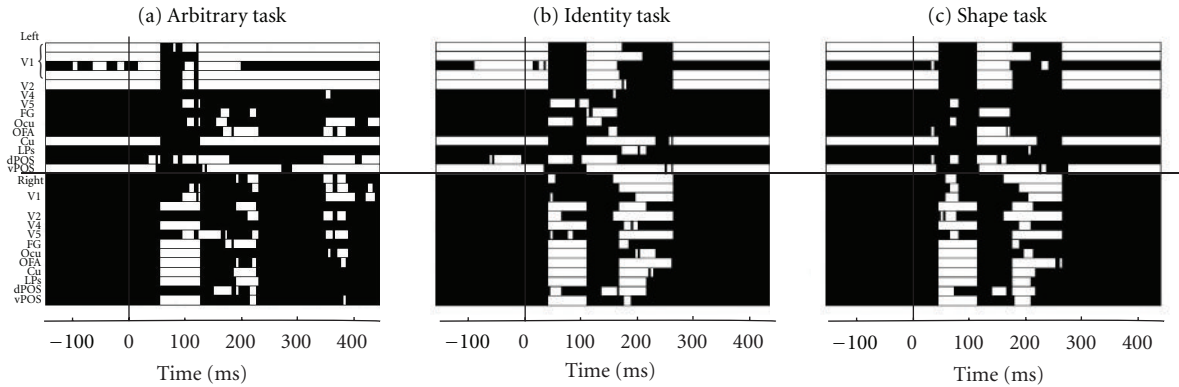


FIGURE 4: Global clustering patterns for each condition, Arbitrary (a), Identity (b) and Shape (c) for subject 1 and presentation the lower left visual field. Membership to the dominant cluster is represented by white and membership to any other cluster by black; the computation for cluster membership was done from the wide band data pooling together letter and pseudoletter stimuli presented in the lower left quadrant of the visual field.

of the dominant clusters (cluster with the highest cohesive index) for two subjects.

Within each subject, the clustering patterns were different in response to stimuli presented in different parts of the visual field (compare different columns in Figure 3), as expected [25], but were very similar across different stimulus categories (compare the rows in Figures 3(a) and 3(b)). The patterns were also very different across subjects (compare Figures 3(a) and 3(b)). These results suggest existence of multiple alternative task-specific mechanisms for large-scale communication in the brain, whereas the employment of the particular mechanism is subject-specific. These results show the suitability of the method for within subject analysis while highlighting the need for care when group analysis is attempted.

We describe in a little more detail the connectivity pattern for subject 1, who was significantly more experienced in the task. For this subject the connectivity pattern in the prestimulus period resolved into 3 to 5 clusters, but only one cluster had a high compactness and it was composed entirely of early visual areas and the cuneus, all in the left hemisphere. Within 100 ms of the stimulus arrival reorganization of connectivity has taken place with distinct patterns of connectivity emerging from the common prestimulus base for each visual field location. Within 30 milliseconds of a stimulus appearing in the left visual field the dominant cluster changes drastically with right hemisphere areas (contralateral to the stimulus) populating the dominant cluster and the left hemisphere ones relegated to the second cluster. For stimuli presented in the right visual field the transition is smoother as more extrastriate areas of the right hemisphere gain membership in the dominant cluster. Within 50 ms some visual areas in the ipsilateral hemisphere become members of the dominant cluster. The stationarity of the main cluster extends from 30 to nearly 200 ms for stimuli presented in the right visual field. For stimuli presented in the left visual field the pattern is stationary for shorter period suggesting that at least two stages of processing are involved. For stimuli presented at the center of the visual field, visual areas from

both the left and the right hemispheres become members of the dominant cluster, which is more cohesive and has more members than in the other two cases.

For the second, less experienced, subject the organization and evolution of the dominant cluster was less organized. However few common features could be noted. In the first 100 ms of the poststimulus period, the dominant cluster was composed mainly of contralateral visual areas, while at later latencies ( $\sim 200$  ms) many areas from the ipsilateral hemispheres also became part of the dominant cluster. Importantly, similar to subject 1, the clustering patterns were similar for the two stimulus categories (letters and pseudoletters).

Figure 4 shows the changes in membership of the dominant cluster (cluster with the highest cohesive index) for stimuli presented in the lower left quadrant of the visual field in the three different tasks for the first subject. Since the responses to letters and pseudoletters were very similar, we combined them within each task. There is a clear difference between the random responses (arbitrary, random response to any stimulus that appears) and the tasks where categorization must take place, either in terms of identity or the shape of the stimuli. In the ipsilateral hemisphere (left) there is only a brief change in membership within the first 100 ms, or very soon after all areas return to the dominant cluster. In the contralateral hemisphere the first response is similar in all tasks. The most noticeable difference is that for the arbitrary task, V2 and V4 are either absent from the dominant cluster, or they participate for shorter periods compared to the other two tasks. This probably reflects the reduced demand for detailed visual stimulus processing in the arbitrary task. Overall, in the second phase of processing the participation of most visual areas in the dominant cluster is weaker for the arbitrary task.

The presentations in terms of the dominant clusters provide a global view of the topological organization of FCG. While for each subject such presentations revealed clear differences related to the stimulated part of the visual field, they revealed only minute differences related to the stimulus

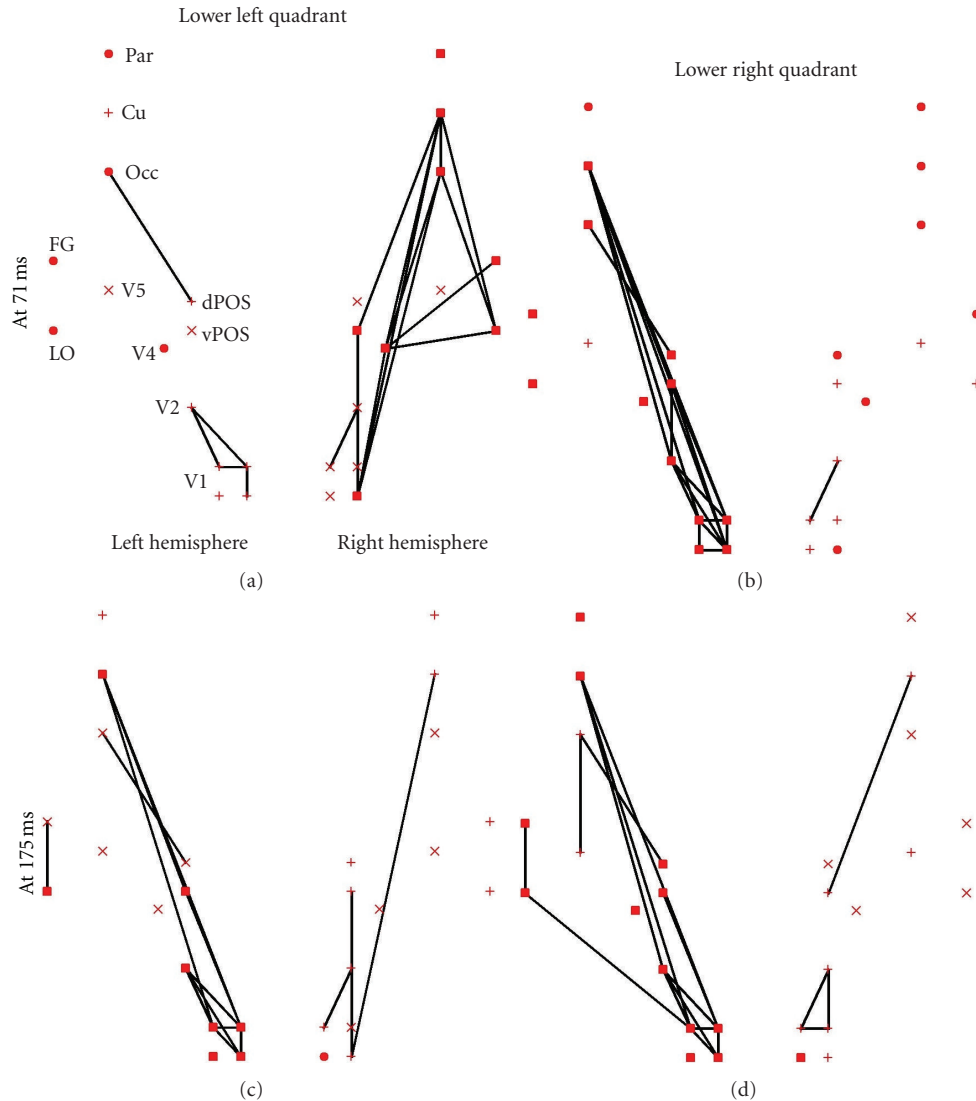


FIGURE 5: The strongest links between ROIs elicited by letters, computed from the wide band data with window center at 71 ms (top part of (a) and (b)) and 175 ms (bottom part of (c) and (d)). The results are shown separately for stimuli presented in the lower left (left part of (a) and (c)) and lower right (right part of (b) and (d)) quadrants of the visual field. Only the top 5% links are displayed that have also passed the threshold of  $FDR < 0.001$ . The results obtained from one subject are shown.

category (letters and pseudoletters) and active tasks (identity and shape discrimination). Clearly much detail remains hidden from the analysis presented in Figures 3 and 4. To study the subtle differences that distinguish the processing of different stimuli we use graph displays at key latencies extracted from wide band (Figures 5 and 6) and the  $\gamma$ -band (Figures 7 and 8). In these figures, we preserve the  $k = 5\%$  of the strongest connections that also satisfy a significance test with  $FDR < 0.001$ ; membership in the dominant cluster is indicated by a filled square symbol and membership to the second, third and fourth most cohesive clusters by an “x” a “+” and filled circle.

Figures 5 and 6 show for two subjects, respectively, the connectivity patterns elicited by each stimulus category (letters and pseudoletters) at around 70 and 170 ms using the results from the tomographic analysis of the wideband MEG

signals. At  $\sim 70$  ms the dominant cluster (filled squares) is composed mainly of visual areas in the hemisphere contralateral to the stimulus presentation. For the first subject the separation is complete, that is, only areas of the contralateral hemisphere belong to the dominant cluster. For the second subject a small number of areas from the ipsilateral hemisphere are clustered together with the contralateral hemisphere areas.

At  $\sim 170$  ms we see a different pattern for each subject. For the first subject, the dominant cluster is mainly in the left hemisphere independent of where the stimulus is presented; for stimuli in the right visual field the dominant cluster includes all left hemisphere areas related to visual processing and the cuneus. For stimuli presented on the left hemisphere the dominant cluster involves early visual areas and the left cuneus, while the second dominant cluster (“x”) involves

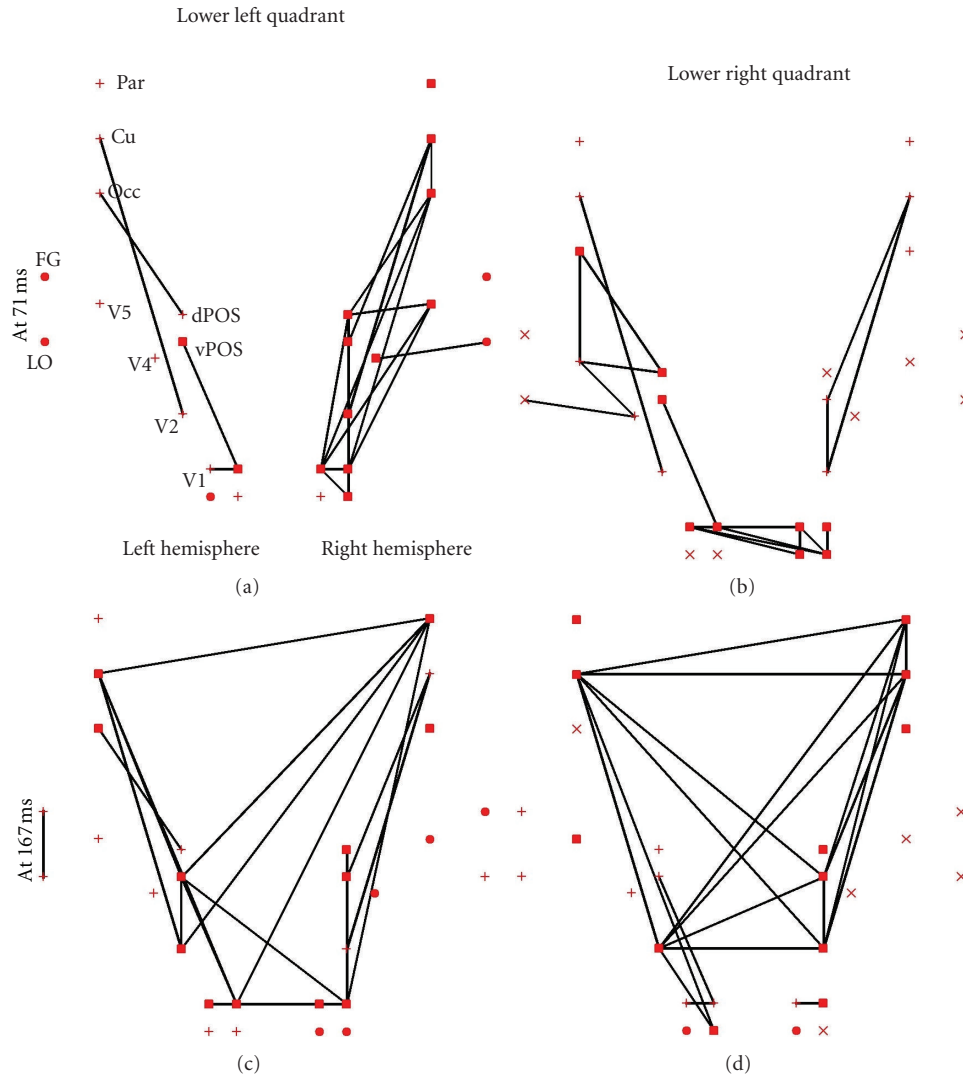


FIGURE 6: The same as in Figure 5, but the results obtained from the second subject are shown.

all visual areas and the cuneus on the contralateral (right) hemisphere and the extrastriate visual areas V4, V5, and FG of the ipsilateral (left) hemisphere. For the second subject, at the second phase of processing ( $\sim 170$  ms), the dominant cluster is made up of visual areas from both hemispheres. The difference in the clustering pattern is reflected in the connections between areas. For the first subject the connections are primarily within each hemisphere, while for the second subject there are more links between areas of the left and right hemispheres.

Across both the early ( $\sim 70$  ms) and late ( $\sim 170$  ms) phases of processing the regional activity and connections of the cuneus seem to reflect the overall connectivity pattern. A strong separation of clustering and connections in one hemisphere is associated with strong connections between the cuneus of the same hemisphere and the areas of the dominant cluster. In cases where the connections and dominant cluster involve areas from both hemisphere, the cuneus of one hemisphere (mainly in the hemisphere contralateral to

the stimulated visual field) has connections with areas in both hemispheres.

Figures 7 and 8 show for the two subjects the connectivity patterns at 71 ms elicited by letters and pseudoletters in the  $\gamma$ -band (30 to 45 Hz). Since the window extends for 30 ms on either side of the centre latency, the results display the  $\gamma$ -band connectivity pattern at the earliest stages of processing; nevertheless it is clear that the processing does not fractionate into clusters, but that almost in all cases all areas belong to one cluster. For both subjects stimulation of the lower left part of the visual field produces strong links (that survive the threshold criteria) in both hemispheres with links extending across the two hemispheres. Furthermore for left visual field stimuli links in the  $\gamma$ -band involve not only the contralateral, right cuneus, but also the left hemisphere cuneus and the extrastriate areas specialized for character processing (LO and FG); these links often connect these extrastriate areas with early visual areas (V1 and V2) of the opposite hemisphere.

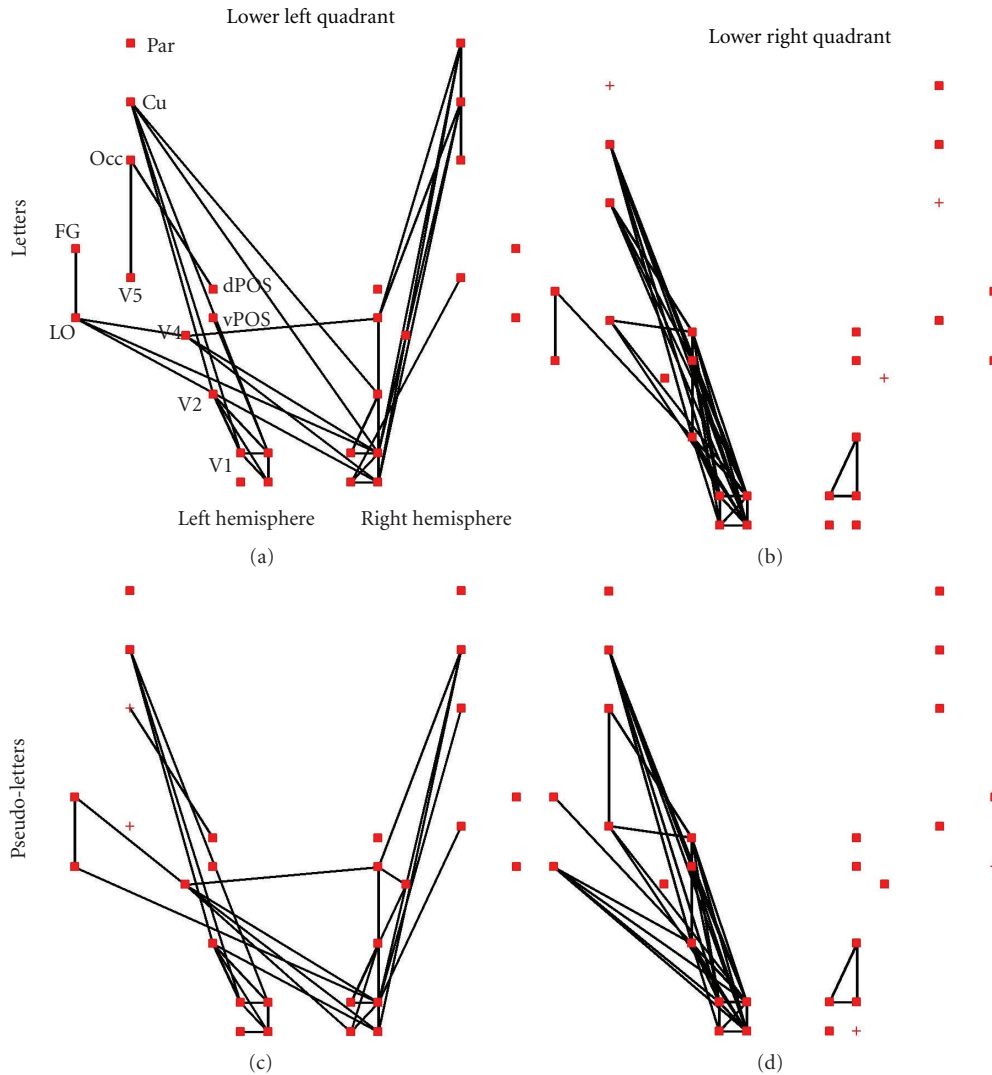


FIGURE 7: The strongest links between ROIs computed from the  $\gamma$ -band data with window center at 71 ms. The results for letters are shown in the top part of (a) and (b), and the results for pseudoletters on the bottom part of (c) and (d). The results are shown separately for stimuli presented in the lower left (left part of (a) and (c)) and lower right (right part of (b) and (d)) quadrants of the visual field. Only the top 10% links are displayed that have also passed the threshold of  $FDR < 0.001$ .

Stimuli presented in the right visual field produce strong early links in the  $\gamma$ -band almost exclusively between areas of the left (contralateral) hemisphere for subject 1. For the second subject there is a preponderance of left hemisphere areas involved in the links in the  $\gamma$ -band but with involvement of some areas from the right hemisphere, especially V1.

In contrast to wide band, in the  $\gamma$ -band the differences are apparent in the connectivity patterns between letters and pseudoletters, even at the early latencies depicted in Figures 7 and 8. These differences become prominent after 100 ms poststimulus (data not shown). In both subjects and for all stimuli the LO and FG in the left hemisphere, that is, the two areas best known for letter processing, show prominent links in response to both letters and pseudoletters. These two left hemisphere areas are also linked to each other for all letter stimulus cases, irrespective of which hemisphere these are

presented, but they are not linked for pseudoletters presented in the contralateral (right) visual field.

#### 4. Discussion

In the present study, we investigated the dynamic changes of connectivity organization and the way transient cluster formation is associated with the preparation and execution of visual tasks. The adapted techniques have been previously introduced for tracking the formation of functional clusters in an EEG resting-state paradigm [4] and during sleep [45]. Recently, a similar in spirit methodology for tracking evolving modularity was applied to data from an fMRI experiment [46] and succeeded in showing the reconfiguration of brain networks with respect to a particular learning task. Our methodology shares with few other studies the

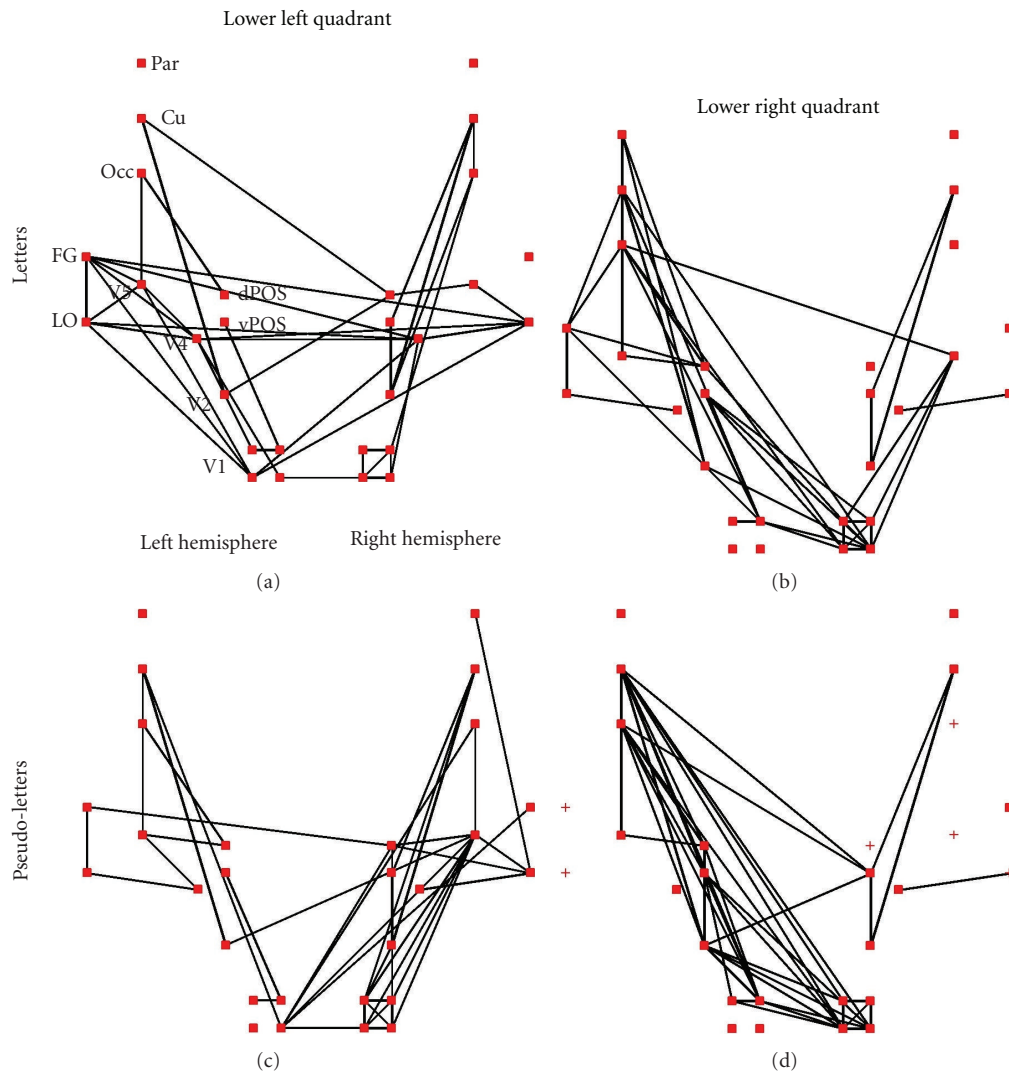


FIGURE 8: The same as in Figure 7, but the results obtained from the second subject are shown.

more generic perspective of dynamic changes in clustering as the relevant framework for understanding brain function and the common goal of an objective characterization of time-varying functional connectivity. In two of the earliest attempts adaptive multivariate processes were adopted for modeling connectivity signals [47] and event-related networks were characterized based on multichannel recordings from a visual stimulation paradigm [19]. In one of the most recent works, fluctuations of functional connectivity among the nodes comprising the oculomotor network were studied in both awake humans and anesthetized macaques based on BOLD signals [48]. The general trend of combining information from different modalities is having some influence in network analysis, for example for the fusion of EEG and fMRI in network space [49].

The critical novelty in our current work is the use of real time, millisecond by millisecond detailed tomographic estimates of brain activity, which allowed us to describe cluster organization at the level of the key brain

areas involved in the task, and with time resolution that is within the processing periods of these areas and the transit time of information between them. Specifically we demonstrated that phase couplings in  $\alpha$  and  $\beta$  bands within the visual cortical network differentiate between attended and ignored stimuli. These results suggest at least two different mechanisms by which spatial attention affects the neural processing. First, because the increased  $\beta$  oscillations are associated with efficient cortical processing, the visual cortical network synchronization in this band facilitates the neural processing of attended stimuli. On the other hand, the  $\alpha$  activity band can be interpreted as an indicator of cortical inhibition and therefore the increased phase coupling in this band, especially involving a key attentional control area (IPL), realizes the top-down suppression of ignored stimuli.

In our previous analysis of MEG data elicited by letter and pseudoletter stimuli we identified the cuneus and the FG as key areas [7]. The timing and nature of the cuneus activations suggested that this structure is related

to visual field and task demands, in a role that combined active anticipation and specialized routing of activity in visual processing. Our connectivity analysis revealed that the contralateral cuneus was one of the best connected areas at the earliest latencies after the stimulus onset (e.g., as seen in Figure 5), fully justifying the earlier interpretation of it having an important role in specialized routing of activity during visual processing. In our previous study, the specialized involvement of the FG emerged rather late, between 150 and 350 ms after stimulus onset in the right FG, reflecting task demands, while those in the left FG between 300 and 400 ms showing selectivity for graphemes. The connectivity analysis showed that the involvement of these two areas on the left hemisphere starts much earlier, within 100 ms in the  $\gamma$ -band with stronger participation of the left FG, irrespective of the stimulated location in the visual field.

We have presented evidence for fast reorganization of human brain networks associated with well-defined visual tasks. We have used data from two sets of experiments where the more established methodology based on the analysis of individual regional activations showed significant results across the sets of subjects studied [6, 7]. Our results show that the view obtained from the separate study of regional activations emerges from a network activity that is very rich and with subtle dependence on task and stimulus categories, the network changes become evident well before the changes in regional activities become apparent. While the common regional activations across subjects are preserved in our connectivity analysis the details in the connectivity patterns vary a lot from subject to subject, probably reflecting different mechanisms that each subject can recruit to tackle a problem. We presented results for two subjects to demonstrate the nature of both key common features and differences across subjects as these emerge from the analysis.

There are of course a number of ways to adapt the proposed methodology for group analysis. An obvious way is to first do it independently for each subject referring to the same set of ROIs for each subject (after appropriate transformation to a common source-space). The time series of clusterings will then be forced to refer to a common timeline and can therefore be easily combined using the principles of consensus clustering [50]. After alignment the clusterings (from all subjects) can be fed to a “vector-median” computation [45] and in this way the most reliable among the individual-clusterings is selected as the representative for the whole group. The alignment can be done either by using the same latency for all subjects or allowing a different latency for each subject after time dilation and stretching to fit a given scenario (defined in advance or extracted from the data). There are however serious questions to be addressed when attempting to pool the data across subjects. First the actual anatomy differs both in terms of regional location and gray matter content of individual areas and probably even more so the effectiveness of anatomical connections. In addition the influence of activity from different brain areas on the EEG and/or MEG signal varies and in the worst case scenario the activity from some areas may produce very little EEG and MEG signal. All these problems are eliminated when the

comparisons are restricted within a subject, for example, by comparing different conditions for the same subject as we have done for most of the work we presented in this paper.

Our view is that this is an area where much work is needed before reliable across subject summaries can be obtained. The methodology is therefore ideal for within subject studies and to emphasize the point we emphasized in the presentation of our results the results from the individual subject connectivity analysis. In our opinion, the main impact of the work we have outlined will be in allowing noninvasive access to the fine details of the exquisite neural codes of individual subjects. We believe that comparing conditions within a subject could well lead to novel ways of personalized monitoring of healthy brain function and the online evaluation of remediation and rehabilitation programs, for example in developmental dyslexia training and rehabilitation after stroke.

## Acknowledgments

This work was supported by a Cyprus Research Promotion Foundation grant ΕΠΙΧΕΙΡΗΣΕΙΣ/ΠΡΟΙΟΝ/0609/76 and cofunded by the European Regional Development Fund of the EU.

## References

- [1] A. A. Ioannides, G. K. Kostopoulos, N. A. Laskaris et al., “Timing and connectivity in the human somatosensory cortex from single trial mass electrical activity,” *Human Brain Mapping*, vol. 15, no. 4, pp. 231–246, 2002.
- [2] L. C. Liu and A. A. Ioannides, “A correlation study of averaged and single trial MEG signals: the average describes multiple histories each in a different set of single trials,” *Brain Topography*, vol. 8, no. 4, pp. 385–396, 1996.
- [3] S. I. Dimitriadis, N. A. Laskaris, V. Tsirka, M. Vourkas, S. Micheloyannis, and S. Fotopoulos, “Tracking brain dynamics via time-dependent network analysis,” *Journal of Neuroscience Methods*, vol. 193, no. 1, pp. 145–155, 2010.
- [4] S. I. Dimitriadis, N. A. Laskaris, V. Tsirka, M. Vourkas, and S. Micheloyannis, “An EEG study of brain connectivity dynamics at the resting state,” *Nonlinear Dynamics, Psychology, and Life Sciences*, vol. 16, no. 1, pp. 5–22, 2012.
- [5] A. A. Ioannides, “Magnetoencephalography as a research tool in neuroscience: state of the art,” *Neuroscientist*, vol. 12, no. 6, pp. 524–544, 2006.
- [6] V. Poghosyan and A. A. Ioannides, “Attention modulates earliest responses in the primary auditory and visual cortices,” *Neuron*, vol. 58, no. 5, pp. 802–813, 2008.
- [7] G. Plomp, C. Leeuwen, and A. A. Ioannides, “Functional specialization and dynamic resource allocation in visual cortex,” *Human Brain Mapping*, vol. 31, no. 1, pp. 1–13, 2010.
- [8] S. H. Strogatz, “Exploring complex networks,” *Nature*, vol. 410, no. 6825, pp. 268–276, 2001.
- [9] M. E. J. Newman, “The structure and function of complex networks,” *SIAM Review*, vol. 45, no. 2, pp. 167–256, 2003.
- [10] S. Boccaletti, V. Latora, Y. Moreno, M. Chavez, and D. U. Hwang, “Complex networks: structure and dynamics,” *Physics Reports*, vol. 424, no. 4–5, pp. 175–308, 2006.

- [11] D. S. Bassett and E. T. Bullmore, "Human brain networks in health and disease," *Current Opinion in Neurology*, vol. 22, no. 4, pp. 340–347, 2009.
- [12] D. S. Bassett and E. Bullmore, "Small-world brain networks," *Neuroscientist*, vol. 12, no. 6, pp. 512–523, 2006.
- [13] C. J. Stam and J. C. Reijneveld, "Graph theoretical analysis of complex networks in the brain," *Nonlinear Biomedical Physics*, vol. 1, article 3, 2007.
- [14] E. Bullmore and O. Sporns, "Complex brain networks: graph theoretical analysis of structural and functional systems," *Nature Reviews Neuroscience*, vol. 10, no. 3, pp. 186–198, 2009.
- [15] A. A. Ioannides, "Dynamic functional connectivity," *Current Opinion in Neurobiology*, vol. 17, no. 2, pp. 161–170, 2007.
- [16] S. L. Bressler, "Large-scale cortical networks and cognition," *Brain Research Reviews*, vol. 20, no. 3, pp. 288–304, 1995.
- [17] G. M. Hoerzer, S. Liebe, A. Schloegl, N. K. Logothetis, and G. Rainer, "Directed coupling in local field potentials of macaque v4 during visual short-term memory revealed by multivariate autoregressive models," *Frontiers in Computational Neuroscience*, vol. 4, p. 14, 2010.
- [18] D. Gupta, P. Ossenblok, and G. van Luijckelaar, "Space-time network connectivity and cortical activations preceding spike wave discharges in human absence epilepsy: a MEG study," *Medical and Biological Engineering and Computing*, vol. 49, no. 5, pp. 555–565, 2011.
- [19] M. Valencia, J. Martinerie, S. Dupont, and M. Chavez, "Dynamic small-world behavior in functional brain networks unveiled by an event-related networks approach," *Physical Review E*, vol. 77, no. 5, Article ID 050905, 4 pages, 2008.
- [20] S. I. Dimitriadis, N. A. Laskaris, A. Tzelepi, and G. Economou, "Analyzing functional brain connectivity by means of commute times: a new approach and its application to track event-related dynamics," *IEEE Transactions on Biomedical Engineering*, vol. 59, no. 5, pp. 1302–1309, 2012.
- [21] J. M. Schoffelen and J. Gross, "Source connectivity analysis with MEG and EEG," *Human Brain Mapping*, vol. 30, no. 6, pp. 1857–1865, 2009.
- [22] J. P. Owen, D. P. Wipf, H. T. Attias, K. Sekihara, and S. S. Nagarajan, "Accurate reconstruction of brain activity and functional connectivity from noisy MEG data," in *Proceedings of the Annual International Conference of the IEEE Engineering in Medicine and Biology Society (EMBC '09)*, pp. 65–68, September 2009.
- [23] J. Chiang, Z. Wang, and M. McKeown, "A generalized multivariate autoregressive (GmAR)-based approach for EEG source connectivity analysis," *IEEE Transactions on Signal Processing*, vol. 60, no. 1, pp. 453–465, 2012.
- [24] F. de Vico Fallani, V. Latora, L. Astolfi et al., "Persistent patterns of interconnection in time-varying cortical networks estimated from high-resolution EEG recordings in humans during a simple motor act," *Journal of Physics A*, vol. 41, no. 22, Article ID 224014, 2008.
- [25] L. C. Liu and A. A. Ioannides, "Spatiotemporal dynamics and connectivity pattern differences between centrally and peripherally presented faces," *NeuroImage*, vol. 31, no. 4, pp. 1726–1740, 2006.
- [26] A. A. Ioannides, V. Poghosyan, J. Dammers, and M. Streit, "Real-time neural activity and connectivity in healthy individuals and schizophrenia patients," *NeuroImage*, vol. 23, no. 2, pp. 473–482, 2004.
- [27] A. A. Ioannides, P. B. C. Fenwick, and L. C. Liu, "Widely distributed magnetoencephalography spikes related to the planning and execution of human saccades," *Journal of Neuroscience*, vol. 25, no. 35, pp. 7950–7967, 2005.
- [28] M. X. Cohen, "Assessing transient cross-frequency coupling in EEG data," *Journal of Neuroscience Methods*, vol. 168, no. 2, pp. 494–499, 2008.
- [29] J. P. Lachaux, E. Rodriguez, J. Martinerie, and F. J. Varela, "Measuring phase synchrony in brain signals," *Human Brain Mapping*, vol. 8, no. 4, pp. 194–208, 1999.
- [30] C. J. Stam, G. Nolte, and A. Daffertshofer, "Phase lag index: assessment of functional connectivity from multi channel EEG and MEG with diminished bias from common sources," *Human Brain Mapping*, vol. 28, no. 11, pp. 1178–1193, 2007.
- [31] P. Graben, C. Zhou, M. Thiel, and J. Kurths, *Lectures in Supercomputational Neuroscience: Dynamics in Complex Brain Networks (Understanding Complex Systems)*, Springer, New York, NY, USA, 2008.
- [32] F. Varela, J. P. Lachaux, E. Rodriguez, and J. Martinerie, "The brainweb: phase synchronization and large-scale integration," *Nature Reviews Neuroscience*, vol. 2, no. 4, pp. 229–239, 2001.
- [33] J. Fell and N. Axmacher, "The role of phase synchronization in memory processes," *Nature Reviews Neuroscience*, vol. 12, no. 2, pp. 105–118, 2011.
- [34] S. I. Dimitriadis, K. Kanatsouli, N. A. Laskaris, V. Tsirka, M. Vourkas, and S. Micheloyannis, "Surface EEG shows that functional segregation via phase coupling contributes to the neural substrate of mental calculations," *Brain and Cognition*, vol. 80, no. 1, pp. 45–52, 2012.
- [35] N. I. Fisher, *Statistical Analysis of Circular Data*, Cambridge University Press, Cambridge, Mass, USA, 1993.
- [36] Y. Benjamini and Y. Hochberg, "Controlling the false discovery rate: a practical and powerful approach to multiple testing," *Journal of the Royal Statistical Society B*, vol. 57, no. 1, pp. 289–300, 1995.
- [37] M. Rubinov and O. Sporns, "Complex network measures of brain connectivity: uses and interpretations," *NeuroImage*, vol. 52, no. 3, pp. 1059–1069, 2010.
- [38] S. L. Simpson, M. N. Moussa, and P. J. Laurienti, "An exponential random graph modeling approach to creating group-based representative whole-brain connectivity networks," *Neuroimage*, vol. 60, no. 2, pp. 1117–11126, 2012.
- [39] V. Latora and M. Marchiori, "Economic small-world behavior in weighted networks," *The European Physical Journal B*, vol. 32, no. 2, pp. 249–263, 2003.
- [40] S. Achard and E. Bullmore, "Efficiency and cost of economical brain functional networks," *PLoS Computational Biology*, vol. 3, no. 2, p. e17, 2007.
- [41] A. A. Ioannides and V. Poghosyan, "Spatiotemporal dynamics of early spatial and category-specific attentional modulations," *NeuroImage*, vol. 60, no. 3, pp. 1638–1651, 2012.
- [42] V. Poghosyan, T. Shibata, and A. A. Ioannides, "Effects of attention and arousal on early responses in striate cortex," *European Journal of Neuroscience*, vol. 22, no. 1, pp. 225–234, 2005.
- [43] S. Kastner and L. G. Ungerleider, "Mechanisms of visual attention in the human cortex," *Annual Review of Neuroscience*, vol. 23, pp. 315–341, 2000.
- [44] M. Corbetta, J. M. Kincade, J. M. Ollinger, M. P. McAvoy, and G. L. Shulman, "Voluntary orienting is dissociated from target detection in human posterior parietal cortex," *Nature Neuroscience*, vol. 3, no. 3, pp. 292–297, 2000.
- [45] S. I. Dimitriadis, N. A. Laskaris, Y. Rio-Portilla, and G. C. Koudounis, "Characterizing dynamic functional connectivity across sleep stages from EEG," *Brain Topography*, vol. 22, no. 2, pp. 119–133, 2009.
- [46] D. S. Bassett, N. F. Wymbs, M. A. Porter, P. J. Mucha, J. M. Carlson, and S. T. Grafton, "Dynamic reconfiguration of

- human brain networks during learning,” *Proceedings of the National Academy of Sciences of the United States of America*, vol. 108, no. 18, pp. 7641–7646, 2011.
- [47] L. Astolfi, F. Cincotti, D. Mattia et al., “Tracking the time-varying cortical connectivity patterns by adaptive multivariate estimators,” *IEEE Transactions on Biomedical Engineering*, vol. 55, no. 3, pp. 902–913, 2008.
- [48] R. M. Hutchison, T. Womelsdorf, J. S. Gati, S. Everling, and R. S. Menon, “Resting-state networks show dynamic functional connectivity in awake humans and anesthetized macaques,” *Human Brain Mapping*. In press.
- [49] X. Lei, D. Ostwald, J. Hu et al., “Multimodal functional network connectivity: an EEG-fMRI fusion in network space,” *PLoS ONE*, vol. 6, Article ID e24642, 2011.
- [50] A. Lancichinetti and S. Fortunato, “Consensus clustering in complex networks,” *Scientific Reports*, vol. 2, article 336, 2012.

## Research Article

# Weighted Phase Lag Index and Graph Analysis: Preliminary Investigation of Functional Connectivity during Resting State in Children

Erick Ortiz,<sup>1</sup> Krunoslav Stingl,<sup>1</sup> Jana Münßinger,<sup>1</sup> Christoph Braun,<sup>1,2,3</sup>  
Hubert Preissl,<sup>1,4</sup> and Paolo Belardinelli<sup>1</sup>

<sup>1</sup>MEG Center, University of Tübingen, Germany

<sup>2</sup>Center of Mind/Brain Sciences (CIMeC), University of Trento, 38068 Rovereto, Italy

<sup>3</sup>Department of Cognitive and Educational Sciences (DiSCoF), University of Trento, 38068 Rovereto, Italy

<sup>4</sup>Department of Obstetrics and Gynecology, University of Arkansas for Medical Sciences, Little Rock, AR 72205, USA

Correspondence should be addressed to Paolo Belardinelli, paolo.belardinelli@gmail.com

Received 30 March 2012; Revised 27 June 2012; Accepted 28 July 2012

Academic Editor: Fabrizio De Vico Fallani

Copyright © 2012 Erick Ortiz et al. This is an open access article distributed under the Creative Commons Attribution License, which permits unrestricted use, distribution, and reproduction in any medium, provided the original work is properly cited.

Resting state functional connectivity of MEG data was studied in 29 children (9–10 years old). The weighted phase lag index (WPLI) was employed for estimating connectivity and compared to coherence. To further evaluate the network structure, a graph analysis based on WPLI was used to determine clustering coefficient ( $C$ ) and betweenness centrality ( $BC$ ) as local coefficients as well as the characteristic path length ( $L$ ) as a parameter for global interconnectedness. The network's modular structure was also calculated to estimate functional segregation. A seed region was identified in the central occipital area based on the power distribution at the sensor level in the alpha band. WPLI reveals a specific connectivity map different from power and coherence.  $BC$  and modularity show a strong level of connectedness in the occipital area between lateral and central sensors.  $C$  shows different isolated areas of occipital sensors. Globally, a network with the shortest  $L$  is detected in the alpha band, consistently with the local results. Our results are in agreement with findings in adults, indicating a similar functional network in children at this age in the alpha band. The integrated use of WPLI and graph analysis can help to gain a better description of resting state networks.

## 1. Introduction

Resting state networks (RSN), that is, functionally linked brain areas detectable independent of any task, are important for the understanding of brain function during development and in disease [1–8]. However, the neuronal mechanisms underlying functional connectivity at rest remain poorly understood. Recently, some limits of traditional approaches to the description of functional brain networks by means of fMRI have been reported by Power et al. [9].

We investigated the synchrony of rhythmic activity in children brain networks with magnetoencephalography (MEG). To capture the complexity of these networks, graph theory was employed on the basis of the phase-synchronization weighted phase lag index (WPLI) index. Rhythmic activity has a relevant role in the human nervous

systems and has been implicated in numerous functions. Oscillatory activity in different brain areas can be synchronized (i.e., phase-coupled). Such characteristic has been hypothesized to be an important mechanism for creating an effective functional communication structure between different areas [9–13]. In this respect, the fundamental task is the application of reliable estimators to determine the phase relationship between two signals.

Here, in a first step we compared sensor connectivity mapping based on WPLI and spectral coherence which has been extensively employed for connectivity studies using MEG [10, 11, 14, 15]. Then, we used this new index to calculate graph-theoretical measures to quantify basic properties of the WPLI connectivity matrix. WPLI cannot overestimate the phase lag values due to volume conduction effects of uncorrelated noise sources. Furthermore, WPLI is

less sensitive to noise than PLI and even in conditions of high signal-to-noise ratio, it shows a more reliable relationship with true phase consistency [16]. These characteristics make WPLI a suitable tool for graph analysis. We considered the MEG sensors as nodes of our graph network and the WPLI values between sensor signals as the links between the nodes.

We calculated the weighted clustering coefficient  $C$ , which describes local interconnectedness, and weighted path length  $L$ , a measure of global interconnectedness, were computed. As a measure of centrality, we calculated betweenness (BC) for each node, which is the fraction of all shortest paths in the network that pass through it. Since networks are often composed by densely interconnected groups of regions, the structure of these groups (the community structure) was also determined. Community structure consists of a separation into groups of nodes where the number of within-group links is maximized and the number of between-group links is minimized.

We tested this analysis approach with a simplified setting: by studying resting state connectivity in children, we investigated the interactions between a reference signal obtained from the peak sensor in a power cluster of channels in the occipital area and all other sensors.

*1.1. Resting State Connectivity from Infancy to Adult Age.* We are analyzing preadolescents during resting state. Several fMRI studies have shown that the horizontal interhemispheric functional connections are already established in preadolescent children. In contrast, the anterior-posterior connections are largely reduced, compared to adults [17]. Over adolescence, short range correlation tend to weaken, whereas long-range, especially anterior-posterior connection start to strengthen [18]. The long-range connections increase over development to form complete networks like the default mode network (DMN) in adults [6, 19]. Overall, no significant connections have been found in infants between frontal and parietal areas, although the parietal area appears to contain midline and lateral parietal connections, similar to the posterior part of the DMN [20, 21]. In addition it has been shown with electroencephalography (EEG) that, between childhood and adulthood, the power in the occipital areas decreases significantly in the alpha and theta bands [22].

## 2. Methods

*2.1. Participants.* Twenty-nine children between the ages of 9 and 10 years ( $M_{\text{age}} = 9.70$  years,  $SD \pm 0.47$ ) participated in the current study. Children who were taking any kind of medication or were diagnosed with type I diabetes, attention deficit hyperactivity disorder (ADHD) or any other chronic disease were excluded. Written informed consent was given by all children and their parents before participation. The study was approved by the Ethical Committee of the Medical Faculty of the University of Tübingen.

*2.2. MEG Data Acquisition.* Data was recorded using a 275-sensor whole-head system (VSM MedTech Ltd., Port Coquitlam, Canada). To ensure continuous recordings of the head position relative to the MEG sensors during the

measurement, localization coils were attached to the nasion and the preauricular points on each side of the head of the subject. To avoid any magnetic influence from the surroundings, the MEG system was located in a magnetically shielded room (Vakuumschmelze, Germany).

The recording sampling frequency was 586 Hz. Due to technical reasons, for the present analysis, 2 of the 275 MEG sensors could not be used. Children were asked to sit quietly and relaxed with their eyes closed. Beginning and end of the 4 min resting state interval were indicated to the children by an auditory signal.

*2.3. Data Processing.* Data analysis was performed using the Fieldtrip toolbox [23]. The first 20 seconds were removed from the analysis to account for initial accommodation, and the data was divided in 2-second epochs, yielding about 110 trials per dataset. A high-pass filter at 2 Hz was applied. Frequency analysis was performed in each of these trials between 2 and 30 Hz, which include the major power contribution in children. We used a multitaper smoothing of 2 Hz. The frequency range was separated in the standard frequency bands (from delta to high beta, that is, from 2 to 30 Hz, see Figure 1).

*2.4. WPLI Description.* The complex cross-spectrum  $C$  for two real-valued signals  $x(t)$  and  $y(t)$  is computed by Fourier-transforming them into  $X(f)$  and  $Y(f)$ . Then,  $X$  and  $Y$  are used to compute the cross-spectrum  $C(f) = X(f)Y^*(f)$ , where  $Y^*$  indicates the complex conjugate of  $Y$ . If we focus on a particular frequency of interest  $f^*$ , we can consider the complex nondiagonal part of  $C$  as  $Z$ .

Then, PLI is defined as absolute value of the sign of the imaginary part of  $Z$ ,  $\Im$  [24]:

$$PLI \equiv |E\{\text{sgn}(\Im(Z))\}|. \quad (1)$$

Differently from PLI, WPLI weights the cross-spectrum according to the magnitude of the imaginary component. This allows it to limit the influence of cross-spectrum elements around the real axes which are at risk of changing their “true” sign with small noise perturbations.

Such an index of phase synchronization was proposed by Vinck and colleagues [16]:

$$WPLI \equiv \frac{|E\{\Im(Z)\}|}{E\{\Im(Z)\}} = \frac{|E\{|\Im(Z)| \text{sgn}(\Im(Z))\}|}{E\{|\Im(Z)\}|}. \quad (2)$$

This index is based only on the imaginary component of the cross-spectrum. This implies robustness to noise because uncorrelated noise sources will cause an increase of signal power. It has been shown that WPLI outperforms PLI, coherence, and imaginary coherence (IC) with real local field potentials (LFP) data [16].

### 2.5. Graph Theory Analysis

*2.5.1. Network Construction.* In order to apply graph theory methods, a network based on WPLI functional measures was constructed. We employed an undirected weighted network

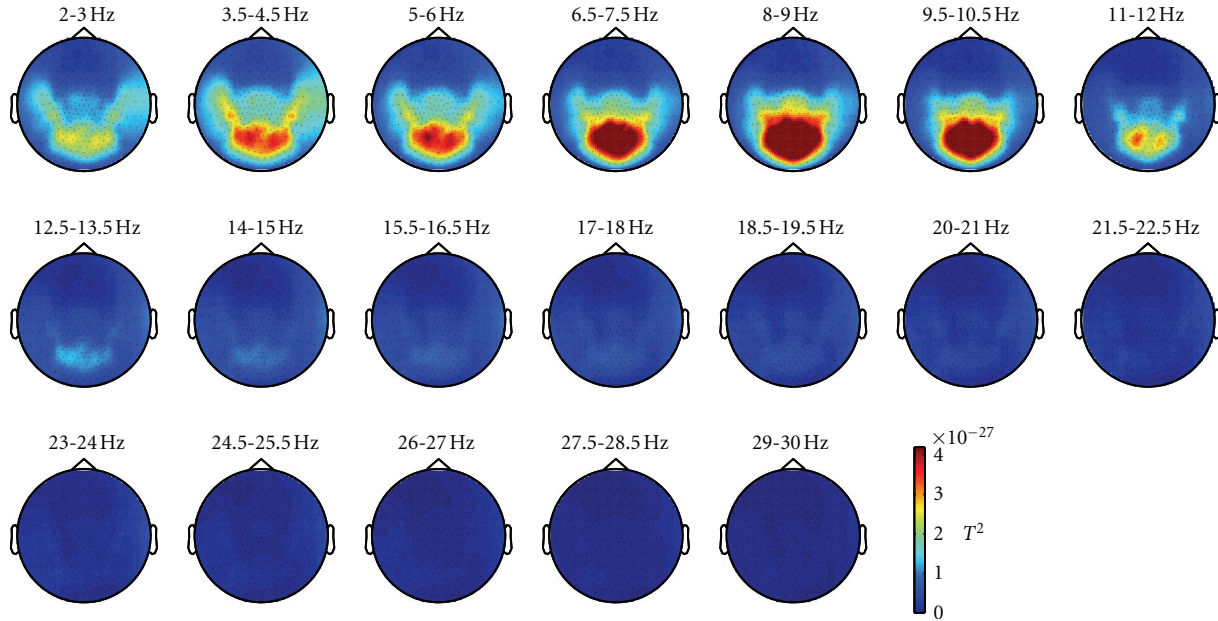


FIGURE 1: Topographic plots of sensor power in 1.5 Hz wide frequency bands, from 2 to 30 Hz. A cluster of sensors with high power is discernible in the alpha range.

[25, 26], where the nodes are the sensors, and the link weights are the WPLI values between them.

In some cases, very weak links may obscure the topology of the significant connections. These can be removed by using a threshold, whose value is often arbitrary: therefore, a broad range of values was tested [27]. We found that most network measures were preserved over a rather broad range of threshold values.

**2.5.2. Network Measures.** We characterized the network by using measures of segregation, integration, and centrality. For segregation, we used cluster coefficient for integration, characteristic path length, and global efficiency as well as for centrality, the betweenness centrality.

The clustering coefficient shows the fraction of the node's neighbors that are also neighbors of each other; on the other hand, betweenness of a node is defined as the fraction of all shortest paths in the network that pass through that node. The nodes with high betweenness usually bridge disparate parts in a network.

**2.6. Community Structure and Modularity.** The optimal community structure is a subdivision of the network into nonoverlapping groups of nodes in a way that maximizes the number of within-group edges, and minimizes the number of between-group edges [28, 29]. The modularity  $Q$  is a statistic that quantifies the degree to which the network may be subdivided into such clearly delineated groups; its values range between  $-1$  and  $1$ , measuring density of links inside communities as compared to links between communities.

Also, it is possible to determine a hierarchical structure of these modules [30]. Lowering the link removal threshold enabled us to reveal additional community structure.

### 3. Results

A cluster of sensors in the occipital part of the sensor array was identified as the region of interest based on the peak of the power distribution. A cut-off threshold was set at the full width at half maximum (FWHM) of the mean power spread in the alpha band (8–13 Hz). The cluster comprised 29 sensors. The signal defined by the power peak in the cluster area (central occipital sensor on the left of the midline, MLO11 in CTF MEG systems) was employed to calculate connectivity between it and the other channels (one-to-all connections).

Since a clear peak was shown for both connectivity measures in the range between 3 and 12 Hz (Figure 2, mean value across subjects), we focused on this range for a topographical comparison between power, coherence and WPLI. Moreover, in this range a minimum of intersubject variability is detectable (red and blue areas for coherence and WPLI, resp.).

Topographically, coherence coincides well with power (Figure 3). Between 3 and 11 Hz, a single cluster of high coherence value in the occipital area was detected in coherence and power. Differently, WPLI provides a more articulated and extended connectivity map in the alpha range between 6.5 and 11 Hz. Here, an onset of different clusters (one central and two lateral ones, mostly overlapping with the power cluster) was detected in the occipital area of the sensor surface.

It should be noted that the reduced variability of WPLI values in the alpha band is not due to the choice of the epoch length. Actually, this parameter showed high intersubject reliability: in 25 subjects out of 29 the channel average of WPLI values in the alpha is stronger than in the other frequency bands (Figure 4).

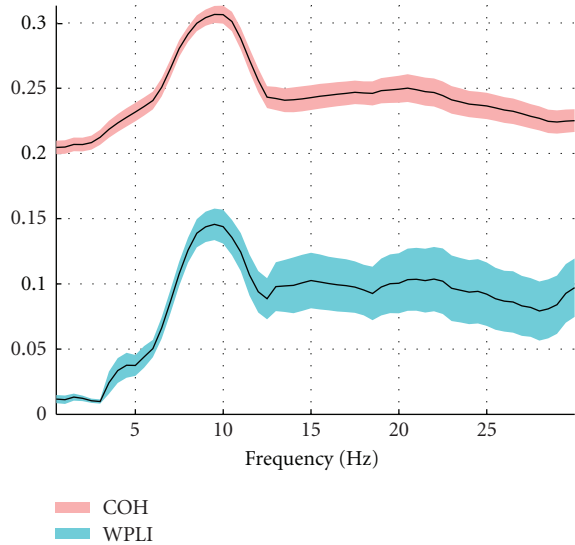


FIGURE 2: Plots of mean coherence and WPLI across subjects. Red and blue areas represent the standard error of the mean (SEM) across subjects.

**3.1. Deriving a Graph from WPLI.** Being WPLI an inherently nonlinear measure (i.e., not proportional to either magnitude or phase of the signal frequency content), the change in the estimator value from negligible to significant values is very steep. In Figure 5, we show the distribution of values for coherence and WPLI. The WPLI distribution is relevantly steeper than the coherence distribution, representing mid-range connectivity by smaller values. Moreover, whereas coherence has non-negligible values for every combination of channels and never actually gets smaller than 0.02, WPLI has a large number of near-zero values.

The distinctions between the respective distributions are a direct consequence of the different approaches: coherence suffers from volume conduction effects, hence near-zero values will be rare. Also, WPLI is expected to be steeper, since it is a statistic on a discrete value (a sign function). Moreover, this index is weighted by the imaginary part of coherence, which is generally a minor quantity of the coherence value. As a consequence, WPLI seldom reach values near 1.

Since WPLI's values for low connectivity are very small, when assigning the weights to the network, their inverse is very high. Having fewer midrange values that map to short link lengths, good connectivity on a WPLI network is represented by comparatively longer path lengths than in a similar network drawn by coherence measures. This could be interpreted in terms of the higher specificity of the WPLI, showing fewer but more robust connections.

On constructing the network, we tested proportional thresholds for link removal from 1.0 (no links removed) to 0.1 (i.e., only 10% of links is preserved). From 1.0 to 0.3, the differences were nearly negligible; from 0.3 to 0.1, the network topology was distorted very quickly. This is not unexpected: given that WPLI tends to have a large number of near-zero values, thresholding them would make little difference indeed.

**3.2. Local Graph Measures.** One-to-all WPLI values were used as an input for graph theory local parameters: the clustering coefficient ( $C$ ), betweenness centrality ( $BC$ ), and modularity. Results in the alpha band show that while the cluster coefficient depicts two central and right lateral areas as separate structures, betweenness shows a clear peak on a sensor (MRO21) which is located between the areas shown by the  $C$  plotting (Figure 6).

**3.3. Global Graph Measures.** The characteristic path length  $L$  [27] was calculated as a measure of global interconnectedness based on all-to-all WPLI channel values. We considered WPLI values as weights and the mapping function as the inverse of these values. The characteristic path length was then computed for the network associated to each frequency bin, for each subject.

The results are shown in Figure 7 over the whole investigated frequency interval.

The alpha band shows the shortest characteristic path length, although the minimum is not statistically significant.

To further investigate the relationship between sensor power and functional connectivity, we performed a linear regression between power and characteristic path length based on WPLI. The results are presented in Table 1: power does not significantly predict the characteristic path length in any band.

**3.4. Community Structure.** Community structure was analyzed by the approach described by Blondel et al. [30], which deals efficiently with large networks and enables also to distinguish a hierarchy of modules. In a first pass, small modules are formed, and in successive passes, these are fused in larger modules while modularity  $Q$  increases. This is in our analysis the only case in which removing the weak links of the network led to new information. While high thresholds revealed only a large module in the occipital area, approximately corresponding to the frequency power map, we could discriminate with a threshold of 0.4 a second hierarchical level: it was composed of two smaller modules, roughly lateralized. Figure 8 summarizes the modular structure analysis. Lowering the threshold below this level quickly degraded the analysis and did not add new information.

This hierarchy is especially relevant if integrated with the information of Figure 6(b): the nodes with highest betweenness are the ones that lie at the border of the two modules. Note that the algorithms to calculate betweenness and modularity are radically different, rendering this result more important for being revealed by two independent methods.

## 4. Discussion

The oscillatory dynamics of resting state networks in the brain is not completely understood in both children and adults [1, 31, 32]. Some recent studies employing different neuroimaging techniques have reported that children resting activity is mainly localized in the occipital lobe, with less

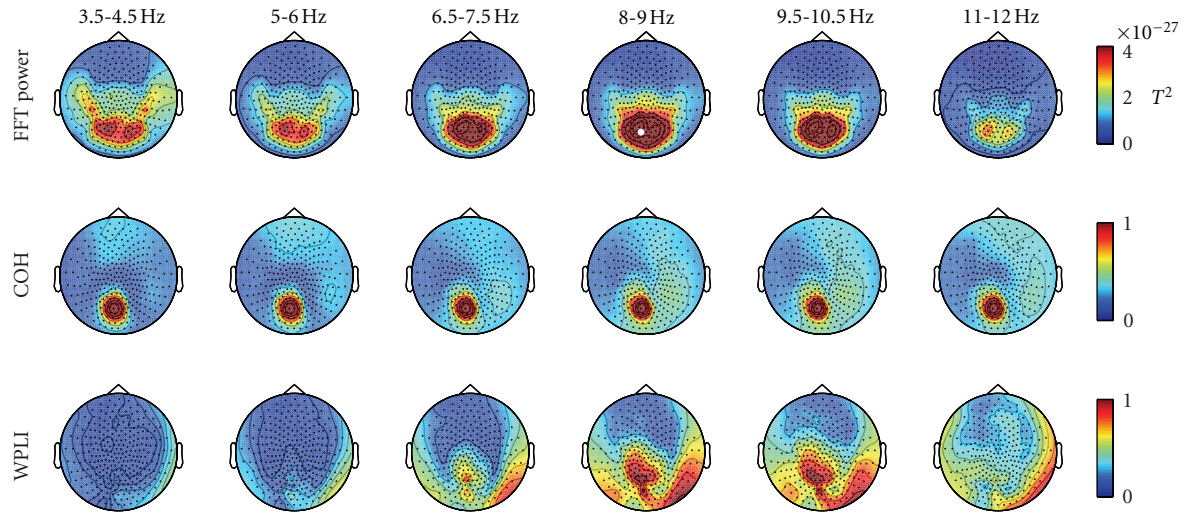


FIGURE 3: Topographic group results of sensor power, coherence, and WPLI in 1.5 Hz wide frequency bands, from 3.5 to 12 Hz. A cluster of sensors with high power is detectable in the alpha band. The sensor with the highest FFT power (MLO11, indicated by a white dot) was selected as reference node for the connectivity calculations (one-to-all connectivity). Note that the coherence topography is roughly uninformative across frequencies and strongly affected by volume conduction effects, while WPLI compares favorably in both criteria. Much more detail is discernible in the WPLI topography.

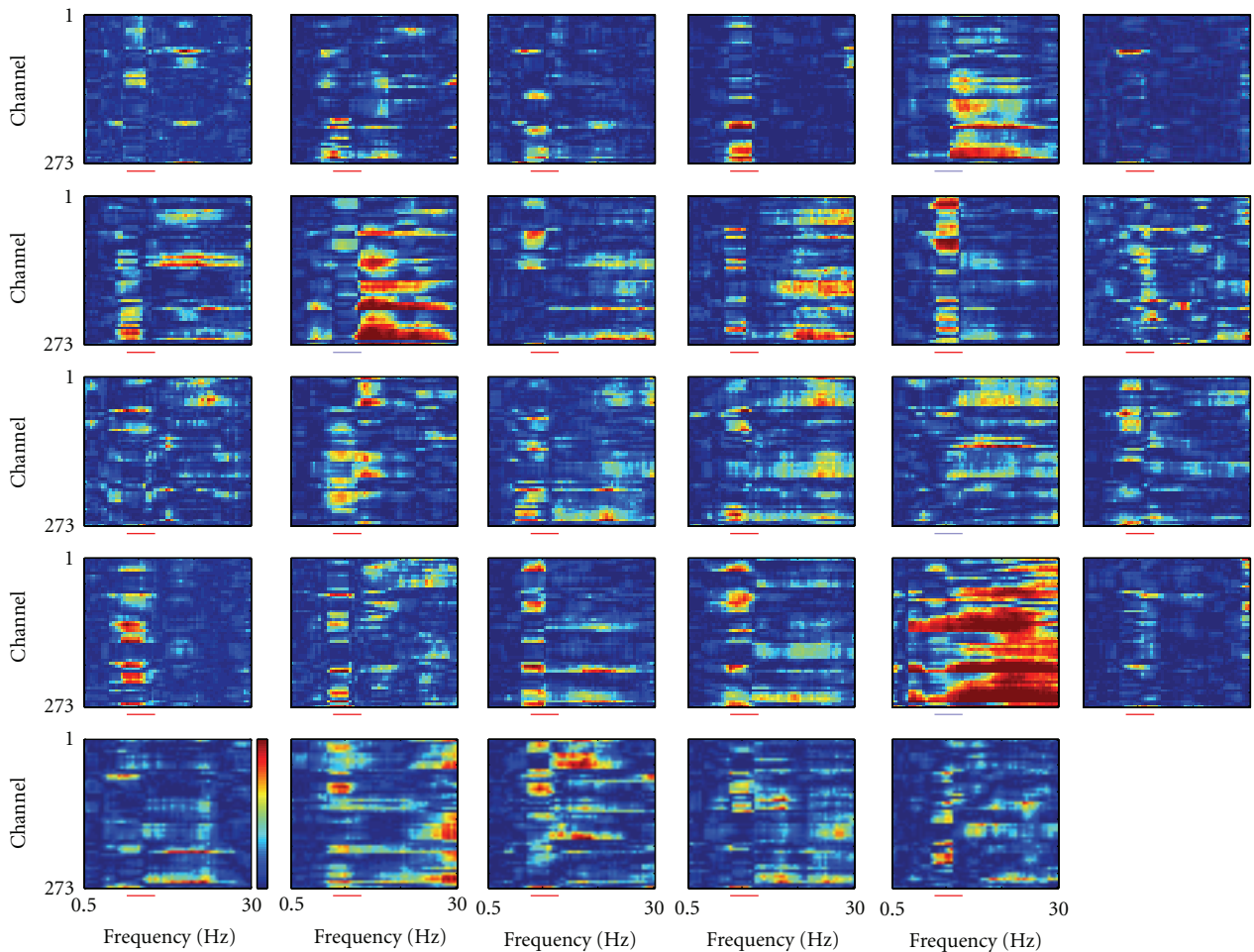


FIGURE 4: Normalized WPLI connectivity values, from/to sensor MLO11 for all frequencies. The alpha band (8 to 13 Hz) is shown by a colored bar under each plot. The color indicates whether the average WPLI in this frequency band is higher (red, 25 subjects) or lower (light blue, 4 subjects) than the average WPLI value including all frequencies.

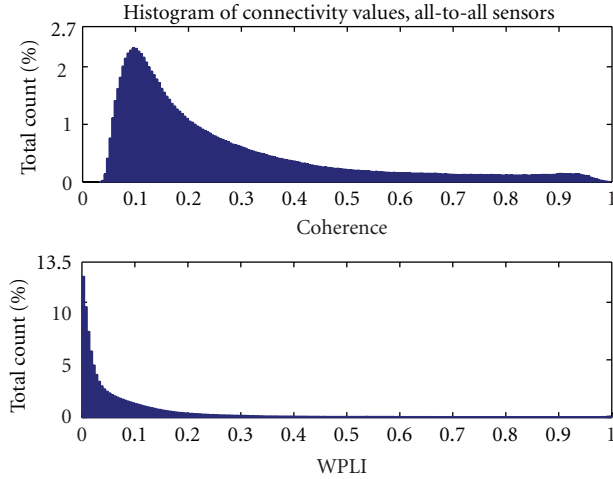


FIGURE 5: Distribution of coherence and WPLI values. Mean values across subjects are shown.

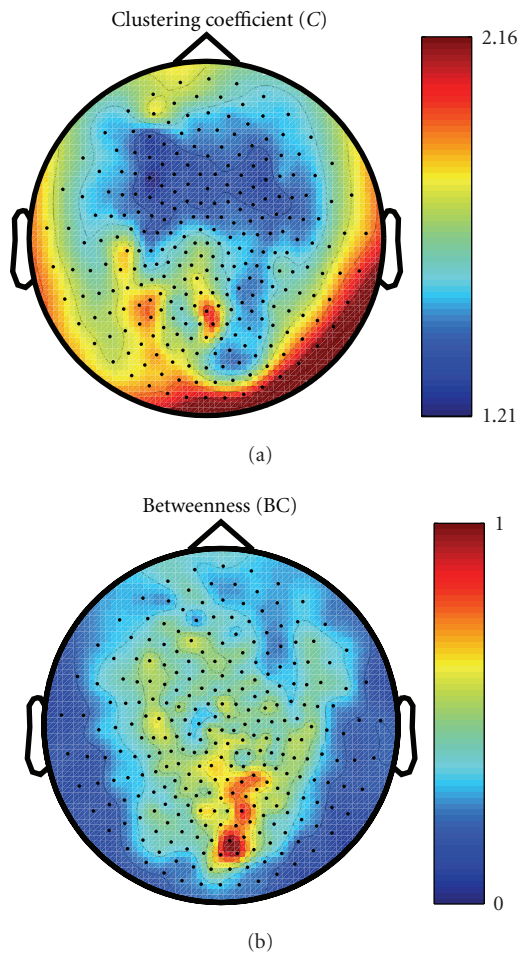


FIGURE 6: Topographic plots of graph-theoretical node-wise measures, calculated on WPLI for the alpha band, averaged across subjects. betweenness centrality BC was normalized by the plot's maximum value, while clustering coefficient was normalized by the standard deviation across subjects to minimize border artifacts.

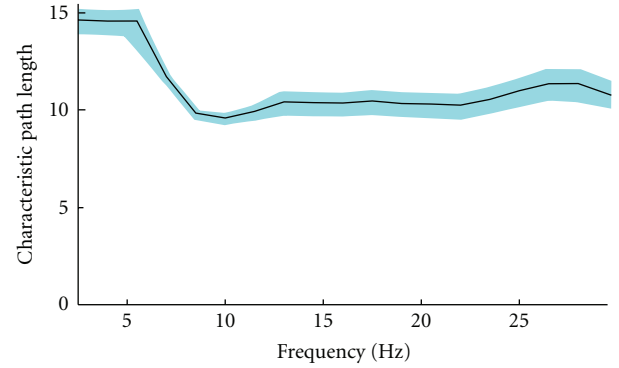


FIGURE 7: Characteristic path length, calculated on WPLI for the alpha band, averaged across subjects. The error bars show the standard error (SEM). Note how the alpha band displays not only shorter path lengths, but also smaller SEM, indicating more consistency.

TABLE 1:  $P$  and  $R^2$  values for the linear regression of power with  $L$  as a function of WPLI in the different frequency bands.

Frequency band (Hz)	$P$ values	$R^2$
Delta (2–4)	0.8180	0.0020
Theta (4–8)	0.4675	0.0197
Alpha (8–13)	0.8675	0.0011
Low beta (13–20)	0.9501	0.0001
High beta (20–30)	0.9081	0.0005

connections to the orbitofrontal cortex than adults [20, 33, 34]. Moreover, a prevalence of low frequency (theta and alpha) oscillations has been shown in the occipital area [22]. In accordance with these findings, we found highest power between theta and alpha band (4–11 Hz). Furthermore, using a similar approach as in [1] we have used the sensor showing the peak of the power cluster as a seed for a connectivity study by means of an advanced index of phase lag synchronization (WPLI, [16]). A clear peak around 10 Hz of the mean value across subjects and channels was detected for both WPLI and coherence, roughly coinciding with a decrease of intersubject variability as measured by SEM (Figure 2).

Comparing power, coherence and WPLI (Figure 3), two relevant differences emerge between the two connectivity indices. First, while the relevant values of coherence appear to follow the power cluster as frequency increases from 3.5 to 12 Hz, the WPLI connectivity pattern is detectable exclusively in the alpha band. Secondly, a more extended and articulated picture is observable in this band in comparison to coherence and power. This is possibly due to the fact that only imaginary components of signals are considered in WPLI processing. In this way, the components propagating across close sensors with zero lag delay are discarded, avoiding overestimates of local connectivity. It can only be speculated about an analogy between the WPLI plot shown in Figure 3 and the posterior regions of the well-known default mode network [6]. It is worth noting that the local graph theory results plotted using WPLI as an input appear to be consistent with such speculation: the clustering coefficient  $C$ ,

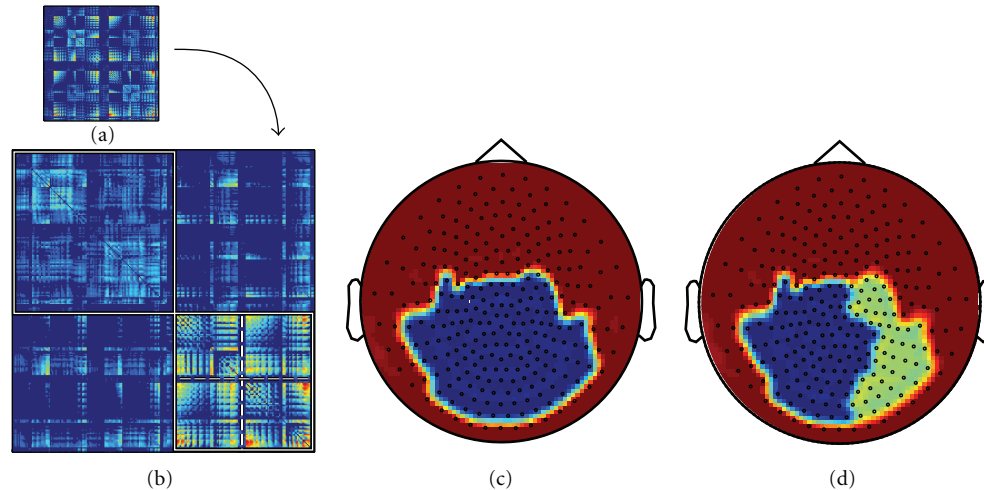


FIGURE 8: Community structure of functional connectivity in the alpha band. (a) Network connections based on WPLI, with a proportional threshold of 0.4. (b) Network reordered according to modular structure: the two top level modules are indicated by solid white lines. (c) Top level modules ( $Q = 0.2446$ ). (d) The large occipital module can be subdivided in two smaller ones, indicated in (b) by dashed lines ( $Q = 0.2391$ ).

a parameter for local segregation, shows a roughly similar pattern to the WPLI topographic plot. Moreover, a high level of betweenness was detected in an area revealed by WPLI. Betweenness quantifies the number of possible shortest paths in a network. The occipital central peak revealed in the right panel of Figure 5 (sensor MOR21) seems to confirm that this point has a relevant maximum of network connections. This result matches well with the results we obtained in an independent way for community structure (Figure 8). It is important to note that, with a small change of the modularity  $Q$ , the single occipital module detected in Figure 8(c) is split in two left and right modules (Figure 8(d)). The peak of betweenness lies on the border of the two modules. This set of results seems to confirm that resting state connectivity is mainly interhemispheric in preadolescent children [9].

In a future study we intend to perform a connectivity study at source level which can possibly provide further evidence of such a network. Our results agree with a previous similar study by Hillebrand and colleagues [4], showing no significant relationship between power and connectivity measures based on the imaginary part of Fourier transformed signals as WPLI (Table 1). Differently from that study, our results for the phase-lag index show a topologically different picture from power at the sensor level.

Furthermore, from all-to-all WPLI values we calculated the characteristic path length  $L$  of the network as an index of connectivity in all frequency bands. Consistently with [4], it was found that the alpha band showed the shortest mean path length. The strongest functional connections appear in the alpha band as the highest level of signal power does. Nevertheless, the two quantities appear to be rather independent, as shown in Table 1. This substantial agreement with adult data suggests that, despite of the evidence that the functional brain networks tend to develop from a local configuration to more distributed patterns (a path from segregation to integration) [33], several large-scale

network properties are established early in development [9]. Our study used children data for the testing of different connectivity measures and associated network parameters. The current result mainly shows that the WPLI approach is justified and that our restrictive approach reveals basic network topology. It has to be stressed that this approach has to be extended to all frequency bands and applied to the source level.

## Acknowledgments

J. Münßinger and H. Preissl are supported by the Grant Fortüne (1982-0-0). E. Ortiz's work is supported by an award from the Center for Integrated Neuroscience (CIN) of Tübingen (Germany) (Pool Project no. 2010-17).

## References

- [1] F. De Pasquale, S. Della Penna, A. Z. Snyder et al., "Temporal dynamics of spontaneous MEG activity in brain networks," *Proceedings of the National Academy of Sciences of the United States of America*, vol. 107, no. 13, pp. 6040–6045, 2010.
- [2] M. D. Fox, M. Corbetta, A. Z. Snyder, J. L. Vincent, and M. E. Raichle, "Spontaneous neuronal activity distinguishes human dorsal and ventral attention systems," *Proceedings of the National Academy of Sciences of the United States of America*, vol. 103, no. 26, pp. 10046–10051, 2006.
- [3] M. D. Fox, A. Z. Snyder, J. L. Vincent, M. Corbetta, D. C. Van Essen, and M. E. Raichle, "The human brain is intrinsically organized into dynamic, anticorrelated functional networks," *Proceedings of the National Academy of Sciences of the United States of America*, vol. 102, no. 27, pp. 9673–9678, 2005.
- [4] A. Hillebrand, G. R. Barnes, J. L. Bosboom, H. W. Berendse, and C. J. Stam, "Frequency-dependent functional connectivity within resting-state networks: an atlas-based MEG beamformer solution," *NeuroImage*, vol. 59, no. 4, pp. 3909–3921, 2012.

- [5] C. M. Lewis, A. Baldassarre, G. Committeri, G. L. Romani, and M. Corbetta, "Learning sculpts the spontaneous activity of the resting human brain," *Proceedings of the National Academy of Sciences of the United States of America*, vol. 106, no. 41, pp. 17558–17563, 2009.
- [6] M. E. Raichle, A. M. MacLeod, A. Z. Snyder, W. J. Powers, D. A. Gusnard, and G. L. Shulman, "A default mode of brain function," *Proceedings of the National Academy of Sciences of the United States of America*, vol. 98, no. 2, pp. 676–682, 2001.
- [7] C. J. Stam, B. F. Jones, I. Manshanden et al., "Magnetoencephalographic evaluation of resting-state functional connectivity in Alzheimer's disease," *NeuroImage*, vol. 32, no. 3, pp. 1335–1344, 2006.
- [8] D. Mantini, M. Corbetta, M. G. Perrucci, G. L. Romani, and C. Del Gratta, "Large-scale brain networks account for sustained and transient activity during target detection," *NeuroImage*, vol. 44, no. 1, pp. 265–274, 2009.
- [9] J. D. Power, D. A. Fair, B. L. Schlaggar, and S. E. Petersen, "The development of human functional brain networks," *Neuron*, vol. 67, no. 5, pp. 735–748, 2010.
- [10] P. Fries, "A mechanism for cognitive dynamics: neuronal communication through neuronal coherence," *Trends in Cognitive Sciences*, vol. 9, no. 10, pp. 474–480, 2005.
- [11] J. Gross, J. Kujala, M. Hämäläinen, L. Timmermann, A. Schnitzler, and R. Salmelin, "Dynamic imaging of coherent sources: studying neural interactions in the human brain," *Proceedings of the National Academy of Sciences of the United States of America*, vol. 98, no. 2, pp. 694–699, 2001.
- [12] J. Kujala, K. Pammer, P. Cornelissen, A. Roebroeck, E. Formisano, and R. Salmelin, "Phase coupling in a cerebrocerebellar network at 8–13 Hz during reading," *Cerebral Cortex*, vol. 17, no. 6, pp. 1476–1485, 2007.
- [13] P. Tass, M. G. Rosenblum, J. Weule et al., "Detection of n:m phase locking from noisy data: application to magnetoencephalography," *Physical Review Letters*, vol. 81, no. 15, pp. 3291–3294, 1998.
- [14] J. M. Schoffelen, R. Oostenveld, and P. Fries, "Neuronal coherence as a mechanism of effective corticospinal interaction," *Science*, vol. 308, no. 5718, pp. 111–113, 2005.
- [15] C. Gerloff, C. Braun, M. Staudt, Y. L. Hegner, J. Dichgans, and I. Krägeloh-Mann, "Coherent corticomuscular oscillations originate from primary motor cortex: evidence from patients with early brain lesions," *Human Brain Mapping*, vol. 27, no. 10, pp. 789–798, 2006.
- [16] M. Vinck, R. Oostenveld, M. Van Wingerden, F. Battaglia, and C. M. A. Pennartz, "An improved index of phase-synchronization for electrophysiological data in the presence of volume-conduction, noise and sample-size bias," *NeuroImage*, vol. 55, no. 4, pp. 1548–1565, 2011.
- [17] D. A. Fair, A. L. Cohen, N. U. F. Dosenbach et al., "The maturing architecture of the brain's default network," *Proceedings of the National Academy of Sciences of the United States of America*, vol. 105, no. 10, pp. 4028–4032, 2008.
- [18] D. A. Fair, N. U. F. Dosenbach, J. A. Church et al., "Development of distinct control networks through segregation and integration," *Proceedings of the National Academy of Sciences of the United States of America*, vol. 104, no. 33, pp. 13507–13512, 2007.
- [19] A. M. C. Kelly, A. Di Martino, L. Q. Uddin et al., "Development of anterior cingulate functional connectivity from late childhood to early adulthood," *Cerebral Cortex*, vol. 19, no. 3, pp. 640–657, 2009.
- [20] P. Fransson, U. Åden, M. Blennow, and H. Lagercrantz, "The functional architecture of the infant brain as revealed by resting-state fMRI," *Cerebral Cortex*, vol. 21, no. 1, pp. 145–154, 2011.
- [21] P. Fransson, B. Skiöld, M. Engström et al., "Spontaneous brain activity in the newborn brain during natural sleep—an fMRI study in infants born at full term," *Pediatric Research*, vol. 66, no. 3, pp. 301–305, 2009.
- [22] R. Lüchinger, L. Michels, E. Martin, and D. Brandeis, "Brain state regulation during normal development: intrinsic activity fluctuations in simultaneous EEG-fMRI," *NeuroImage*, vol. 60, no. 2, pp. 1426–1439, 2012.
- [23] R. Oostenveld, P. Fries, E. Maris, and J. M. Schoffelen, "Field-Trip: open source software for advanced analysis of MEG, EEG, and invasive electrophysiological data," *Computational Intelligence and Neuroscience*, vol. 2011, Article ID 156869, 9 pages, 2011.
- [24] C. J. Stam, G. Nolte, and A. Daffertshofer, "Phase lag index: assessment of functional connectivity from multi channel EEG and MEG with diminished bias from common sources," *Human Brain Mapping*, vol. 28, no. 11, pp. 1178–1193, 2007.
- [25] M. E. J. Newman, "Fast algorithm for detecting community structure in networks," *Physical Review E*, vol. 69, no. 6 2, Article ID 066133, 5 pages, 2004.
- [26] C. J. Stam and J. C. Reijneveld, "Graph theoretical analysis of complex networks in the brain," *Nonlinear Biomedical Physics*, vol. 1, article 3, 2007.
- [27] M. Rubinov and O. Sporns, "Complex network measures of brain connectivity: uses and interpretations," *NeuroImage*, vol. 52, no. 3, pp. 1059–1069, 2010.
- [28] M. E. J. Newman and M. Girvan, "Finding and evaluating community structure in networks," *Physical Review E*, vol. 69, no. 2, Article ID 026113, 15 pages, 2004.
- [29] M. Girvan and M. E. J. Newman, "Community structure in social and biological networks," *Proceedings of the National Academy of Sciences of the United States of America*, vol. 99, no. 12, pp. 7821–7826, 2002.
- [30] V. D. Blondel, J. L. Guillaume, R. Lambiotte, and E. Lefebvre, "Fast unfolding of communities in large networks," *Journal of Statistical Mechanics*, vol. 2008, no. 10, Article ID P10008, 2008.
- [31] G. Buzsáki and A. Draguhn, "Neuronal oscillations in cortical networks," *Science*, vol. 304, no. 5679, pp. 1926–1929, 2004.
- [32] C. Michel, T. Koenig, D. Brandeis, L. Gianotti, and J. Wackermann, *Electrical Neuroimaging*, Cambridge University Press, New York, NY, USA, 2009.
- [33] D. A. Fair, A. L. Cohen, J. D. Power et al., "Functional brain networks develop from a 'local to distributed' organization," *PLoS Computational Biology*, vol. 5, no. 5, Article ID e1000381, 2009.
- [34] P. Fransson, B. Skiöld, S. Horsch et al., "Resting-state networks in the infant brain," *Proceedings of the National Academy of Sciences of the United States of America*, vol. 104, no. 39, pp. 15531–15536, 2007.

## Research Article

# How the Statistical Validation of Functional Connectivity Patterns Can Prevent Erroneous Definition of Small-World Properties of a Brain Connectivity Network

**J. Toppi,<sup>1,2</sup> F. De Vico Fallani,<sup>2,3</sup> G. Vecchiato,<sup>2,3</sup> A. G. Maglione,<sup>2,4</sup> F. Cincotti,<sup>1,2</sup> D. Mattia,<sup>2</sup> S. Salinari,<sup>1</sup> F. Babiloni,<sup>2,3</sup> and L. Astolfi<sup>1,2</sup>**

<sup>1</sup>Department of Computer, Control, and Management Engineering, Sapienza University of Rome, 00185 Rome, Italy

<sup>2</sup>Neuroelectrical Imaging and BCI Laboratory, Fondazione Santa Lucia Hospital, 00179 Rome, Italy

<sup>3</sup>Department of Physiology and Pharmacology, Sapienza University of Rome, 00185 Rome, Italy

<sup>4</sup>Department of Anatomy, Histology, Forensic Medicine and Orthopedics, Sapienza University of Rome, 00185 Rome, Italy

Correspondence should be addressed to L. Astolfi, [laura.astolfi@uniroma1.it](mailto:laura.astolfi@uniroma1.it)

Received 2 April 2012; Accepted 1 June 2012

Academic Editor: Danielle Bassett

Copyright © 2012 J. Toppi et al. This is an open access article distributed under the Creative Commons Attribution License, which permits unrestricted use, distribution, and reproduction in any medium, provided the original work is properly cited.

The application of Graph Theory to the brain connectivity patterns obtained from the analysis of neuroelectrical signals has provided an important step to the interpretation and statistical analysis of such functional networks. The properties of a network are derived from the adjacency matrix describing a connectivity pattern obtained by one of the available functional connectivity methods. However, no common procedure is currently applied for extracting the adjacency matrix from a connectivity pattern. To understand how the topographical properties of a network inferred by means of graph indices can be affected by this procedure, we compared one of the methods extensively used in Neuroscience applications (i.e. fixing the edge density) with an approach based on the statistical validation of achieved connectivity patterns. The comparison was performed on the basis of simulated data and of signals acquired on a polystyrene head used as a phantom. The results showed (i) the importance of the assessing process in discarding the occurrence of spurious links and in the definition of the real topographical properties of the network, and (ii) a dependence of the small world properties obtained for the phantom networks from the spatial correlation of the neighboring electrodes.

## 1. Introduction

The concept of brain connectivity (i.e., how the cortical areas communicate one to each other during the execution of a specific task) is central for the understanding of the organized behavior of cortical regions beyond the simple mapping of their activity [1, 2]. In the last two decades, several studies have been carried on in order to understand neuronal networks at the basis of brain processes. These networks are characterized by lots of interactions between different and differently specialized cortical sites in relation to the specific executed task.

Cortical connectivity estimation techniques aim at describing interactions between cortical areas as connectivity patterns holding the direction and strength of the information flow between such areas. The functional connectivity

between cortical areas is then defined as the temporal correlation between spatially neuronal events and it could be estimated by using different methods both in time as well as in frequency domain based on bivariate or multivariate autoregressive models [3–6] applied to hemodynamic or neuroelectrical signals. Past studies demonstrated that multivariate methods provide better estimates of connectivity patterns than bivariate approaches [7], which cannot distinguish between direct influence between two signals and the indirect common influence from a third signal [8]. For this reason, bivariate methods usually give rise to very dense patterns of propagation, thus making it impossible to find the sources of propagation [9, 10]. Different estimators, defined in time or in frequency domain and based on a bivariate or multivariate approach, rely on the concept of Granger causality between time series [11]. According to Granger's definition, an

observed time series  $x(n)$  causes another series  $y(n)$  if the inclusion of  $x(n)$ 's past into an autoregressive model of  $y(n)$  significantly improves prediction of  $y(n)$ . Among the more advanced estimators based on this concept, partial directed coherence (PDC) [5] is a spectral, multivariate approach allowing to describe connectivity patterns with a good accuracy and to distinguish direct from indirect information flows [5, 12].

The extraction of salient characteristics from brain connectivity patterns is a challenging topic, given the often complex structure of the estimated cerebral networks. For this reason, in the last ten years, a graph theoretical approach was proposed for the characterization of the topographical properties of real complex networks [13, 14]. In fact, it was demonstrated that tools already implemented and used for the treatments of graphs as mathematical objects could be applied to functional connectivity networks estimated from electroencephalographic (EEG), magnetoencephalographic (MEG), or hemodynamic (fMRI) recordings [15–19]. The use of characteristic indexes, borrowed by graph theory, allows the evaluation of real networks in terms of density of connections incoming or outgoing from a node, tendency to cluster, centrality of some nodes or edges, and distances between nodes [14, 20, 21].

The computation of graph indexes can be performed on adjacency matrices achieved by applying a threshold on the estimated connectivity values obtained by means of different estimators. The application of a thresholding procedure allows to convert the connectivity values into edges. An edge connecting two nodes exists if the connectivity value between those nodes is above a certain threshold; otherwise the edge is null. The choice of the threshold should not depend on the application and if done in an arbitrary way could affect the results. In fact, the threshold influences the number of connections considered for the subsequent graph analysis and thus affects the indices extracted from the networks [22]. Different methodologies are available for defining such threshold. A possible approach is to select a fixed threshold. In this respect, three criteria are typically adopted: 5% significant level as a threshold fixed for discarding connectivity values from the random case [23–25]; an arbitrary value in order to discard the weak connections [26]; the largest possible threshold allowing all nodes to be connected at least to another node in the network [27]. The second way to extract a threshold is to fix the average degree within the networks in order to maximize the small-world properties of the network [28–32]. A third way to define a threshold is to fix the edge density of the network, that is, the number of existing edges divided by the number of possible edges [32]. This approach is useful if we are interested in comparing different conditions but can produce modifications in the topology of the studied network [22].

All the approaches described above are empirical and do not take into account the intrinsic statistical significance of the estimator used in functional connectivity estimation process. In fact, when the adjacency matrix is achieved by imposing a threshold and fixing the number of residual connections of the network, we cannot exclude a priori that

a percentage of such residual connections is estimated by chance. The idea is thus to take into account the statistical significance of the estimator used for functional connectivity estimation in the construction of adjacency matrix. In the case of PDC, the threshold is extracted by applying a percentile, for a defined significance level, on the distribution achieved for such estimator in the null case. Thus, an edge exists in the adjacency matrix describing the considered network only if it is statistically different from the null case.

Due to the nonlinear dependence of PDC estimator from the parameters of MVAR, the theoretical distribution of PDC in the null case is not known, so it should be constructed in an empiric way. The shuffling procedure, which has been introduced in 2001 for the similar estimator of directed transfer function (DTF) [33], allows to reconstruct the null case distribution by iterating the estimation of PDC, each time on different surrogate data sets obtained by shuffling the phases of original traces, in order to disrupt the temporal relations between them. In this way, it is possible to extract a threshold value for each couple of nodes, each direction and each frequency sample. Due to the high number of comparisons between the estimate and the null case distribution, corrections for multiple comparisons have to be taken into account. However, statistical theory offers a lot of solutions for adequately managing the occurrence of type I errors during the execution of multiple univariate tests [34, 35].

The general aim of this study is to understand how the methods for extracting the adjacency matrix could affect the graph theory indices and their interpretation, in order to define a reliable approach for the derivation of salient indices from connectivity networks estimated by means of multivariate methods. In particular, we used two different datasets with the purpose of comparing one of the methods extensively used in graph theory applications for extracting adjacency matrices from the connectivity patterns (i.e., the method based on fixing the edge density) with the statistical validation of achieved connectivity patterns by means of a shuffling procedure. The first dataset we used consisted of a set of random uncorrelated signals, which should represent a null model for functional connectivity estimates and a random case for graph theory indices. In fact, since no correlation exists between signals, the connectivity estimation process should almost entirely discard the information flows between signals, leaving only a few percentage of connections, estimated by chance and organized according to a random network. This dataset can be seen as an ideal “null case” model, but it does not take into account some factors strictly related to an electroencephalographic recording, such as the existence of a correlation between the recorded signals, due to effects of volume conduction, to the spatial positions of electrodes disposed on the scalp, and to the location of the reference [36]. For this reason, we introduced a second dataset, composed by signals recorded from a mannequin head during a pseudo experiment. This situation represents the null model for functional connectivity estimates inferred by applying partial directed coherence on EEG signals recorded at scalp level. In fact, the absence of physiological content in the recorded signals allows to model the absence of information flows between electrodes, but at the same time,

the use of a real EEG cap, with electrodes positioned as 10–20 systems and references placed at the earlobes, models the effects of some factors typical of an EEG recording situation.

We estimated the functional connectivity patterns associated to both applications and we extracted the correspondent adjacency matrices by means of two approaches: fixed edge density  $k$  and shuffling procedure for a significance level of 5%. This second approach was explored by applying no corrections for multiple comparisons and by applying false discovery rate (FDR) correction. Several graph indexes were computed on binary adjacency matrices achieved with both methodologies. The results, achieved on the two different datasets by means of the two methods, were normalized by means of 100 random graphs with the same number of connections of the graphs obtained on simulated and mannequin data. A statistical analysis of variance (ANOVA) was performed on the results obtained by the two approaches in each dataset to study the effect of the methodology applied to the properties extracted from the networks.

## 2. Materials and Methods

**2.1. Partial Directed Coherence.** The PDC [5] is a full multivariate spectral measure, used to determine the directed influences between any given pair of signals in a multivariate data set. PDC is a frequency domain representation of the existing multivariate relationships between simultaneously analyzed time series that allows the inference of functional relationships between them. This estimator was demonstrated to be a frequency version of the concept of Granger causality [11], according to which a time series  $x[n]$  can be said to have an influence on another time series  $y[n]$  if the knowledge of past samples of  $x$  significantly reduces the prediction error for the present sample of  $y$ . In this study, the PDC technique was applied to the subset of signals  $S$ :

$$S = [s_1(t), s_2(t), \dots, s_N(t)]^T. \quad (1)$$

Let us suppose that the following MVAR process is an adequate description of the data set  $S$ :

$$\sum_{k=0}^p \Lambda_k S(t-k) = E(t) \quad \text{with } \Lambda_0 = I. \quad (2)$$

In this expression,  $E(t) = [e_1(t), e_2(t), \dots, e_N(t)]^T$  is a vector of multivariate zero-mean uncorrelated white noise process,  $\Lambda_1, \Lambda_2, \dots, \Lambda_p$  are the  $N \times N$  matrices of model coefficients and  $p$  is the model order, chosen, in this case, by means of the Akaike information criteria (AIC) for MVAR processes [37]. Once an MVAR model is adequately estimated, it becomes the basis for subsequent spectral analysis. In order to investigate the spectral properties of the examined process, (2) is transformed to the frequency domain

$$\Lambda(f)S(f) = E(f), \quad (3)$$

where

$$\Lambda(f) = \sum_{k=0}^p \Lambda_k e^{-j2\pi f \Delta t k}, \quad (4)$$

and  $\Delta t$  is the temporal interval between two samples.

It is then possible to define PDC as

$$\pi_{ij}(f) = \frac{\Lambda_{ij}(f)}{\sqrt{\sum_{k=1}^N \Lambda_{kj}(f) \Lambda_{kj}^*(f)}}. \quad (5)$$

Such formulation was derived by the well-known concept of partial coherence [5]. The PDC from  $j$  to  $i$ ,  $\pi_{ij}(f)$  describes the directional flow of information from the signal  $s_j(n)$  to  $s_i(n)$ , whereupon common effects produced by other electrodes  $s_k(n)$  on the latter are subtracted leaving only a description that is exclusive from  $s_j(n)$  to  $s_i(n)$ .

PDC values are in the interval  $[0, 1]$  and the normalization condition

$$\sum_{n=1}^N |\pi_{nj}(f)|^2 \quad (6)$$

is verified. According to this condition,  $\pi_{ij}(f)$  represents the fraction of the time evolution of electrode  $j$  directed to electrode  $i$ , as compared to all of  $j$ 's interactions to other electrodes.

Even if this formulation derived directly from information theory, the original definition was modified in order to give a better physiological interpretation to the estimation results achieved on electrophysiological data. In particular, two modifications have been proposed. First, a new type of normalization, already used for another connectivity estimator such as directed transfer function [4] was introduced by dividing each estimated value of PDC for the root squared sums of all elements of the relative row, then a squared version of the PDC was introduced [38]:

$$\text{sPDC}_{ij}(f) = \frac{|\Lambda_{ij}(f)|^2}{\sum_{m=1}^N |\Lambda_{im}(f)|^2}. \quad (7)$$

The better performances of sPDC have been demonstrated in simulation studies which revealed reduced error levels both in the estimation of connectivity patterns on data characterized by different lengths and SNR and in distinction between direct and indirect paths [38]. Such formulation was used in this study for the estimation of functional connectivity.

**2.2. Statistical Validation of Connectivity Patterns.** Random correlation between signals induced by environmental noise or by chance can lead to the presence of spurious links in the connectivity estimation process. To assess the significance of the estimated patterns, each value of functional connectivity has to be statistically compared with a threshold level which is related to the lack of transmission between the considered signals at a certain probability. A possible procedure is to generate an empirical distribution of the null case based on the generation of sets of surrogate data [39] with the same spectral properties of the original dataset, but with no functional connections by construction, for example, by randomly shuffling the time series of each channel. In this study, original data were transformed from the time domain to the frequency domain, by means of Fourier Transform;

then, their phases were randomly shuffled without modifying their amplitude, and finally the shuffled signals were back-transformed in the time domain. This procedure is able to keep the amplitude of the power spectrum of the time series unaltered, but at the same time to disrupt any temporal correlation between signals. A model was fit to surrogate data set and connectivity estimates were derived from the model. Iterating this process many times, each time on a new surrogate data set, allowed to build an empirical distribution of the null hypothesis for the causal estimator [33]. Once obtained the empirical distribution, we assessed the significance of the estimated connectivity patterns for a given significance level. In particular, the threshold value was evaluated for each couple of signals and for each frequency by applying a percentile, corresponding to a predefined significance level of 5%, on the null case empirical distribution. Only the connections whose values exceeded the threshold were considered significant.

**2.3. Preventing the Occurrence of Type I Errors in Validation Process.** The statistical validation process has to be applied on each couple of signals for each frequency sample. This leads to the execution of a high number of simultaneous univariate statistical tests, with consequences in the occurrence of type I errors (false positives). The statistic theory provides several techniques that can be usefully applied in the context of the assessment of connectivity patterns in order to avoid the occurrence of false positives [40]. The first one, proposed by Bonferroni in 1936, is based on the consideration that if we perform  $N$  independent univariate tests, each with a significance probability  $\beta$ , the probability  $p$  that at least one of the tests is significant is given by

$$p < N\beta. \quad (8)$$

This means that if  $N = 20$ , tests are performed with the usual probability  $\beta = 0.05$ , then on average one of them is expected to become significant, just by chance. This means that if  $N = 20$ , tests are performed with the usual probability  $\beta = 0.05$ , at least one of them is expected to result, significant by chance alone. So, if we want the probability  $p$  for which this event could occur (i.e., one result being statistically significant just by chance) to be equal to  $\alpha$ , we can apply a correction to  $\beta$ . The single test will then be performed at a probability

$$\beta^* = \frac{\alpha}{N}. \quad (9)$$

This  $\beta^*$  is the actual probability at which the statistical tests have to be performed to conclude that all the tests are performed at level of statistical significance  $\alpha$ , Bonferroni adjusted for multiple comparisons.

The Bonferroni method can be too conservative, for instance when the statistical tests are highly dependent, like in the case of physiological measurements. This may lead to an increase of Type-II errors (false negatives). To mitigate the severity of Bonferroni approach, the false discovery rate (FDR) approach was proposed [34]. Such methodology is based on the expected proportion of erroneous rejections

among all rejections. Considering  $V$  as the number of false positives and  $S$  as the number of true positives, the FDR is given by

$$\text{FDR} = E\left[\frac{V}{V+S}\right]. \quad (10)$$

Let  $H_1, H_2, \dots, H_m$  be the null hypothesis, with  $m$  as the number of univariate test to be performed, and  $\mathbf{p}_1, \mathbf{p}_2, \dots, \mathbf{p}_m$  their corresponding  $P$  values. These values were ordered in increasing order as  $\mathbf{P}_{(1)} \leq \mathbf{P}_{(2)} \leq \dots \leq \mathbf{P}_{(m)}$  and the value  $k$  was chosen as the largest  $i$  for which

$$P_{(i)} \leq \frac{i}{m}\alpha. \quad (11)$$

At the end, the hypothesis  $\mathbf{H}_{(i)}$  with  $i = 1, \dots, k$  has to be rejected. In the case of independent tests, an approximation for evaluating corrected significance level has been introduced [35]:

$$\beta^* = \frac{(m+1)}{2m}\alpha. \quad (12)$$

**2.4. Graph Indexes.** A graph consists of a set of vertices (or nodes) and a set of edges (or connections) indicating the presence of some sort of interaction between the vertices. The adjacency matrix  $A$  contains the information about the connectivity structure of the graph. When a directed edge exists from the node  $j$  to the node  $i$ , the corresponding entry of the adjacency matrix is  $A_{ij} = 1$ , otherwise  $A_{ij} = 0$ . In graph theory, a path or a walk is a sequence of vertices in which from each of its vertices there is an edge to the next vertex in the sequence. Such adjacency matrix can be used for the extraction of salient information about the characteristic of the investigated network by defining several indices based on the elements of such matrix.

**2.4.1. Adjacency Matrix Extraction.** Once the functional connectivity pattern is estimated, it is necessary to define an associated adjacency matrix for each network, on which graph theory will be applied to extract salient indices able to characterize the network properties. The generic  $ij$ th entry of a directed binary adjacency matrix is equal to 1 if there is a functional link directed from the  $j$ th to the  $i$ th signal and to 0 if no link exists. As explained in Section 1, the construction of an adjacency matrix can be performed by comparing each estimated connectivity value to its correspondent threshold value. In particular,

$$G_{ij} = \begin{cases} 1 \rightarrow A_{ij} \geq \tau_{ij} \\ 0 \rightarrow A_{ij} < \tau_{ij} \end{cases}, \quad (13)$$

where  $G_{ij}$  and  $A_{ij}$  represent the entry  $(i, j)$  of an adjacency matrix  $G$  and a connectivity matrix  $A$ , respectively, and  $\tau_{ij}$  is the corresponding threshold. It is possible to derive the adjacency matrix simply by applying the same threshold for all the links of the network. In this case, (13) becomes

$$G_{ij} = \begin{cases} 1 \rightarrow A_{ij} \geq \tau \\ 0 \rightarrow A_{ij} < \tau \end{cases}, \quad (14)$$

where  $\tau$  represents the threshold to be applied to all the links in the network.

Different approaches have been developed for evaluating the threshold values, as already described in Section 1. In particular, in this study, we compared a methodology extensively used in literature and a more rigorous one proposed as an alternative in this paper. According to the first approach, the threshold is selected as the value which imposes a predefined edge density  $k$  (i.e., a percentage number of existing connections with respect to all possible connections, given the number of nodes in the network) for the resultant adjacency matrix. In this case, the threshold is the same for all links. The second method is based on the use of the intrinsic statistical significance of the estimator used for functional connectivity estimation. The threshold is evaluated as  $(1 - \alpha)$ th percentile extracted from the null case distribution of PDC estimator built by means of the shuffling procedure.  $\alpha$  is the significance level imposed in the statistical test and it was set at 0,05. In this case, a statistical threshold is evaluated for each link.

**2.5. Graph Theory Indices.** Different indices can be defined on the basis of the adjacency matrix extracted from a given connectivity pattern. In this study, we evaluated the most commonly used, described as follows.

**2.5.1. Characteristic Path Length.** The characteristic path length is the average shortest path length in the network, where the shortest path length between two nodes is the minimum number of edges that must be traversed to get from one node to another. It can be defined as follows:

$$L = \frac{1}{n} \sum_{i \in N} L_i = \frac{1}{n} \sum_{i \in N} \frac{\sum_{j \in N, j \neq i} d_{ij}}{n-1}, \quad (15)$$

where  $L_i$  is the average distance between node  $i$  and all other nodes and  $d_{ij}$  is the distance between node  $i$  and node  $j$  [14].

**2.5.2. Clustering Coefficient.** The clustering coefficient describes the intensity of interconnections between the neighbors of a node [41]. It is defined as the fraction of triangles around a node or the fraction of node's neighbors that are neighbors of each other. The binary directed version of clustering coefficient is defined as follows [21].

$$\begin{aligned} C &= \frac{1}{n} \sum_{i \in N} C_i \\ &= \frac{1}{n} \sum_{i \in N} \frac{t_i}{(k_i^{\text{out}} + k_i^{\text{in}})(k_i^{\text{out}} + k_i^{\text{in}} - 1) - 2 \sum_{j \in N} g_{ij} g_{ji}}, \end{aligned} \quad (16)$$

where  $t_i$  represents the number of triangles involving node  $i$ ,  $k_i^{\text{in}}$  and  $k_i^{\text{out}}$  are the number of incoming and outgoing edges of nodes  $i$ , respectively, and  $g_{ij}$  is the entry  $ij$  of adjacency matrix.

**2.5.3. Small Worldness.** A network  $G$  is defined as small-world network if  $L_G \geq L_{\text{rand}}$  and  $C_G \gg C_{\text{rand}}$  where  $L_G$  and



FIGURE 1: Experimental setup employed for the simulated electrical recording on a mannequin head by means of a 61-channel EEG cap. The polystyrene mannequin head was posed in front of a screen to include the interferences on signals due to the presence of a monitor.

$C_G$  represent the characteristic path length and the clustering coefficient of a generic graph and  $L_{\text{rand}}$  and  $C_{\text{rand}}$  represent the correspondent quantities for a random graph. On the basis of this definition, a measure of small-worldness of a network can be introduced as follows:

$$S = \frac{C_G/C_{\text{rand}}}{L_G/L_{\text{rand}}}. \quad (17)$$

So, a network is said to be a small world network if  $S > 1$  [42].

**2.6. Simulated Data.** The first dataset we used to compare the two approaches was generated to build the null case (complete lack of correlation between the signals). To this purpose, we generated random datasets of signals with the same average amplitude and the same standard deviation of the data acquired on the mannequin head (see following paragraph for details) to avoid differences between the two datasets due to different signals amplitudes. In particular, each dataset is composed by 20 signals segmented in 50 trials of 3s each. 20 electrodes are the typical number of sensors used for connectivity measures estimated by means of multivariate method on scalp EEG signals.

In the following, we will refer to this dataset as “simulated data”.

**2.7. Mannequin Data.** We simulated an EEG recording on a head of a synthetic mannequin by using a 61-channel system (Brain Amp, Brain-Products GmbH, Germany). The sampling frequency was set to 200 Hz. In order to keep the impedance below the 10 k $\Omega$ , the mannequin was equipped with a cap positioned over a humidifying towel. It must be noted that there were not electromagnetic sources inserted within the mannequin's head, that is instead composed only by polystyrene. Thus, the mannequin head cannot produce any possible electromagnetic signals on the electric sensors disposed on the recording cap. Figure 1 presents the experimental setup employed for the electrical recordings. The mannequin was put in front of a screen to take into

account the interferences of a monitor on EEG recording. To avoid any differences between the two datasets we used the same number of trials and samples per trial of simulated data.

We referred to this dataset as “mannequin data.”

**2.8. Signal Processing.** Both datasets were subjected to the same signal processing procedure, made by the following steps:

- (1) generation of 20 simulated signals (simulated data) or selection of 20 channels randomly chosen among the 61 used for the recording (mannequin data);
- (2) functional connectivity estimation, performed by means of sPDC;
- (3) extraction of the correspondent binary adjacency matrices by applying a threshold  $\tau$  achieved in two different ways:
  - (a) by means of shuffling procedure for a significance level of 5% in two conditions: (i) not corrected for multiple comparisons and (ii) adjusted for multiple comparisons by false discovery rate, and
  - (b) by fixing the edge density  $k$  to predefined values. The levels of such values were chosen equal to those achieved by the shuffling procedure, to avoid different performances between the two methods due to the selection of a different density;
- (4) extraction of the graph indices described above from the adjacency matrices achieved with both methodologies;
- (5) normalization of the indices achieved at point 4 with those extracted from 100 random graphs generated by maintaining the same number of connections of the correspondent adjacency matrix, to normalize the values to the model dimension.

**2.9. Analysis of Variance.** The signal processing procedure (point 1 to 5 of the previous paragraph) has been repeated 50 times to increase the power of the statistical test (ANOVA) computed for comparing the two different modalities used for the extraction of the adjacency matrices.

We computed a two-way ANOVA with each graph index as dependent variable. The main factors were

- (i) the method used for extracting adjacency matrices (METHOD), with two levels;
  - (a) shuffling procedure,
  - (b) fixed Edge Density procedure;
- (ii) the edge density (EDGE) corresponding to two cases:
  - (a) Case 1: percentage of edges survived to the shuffling procedure for a significance level 5% not corrected. This percentage was resulting

from the application of the shuffling procedure and was consequently imposed also to the fixed edges procedure, to avoid different performances due to different densities,

- (b) Case 2: percentage of edges survived to the shuffling procedure for a significance level 5% corrected by FDR. Same procedure described above.

The ANOVA was applied to both simulated and mannequin data.

### 3. Results

**3.1. Simulated Data.** To describe how we selected the edge density to be used in the two approaches, we reported in Figure 2 the histograms describing the distribution of the edge density characterizing the adjacency matrices extracted during different iterations of functional connectivity estimation process on simulated data. The situations described in the two panels represent the levels Case 1 (Figure 2(a)) and Case 2 (Figure 2(b)) used for the ANOVA analysis. In particular, the average edge density resulting from the shuffling procedure applied to simulated (random uncorrelated) data was 7% for the not corrected case and 4% for the FDR corrected case.

This first result confirmed the importance of statistical validation process combined with the correction for multiple comparisons. In fact, only the application of the shuffling procedure in the FDR case allowed to discard spurious links (obtained in this case on random, uncorrelated signals) at the correct level (below 5%). The edge densities obtained for the shuffling procedure, reported in Figure 2, were used also in the fixed edges method, to avoid different performance of the two methods to be due to the different number of connections. In particular, in the fixed edges method, if the imposed edge density is  $k$ , the threshold is chosen as the value which allowed to keep the  $k$  higher connections of the graph.

The two approaches were statistically compared by means of an ANOVA performed as described in Section 2 with each graph derived index as a dependent variable. The indices were normalized with the values obtained from 100 random graphs generated by keeping the number of connections of the correspondent adjacency matrix. This process was repeated 50 times in order to increase the robustness of the statistical analysis.

The ANOVA analysis was computed considering the small-worldness index as dependent variable and the methods used for adjacency matrices extraction (METHOD) and the edge density of the achieved adjacency matrix (EDGE) as within main factors. The main factor METHOD was composed by two levels: shuffling procedure, fixed edge density method. The main factor EDGE was composed by two levels: Case 1 (edge density associated to significance level 5%, not corrected for multiple comparisons) and Case 2 (edge density associated to significance level 5%, FDR corrected). Results revealed a statistical influence of the main factors METHOD ( $P < 0.00001$ ,  $F = 34.87$ ) and METHOD  $\times$  EDGE ( $P < 0.00001$ ,  $F = 13.46$ ) on the small-worldness

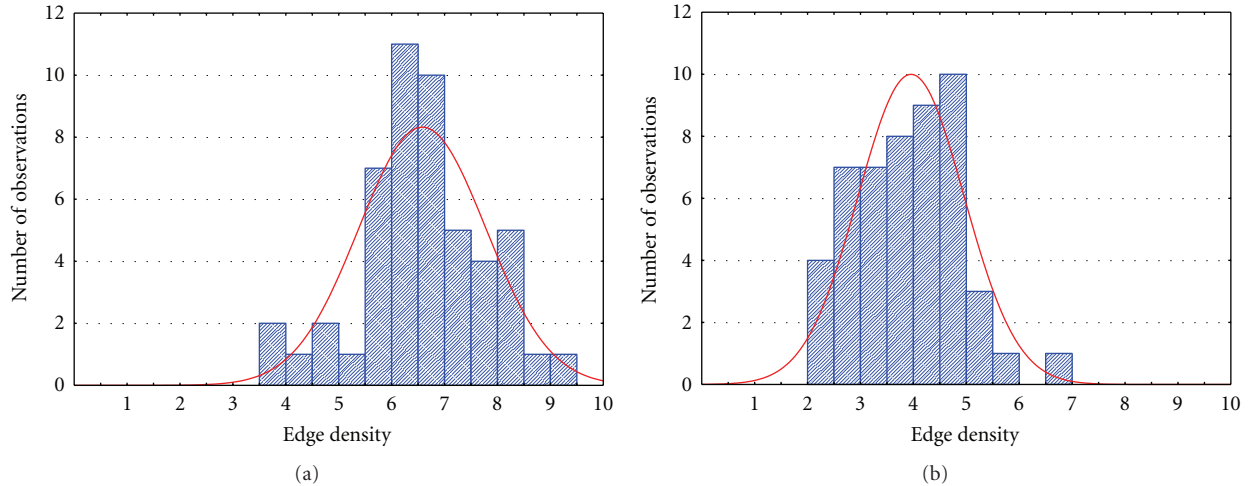


FIGURE 2: Distribution of the edge density characterizing the adjacency matrices extracted during the different iterations of the connectivity estimation process on simulated data in two different cases: Case 1 (a) → percentage of edges survived to shuffling procedure for a significance level of 5% not corrected for multiple comparison; Case 2 (b) → percentage of edges survived to shuffling procedure for a significance level of 5% corrected for multiple comparisons by means of FDR.

index computed on connectivity networks inferred from simulated data.

In Figure 3, we reported results of the ANOVA performed on the small world index considering METHOD  $\times$  EDGE as main factor. The diagram shows the mean value for the small-worldness computed on adjacency matrices extracted by means of shuffling procedure (blue line) and fixed edge density (red line), from the connectivity patterns estimated on simulated data. The bar represented their relative 95% confidence interval. Considering that the edge density is equal by construction for the two methods, the diagram shows significant differences between the two methods in the description of the network in terms of small-worldness, confirmed by the post hoc analysis computed by means of Tukey's test (\* symbol in Figure 3). In fact, the use of the method based on a fixed edge density revealed small-world properties of the network obtained from uncorrelated signals, for both density values. On the contrary, the application of the shuffling procedure allowed to correctly identify the absence of small-worldness in the network.

To understand if the erroneous attribution of small-worldness to the networks achieved by means of the fixed edge density method is mainly due to the clustering coefficient or to the characteristic path length, correlations between the small-worldness index and these two indices were computed for the two different edge densities. The results achieved in the Case 2 (edge density as Figure 2(b)) were shown in Figure 4. The diagram showed the scatter plot of small worldness versus clustering coefficient (Figure 4(a)) and small-worldness versus path length (Figure 4(b)) for each iteration of the adjacency matrix extraction process computed by means of the fixed edge density method, in the case of edge density correspondent to those achieved in Case 2 (edge density as Figure 2(b)). The line in the figure represents the linear fitting computed on the data. In the box, the associated values of correlation ( $r$ ) and  $r$ -square ( $r^2$ ) were reported. From these results, it can be inferred

that the small-worldness of networks achieved by means of fixed edge density method in Case 2 can be mainly due to the clustering coefficient, with a correlation of 0.93 and a  $r$ -square of 0.86. A minor dependence of small-worldness from path length index is highlighted by low values of correlation coefficient ( $-0.36$ ) and  $r$ -square (0.13). The same effect can be described for Case 1 (small-worldness versus clustering  $r = 0.91$ ,  $r^2 = 0.82$ ; small-worldness versus path length  $r = -0.38$ ,  $r^2 = 0.15$ ).

**3.2. Mannequin Data.** The simulated dataset used as null model for functional connectivity estimations represents an ideal case, because it does not take into account the spatial correlation between neighboring electrodes which always occurs during an EEG recording. For this reason, we used a second dataset, composed by signals acquired simultaneously from a mannequin head equipped with a cap positioned over a humidified towel, which, with its absence of physiological signals but with its correlation between neighboring electrodes, represents the null model for connectivity inferred from signals acquired during an EEG experiment. In the second dataset, we randomly selected 20 channels among the 61 acquired (same number of signals used for simulated data) and subjected them to functional connectivity estimation process. Then the correspondent adjacency matrix was extracted by means of the two considered methods and some graph indices, such as small-worldness, path length, and clustering coefficient, were computed. The indices were normalized with the values obtained from 100 random graphs generated by keeping the number of connections of the correspondent adjacency matrix. This process was repeated 50 times in order to increase the robustness of the following statistical analysis.

The shuffling procedure was applied for a significance level of 5%, both in the not corrected case and in the case of FDR correction. In Figure 5, we reported two histograms describing the distribution of the edge density characterizing

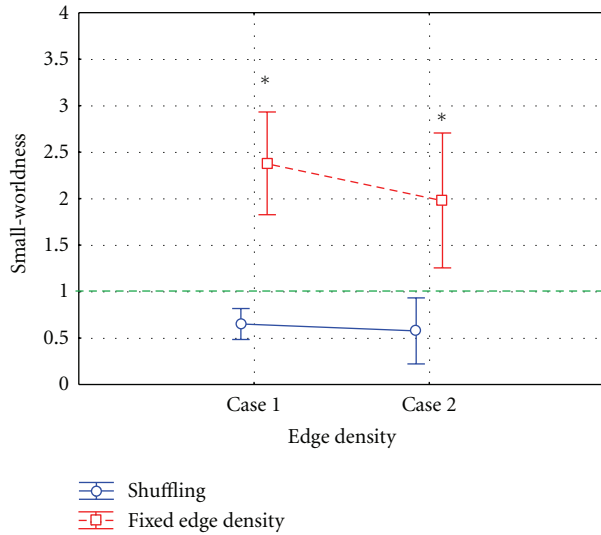


FIGURE 3: Results of ANOVA performed on the small-world index computed on networks inferred from simulated data, using METHOD and EDGE as within main factors. The diagram shows the mean value for the small-worldness computed on the adjacency matrices extracted by means of the shuffling procedure (blue line) and fixed edge density method (red line) in Case 1 (edge density as described in Figure 2(a)) and Case 2 (edge density as described in Figure 2(b)). The bars represent their relative 95% confidence intervals. The green dotted line represents the threshold above which a network is said to be “small world.” The symbol (\*) indicates a statistical difference between shuffling procedure and fixed edge density method, highlighted by Tukey’s post hoc test ( $P < 0.05$ ).

the adjacency matrices extracted during the different iterations of functional connectivity estimation process on mannequin data, for the uncorrected case (Case 1, Figure 5(a)) and for the FDR corrected case (Case 2, Figure 5(b)). In particular, the average edge density was 22% for the not corrected case and 16% for the case corrected by means of FDR. This result showed the effect on connectivity measures due to the spatial correlation of neighboring electrodes. In fact, the statistical validation process combined with the correction for multiple comparisons couldn’t completely discard spurious links due to random fluctuations of the signals (residual edge density above 5%). The same edge densities, reported in Figure 5, were used in the second method in order to avoid differences between the two methods due to the different number of connections.

The same statistical analysis described in the previous paragraph for simulated data was computed on graph indices extracted from mannequin data networks. In the ANOVA, computed considering the small worldness as dependent variable and the methods use for adjacency matrices extraction (METHOD) and the edge density of the achieved adjacency matrix (EDGE) as within main factors, the main factor METHOD was composed by two levels: shuffling procedure and fixed edge density method. The main factor EDGE was composed by two levels: Case 1 (edge density as in Figure 5(a)) and Case 2 (edge density as in Figure 5(b)). Results revealed statistical influence of the main

factors METHOD ( $P = 0.00001$ ,  $F = 23.42$ ), EDGE ( $P < 0.00001$ ,  $F = 104.47$ ), and METHOD  $\times$  EDGE ( $P < 0.00021$ ,  $F = 15.99$ ) on the small-worldness index computed on connectivity networks inferred from mannequin data.

In Figure 6, we reported results of the ANOVA performed on the small world index considering METHOD  $\times$  EDGE as main factor. The diagram shows the mean value for the small-worldness computed on adjacency matrices extracted, by means of shuffling procedure (blue line) and fixed edge density (red line), from the connectivity patterns estimated on mannequin data. The bar represented their relative 95% confidence interval. The small-worldness index is above 1 for both methodologies, with statistically higher values for fixed edge density in respect to shuffling procedure in Case 2 as confirmed by the post hoc analysis computed by means of Tukey’s.

In order to understand which indices, between the clustering coefficient and the characteristic path length, mainly contributed to the small worldness of the networks achieved by means of shuffling procedure and fixed edge density method, correlations between the small-worldness index and these two indices were computed for the two edge density cases. The results achieved in the case of edge density correspondent to Case 2 (edge density as Figure 2(b)) were showed in Figure 7. The diagram showed the scatterplot of small-woldness versus clustering coefficient (Figures 7(a) and 7(c)) and small-worldness versus path length (Figures 7(b) and 7(d)) for each iteration of the adjacency matrix extraction process computed by means of shuffling procedure (first row) and fixed edge density method (second row) in the case of edge density correspondent to those achieved in Case 2 (edge density as Figure 5(b)). The solid lines in the figure represent the linear fitting computed on the data. In the box, the associated values of correlation ( $r$ ) and  $r$ -square ( $r^2$ ) were reported. The small-worldness of networks achieved by means of shuffling procedure in Case 2 can be due, at the same time, to the clustering coefficient, with a correlation of 0.92 and a  $r$ -square of 0.85 and to the path length with a correlation coefficient of  $-0.69$  and a  $r$ -square of 0.48. Same consideration could be done for fixed edge density method (small-worldness versus clustering  $r = 0.83$ ,  $r^2 = 0.70$ ; small-worldness versus path length  $r = -0.79$ ,  $r^2 = 0.63$ ). The same effect could be described for Case 1 (shuffling procedure: small-worldness versus clustering  $r = 0.92$ ,  $r^2 = 0.83$ ; small-worldness versus Path Length  $r = -0.79$ ,  $r^2 = 0.63$ ; fixed edge density: small-worldness versus clustering  $r = 0.91$ ,  $r^2 = 0.83$ ; smal-worldness versus path length  $r = -0.87$ ,  $r^2 = 0.76$ ).

#### 4. Discussion

The strong dependence of graph measures from the number of nodes, the edge density, and the degree of the networks under analysis should lead to reflect on the modalities used for adjacency matrix extraction [22]. Different methodologies are currently used for this purpose; some of them based on the definition of fixed thresholds [26, 27], others based on fixed average degree [28–32], and others on fixed edge density [32]. The choice of a threshold in order to fix the

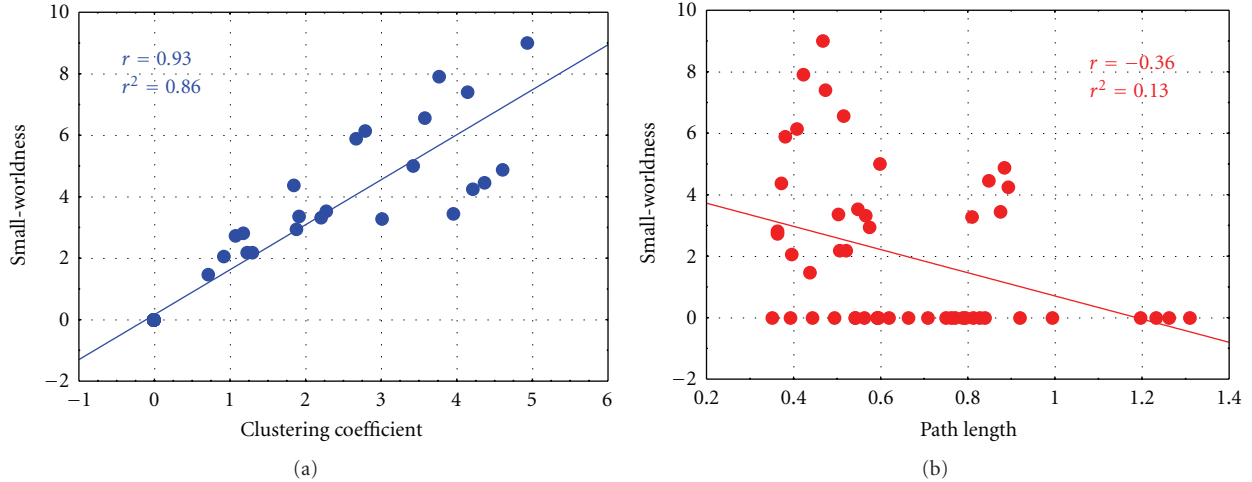


FIGURE 4: Scatterplot of small-worldness versus clustering coefficient (a) and small-worldness versus path length (b) for each iteration of the adjacency matrix extraction process computed by means of fixed edge density method for edge densities correspondent to those achieved in Case 2 (as from Figure 2(b)). The solid line represents the linear fitting computed on the data. The associated values of correlation ( $r$ ) and  $r$ -square ( $r^2$ ) were reported in the boxes.

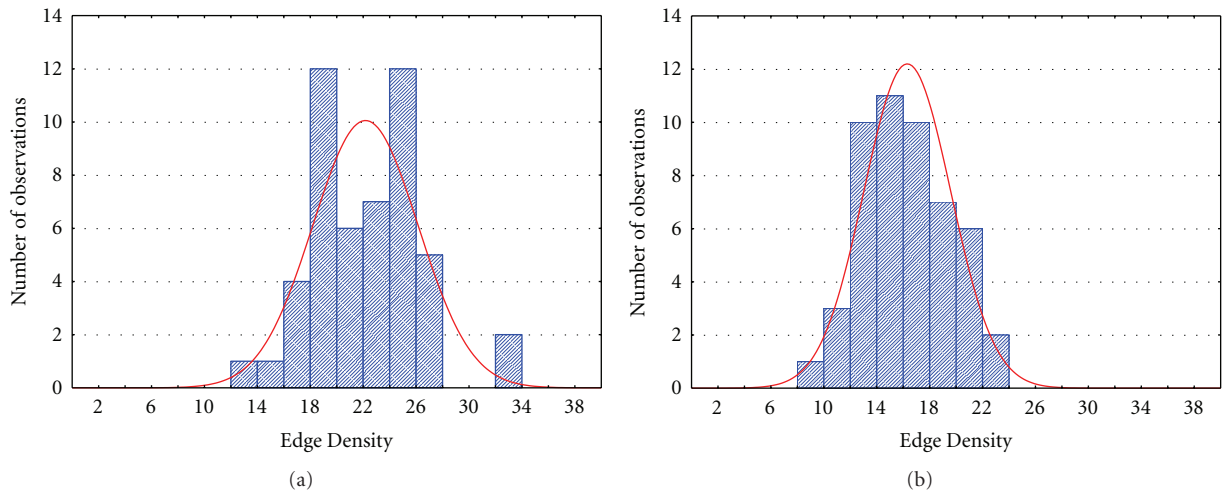


FIGURE 5: Distribution of the edge density characterizing the adjacency matrices extracted during the different iterations of connectivity estimation process on mannequin data in two different cases: Case 1 (a) → percentage of edges survived to shuffling procedure for a significance level of 5%, not corrected for multiple comparisons; Case 2 (b) → percentage of edges survived to shuffling procedure for a significance level of 5%, FDR corrected.

number of edges or the degree allows to avoid size and density effects in the comparison of networks inferred from two different conditions, but can affect the structure of the network by enforcing nonsignificant links and ignoring significant connections [22]. To understand the effects on the structural properties of a network due to the method applied for adjacency matrix extraction, we computed a statistical comparison between one of the methods most extensively used in graph theory applications for extracting adjacency matrices from brain connectivity patterns (i.e., the method based on fixing the edge density) with an approach based on the statistical validation of achieved connectivity patterns by means of a shuffling procedure. The comparison was performed on two different datasets, one composed by random and uncorrelated simulated data, modeling the

null case for the connectivity estimates, and another one composed by signals acquired on a mannequin head, taking into account the spatial correlation between neighboring electrodes [36].

The results presented in this section allow to discuss about some open problems which affect the application of graph measures to the functional connectivity estimates.

The first issue addressed in the present paper is the necessity to statistically validate the connectivity measures in order to discard the spurious links due to random fluctuations of the signals considered simultaneously in the multivariate [33, 43, 44] or bivariate model [45, 46]. In this paper, we confirmed the importance of the statistical validation combined with the corrections for multiple comparisons in multivariate estimates [47] by showing

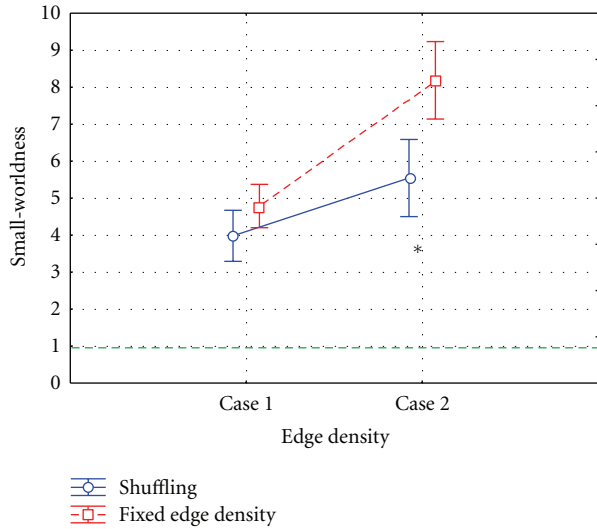


FIGURE 6: Results of ANOVA performed on the small-worldness index computed on networks inferred from mannequin data, using METHOD and EDGE as within main factors. The diagram shows the mean value for the small worldness computed on the adjacency matrices extracted by means of Shuffling procedure (blue line) and fixed edge density method (red line) in two cases, Case 1 (edge density as in Figure 5(a)) and Case 2 (edge density as in Figure 5(b)). The bar represents their relative 95% confidence interval. The green dotted line represents the threshold above which a network is said to be “small world.” The symbol (\*) indicates a statistical difference between shuffling procedure and fixed edge density method, highlighted by Tukey’s post hoc test ( $P < 0.05$ ).

the edge densities survived to the shuffling procedure on the simulated data (Figure 2). Being the simulated data a null model for connectivity estimation, all the survived links can be seen as false positives. The application of the shuffling procedure for a significance level of 5% not corrected produces 7% of false positives. Only applying the statistical correction of FDR the false positives went down the threshold of 5%. Unfortunately, the application of shuffling procedure to connectivity networks inferred on mannequin data led to a high number of false positives (22% in the not corrected case and 16% in the case of FDR correction). This could be explained by taking into account that some of the survival links are due to real correlations between neighboring electrodes induced by the registration on a wet towel, but which can occur also in real EEG recordings [48, 49].

A second issue to be considered as relevant in graph theory concerns the modality in which the adjacency matrix is extracted from the connectivity network. As already said in the previous sections, the threshold choice is crucial for the computation of graph measures because it affects the topographical properties of real networks. In the present study, we made a comparison between one of the methods extensively used in graph theory applications for extracting adjacency matrices from the connectivity patterns (i.e., the method based on fixing the edge density) and an approach based on the statistical validation of achieved connectivity patterns by means of a shuffling procedure, to

describe the effects of the modalities for adjacency matrix extraction on the “small-world” properties of the network. The results achieved on simulated data highlighted small-world properties of the analyzed networks even in random, uncorrelated data, when the fixed edge density method was applied. Such small-worldness is mainly correlated with an increase of the clustering coefficient and disappeared when shuffling procedure was used. The fixed edge density criterion led to an erroneous diagnosis of small-worldness for the connectivity patterns estimated on simulated data, independently from the edge density chosen. In fact, the simulated data, being uncorrelated, should produce connectivity patterns without any topographical properties of small-worldness. These results led to two conclusions. The first is that the shuffling procedure does not just preserve the strongest connections, as demonstrated by different results obtained by means of fixed edge density which is based on this criterion. It means that the significance of a link is not merely related to its strength. The second conclusion is that the choice of an empirical threshold can affect so much the topography of the network that an erroneous definition of small-worldness could result. Thus, a statistical validation, combined with multiple comparisons adjustments, to be applied on connectivity networks, is necessary to define the significance of each edge within the adjacency matrix, in order to extract graph measures able to describe the real properties of the considered network.

The results achieved on mannequin data showed small world properties of the networks extracted by applying both methodologies. In this case, the shuffling procedure couldn’t prevent the description of mannequin networks as small world networks, even applying the corrections for multiple comparisons, but the entity of small-worldness is lower than those achieved by means of fixed edge density method. In both cases the small-worldness is equally correlated with an increase of the clustering coefficient and with a decrease of the path length. This effect could be explained with the existence of real correlations between electrodes, which can occur in real EEG data, due to volume conduction effect and to the location of the reference [36, 50, 51]. These considerations led to a possible redefinition of the meaning of the small-worldness index. In fact, it cannot be considered as an absolute measure, because its value contains some of the real correlations due to neighboring electrodes. A possible solution is to consider only variations of this measure between two conditions within the same subject, or between two subjects in the same conditions, in order to discard all the effects due to the position of the electrodes on the scalp. Another way to mitigate such effect is to apply the connectivity estimation process to the data obtained by methods which allow to reduce the spatial correlation between electrodes, such as all the approaches for the reconstruction of cortical sources from high-resolution EEG recordings [52–55]. Such methodologies allow to focus the activations of cerebral sources by means of a high number of sensors, realistic head models, and the solution of the associated linear inverse problem [56–58]. It must be also noted that other methods used for reducing spatial correlation at the scalp level, such as blind source separation

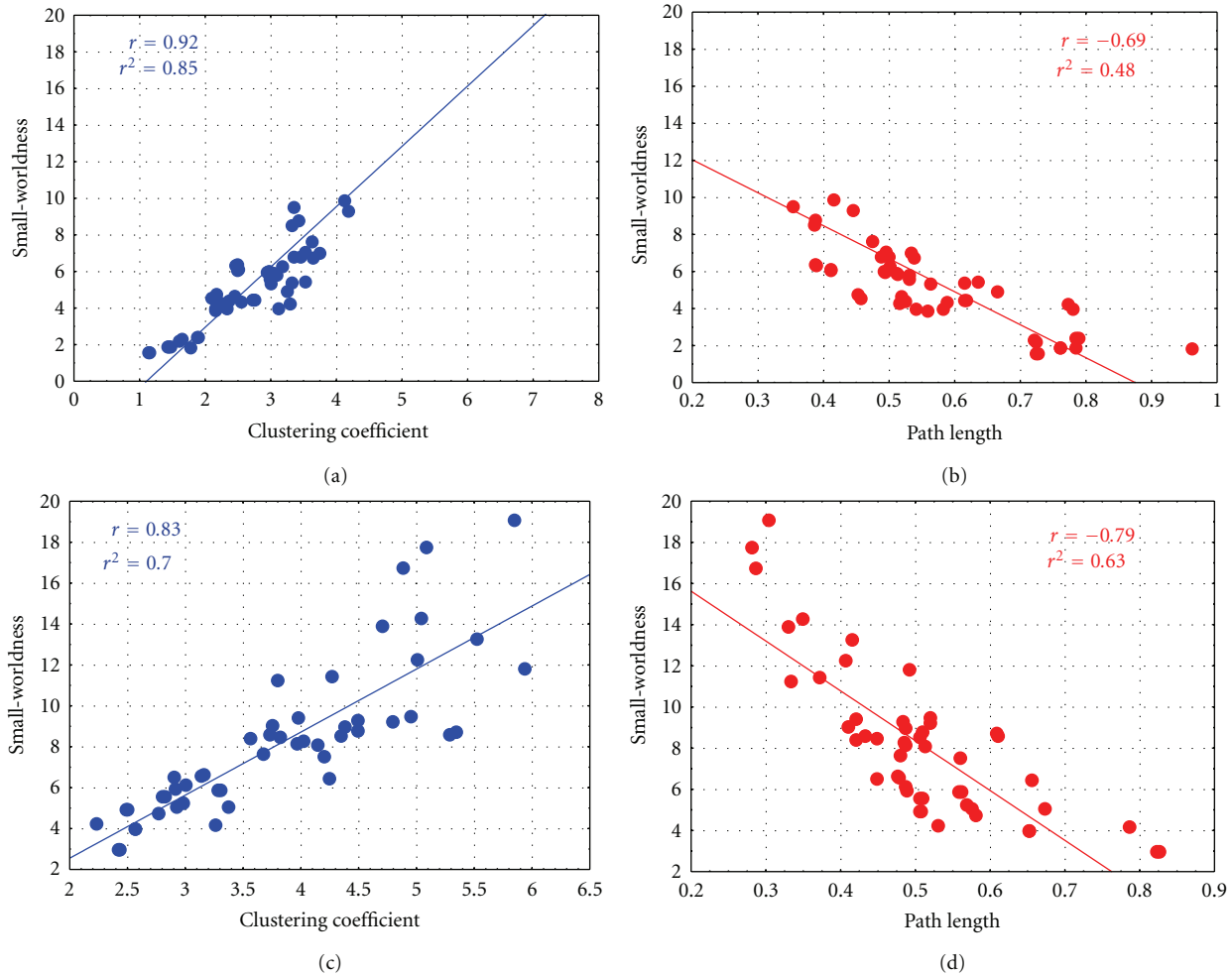


FIGURE 7: Scatterplot of small-worldness clustering coefficient ((a) and (c)) and small-worldness versus path length ((b) and (d)) for each iteration of the adjacency matrix extraction process computed by means of shuffling procedures (first row) and fixed edge density method (second row) for edge densities correspondent to those achieved in Case 2 (edge density as in Figure 5(b)). The line represents the linear fitting computed on the data. The associated values of correlation ( $r$ ) and  $r$ -square ( $r^2$ ) were reported in the boxes.

and superficial laplacian [59], cannot be used, due to the correlation they induce in the data, which would, in turn, produces spurious results.

### 5. Conclusion

The present work aims at highlighting some erroneous results that can be obtained by the application of commonly used approaches for the extraction of adjacency matrix from connectivity patterns, and to describe how such procedures can affect the topographical properties of a network inferred by means of graph measures. For this reason, we computed a statistical comparison between one of the methods extensively used in graph theory applications for extracting adjacency matrices from the connectivity patterns (i.e., fixing the edge density) with an approach based on the statistical validation of achieved connectivity patterns by means of a shuffling procedure. The results achieved on simulated data highlighted the importance of a statistical validation of connectivity patterns which allows from one side to prevent

the occurrence of false positives due to random fluctuations of signals, and from the other side to extract graph measures able to describe the real properties of the considered network. The results achieved on mannequin data showed an effect of the spatial correlations between electrodes and of the location of the reference on small-worldness index. Such effect could be mitigated by applying methodologies for the reconstruction of cortical sources.

### Acknowledgments

This work is supported by a grant of Ministero dell’Istruzione, dell’Università e della Ricerca, in a bilateral project between Italy and Hungary and by the European STREP Program—Collaborative Project no. FP7-287320-CONTRAST. Possible inaccuracies of information are under the responsibility of the project team. The text reflects solely the views of its authors. The European Commission is not liable for any use that may be made of the information contained therein.

## References

- [1] B. Horwitz, "The elusive concept of brain connectivity," *NeuroImage*, vol. 19, no. 2, pp. 466–470, 2003.
- [2] L. Lee, L. M. Harrison, and A. Mechelli, "A report of the functional connectivity workshop, Dusseldorf 2002," *NeuroImage*, vol. 19, no. 2, pp. 457–465, 2003.
- [3] C. C. Turbes, G. T. Schneider, and R. J. Morgan, "Partial coherence estimates of brain rhythms," *Biomedical Sciences Instrumentation*, vol. 19, pp. 97–102, 1983.
- [4] M. J. Kaminski and K. J. Blinowska, "A new method of the description of the information flow in the brain structures," *Biological Cybernetics*, vol. 65, no. 3, pp. 203–210, 1991.
- [5] L. A. Baccalá and K. Sameshima, "Partial directed coherence: a new concept in neural structure determination," *Biological Cybernetics*, vol. 84, no. 6, pp. 463–474, 2001.
- [6] K. J. Blinowska, "Review of the methods of determination of directed connectivity from multichannel data," *Medical and Biological Engineering and Computing*, vol. 49, no. 5, pp. 521–529, 2011.
- [7] R. Kuś, M. Kamiński, and K. J. Blinowska, "Determination of EEG activity propagation: pair-wise versus multichannel estimate," *IEEE Transactions on Biomedical Engineering*, vol. 51, no. 9, pp. 1501–1510, 2004.
- [8] K. J. Blinowska, R. Kuś, and M. Kamiński, "Granger causality and information flow in multivariate processes," *Physical Review E*, vol. 70, no. 5, Article ID 050902, 4 pages, 2004.
- [9] O. David, D. Cosmelli, and K. J. Friston, "Evaluation of different measures of functional connectivity using a neural mass model," *NeuroImage*, vol. 21, no. 2, pp. 659–673, 2004.
- [10] K. J. Blinowska, M. Kaminski, J. Kaminski, and A. Brzezicka, "Information processing in brain and dynamic patterns of transmission during working memory task by the SDTF function," in *Proceedings of the 32nd Annual International Conference of the IEEE Engineering in Medicine and Biology Society (EMBC '10)*, pp. 1722–1725, September 2010.
- [11] C. W. J. Granger, "Investigating causal relations by econometric models and cross-spectral methods," *Econometrica*, vol. 37, pp. 424–438, 1969.
- [12] L. Astolfi, F. Cincotti, D. Mattia et al., "Comparison of different cortical connectivity estimators for high-resolution EEG recordings," *Human Brain Mapping*, vol. 28, no. 2, pp. 143–157, 2007.
- [13] S. H. Strogatz, "Exploring complex networks," *Nature*, vol. 410, no. 6825, pp. 268–276, 2001.
- [14] O. Sporns, D. R. Chialvo, M. Kaiser, and C. C. Hilgetag, "Organization, development and function of complex brain networks," *Trends in Cognitive Sciences*, vol. 8, no. 9, pp. 418–425, 2004.
- [15] C. J. Stam, "Functional connectivity patterns of human magnetoencephalographic recordings: a "small-world" network?" *Neuroscience Letters*, vol. 355, no. 1-2, pp. 25–28, 2004.
- [16] C. J. Stam and J. C. Reijneveld, "Graph theoretical analysis of complex networks in the brain," *Nonlinear Biomedical Physics*, vol. 1, article 3, 2007.
- [17] E. Bullmore and O. Sporns, "Complex brain networks: graph theoretical analysis of structural and functional systems," *Nature Reviews Neuroscience*, vol. 10, no. 3, pp. 186–198, 2009.
- [18] F. De Vico Fallani, J. Toppi, C. Di Lanzo et al., "Redundancy in functional brain connectivity from EEG recordings," *International Journal of Bifurcation and Chaos*. In press.
- [19] L. Astolfi, F. Cincotti, C. Babiloni et al., "Estimation of the cortical connectivity by high-resolution EEG and structural equation modeling: simulations and application to finger tapping data," *IEEE Transactions on Biomedical Engineering*, vol. 52, no. 5, pp. 757–768, 2005.
- [20] V. Latora and M. Marchiori, "Efficient behavior of small-world networks," *Physical Review Letters*, vol. 87, no. 19, Article ID 198701, pp. 1–4, 2001.
- [21] G. Fagiolo, "Clustering in complex directed networks," *Physical Review E*, vol. 76, no. 2, Article ID 026107, 2007.
- [22] B. C. M. van Wijk, C. J. Stam, and A. Daffertshofer, "Comparing brain networks of different size and connectivity density using graph theory," *PLoS ONE*, vol. 5, no. 10, Article ID e13701, 2010.
- [23] R. Salvador, J. Suckling, M. R. Coleman, J. D. Pickard, D. Menon, and E. Bullmore, "Neurophysiological architecture of functional magnetic resonance images of human brain," *Cerebral Cortex*, vol. 15, no. 9, pp. 1332–2342, 2005.
- [24] Z. J. Chen, Y. He, P. Rosa-Neto, J. Germann, and A. C. Evans, "Revealing modular architecture of human brain structural networks by using cortical thickness from MRI," *Cerebral Cortex*, vol. 18, no. 10, pp. 2374–2381, 2008.
- [25] L. Ferrarini, I. M. Veer, E. Baerends et al., "Hierarchical functional modularity in the resting-state human brain," *Human Brain Mapping*, vol. 30, no. 7, pp. 2220–2231, 2009.
- [26] M. P. Van Den Heuvel, C. J. Stam, R. S. Kahn, and H. E. Hulshoff Pol, "Efficiency of functional brain networks and intellectual performance," *Journal of Neuroscience*, vol. 29, no. 23, pp. 7619–7624, 2009.
- [27] D. S. Bassett, A. Meyer-Lindenberg, S. Achard, T. Duke, and E. Bullmore, "Adaptive reconfiguration of fractal small-world human brain functional networks," *Proceedings of the National Academy of Sciences of the United States of America*, vol. 103, no. 51, pp. 19518–19523, 2006.
- [28] R. Ferri, F. Rundo, O. Bruni, M. G. Terzano, and C. J. Stam, "The functional connectivity of different EEG bands moves towards small-world network organization during sleep," *Clinical Neurophysiology*, vol. 119, no. 9, pp. 2026–2036, 2008.
- [29] Y. He, Z. Chen, and A. Evans, "Structural insights into aberrant topological patterns of large-scale cortical networks in Alzheimer's disease," *Journal of Neuroscience*, vol. 28, no. 18, pp. 4756–4766, 2008.
- [30] W. de Haan, Y. A. L. Pijnenburg, R. L. M. Strijers et al., "Functional neural network analysis in frontotemporal dementia and Alzheimer's disease using EEG and graph theory," *BMC Neuroscience*, vol. 10, article 101, 2009.
- [31] M. Rubinov and O. Sporns, "Complex network measures of brain connectivity: uses and interpretations," *NeuroImage*, vol. 52, no. 3, pp. 1059–1069, 2010.
- [32] J. Wang, L. Wang, Y. Zang et al., "Parcellation-dependent small-world brain functional networks: a resting-state fmri study," *Human Brain Mapping*, vol. 30, no. 5, pp. 1511–1523, 2009.
- [33] M. Kamiński, M. Ding, W. A. Truccolo, and S. L. Bressler, "Evaluating causal relations in neural systems: Granger causality, directed transfer function and statistical assessment of significance," *Biological Cybernetics*, vol. 85, no. 2, pp. 145–157, 2001.
- [34] Y. Benjamini and Y. Hochberg, "Controlling the false discovery rate: a practical and powerful approach to multiple testing," *Journal of the Royal Statistical Society*, vol. 57, no. 1, pp. 289–300, 1995.
- [35] Y. Benjamini and D. Yekutieli, "The control of the false discovery rate in multiple testing under dependency," *Annals of Statistics*, vol. 29, no. 4, pp. 1165–1188, 2001.
- [36] P. L. Nunez, R. Srinivasan, A. F. Westdorp et al., "EEG coherency I: statistics, reference electrode, volume conduction,

- Laplacians, cortical imaging, and interpretation at multiple scales,” *Electroencephalography and Clinical Neurophysiology*, vol. 103, no. 5, pp. 499–515, 1997.
- [37] H. Akaike, “A new look at statistical model identification,” *IEEE Transactions on Automatic Control*, vol. AC-19, no. 6, pp. 716–723, 1974.
- [38] L. Astolfi, F. Cincotti, D. Mattia et al., “Assessing cortical functional connectivity by partial directed coherence: simulations and application to real data,” *IEEE Transactions on Biomedical Engineering*, vol. 53, no. 9, pp. 1802–1812, 2006.
- [39] J. Theiler, S. Eubank, A. Longtin, B. Galdrikian, and J. Doynne Farmer, “Testing for nonlinearity in time series: the method of surrogate data,” *Physica D*, vol. 58, no. 1–4, pp. 77–94, 1992.
- [40] T. Nichols and S. Hayasaka, “Controlling the familywise error rate in functional neuroimaging: a comparative review,” *Statistical Methods in Medical Research*, vol. 12, no. 5, pp. 419–446, 2003.
- [41] D. J. Watts and S. H. Strogatz, “Collective dynamics of “small-world” networks,” *Nature*, vol. 393, no. 6684, pp. 440–442, 1998.
- [42] M. D. Humphries and K. Gurney, “Network “small-worldness”: a quantitative method for determining canonical network equivalence,” *PLoS ONE*, vol. 3, no. 4, Article ID e2051, 2008.
- [43] B. Schelter, M. Winterhalder, M. Eichler et al., “Testing for directed influences among neural signals using partial directed coherence,” *Journal of Neuroscience Methods*, vol. 152, no. 1–2, pp. 210–219, 2006.
- [44] D. Y. Takahashi, L. A. Bacal, and K. Sameshima, “Connectivity inference between neural structures via partial directed coherence,” *Journal of Applied Statistics*, vol. 34, no. 10, pp. 1259–1273, 2007.
- [45] A. M. Amjad, D. M. Halliday, J. R. Rosenberg, and B. A. Conway, “An extended difference of coherence test for comparing and combining several independent coherence estimates: theory and application to the study of motor units and physiological tremor,” *Journal of Neuroscience Methods*, vol. 73, no. 1, pp. 69–79, 1997.
- [46] J. R. Rosenberg, A. M. Amjad, P. Breeze, D. R. Brillinger, and D. M. Halliday, “The Fourier approach to the identification of functional coupling between neuronal spike trains,” *Progress in Biophysics and Molecular Biology*, vol. 53, no. 1, pp. 1–31, 1989.
- [47] J. Toppi, F. Babiloni, G. Vecchiato et al., “Testing the asymptotic statistic for the assessment of the significance of Partial Directed Coherence connectivity patterns,” *Conference Proceedings: Annual International Conference of the IEEE Engineering in Medicine and Biology Society. IEEE Engineering in Medicine and Biology Society. Conference*, vol. 2011, pp. 5016–5019, 2011.
- [48] S. P. Van Den Broek, F. Reinders, M. Donderwinkel, and M. J. Peters, “Volume conduction effects in EEG and MEG,” *Electroencephalography and Clinical Neurophysiology*, vol. 106, no. 6, pp. 522–534, 1998.
- [49] J. Haueisen, D. S. Tuch, C. Ramon et al., “The influence of brain tissue anisotropy on human EEG and MEG,” *NeuroImage*, vol. 15, no. 1, pp. 159–166, 2002.
- [50] S. Bialonski, M. T. Horstmann, and K. Lehnertz, “From brain to earth and climate systems: small-world interaction networks or not?” *Chaos*, vol. 20, no. 1, p. 013134, 2010.
- [51] F. Gerhard, G. Pipa, B. Lima, S. Neuenschwander, and W. Gerstner, “Extraction of network topology from multi-electrode recordings: is there a small-world effect?” *Frontiers in Computational Neuroscience*, vol. 5, no. 4, 2011.
- [52] C. Babiloni, F. Babiloni, F. Carducci et al., “Mapping of early and late human somatosensory evoked brain potentials to phasic galvanic painful stimulation,” *Human Brain Mapping*, vol. 12, no. 3, pp. 168–179, 2001.
- [53] C. Babiloni, F. Carducci, F. Vecchio et al., “Functional frontoparietal connectivity during short-term memory as revealed by high-resolution EEG coherence analysis,” *Behavioral Neuroscience*, vol. 118, no. 4, pp. 687–697, 2004.
- [54] C. Babiloni, A. Brancucci, F. Babiloni et al., “Anticipatory cortical responses during the expectancy of a predictable painful stimulation. A high-resolution electroencephalography study,” *European Journal of Neuroscience*, vol. 18, no. 6, pp. 1692–1700, 2003.
- [55] A. Brancucci, C. Babiloni, F. Babiloni et al., “Inhibition of auditory cortical responses to ipsilateral stimuli during dichotic listening: evidence from magnetoencephalography,” *European Journal of Neuroscience*, vol. 19, no. 8, pp. 2329–2336, 2004.
- [56] L. Astolfi, F. Cincotti, D. Mattia et al., “Estimation of the effective and functional human cortical connectivity with structural equation modeling and directed transfer function applied to high-resolution EEG,” *Magnetic Resonance Imaging*, vol. 22, no. 10, pp. 1457–1470, 2004.
- [57] L. Astolfi, F. De Vico Fallani, F. Cincotti et al., “Imaging functional brain connectivity patterns from high-resolution EEG and fMRI via graph theory,” *Psychophysiology*, vol. 44, no. 6, pp. 880–893, 2007.
- [58] R. Grave De Peralta Menendez and S. L. Gonzalez Andino, “Backus and Gilbert method for vector fields,” *Human Brain Mapping*, vol. 7, no. 3, pp. 161–165, 1999.
- [59] A. Delorme, J. Palmer, J. Onton, R. Oostenveld, and S. Makeig, “Independent EEG sources are dipolar,” *PLoS ONE*, vol. 7, no. 2, Article ID e30135, 2012.

## Research Article

# A Signal-Processing-Based Approach to Time-Varying Graph Analysis for Dynamic Brain Network Identification

Ali Yener Mutlu,<sup>1</sup> Edward Bernat,<sup>2</sup> and Selin Aviyente<sup>1</sup>

<sup>1</sup>Department of Electrical and Computer Engineering, Michigan State University, East Lansing, MI 48824, USA

<sup>2</sup>Department of Psychology, Florida State University, Tallahassee, FL 32306, USA

Correspondence should be addressed to Ali Yener Mutlu, mutluali@msu.edu

Received 30 March 2012; Revised 3 July 2012; Accepted 10 July 2012

Academic Editor: Tianzi Jiang

Copyright © 2012 Ali Yener Mutlu et al. This is an open access article distributed under the Creative Commons Attribution License, which permits unrestricted use, distribution, and reproduction in any medium, provided the original work is properly cited.

In recent years, there has been a growing need to analyze the functional connectivity of the human brain. Previous studies have focused on extracting static or time-independent functional networks to describe the long-term behavior of brain activity. However, a static network is generally not sufficient to represent the long term communication patterns of the brain and is considered as an unreliable snapshot of functional connectivity. In this paper, we propose a dynamic network summarization approach to describe the time-varying evolution of connectivity patterns in functional brain activity. The proposed approach is based on first identifying key event intervals by quantifying the change in the connectivity patterns across time and then summarizing the activity in each event interval by extracting the most informative network using principal component decomposition. The proposed method is evaluated for characterizing time-varying network dynamics from event-related potential (ERP) data indexing the error-related negativity (ERN) component related to cognitive control. The statistically significant connectivity patterns for each interval are presented to illustrate the dynamic nature of functional connectivity.

## 1. Introduction

The human brain is known to be one of the most complex systems and understanding its connectivity patterns for normal and disrupted brain behavior remains as a challenge. Over the last decade, there has been a growing interest in studying brain connectivity. In literature, three kinds of brain connectivity have been addressed to define interactions between different regions of the human brain: anatomical connectivity, functional connectivity, and effective connectivity [1, 2]. Anatomical connectivity is defined as the set of connections at the physical or structural layer which links neuronal units at a given time and can be analyzed using techniques such as diffusion tensor imaging [3, 4]. Functional connectivity is defined as the statistical dependencies among remote neurophysiological events, which indicate the integration of functionally segregated brain regions. Finally, effective connectivity refers to causal relations between neural systems where causality is understood in at least two distinct ways: temporal precedence and physical influence

[5–7]. In this paper, we limit our focus on discovering functional connectivity where reciprocal interactions are investigated.

Functional connectivity can be inferred from different neuroimaging data such as the functional magnetic resonance imaging (fMRI), electroencephalography (EEG), and magnetoencephalography (MEG) [8]. fMRI provides a high spatial resolution whereas EEG, and MEG have more limited spatial resolution. However, EEG and MEG offer higher temporal resolution required for quantifying the time-varying relationships between neuronal oscillations compared to fMRI which makes these recording techniques more appealing for quantifying the functional brain connectivity. Various measures, such as spectral coherence and phase synchrony, have been proposed for quantifying the functional relationships among different brain regions [9]. However, these measures are limited to quantifying pairwise relationships and cannot provide an understanding of the collective behavior of different brain regions. Attempts to characterize the topologies of these large networks led to

the emergence of a new, multidisciplinary approach to the study of complex systems based on graph theory, which has been used to analyze models of neural networks, anatomical connectivity, and functional connectivity based upon fMRI, EEG and MEG. Network characterization of functional connectivity data is motivated by the development of neurobiologically meaningful and easily computable measures, such as graph theory-based clustering coefficient and characteristic path length, that reliably quantify brain networks [1, 10–13]. These measures also offer a simple way to compare functional network topologies between subject populations and have been shown to reveal presumed connectivity abnormalities in neurological and psychiatric disorders [14, 15].

A network is a mathematical representation of a real-world complex system with relational information and can be represented by a graph consisting of a set of vertices (or nodes) and a set of edges (or connections) between pairs of nodes. The presence of a connection between two vertices means that there is some kind of relationship or interaction between the nodes. In order to emphasize the strength of the connectivity between nodes, one can assign weights to each of the edges and the corresponding graph is called a weighted graph. In the study of functional brain networks, nodes represent the different brain regions and the edges correspond to the functional connectivity between these nodes which are usually quantified by the magnitudes of temporal correlations in activity. Depending on the measure, functional connectivity may reflect linear interactions such as correlation or nonlinear interactions such as phase synchrony [9]. Graph theory provides a way to capture the topology of this network and to quantify the multivariate relationships among neuronal activations across brain regions as well as to suggest models for functional brain networks which may allow us to better understand the relation between network structure and the processes taking place on these networks. One such model is the “small-world” network introduced by Watts and Strogatz [16], that demonstrates both clustered “cliquish” interconnectivity within groups of nodes (like regular lattices) and a short path length between any two nodes (like random graphs). This is an attractive configuration for the functional architecture of the brain, because small-world networks are known to optimize information transfer, increase the rate of learning, and support both segregated and distributed information processing. Recently, there have been multiple functional network studies using graph theory based on fMRI [17], EEG [14, 18], and MEG data [12, 19] which have shown small-world patterns in functional networks of healthy subjects. Several studies have also shown how brain pathology, such as schizophrenia and Alzheimer’s diseases, may interfere with the normal small-world architecture [10–12, 14, 20].

Currently, topological features of functional brain networks such as clustering coefficient, path length, small world parameter [21], modularity, global, and local efficiency are defined over long periods of time, thus focusing on static networks and neglecting possible time-varying properties of the topologies [22–24]. This consideration might be reasonable for anatomical connectivity; however, a single

graph is not sufficient to represent the communication patterns of the brain and can be considered as an unreliable snapshot of functional connectivity. Evidence suggests that the emergence of a unified neural process is mediated by the continuous formation and destruction of functional links over multiple time scales [21].

In recent years, there has been an interest in characterizing the dynamic evolution of functional brain networks. Most of the existing approaches to dynamic network analysis are either graph theory based such as direct extensions of component finding [25–27] and community detection [28] from the static to the dynamic case or are feature based where features extracted from each graph in the time series are used to form time-varying graph metrics [29, 30]. This extension to dynamic networks reveals that the processing of a stimulus involves optimized functional integration of distant brain regions by dynamic reconfiguration of links. More recently, the dynamic nature of the modular structure in the functional brain networks has been investigated by finding modules for each time window and comparing the modularity of the partitions across time [31]. However, this approach does not evaluate the dynamic evolution of the clusters across time and is basically an extension of static graph analysis for multiple static graphs. Mucha et al. [28] proposed a new time-varying clustering algorithm which addresses this issue by defining a new modularity function across time. All of these module finding algorithms result in multiple clustering structures across time and there is a need to reduce this multitude of data into a few representative networks or to quantify the evolution of the network in time using reliable metrics. Therefore, these approaches do not track the change in connectivity or clustering patterns and cannot offer meaningful summarizations of time-varying network topology.

Recently, researchers in signal processing have addressed problems in dynamic network analysis such as detection of anomalies or distinct subgraphs in large, noisy background [32] and tracking dynamic networks [33]. Simple approaches such as sliding window or exponentially weighted moving averaging have been proposed for inferring long-term information or trends [34, 35]. However, these methods have some disadvantages such as preserving historical affinities indefinitely, which makes the network topology denser as time evolves [34]. In this paper, we will contribute to this line of work by finding the event intervals in functional brain connectivity patterns, revealing the most relevant and informative information for each interval and summarizing brain network activity with a few number of representative networks, similar to data reduction in signal processing where the ideal summary should conserve the minimum redundancy in representing the dynamics of the particular interval. Recently, similar data reduction problems in psychophysiological studies involving evoked brain potential activity across time, frequency, and space have been addressed [36, 37]. However, the work in this area focuses on reducing activation patterns across time, frequency, and space using a Bayesian classification approach [37]. Unlike this paper which considers the activation of each electrode individually in time- and frequency, our paper considers functional

connectivity or multivariate relationships between electrode pairs and tries to reduce this relational information using a segmentation approach along time.

In this paper, we first construct time-varying graphs, which are needed to describe the brain activity across time, by quantifying the time-varying phase synchrony between different electrodes of the EEG data [38]. Then, a framework for summarizing or reducing the information in dynamic brain networks into a few representative networks will be proposed by computing the distances between subsequent graphs, detecting changes in distances to determine the event boundaries, and, finally, forming a key network for each interval such that this key network summarizes the particular interval with minimal redundancy.

## 2. Background

Phase synchrony is defined as the temporal adjustment of the rhythms of two oscillators while the amplitudes can remain uncorrelated. The first step in quantifying the phase synchrony between two signals is to estimate the instantaneous phase of the individual signals,  $\Phi_i(t, \omega)$ , around the frequency of interest,  $\omega$ . Once the phase difference,  $\Phi_{i,j}(t, \omega) = |\Phi_i(t, \omega) - \Phi_j(t, \omega)|$ , between the two signals,  $x_i$  and  $x_j$ , is estimated, phase synchronization can be quantified by means of the phase-locking value (PLV) which ranges in  $[0, 1]$ :

$$\text{PLV}_{i,j}(t, \omega) = \frac{1}{K} \left| \sum_{k=1}^N \exp(j\Phi_{i,j}^k(t, \omega)) \right|, \quad (1)$$

where  $K$  is the number of trials and  $\Phi_{i,j}^k(t, \omega)$  is the time-varying phase difference estimate for the  $k$ th trial. If the phase difference varies little across the trials, PLV is close to 1 which indicates high phase synchrony pair signals.

Two major approaches to extracting the instantaneous phase are the Hilbert transform and the complex wavelet transform. The Hilbert transform-based method obtains an analytic form of the signal and estimates the instantaneous phase from this analytic form [39]. However, one has to ensure that the signal is composed of a narrowband of frequencies and this requires the bandpass filtering of the signal around a frequency of interest which is followed by the application of the Hilbert transform to obtain the instantaneous phase. The second approach to phase synchrony computes a time-varying complex energy spectrum using the continuous wavelet transform (CWT) with a complex Morlet wavelet [40]. The main drawback of this measure is the nonuniform time-frequency tiling where the frequency resolution is high at low frequencies and low at high frequencies. Although this property is desirable in detecting high frequency transients in a given signal, it inherently imposes a non-uniform time-frequency resolution which results in biased energy and phase estimates. In this paper, we propose to use a new time-varying phase estimation method based on the Reduced Interference Rihaczek (RID-Rihaczek) distribution belonging to Cohen's class [38]. This distribution offers phase estimates with uniformly high time-frequency resolution which can be used for defining time-

and frequency-dependent phase synchrony. Compared to the existing measures, in our previous work we have shown through both simulation and analysis that RID-Rihaczek-based phase and phase synchrony estimators are more robust to noise, have uniformly better time-frequency resolution with less bias in extracting time- and frequency-dependent phase, and perform superior at detecting actual synchrony within a group of oscillators [38].

It is important to note some limitations of PLV that have been investigated in recent work, specifically in the context of intertrial phase synchrony [41]. Specifically, the PLV cannot discriminate between additive versus phase-resetting activation in ERPs from trial to trial, and thus is not a reliable measure for studying event-related brain dynamics (ERBD [42]). Some recent approaches based on t-statistics type measures from complex time-frequency distribution coefficients offer some methods to decompose constituent contributions of amplitude and phase resetting to the PLV for intertrial measures [43]. However, it is not clear what role these components have in PLV when measuring functional connectivity.

*2.1. RID-Rihaczek Distribution.* Rihaczek distribution is a complex time-frequency distribution that provides both a time-varying energy spectrum as well as a phase spectrum with good time-frequency localization for phase modulated signals [44] and is defined as

$$C_i(t, \omega) = \frac{1}{\sqrt{2\pi}} x_i(t) X_i^*(\omega) e^{-j\omega t}, \quad (2)$$

where  $x_i(t)$  is the signal and  $X_i(\omega)$  is its Fourier transform. The time- and frequency dependent phase estimate based on this distribution can be found as

$$\Phi_i(t, \omega) = \arg \left[ \frac{C_i(t, \omega)}{|C_i(t, \omega)|} \right] = \phi_i(t) - \theta_i(\omega) - \omega t, \quad (3)$$

where  $\phi_i(t)$  and  $\theta_i(\omega)$  refer to the phase in the time and the frequency domains, respectively. Once the phase estimate in the time-frequency domain is obtained, the phase difference between two signals,  $x_i(t)$  and  $x_j(t)$ , can be computed as

$$\begin{aligned} \Phi_{i,j}(t, \omega) &= \arg \left[ \frac{C_i(t, \omega)}{|C_i(t, \omega)|} \frac{C_j^*(t, \omega)}{|C_j(t, \omega)|} \right] \\ &= (\phi_i(t) - \phi_j(t)) - (\theta_i(\omega) - \theta_j(\omega)). \end{aligned} \quad (4)$$

For multicomponent signals, cross-terms occur at the same time- and frequency locations as the original signals and will lead to biased energy and phase estimates. In order to eliminate these cross-terms, we proposed a reduced interference version of the Rihaczek-distribution, which is referred to as RID-Rihaczek, by applying a Choi-Williams

(CW) kernel function to filter the cross-terms in the ambiguity domain [45, 46]:

$$C_i(t, \omega) = \int \int \underbrace{\exp\left(-\frac{(\theta\tau)^2}{\sigma}\right)}_{\text{CW kernel}} \underbrace{\exp\left(j\frac{\theta\tau}{2}\right)}_{\text{Rihaczek kernel}} A(\theta, \tau) e^{-j(\theta t + \tau\omega)} d\tau d\theta, \quad (5)$$

where  $\exp(j(\theta\tau/2))$  is the kernel function for the Rihaczek distribution and  $A(\theta, \tau) = \int x_i(u + \tau/2)x_i^*(u - \tau/2)e^{j\theta u} du$  is the ambiguity function of the signal,  $x_i(t)$ .

### 3. Dynamic Network Summarization

Let  $G = \{G_t\}_{t=1,2,\dots,T}$  be a time sequence of weighted and undirected graphs where  $G_t$  is an  $N \times N$  weighted and undirected graph at time  $t$ ,  $T$  is the total number of time points, and  $N$  is the number of nodes within the network. The connectivity strength or the edge between nodes  $i$  and  $j$  at time  $t$  is represented by  $G_t(i, j)$  and is in the range of  $[0, 1]$ .

We propose a dynamic graph summarization framework consisting of constructing time-varying graphs from pairwise phase synchrony measure, identifying event windows, revealing the most important and informative connectivity patterns to summarize each event window with a key graph and to describe the dynamic evolution of the network over time.

**3.1. Forming Time-Varying Graphs via Phase Synchronization.** In order to describe the evolution of time-varying connectivity patterns in the brain network, we first need to obtain the time-varying graphs. We quantify the bivariate relationship between nodes within the network and construct the time-varying graphs by considering the average synchrony within a frequency band at a certain time as

$$G_t(i, j) = \frac{1}{W} \sum_{\omega=\omega_a}^{\omega_b} \text{PLV}_{i,j}(t, \omega), \quad (6)$$

where  $G_t(i, j)$  represents the connectivity strength between the nodes  $i$  and  $j$  within the frequency band of interest,  $[\omega_a, \omega_b]$ , and  $W$  is the number of frequency bins in that band. In this paper, our focus is to evaluate the dynamics of the networks over time and the proposed framework is designed accordingly. However, one can extend this framework to consider each time and frequency bin separately to evaluate the network changes over both time and frequency.

**3.2. Event Interval Detection.** Once the time-varying graphs are obtained, we need to identify meaningful time intervals which may account for the underlying neurophysiological events such as error-related negativity or Pe event-related potential elicited in the process of decision making. For this purpose, we propose to quantify the change in node  $i$ 's

connectivity with other nodes from time point  $t$  to  $t + 1$  as

$$d_{t,t+1}(i) = \|g_i(t+1) - g_i(t)\|_{\infty} = \max_k \left\{ \left| g_i^k(t+1) - g_i^k(t) \right| \right\}, \quad k = 1, 2, \dots, N, \quad (7)$$

where  $g_i^k(t)$  is the  $k$ th element of  $i$ th row of  $G_t$  and  $d_{t,t+1}(i)$  is in the range of  $[0, 1]$ .  $l_{\infty}$  norm highlights the maximum change in a node's connectivity from time  $t$  to  $t + 1$  instead of the average change in the node's connectivity and, thus, is better at filtering out connections that are insignificant for that particular node. The average distance,  $D_{t,t+1}$ , between the graphs  $G_t$  and  $G_{t+1}$  is then defined as

$$D_{t,t+1} = \frac{1}{N} \sum_{i=1}^N d_{t,t+1}(i). \quad (8)$$

In order to detect the abrupt changes in the distance measure  $D_{t,t+1}$  at any time, we propose to employ a standard change detection algorithm based on adaptive thresholding:

$$I(t, t+1) = \begin{cases} 1, & \text{if } |D_{t,t+1} - \mu_t| \geq 2\sigma_t \\ 0, & \text{if } |D_{t,t+1} - \mu_t| < 2\sigma_t, \end{cases} \quad (9)$$

where an event boundary is detected,  $I(t, t+1) = 1$ , depending on the deviation of  $D_{t,t+1}$  from the moving average,  $\mu_t = (1/\delta) \sum_{k=1}^{\delta} D_{t-k, t-k+1}$ . Adaptive thresholding value,  $2\sigma_t$ , is based on the standard deviation,  $\sigma_t = \sqrt{(1/\delta) \sum_{k=1}^{\delta} (D_{t-k, t-k+1} - \mu_t)^2}$ , and the length of the moving average window,  $\delta$ , can be chosen based on the sampling frequency and total number of time samples,  $T$ .

**3.3. Key Graph Estimation Using Principal Component Analysis.** After determining the event intervals, we need to form key graphs which best summarize the particular intervals. For this purpose, we need to distinguish between transient (high variance) and stationary (low variance) interactions within a given time interval and obtain a key graph which captures the transient or dynamic interactions. The ideal key graph should describe dynamic behavior of the particular interval with minimal redundancy. This is analogous to finding signal components that have low and high variance in a given data set and this separation in terms of variance is usually addressed through principal component analysis (PCA). Hence, we propose to employ PCA in order to extract key graphs and summarize the dynamics of the event intervals with minimal redundancy.

Let  $G_1, G_2, \dots, G_M$  be the set of  $M$  graphs that compose an event interval that we try to summarize. Since the graphs are undirected and symmetric, we create vectors,  $\mathbf{z}_1, \dots, \mathbf{z}_M$ , to equivalently represent the graphs where  $\mathbf{z}_i$  is obtained by stacking the columns of the upper triangular portion of  $G_i$  and has the dimensions  $\binom{N}{2}$

by 1. Hence, we compute the sample covariance matrix as:

$$\mathbf{C} = \frac{1}{M-1} \sum_{i=1}^M (\mathbf{z}_i - \bar{\mathbf{z}})(\mathbf{z}_i - \bar{\mathbf{z}})^T, \quad (10)$$

where  $\bar{\mathbf{z}} = 1/M \sum_{i=1}^M \mathbf{z}_i$ .

Let the eigenvalues of the  $\binom{N}{2} \times \binom{N}{2}$  matrix  $\mathbf{C}$  be denoted by  $\lambda_1, \dots, \lambda_{\binom{N}{2}}$  and arranged in decreasing order,  $\lambda_1 \geq \lambda_2 \geq \dots \geq \lambda_{\binom{N}{2}}$ , so that  $\lambda_1 = \lambda_{\max}$ . The associated eigenvectors are used to construct an  $\binom{N}{2} \times \binom{N}{2}$  matrix  $\mathbf{V} = [\mathbf{v}_1, \dots, \mathbf{v}_{\binom{N}{2}}]$ . We can then write the eigendecomposition equation as  $\mathbf{CV} = \mathbf{V}\Lambda$  where  $\Lambda$  is a diagonal matrix defined by the eigenvalues of matrix  $\mathbf{C}$ .

In order to ensure minimal redundancy, we need to project the original data set,  $\mathbf{z}_1, \dots, \mathbf{z}_M$ , onto a few principal components which correspond to the eigenvectors,  $[\mathbf{v}_1, \dots, \mathbf{v}_L]$ , with the largest  $L$  eigenvalues such that

$$\frac{\sum_{i=1}^L \lambda_i}{\sum_{i=1}^{\binom{N}{2}} \lambda_i} \times 100 \geq \xi \quad (11)$$

the cumulative energy represented by these principal components account for some certain percentage,  $\xi$ , of the total energy in the data set. In this paper, we use  $\xi = 90\%$  to obtain a projected set of vectors as

$$\mathbf{p}_i = [\mathbf{v}_1, \dots, \mathbf{v}_L]^T \mathbf{z}_i, \quad i = 1, \dots, M. \quad (12)$$

The projected vectors are transformed to the original space as

$$\begin{aligned} \tilde{\mathbf{z}}_i &= [\mathbf{v}_1, \dots, \mathbf{v}_L] \mathbf{p}_i \\ &= [\mathbf{v}_1, \dots, \mathbf{v}_L] [\mathbf{v}_1, \dots, \mathbf{v}_L]^T \mathbf{z}_i. \end{aligned} \quad (13)$$

Hence, the new set of vectors,  $\tilde{\mathbf{z}}_1, \dots, \tilde{\mathbf{z}}_M$ , conserves 90% of the total energy within the particular event interval and contains only the most relevant information about the network dynamics. For each event interval, we compute the mean vector:

$$\tilde{\mathbf{z}} = \frac{1}{M} \sum_{i=1}^M \tilde{\mathbf{z}}_i, \quad (14)$$

which will be reshaped such that it constitutes the upper triangular part of the symmetric key graph.

**3.4. Significance Testing for the Key Graph Estimation.** Since the distribution of the interactions under the null hypothesis which form a key graph for a particular interval cannot be obtained analytically, we resort to generating random networks to derive this distribution. For each key graph extracted for a given time interval, we derived an ensemble of 2000 surrogate time-varying networks by randomly reshuffling the edge weights [15]. The key graph estimation algorithm is applied to each surrogate time-varying graph set in each interval which resulted in 2000 surrogate key

graphs. In order to compare the original key graphs with the ones obtained from the surrogate data sets, we selected two different  $P$ -values,  $P < 0.01$  and  $P < 0.001$ , to determine the significant interactions at 99% and 99.9% significance levels, respectively.

## 4. Data

**4.1. EEG Data.** To evaluate the performance of the proposed measure in summarizing the event intervals with biological data, we use a set of EEG data containing the error-related negativity (ERN). The ERN is an event-related potential that occurs following performance errors in a speeded reaction time task [47, 48]. The ERN is observed as a sharp negative trend in EEG recordings which typically peaks from 75–80 ms after the error response. Previously reported EEG data from 62 channels were utilized [49]. This study included 90 (34 male) undergraduate students. (Two of the original 92 participants were dropped due to artifacts rendering computation of the PLV values problematic.) Full methodological details of the recording are available in the previous report [49]. The task was a common speeded-response letter (H/S) flanker, where error and correct response-locked trials from each subject were utilized. A random subset of correct trials was selected, to equate the number of errors relative to correct trials for each participant. Before computing the phase-synchrony measures, all EEG epochs were converted to current source density (CSD) using published methods [50, 51]. This was done to accentuate local activity (e.g., to better index small world properties) and to attenuate distal activity (e.g., volume conduction).

There has been longstanding interest in time-frequency representations of the ERN [36, 52, 53]. It has now been established that the time-frequency energy in the ERN occurs in the theta band (4–8 Hz) of the EEG, occurring medial frontally. This activity has been shown to have primary sources in the anterior cingulate cortex (ACC) [54–56]. Observations of similar theta activity across a number of different tasks has been reported, suggesting that midline frontal theta activity may serve related roles across a number of cognitive processes [57]. New attention has been focused on the functional connectivity occurring during the ERN, to better understand the role of medial-frontal theta activity in functional networks subserving cognitive control. Cavanagh and colleagues [58], for example, found evidence that lateral-prefrontal cortex (LPFC) activity was phase synchronous with medial-frontal theta, supporting the idea that medial-prefrontal (mPFC) and LPFC regions are functionally integrated during error processing. By assessing medial-frontal regions active during the ERN in relation to diffusion tensor imaging (DTI), new work has also helped demonstrate how mPFC regions are highly integrated with other prefrontal areas during control processing [59]. Together, advances in this area support the view that medial-frontal sources serve as a central region of activity during error processing, and that phase-synchrony measures of theta activity can index this functional integration. At the same time, work in this area is nascent, and new research into

the nature of this functional integration is important. The proposed approach is a graph-based data-driven approach to characterizing functional connectivity, and can offer a new look at network patterns occurring during the ERN. Thus, while the primary aims of the current report are methodological (i.e., developing a method for characterizing time-varying graphs), we hypothesize that the medial-frontal region will play a central functional role during the ERN, and will have significant integration with frontal areas, including lateral frontal. Such findings can offer support that the proposed time-varying graph approach produces effects consistent with current theoretical and empirical work in the field.

## 5. Results

**5.1. Event Intervals.** In this paper, we analyzed data from 90 subjects corresponding to the error responses. For each subject, time- and frequency dependent phase synchrony between all possible electrode pairs is computed by RID-Rihaczek-based PLV measure and time-varying graphs,  $G_t^{(q)}$ ,  $t = 1, \dots, 256$ , for the  $q$ th subject are constructed using (6) where the number of nodes,  $N$ , is equal to 62, the frequency band of interest is the theta band (4–8 Hz), and the sampling frequency is 128 Hz. Furthermore, a mean time-varying graph sequence,  $\bar{G}_t$ , is computed over all subjects as

$$\bar{G}_t = \frac{1}{90} \sum_{q=1}^{90} G_t^{(q)}, \quad (15)$$

and the event interval detection algorithm is applied to this average sequence,  $\bar{G}_t$ , where the length of the moving average window,  $\delta$ , is chosen as 2.5% of the sampling period. The value of  $\delta$  is selected such that the window length is able to both detect the abrupt changes in the connectivity patterns and prevent oversmoothing. Different values of moving average window can be chosen depending on the sampling frequency or the application type. We identified 6 different key event intervals based on the proposed change detection algorithm which roughly correspond to the stimulus processing (–1000 to –102 ms), pre-ERN (–101 to 0 ms), ERN (1 to 117 ms), post-ERN (118 to 259 ms), Pe (260 to 461 ms), and intertrial (462 to 1000 ms) intervals, respectively, as shown in Figure 1.

The detected event intervals are consistent with the speeded reaction-time task as the subjects respond to the stimulus at time 0 ms. The first interval indexes complex processing of the imperative stimulus before making a response. The Pre-ERN and Post-ERN intervals, just before and after the ERN, index activity around the incorrect motor response. Importantly, the ERN interval (117 ms time window after the response) and Pe interval (260–461 ms time window) are detected successfully by the event detection algorithm. The Pe (error-positivity) interval corresponds to a P3-like component observed subsequent to the incorrect response [60, 61]. However, measures of P3 energy generally show activity in lower frequency delta bands (e.g., [62–65]), rather than the currently measured theta activity.

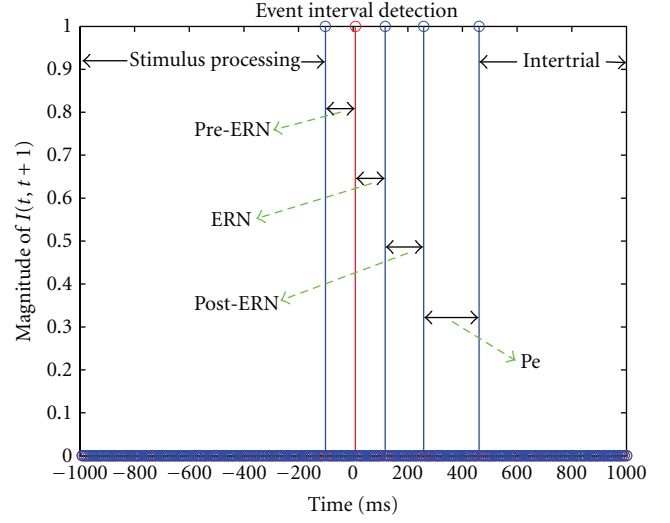


FIGURE 1: Event interval detection: 6 event intervals are identified which roughly correspond to the stimulus processing (–1000 to –102 ms), pre-ERN (–101 to 0 ms), ERN (1 to 117 ms), post-ERN (118 to 259 ms), Pe (260 to 461 ms), and intertrial (462 to 1000 ms) intervals, respectively. The subjects respond to the stimulus at time 0 ms where the response is represented by the red spike.

**5.2. Key Graphs.** For each event interval detected from the mean time-varying graph sequence,  $\bar{G}_t$ ,  $M$  vectors,  $\mathbf{z}_1, \dots, \mathbf{z}_M$ , corresponding to the upper triangular part of the graph, sequences in that interval are formed and the  $\binom{N}{2} \times \binom{N}{2}$  covariance matrix is computed as given in (10) where  $M$  corresponds to the number of graphs that compose the particular event interval and  $N$  is the number of nodes within the network ( $N = 62$ ). Note that  $M$  will change for each time interval. For instance, for this particular study  $M = 115$  for the stimulus processing,  $M = 13$  for the pre-ERN,  $M = 15$  for the ERN,  $M = 18$  for the post-ERN,  $M = 26$  for the Pe and  $M = 69$  for the inter-trial intervals. The  $L$  largest eigenvalues for that event interval are selected such that a 90% energy threshold is satisfied using (11). A corresponding mean vector,  $\bar{\mathbf{z}}$ , which constitutes the upper triangular part of the symmetric key graph for the particular event interval is obtained using (14). Furthermore, we compared the extracted key graphs with the ones obtained from the surrogate time-varying graphs and identified the interactions which are statistically significant as described in Section 3.4. For each event interval, Figure 2 shows the interactions which are significant at two different significance levels where the interactions with  $P < 0.01$  and  $P < 0.001$  are represented in blue and red colors, respectively. As one can see from Figure 2, ERN interval has much more significant connections compared to the Pre-ERN and Post-ERN intervals as expected because of the complex activity associated with the error commission. In particular, the frontal electrodes (F5, FZ, F2, and F4) have significant connections with the central electrode (FCz) with  $P < 0.001$ , consistent with previously observed interactions in theta band between medial prefrontal cortex (mPFC) and lateral prefrontal cortex (lPFC) during error-related cognitive

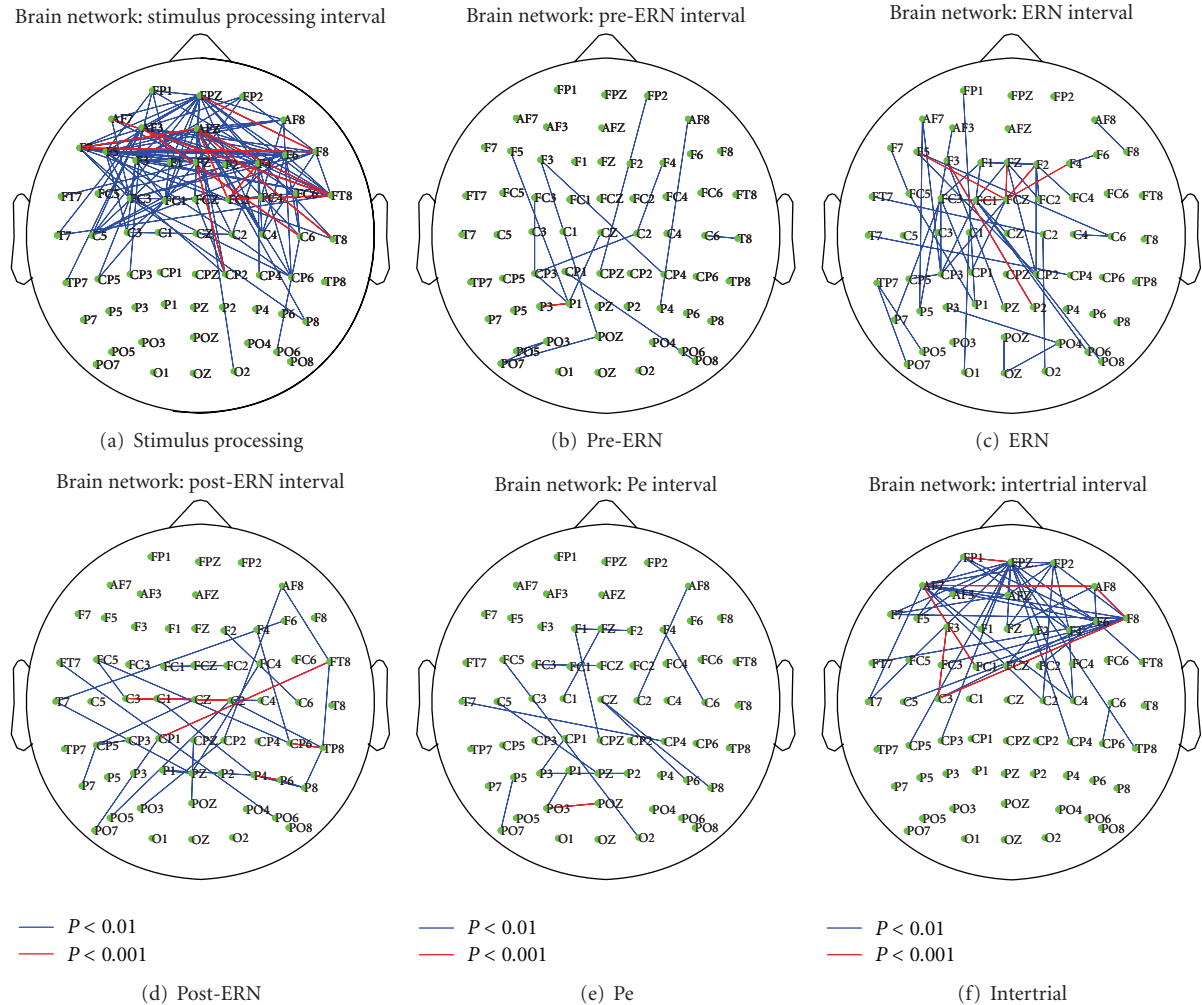


FIGURE 2: For each event interval, a key graph is obtained using the framework described in Section 3. We compared the extracted key graphs with the ones obtained from the surrogate time-varying graphs and identified the interactions which are significant. Using each key graph, the interactions which are found to be significant at two different levels,  $P < 0.01$  and  $P < 0.001$ , are represented in blue and red colors, respectively.

control processes [58], whereas the other event intervals do not include such interactions among frontal and central sites. During the Pe, on the other hand, we observe significant connections only among the parietal and occipital-parietal electrodes with  $P < 0.01$  and  $P < 0.001$ . Hypotheses about theta activity during the Pe are underdeveloped in the literature, because P3-related activity generally occurs at lower frequencies (e.g., 0–3 Hz, as described above). Thus, while the observed pattern of effects could be interpreted, it is more reasonable to note that this interval contains the fewest connections between nodes among the identified intervals.

We also focused on the change in connectivity for FCz electrode with the remaining 61 electrodes within the key graphs for Pre-ERN, ERN, and Post-ERN intervals and compared these connectivity values to identify if FCz has stronger connectivity during the ERN interval compared to the Pre-ERN and Post-ERN intervals. We used a Welch's  $t$ -test at 5% significance level to test the null hypothesis that the connectivity strengths from different key graphs

are independent random samples from normal distributions with equal means. For both comparisons, Pre-ERN versus ERN and Post-ERN versus ERN, the null hypothesis is rejected where FCz has a larger mean connectivity for the ERN interval indicating that the central electrode has significantly larger connectivity with the rest of the brain during the ERN interval. Moreover, we compared the connectivity values for Pre-ERN and Post-ERN where there is no significant difference between the connectivity values from these intervals.

## 6. Conclusions

In this paper, we proposed a new framework to summarize the dynamic evolution of brain networks. The proposed approach is based on finding the event intervals and revealing the informative transient or dynamic interactions within each interval such that the key graph would summarize

the particular interval with minimal redundancy. Expectable results from the application to real EEG data containing the ERN supports the effectiveness of the proposed framework in determining the event intervals of dynamic brain networks and summarizing network activity with a few number of representative networks.

Future work will concentrate on exploring different event interval detection and key graph extraction criteria such as entropy-based divergence measures and Bayesian approaches such as the one discussed in [37], which may result in an improved performance in summarizing dynamic networks. Furthermore, the proposed framework will be extended to compare the dynamic nature of functional networks for error and correct responses to get a more complete understanding of cognitive control. In addition, we will employ the proposed framework to analyze data in other frequency bands including delta, which may be more central to activity during the Pe interval. Future work will also consider exploring single-dipole [56, 66] and distributed-dipole [67] source solutions to the inverse problem for extending our proposed dynamic functional connectivity analysis framework to the source domain. Finally, we will explore different group analysis methods to consider the variability across individual subjects and possibly reveal the distinctive network features for each subject rather than averaging the time-varying graphs from all subjects.

## Acknowledgment

This work was in part supported by the National Science Foundation under Grant no. CAREER CCF-0746971.

## References

- [1] O. Sporns, D. R. Chialvo, M. Kaiser, and C. C. Hilgetag, "Organization, development and function of complex brain networks," *Trends in Cognitive Sciences*, vol. 8, no. 9, pp. 418–425, 2004.
- [2] E. Bullmore and O. Sporns, "Complex brain networks: graph theoretical analysis of structural and functional systems," *Nature Reviews Neuroscience*, vol. 10, no. 3, pp. 186–198, 2009.
- [3] M. A. Koch, D. G. Norris, and M. Hund-Georgiadis, "An investigation of functional and anatomical connectivity using magnetic resonance imaging," *NeuroImage*, vol. 16, no. 1, pp. 241–250, 2002.
- [4] G. Gong, Y. He, L. Concha et al., "Mapping anatomical connectivity patterns of human cerebral cortex using in vivo diffusion tensor imaging tractography," *Cerebral Cortex*, vol. 19, no. 3, pp. 524–536, 2009.
- [5] K. Friston, "Functional and effective connectivity: a review," *Brain Connectivity*, vol. 1, no. 1, pp. 13–36, 2011.
- [6] P. A. Valdes-Sosa, A. Roebroeck, J. Daunizeau, and K. Friston, "Effective connectivity: influence, causality and biophysical modeling," *NeuroImage*, vol. 58, no. 2, pp. 339–361, 2011.
- [7] K. J. Friston, "Functional and effective connectivity in neuroimaging: a synthesis," *Human Brain Mapping*, vol. 2, no. 1-2, pp. 56–78, 1994.
- [8] C. J. Stam, "Nonlinear dynamical analysis of EEG and MEG: review of an emerging field," *Clinical Neurophysiology*, vol. 116, no. 10, pp. 2266–2301, 2005.
- [9] E. Pereda, R. Q. Quiroga, and J. Bhattacharya, "Nonlinear multivariate analysis of neurophysiological signals," *Progress in Neurobiology*, vol. 77, no. 1-2, pp. 1–37, 2005.
- [10] S. Achard, R. Salvador, B. Whitcher, J. Suckling, and E. Bullmore, "A resilient, low-frequency, small-world human brain functional network with highly connected association cortical hubs," *Journal of Neuroscience*, vol. 26, no. 1, pp. 63–72, 2006.
- [11] D. S. Bassett and E. Bullmore, "Small-world brain networks," *Neuroscientist*, vol. 12, no. 6, pp. 512–523, 2006.
- [12] D. S. Bassett, A. Meyer-Lindenberg, S. Achard, T. Duke, and E. Bullmore, "Adaptive reconfiguration of fractal small-world human brain functional networks," *Proceedings of the National Academy of Sciences of the United States of America*, vol. 103, no. 51, pp. 19518–19523, 2006.
- [13] O. Sporns, C. J. Honey, and R. Kötter, "Identification and classification of hubs in brain networks," *PLoS ONE*, vol. 2, no. 10, Article ID e1049, 2007.
- [14] C. J. Stam, B. F. Jones, G. Nolte, M. Breakspear, and P. Scheltens, "Small-world networks and functional connectivity in Alzheimer's disease," *Cerebral Cortex*, vol. 17, no. 1, pp. 92–99, 2007.
- [15] C. J. Stam, W. De Haan, A. Daffertshofer et al., "Graph theoretical analysis of magnetoencephalographic functional connectivity in Alzheimer's disease," *Brain*, vol. 132, no. 1, pp. 213–224, 2009.
- [16] D. J. Watts and S. H. Strogatz, "Collective dynamics of 'small-world' networks," *Nature*, vol. 393, no. 6684, pp. 440–442, 1998.
- [17] K. Supekar, V. Menon, D. Rubin, M. Musen, and M. D. Greicius, "Network analysis of intrinsic functional brain connectivity in Alzheimer's disease," *PLoS Computational Biology*, vol. 4, no. 6, Article ID e1000100, 2008.
- [18] C. J. Stam, M. Breakspear, A. M. Van Cappellen van Walsum, and B. W. Van Dijk, "Nonlinear synchronization in EEG and whole-head MEG recordings of healthy subjects," *Human Brain Mapping*, vol. 19, no. 2, pp. 63–78, 2003.
- [19] L. Douw, M. M. Schoonheim, D. Landi et al., "Cognition is related to resting-state small-world network topology: a magnetoencephalographic study," *Neuroscience*, vol. 175, pp. 169–177, 2011.
- [20] C. J. Stam, T. Montez, B. F. Jones et al., "Disturbed fluctuations of resting state EEG synchronization in Alzheimer's disease," *Clinical Neurophysiology*, vol. 116, no. 3, pp. 708–715, 2005.
- [21] M. Valencia, J. Martinerie, S. Dupont, and M. Chavez, "Dynamic small-world behavior in functional brain networks unveiled by an event-related networks approach," *Physical Review E*, vol. 77, no. 5, Article ID 050905, 2008.
- [22] S. I. Dimitriadis, N. A. Laskaris, V. Tsirka, M. Vourkas, S. Micheloyannis, and S. Fotopoulos, "Tracking brain dynamics via time-dependent network analysis," *Journal of Neuroscience Methods*, vol. 193, no. 1, pp. 145–155, 2010.
- [23] F. De Vico Fallani, L. Astolfi, F. Cincotti et al., "Cortical functional connectivity networks in normal and spinal cord injured patients: evaluation by graph analysis," *Human Brain Mapping*, vol. 28, no. 12, pp. 1334–1346, 2007.
- [24] M. Rubinov and O. Sporns, "Complex network measures of brain connectivity: uses and interpretations," *NeuroImage*, vol. 52, no. 3, pp. 1059–1069, 2010.
- [25] A. Casteigts, P. Flocchini, W. Quattrociocchi, and N. Santoro, "Time-varying graphs and dynamic networks," *Ad-hoc, Mobile, and Wireless Networks*, vol. 6811, pp. 346–359, 2011.
- [26] P. Basu, A. Bar-Noy, R. Ramanathan, and M. Johnson, "Modeling and analysis of time-varying graphs," Arxiv preprint arXiv:1012.0260, 2010.

- [27] V. Nicosia, J. Tang, M. Musolesi, G. Russo, C. Mascolo, and V. Latora, "Components in time-varying graphs," Arxiv preprint arXiv:1106.2134, 2011.
- [28] P. J. Mucha, T. Richardson, K. Macon, M. A. Porter, and J. P. Onnela, "Community structure in time-dependent, multi-scale, and multiplex networks," *Science*, vol. 328, no. 5980, pp. 876–878, 2010.
- [29] J. Tang, S. Scellato, M. Musolesi, C. Mascolo, and V. Latora, "Small-world behavior in time-varying graphs," *Physical Review E*, vol. 81, no. 5, Article ID 055101, 2010.
- [30] N. Santoro, W. Quattrociochi, P. Flocchini, A. Casteigts, and F. Amblard, "Time-varying graphs and social network analysis: temporal indicators and metrics," Arxiv preprint arXiv:1102.0629, 2011.
- [31] M. Chavez, M. Valencia, V. Latora, and J. Martinerie, "Complex networks: new trends for the analysis of brain connectivity," *International Journal of Bifurcation and Chaos*, vol. 20, no. 6, pp. 1677–1686, 2010.
- [32] B. Miller, M. Beard, and N. Bliss, "Matched filtering for subgraph detection in dynamic networks," in *Proceedings of the IEEE Statistical Signal Processing Workshop (SSP '11)*, pp. 509–512, 2011.
- [33] K. Xu, M. Klinger, and A. Hero, "A shrinkage approach to tracking dynamic networks," in *Proceedings of the IEEE Statistical Signal Processing Workshop (SSP '11)*, pp. 517–520, 2011.
- [34] C. Cortes, D. Pregibon, and C. Volinsky, "Computational methods for dynamic graphs," *Journal of Computational and Graphical Statistics*, vol. 12, no. 4, pp. 950–970, 2003.
- [35] H. Tong, S. Papadimitriou, P. S. Yu, and C. Faloutsos, "Proximity tracking on time-evolving bipartite graphs," in *8th SIAM International Conference on Data Mining 2008, Applied Mathematics 130*, pp. 704–715, usa, April 2008.
- [36] E. M. Bernat, W. J. Williams, and W. J. Gehring, "Decomposing ERP time-frequency energy using PCA," *Clinical Neurophysiology*, vol. 116, no. 6, pp. 1314–1334, 2005.
- [37] J. L. Marroquin, T. Harmony, V. Rodriguez, and P. Valdes, "Exploratory EEG data analysis for psychophysiological experiments," *NeuroImage*, vol. 21, no. 3, pp. 991–999, 2004.
- [38] S. Aviyente and A. Y. Mutlu, "A time-frequency-based approach to phase and phase synchrony estimation," *IEEE Transactions on Signal Processing*, vol. 59, no. 7, pp. 3086–3098, 2011.
- [39] P. Tass, M. G. Rosenblum, J. Weule et al., "Detection of n:m phase locking from noisy data: application to magnetoencephalography," *Physical Review Letters*, vol. 81, no. 15, pp. 3291–3294, 1998.
- [40] J. P. Lachaux, A. Lutz, D. Rudrauf et al., "Estimating the time-course of coherence between single-trial brain signals: an introduction to wavelet coherence," *Neurophysiologie Clinique*, vol. 32, no. 3, pp. 157–174, 2002.
- [41] J. Krieg, A. Trébuchon-Da Fonseca, E. Martínez-Montes, P. Marquis, C. Liégeois-Chauvel, and C. G. Bénar, "A comparison of methods for assessing alpha phase resetting in electrophysiology, with application to intracerebral EEG in visual areas," *NeuroImage*, vol. 55, no. 1, pp. 67–86, 2011.
- [42] S. Makeig, S. Debener, J. Onton, and A. Delorme, "Mining event-related brain dynamics," *Trends in Cognitive Sciences*, vol. 8, no. 5, pp. 204–210, 2004.
- [43] E. Martínez-Montes, E. R. Cuspineda-Bravo, W. El-Deredy, J. M. Sánchez-Bornot, A. Lage-Castellanos, and P. A. Valdés-Sosa, "Exploring event-related brain dynamics with tests on complex valued time-frequency representations," *Statistics in Medicine*, vol. 27, no. 15, pp. 2922–2947, 2008.
- [44] A. Rihaczek, "Signal energy distribution in time and frequency," *IEEE Transactions on Information Theory*, vol. 14, no. 3, pp. 369–374, 1968.
- [45] S. Aviyente, E. M. Bernat, S. M. Malone, and W. G. Iacono, "Time-frequency data reduction for event related potentials: combining principal component analysis and matching pursuit," *Eurasip Journal on Advances in Signal Processing*, vol. 2010, Article ID 289571, 4 pages, 2010.
- [46] S. Aviyente, E. M. Bernat, W. S. Evans, and S. R. Sponheim, "A phase synchrony measure for quantifying dynamic functional integration in the brain," *Human Brain Mapping*, vol. 32, no. 1, pp. 80–93, 2011.
- [47] M. Falkenstein, J. Hohnsbein, J. Hoormann, and L. Blanke, "Effects of crossmodal divided attention on late ERP components. II. Error processing in choice reaction tasks," *Electroencephalography and Clinical Neurophysiology*, vol. 78, no. 6, pp. 447–455, 1991.
- [48] W. Gehring, B. Goss, M. Coles, D. Meyer, and E. Donchin, "A neural system for error detection and compensation," *Psychological Science*, vol. 4, no. 6, pp. 385–390, 1993.
- [49] J. R. Hall, E. M. Bernat, and C. J. Patrick, "Externalizing psychopathology and the error-related negativity," *Psychological Science*, vol. 18, no. 4, pp. 326–333, 2007.
- [50] J. Kayser and C. E. Tenke, "Principal components analysis of Laplacian waveforms as a generic method for identifying ERP generator patterns: I. Evaluation with auditory oddball tasks," *Clinical Neurophysiology*, vol. 117, no. 2, pp. 348–368, 2006.
- [51] J. Kayser and C. E. Tenke, "Principal components analysis of Laplacian waveforms as a generic method for identifying ERP generator patterns: II. Adequacy of low-density estimates," *Clinical Neurophysiology*, vol. 117, no. 2, pp. 369–380, 2006.
- [52] P. Luu, P. Luu, and D. M. Tucker, "Regulating action: alternating activation of midline frontal and motor cortical networks," *Clinical Neurophysiology*, vol. 112, no. 7, pp. 1295–1306, 2001.
- [53] L. T. Trujillo and J. J. B. Allen, "Theta EEG dynamics of the error-related negativity," *Clinical Neurophysiology*, vol. 118, no. 3, pp. 645–668, 2007.
- [54] E. Y. Hochman, Z. Eviatar, Z. Breznitz, M. Nevat, and S. Shaul, "Source localization of error negativity: additional source for corrected errors," *NeuroReport*, vol. 20, no. 13, pp. 1144–1148, 2009.
- [55] W. H. R. Miltner, C. H. Braun, and M. G. H. Coles, "Event-related brain potentials following incorrect feedback in a time-estimation task: evidence for a 'generic' neural system for error detection," *Journal of Cognitive Neuroscience*, vol. 9, no. 6, pp. 788–798, 1997.
- [56] S. Dehaene, M. Posner, and D. Tucker, "Localization of a neural system for error detection and compensation," *Psychological Science*, vol. 5, no. 5, pp. 303–305, 1994.
- [57] J. Cavanagh, L. Zambrano-Vazquez, and J. Allen, "Theta lingua franca: a common mid-frontal substrate for action monitoring processes," *Psychophysiology*, vol. 49, no. 2, pp. 220–238, 2012.
- [58] J. F. Cavanagh, M. X. Cohen, and J. J. B. Allen, "Prelude to and resolution of an error: EEG phase synchrony reveals cognitive control dynamics during action monitoring," *Journal of Neuroscience*, vol. 29, no. 1, pp. 98–105, 2009.
- [59] M. X. Cohen, "Error-related medial frontal theta activity predicts cingulate-related structural connectivity," *NeuroImage*, vol. 55, no. 3, pp. 1373–1383, 2011.
- [60] H. Leuthold and W. Sommer, "ERP correlates of error processing in spatial S-R compatibility tasks," *Clinical Neurophysiology*, vol. 110, no. 2, pp. 342–357, 1999.

- [61] T. J. M. Overbeek, S. Nieuwenhuis, and K. R. Ridderinkhof, "Dissociable components of error processing: on the functional significance of the Pe vis-à-vis the ERN/Ne," *Journal of Psychophysiology*, vol. 19, no. 4, pp. 319–329, 2005.
- [62] E. M. Bernat, S. M. Malone, W. J. Williams, C. J. Patrick, and W. G. Iacono, "Decomposing delta, theta, and alpha time-frequency ERP activity from a visual oddball task using PCA," *International Journal of Psychophysiology*, vol. 64, no. 1, pp. 62–74, 2007.
- [63] T. Demiralp, A. Ademoglu, Y. I Stefanopulos, C. Başar-Eroglu, and E. Başar, "Wavelet analysis of oddball P300," *International Journal of Psychophysiology*, vol. 39, no. 2-3, pp. 221–227, 2000.
- [64] C. S. Gilmore, S. M. Malone, E. M. Bernat, and W. G. Iacono, "Relationship between the P3 event-related potential, its associated time-frequency components, and externalizing psychopathology," *Psychophysiology*, vol. 47, no. 1, pp. 123–132, 2010.
- [65] K. A. Jones, B. Porjesz, D. Chorlian et al., "S-transform time-frequency analysis of P300 reveals deficits in individuals diagnosed with alcoholism," *Clinical Neurophysiology*, vol. 117, no. 10, pp. 2128–2143, 2006.
- [66] C. M. Michel, M. M. Murray, G. Lantz, S. Gonzalez, L. Spinelli, and R. Grave De Peralta, "EEG source imaging," *Clinical Neurophysiology*, vol. 115, no. 10, pp. 2195–2222, 2004.
- [67] M. J. Herrmann, J. Römmeler, A. C. Ehlis, A. Heidrich, and A. J. Fallgatter, "Source localization (LORETA) of the error-related-negativity (ERN/Ne) and positivity (Pe)," *Cognitive Brain Research*, vol. 20, no. 2, pp. 294–299, 2004.

## Research Article

# Voxel Scale Complex Networks of Functional Connectivity in the Rat Brain: Neurochemical State Dependence of Global and Local Topological Properties

Adam J. Schwarz,<sup>1,2</sup> Alessandro Gozzi,<sup>1,3</sup> Alessandro Chessa,<sup>4,5</sup> and Angelo Bifone<sup>1,3</sup>

<sup>1</sup>Neurosciences Centre of Excellence in Drug Discovery, GlaxoSmithKline Medicines Research Centre, via Fleming 4, 37135 Verona, Italy

<sup>2</sup>Translational Medicine, Lilly Research Laboratories, Eli Lilly and Company, Indianapolis, IN 46285, USA

<sup>3</sup>Istituto Italiano di Tecnologia, Center for Nanotechnology Innovation @NEST, Piazza San Silvestro 12, 56127 Pisa, Italy

<sup>4</sup>Istituto dei Sistemi Complessi, Consiglio Nazionale delle Ricerche e Dipartimento di Fisica, Università “Sapienza”, Piazzale A. Moro 2, 00185 Rome, Italy

<sup>5</sup>Linkalab, Complex Systems Computational Laboratory, 09129 Cagliari, Italy

Correspondence should be addressed to Angelo Bifone, [angelo.bifone@iit.it](mailto:angelo.bifone@iit.it)

Received 27 March 2012; Revised 21 May 2012; Accepted 25 May 2012

Academic Editor: Fabrizio De Vico Fallani

Copyright © 2012 Adam J. Schwarz et al. This is an open access article distributed under the Creative Commons Attribution License, which permits unrestricted use, distribution, and reproduction in any medium, provided the original work is properly cited.

Network analysis of functional imaging data reveals emergent features of the brain as a function of its topological properties. However, the brain is not a homogeneous network, and the dependence of functional connectivity parameters on neuroanatomical substrate and parcellation scale is a key issue. Moreover, the extent to which these topological properties depend on underlying neurochemical changes remains unclear. In the present study, we investigated both global statistical properties and the local, voxel-scale distribution of connectivity parameters of the rat brain. Different neurotransmitter systems were stimulated by pharmacological challenge (*d*-amphetamine, fluoxetine, and nicotine) to discriminate between stimulus-specific functional connectivity and more general features of the rat brain architecture. Although global connectivity parameters were similar, mapping of local connectivity parameters at high spatial resolution revealed strong neuroanatomical dependence of functional connectivity in the rat brain, with clear differentiation between the neocortex and older brain regions. Localized foci of high functional connectivity independent of drug challenge were found in the sensorimotor cortices, consistent with the high neuronal connectivity in these regions. Conversely, the topological properties and node roles in subcortical regions varied with neurochemical state and were dependent on the specific dynamics of the different functional processes elicited.

## 1. Introduction

Functional connectivity analyses of neuroimaging data aim to elucidate relationships between signals originating in spatially distinct brain regions [1–7] as an indication of coordinated activity in distributed neural systems, an approach that complements the more established univariate approaches in which the responses in each brain region are analyzed independently. Consistent with this emphasis on interactions between distributed brain structures, neuroimaging data can be represented mathematically as a graph, or network, of nodes and links [8–11]. In this framework, image voxels or parcellated brain regions

represent the nodes and a measure of similarity in their responses defines the connections between them [7, 12–17].

Recent developments in the theory of complex networks have shown that the topological and statistical properties of networks can reveal fundamental behaviors of the systems that they model. For example, “small-world” topology, characterized by dense local clustering and few-long range connections [18, 19], can support connectivity at multiple spatial-scales while minimizing wiring costs. Another class of networks of particular interest is that of “scale-free” networks, that is, graphs presenting a power-law distribution of the node degree—the number of other nodes to which each node is connected. Scale-free networks appear to be

almost ubiquitous in real-world situations, including epidemiology, sociology, and cell biology, thus suggesting that their properties satisfy some general principle of efficiency, robustness and cost-effectiveness [18].

Brain functional connectivity is amenable to complex network analysis, and the interest in the statistical properties of these brain networks is growing rapidly [9–11]. The brain presents several features reminiscent of complex networks, including its ability to support both segregated and distributed information processing at multiple scales, its relative robustness to random neuronal loss due to disease or aging, and its efficiency in terms of low energy and wiring costs [20]. Indeed, functional connectivity networks constructed from human fMRI data under a finger tapping paradigm were shown to exhibit scale-free behavior, with the exponent of the power law robust to the specific choice of threshold [13]. Other authors [14] have reported an exponentially truncated power-law distribution for cortical functional connectivity in human subjects. More generally, “small-world” topology has been demonstrated in both “resting-state” functional [14, 16, 21, 22] and anatomical [23, 24] connectivity in the brain.

However, while global statistical parameters may be informative of large scale connectivity properties, they do not capture the heterogeneity of the brain. Indeed, different anatomical structures that evolved at different times may be characterized by different local network topology. Many studies thus far have employed volume of interest (VOI)-level parcellations and focused on cortico-cortical connections in humans and primates [14, 25–27], with less attention on the organization of subcortical networks and their connections to cortical structures. Recently, a voxel-scale analysis of human resting state data confirmed scale-free and small-world global properties of the resulting brain networks, and showed nodes of highest degree localized to regions in the cingulate and superior temporal cortices as well as the thalamus [28]. However, the extent to which the afore-mentioned graph-theoretic properties hold in the mammalian brain more generally has not, to date, been resolved. Another key question is the manner in which functional network properties are constrained by underlying anatomical connections and the relationship between their topological characteristics—an issue which has begun to be elucidated in humans [29–33], where perturbed resting functional network parameters in chronic disease states [16, 21, 22] may be closely coupled to disruptions in anatomical structure and connectivity [34]. In turn, the extent to which network properties are modulated by the active engagement of specific brain circuits has begun to receive attention [35]. In humans, there is evidence that global network structure is preserved in the presence of modified connectivity relationships due to performance of functional tasks [36, 37] or acute drug exposure [15].

In this paper, we report on a complex-network analysis characterizing voxel-scale topological properties of functional connectivity networks in the rat brain under distinct pharmacological conditions. In contrast to human fMRI studies, in which functional connectivity is typically probed in the brain’s resting state or in the context of cognitive tasks,

we examine characteristics of complex networks derived from the response of the rat brain to acute pharmacological challenge with three canonical drugs with distinct pharmacological mechanisms (*d*-amphetamine, fluoxetine, and nicotine), thus probing the dependence of functional connectivity network parameters on the engagement of different neurotransmitter systems. This approach, based on intersubject correlations, follows a procedure established in 2-DG autoradiography [38] and PET [39, 40] and validated in pharmacological MRI (phMRI) [6, 41–43]. Recent network-theoretic investigations of anatomical networks based on cortical gray matter thickness derived from MRI data have also employed this approach [23, 34]. Our aim was to work with explicit network representations of the data with nodes defined at the voxel rather than a regional parcellation scale and, in addition to node degree (the number of connections from a given node to others), to examine the node clustering coefficient (a measure of “cliquishness” in node connections). We mapped the anatomical distribution of these node parameters at single-voxel resolution to investigate at high spatial resolution how network connectivity depends on anatomical substrate and pharmacological stimulus, and compare with VOI-level summary statistics. These high-resolution neuroanatomical distributions of complex network parameters in the rat brain reveal foci of high connectivity in the sensorimotor cortex but also drug-dependent features in sub-cortical and prefrontal regions; in particular, a disjunct distribution of nodes of highest degree versus those with highest clustering coefficient.

## 2. Methods

**2.1. MRI Data Acquisition.** All experiments were carried out in accordance with Italian regulations governing animal welfare and protection. Protocols were also reviewed and consented to by a local animal care committee, in accordance with the guidelines of the Principles of Laboratory Animal Care (NIH publication 86–23, revised 1985). MRI data were acquired from male Sprague-Dawley rats using a Bruker Biospec 4.7T scanner with a cylindrical volume coil for RF transmit and a Bruker quadrature “rat brain” surface receive coil. PhMRI data were acquired as RARE time series, sensitized to changes in relative cerebral blood volume (rCBV) by administration of a 2.67 mL/kg intravenous bolus of the blood pool contrast agent Endorem (Guerbet, France). Experiments were performed under 0.8% halothane maintenance anesthesia, neuromuscular blockade and artificial ventilation with blood gas values maintained within physiological range ( $30 < \text{pCO}_2 < 50$ ;  $\text{pO}_2 > 100$ ), and peripheral blood pressure within the autoregulatory range associated with halothane anesthesia [44, 45]. The data described in this paper originate from three studies, for which acquisition details were substantially similar and which have been published previously [6, 46]. In the first study, the animals were challenged with either *d*-amphetamine (1 mg/kg i.v.,  $N = 17$ ) or vehicle (saline,  $N = 7$ ), respectively [6, 42]. In the second, animals were challenged with fluoxetine (10 mg/kg i.p.,  $N = 7$ ) [6]. In the third, animals were challenged with

nicotine (1 mg/kg i.v.,  $N = 9$ ) [46]. In total, complex networks were constructed as detailed below from four subject cohorts: the *d*-amphetamine and vehicle groups in the first study as well as from the fluoxetine and nicotine groups.

## 2.2. Analysis Details

**2.2.1. MR Image Preprocessing.** Anatomical and time series data were converted to Analyze (AVW 7.5) format and signal intensity changes in each time series were transformed into fractional rCBV on a voxel-wise basis, using a constrained exponential model of the gradual elimination of contrast agent from the blood pool to provide a robust prediction of postinjection background signal and remove the worst effects of this systematic trend in the resulting rCBV data [47]. Data for each subject were then spatially normalized to a stereotaxic rat brain template [48] by computing a nine degree-of-freedom affine transform for the anatomical image and applying the resulting transformation matrix to the accompanying rCBV time series (FSL/FLIRT v.5.2). Finally, the rCBV data were multiplied by a brain parenchyma mask to remove extra-cranial and CSF contributions.

**2.2.2. Time Series Analysis.** Image-based time series analysis of the response in individual subjects was carried out in a general linear model framework in order to calculate 3D maps of the post-injection response amplitude in each subject. The images were spatially smoothed with a Gaussian kernel of FWHM = 0.6 mm, corresponding to  $\sim 2\times$  the in-plane voxel dimension. All image processing was performed with the voxel dimensions scaled up in the image headers by a factor of 10, in order to ensure compatibility with any explicit length scales that may be encoded in algorithms designed for use with human data. However, explicit voxel dimensions are quoted at the original scale. The design matrix for each study comprised a signal model function identified by study-level Wavelet Cluster Analysis (WCA), the temporal derivative of this regressor and a linear ramp [49, 50]. This allows a good model fit to signals whose temporal response profile can vary slightly across subjects and brain regions.

The coefficients of the signal model function thus provided a map of the post-injection response amplitude for each subject. The response maps for the subjects in each study were then stacked together so that each voxel had an associated response vector. The inter-subject correlations analyzed here leverage the differential anatomical profiles of pHMRI response between subjects [6, 42].

**2.3. Creation of Network Representations.** The response maps, calculated at the template dimensions, were rebinned in-plane by a factor of two. This was performed so that subsequent adjacency matrices remained within the memory limits of the IDL software used for much of the processing and also to recover voxel volumes closer to the actual acquisition resolution, since as part of the spatial normalization process the time series' were interpolated to the resolution of the standard space template [48]. The rebinned response

maps thus had  $0.12\text{ mm}^3$  voxels, close to the acquisition resolution size of  $0.09\text{ mm}^3$ . A binary brain mask, covering only slices for which complete data were present for all subjects in all studies, was used to define brain parenchyma voxels for further analysis. This resulted in networks of  $N = 8130$  nodes (voxels).

A fully weighted, complete network was created for each study by considering each voxel as a node and defining the strength of the edge between each pair of voxels based on the linear correlation between the response vectors associated with each. Specifically, the weight of each edge  $w_{ij}$  was defined as the absolute value of the Pearson correlation coefficient  $r_{ij}$  between the inter-subject response amplitudes in each voxel, converted to lie under an approximately normal distribution by applying Fisher's *r*-to-*z* transformation:

$$\begin{aligned} w_{ij} &= |z_{ij}|, \\ z_{ij} &= \frac{1}{2} \log\left(\frac{1+r_{ij}}{1-r_{ij}}\right), \end{aligned} \quad (1)$$

where  $i, j \in \{1, \dots, N_{\text{nodes}}\}$  specify the pair of nodes connected by each edge. Note that these networks are undirected—each edge simply conveys the strength of a connection without regard to a causal direction. Each of the four weighted networks was then converted into a binary one by retaining only the edges with the highest weights (i.e., representing the strongest connections). This step was performed in order to make networks of this size tractable for further analysis; specifically, calculation of nodewise network parameters is substantially faster for sparse binary networks. Although extension of complex network theory to weighted networks is of considerable current interest, properties of binary networks are well established and previous fMRI network studies have also employed a binarization step. We applied a threshold  $z_{\text{thresh}}$  to the link weights, determined as that which retained the strongest 2% of the  $N_{\text{nodes}} \times (N_{\text{nodes}} - 1)/2$  edges in the fully weighted network; that is, we worked with equi-sparse networks, ensuring a consistent number of network edges across data sets to emphasize differences in the relative connection topology rather than overall edge density *per se*. This value was empirically determined as one that allows a diversity of node connectivities, whilst retaining a connected network, and is consistent with the thresholding scheme used in our previous seed region and community structure analyses [43]. The network features and in particular the anatomical profiles of the nodewise connectivity parameters were robust across a range of binarization thresholds (see Supplementary Data available online at doi:10.1155/2012/615709). The threshold values  $z_{\text{thresh}}$  are summarized for each of the four networks analyzed in Table 1.

The resulting binary networks can be represented mathematically by an adjacency matrix  $A$ , whose elements  $a_{ij}$  describe the connectivity:

$$a_{ij} = \begin{cases} 1, & \text{if nodes } i \text{ and } j \text{ are connected} \\ 0, & \text{otherwise.} \end{cases} \quad (2)$$

TABLE 1: Summary of global network parameters for the four phMRI networks and the random networks.

Drug	$z_{\text{thresh}}$	Power law slope	$K$	$C$	$\gamma$	$\sigma_{\text{SW}}$
Amphetamine	0.71	-1.031	162.3	0.387	3.989	3.011
Fluoxetine	0.94	-0.888	183.1	0.453	3.893	2.836
Nicotine	0.96	-0.671	193.2	0.449	4.627	2.898
Vehicle	0.93	-0.844	177.8	0.422	4.795	2.672

For symbol definitions, see Section 2.

**2.4. Nodewise Network Parameters.** Based on the topology defined by the adjacency matrix (2), a number of network parameters can be derived that convey information about the network. Here, we investigate the node degree  $k$  and the clustering coefficient  $c$ , as follows.

The degree  $k_i$  of any node  $i$  is simply the number of nodes to which it is connected, that is, the number of edges incident upon it:

$$k_i = \sum_{j=1}^{N_{\text{nodes}}} a_{ij}. \quad (3)$$

The clustering coefficient  $c_i$  is defined as the fraction of total possible edges  $N_{\text{edges}}(G_i)$  in the sub-network  $G_i$ , defined by all nodes directly connected to node  $i$ , that are actually present:

$$c_i = \frac{2N_{\text{edges}}(G_i)}{k_i(k_i - 1)}. \quad (4)$$

In other words, this parameter reflects how many pairs of nodes connected to a given node are also connected to each other.

Global, whole-network histograms for the parameters  $k$  and  $c$  were generated for each network. These distributions capture global statistical properties of the network and reflect its basic principles of organization. The form of the histogram of node degree  $k$  is of particular interest and in networks derived from human functional imaging data has been observed to show power law behavior (a straight line when plotted on logarithmic scales) up to a high-degree cutoff [13, 14]. The power law behavior of the networks in the present study was quantified by fitting an equation of the form  $\gamma = k^{-\gamma}$  to the linear portion of the histogram, where  $\gamma$  is the frequency (number of nodes in the bin) and  $k$  is the mean value of each bin in the histogram.

Each network was further characterized by calculating the following global summary parameters:

- (i) The power law decay constant from the degree distribution histogram;
- (ii)  $K$ , the average degree  $k_i$  over all nodes in the network;
- (iii)  $C$ , the average clustering coefficient  $c_i$  over all nodes in the network.

The presence of long-distance links in random networks results in small values of  $L$ , the average shortest path between all node pairs, compared, for example, to regular

lattices with only next-neighbor links, with  $L$  scaling as the logarithm of  $N$  (the total number of nodes). Watts and Strogatz [18] identified a particular class of networks, dubbed “small-world” networks, with comparable values and scaling properties of  $L$  ( $L \approx L_{\text{random}}$ ) in the presence of a high degree of local clustering  $C \gg C_{\text{random}}$  (where  $L_{\text{random}}$  and  $C_{\text{random}}$  are the values from equivalent random networks with the same  $N_{\text{nodes}}$  and link density). We thus also report two indices that explicitly compare these properties in the phMRI networks with those in appropriate comparator networks, namely:

- (i)  $\gamma = (C/C_{\text{random}})$ , a measure of local clustering;
- (ii)  $\sigma_{\text{SW}} = (C/C_{\text{random}})/(L/L_{\text{random}})$ , often referred to as the “small world index” [19, 24].

For each phMRI network, we used 10 randomly rewired versions of the network as a comparator null model [51]. All network parameters were calculated using the brain connectivity toolbox in Matlab [52].

In addition, since each node corresponds to a position in the image volume, their anatomical locations in the brain were used to generate voxel-wise maps and profiles by anatomical structure of each of the above parameters. In this way, the dependence of the above parameters on brain region was evaluated for networks associated with each drug.

For the anatomical structure profiling, volumes of interest (VOIs) corresponding to specific brain structures were selected to enable a formal statistical comparison of differences in network parameters suggested by examination of the parameter maps. VOIs were defined bilaterally using a 3D reconstruction of a rat brain atlas coregistered with the anatomical MRI template [48]. The VOIs selected were: caudate putamen, cingulate cortex, insular cortex, medial prefrontal cortex, parietal association cortex, visual cortex, anterodorsal hippocampus, subiculum, ventral hippocampus, primary motor cortex, whisker barrel field of the primary somatosensory cortex, forelimb field of the primary somatosensory cortex, dorsolateral thalamus, midline dorsal thalamus and ventromedial thalamus.

### 3. Results

**3.1. Global Network Properties.** We first examined the global characteristics of the rat brain networks. A summary of the global parameters is provided in Table 1. Values of the parameters  $\gamma$  and  $\sigma_{\text{SW}}$  were substantially greater than unity and consistent with “small-world” behavior, whereby any one node is connected to any other node in the network by a far fewer number of edges than in a random network with the same overall number of nodes and edges.

The degree histograms for all four of the phMRI networks exhibited power law (count  $\sim k^{-\gamma}$ ) behavior, characterized by a near linear dependence of frequency on  $k$  when displayed on a log-log plot, up to a high- $k$  cutoff of  $k \sim 800\text{--}900$  (Figure 1(a)). The presence of a cutoff in the distribution of  $k$  reflects the finite size of the networks. The decay parameters  $\gamma$  were similar in each case,

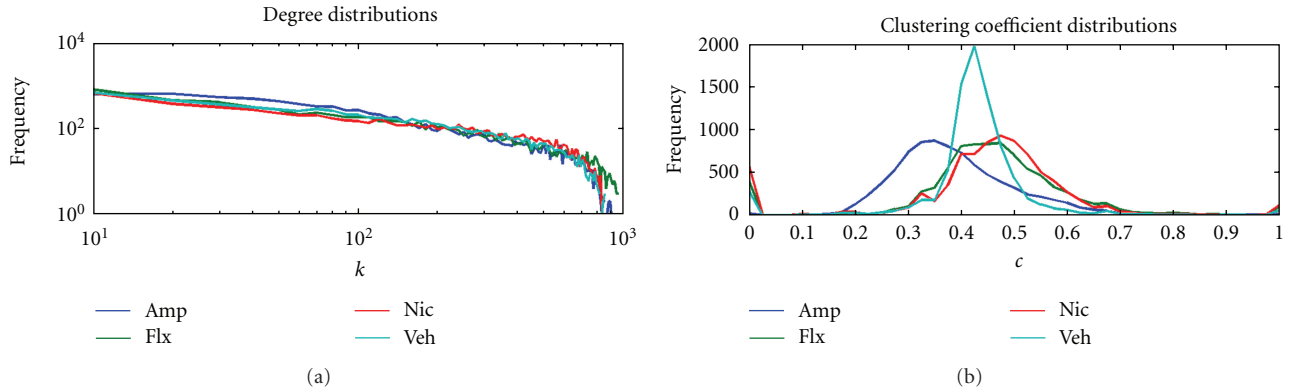


FIGURE 1: Global parameter histograms. (a) Histograms of the node degree ( $k$ ) reveal a power law dependence of frequency on  $k$  (evident as a linear relationship in this log-log display) up to a high-frequency cutoff for all networks. The slope of the linear portion of the histograms is similar in each network as indicated by the lines of linear fit (shown here offset below the data for visual clarity) and the values of  $\gamma$  in Table 1. Note that the histogram for the vehicle network reaches zero at a lower value than the three drug challenge networks, indicating fewer nodes with very high degree. (b) Histograms of the clustering coefficient ( $c$ ) for each network reveal an increased spread of values for each of the active drug networks relative to the vehicle network.

ranging from  $-0.67$  for the nicotine network to  $-1.03$  for the amphetamine network (Table 1).

We also examined histograms of the clustering coefficient  $c$  for each network (Figure 1(b)). While some differences in the median values across networks were observed (Table 1), we also found strong drug-dependent changes in the *distribution* of  $c$  values; in particular, each of the three active-drug networks evidenced a profile distinct from the vehicle network and indicated drug-dependent increases and decreases in  $c$ . While all three active drug networks showed a broader spread of  $c$  values compared with vehicle, the amphetamine network contained more nodes with lower values of  $c$ , whereas the fluoxetine and nicotine networks contained more nodes with higher values of  $c$ .

**3.2. Anatomical Dependence of the Local Connectivity Parameter  $k$ .** We next examined the anatomical dependence of node degree and clustering coefficient, both by mapping these parameters nodewise back onto the anatomical brain template and by statistical comparison with the vehicle network in selected brain structures of interest. The maps of the node degree  $k$  revealed a strong dependence of connectivity on brain region in all of the pHMRI networks (Figure 2).

In the amphetamine network, voxels with the highest values of  $k$  were localized in particular to frontal and prefrontal cortical regions, including the orbitofrontal, medial prefrontal, cingulate, insular, motor, and somatosensory cortex (Figure 2(a)). Sub-cortical regions containing highly-connected voxels included parts of the striatum (caudate putamen and accumbens), structures in the ventromedial thalamus and medial hypothalamus, with small foci also in the regions of the ventral subiculum and lateral entorhinal cortex.

In the fluoxetine network (Figure 2(b)), voxels in cortical regions were also characterized by high  $k$ , but there were substantially more highly-connected sub-cortical nodes evidenced by high-connectivity nodes in the caudate putamen,

amygdala and more extensively in the thalamus. Midbrain regions, including parts of the superior colliculi, periaqueductal grey, and medioventral nodes consistent with the raphe nuclei were also highly connected in the fluoxetine network.

The nicotine network also evidenced high connectivity in prefrontal and frontal cortices, parietal association cortex, with focal high- $k$  subcortical foci within the thalamus, hypothalamus and amygdala (Figure 2(c)).

In contrast, the anatomical distribution of  $k$  in the vehicle network was scattered with a noisier and overall less symmetric appearance than for the networks derived from the three psychoactive drugs (see Supplementary Data)—only slight anatomical dependence was evident with regions of relatively higher connectivity including the medial prefrontal cortex, and nodes within the thalamus and ventral hippocampus/entorhinal cortical regions.

**3.3. Anatomical Dependence of the Clustering Coefficient  $c$ .** The anatomical distributions of the cluster coefficient  $c$  are shown in Figure 3. Again, similarities and differences in the anatomical features across networks are evident.

In the amphetamine network (Figure 3(a)), the regions of high  $c$  showed some commonality with those of high  $k$  (cf. Figure 2(a))—in particular in frontal (somatosensory, motor) and prefrontal cortices. However, high- $k$  foci in the ventromedial thalamus and hypothalamus were not evident in the  $c$  map. Moreover, in the caudate putamen, high- $c$  nodes were found more rostrally than high- $k$  nodes.

In the fluoxetine network (Figure 3(b)), the regions of high- $c$  in the frontal slices were more medial and preferentially localized to the mPFC and accumbens, in contrast to the  $k$  map where the high- $k$  voxels were distributed across the motor cortex and more widely in the caudate putamen. Compared with the amphetamine network, more high- $c$  nodes were localized in more caudal regions, including the midbrain areas identified above.

In the nicotine network, regions of high- $c$  appear less well-defined than those of high- $k$ , but high- $c$  regions in the

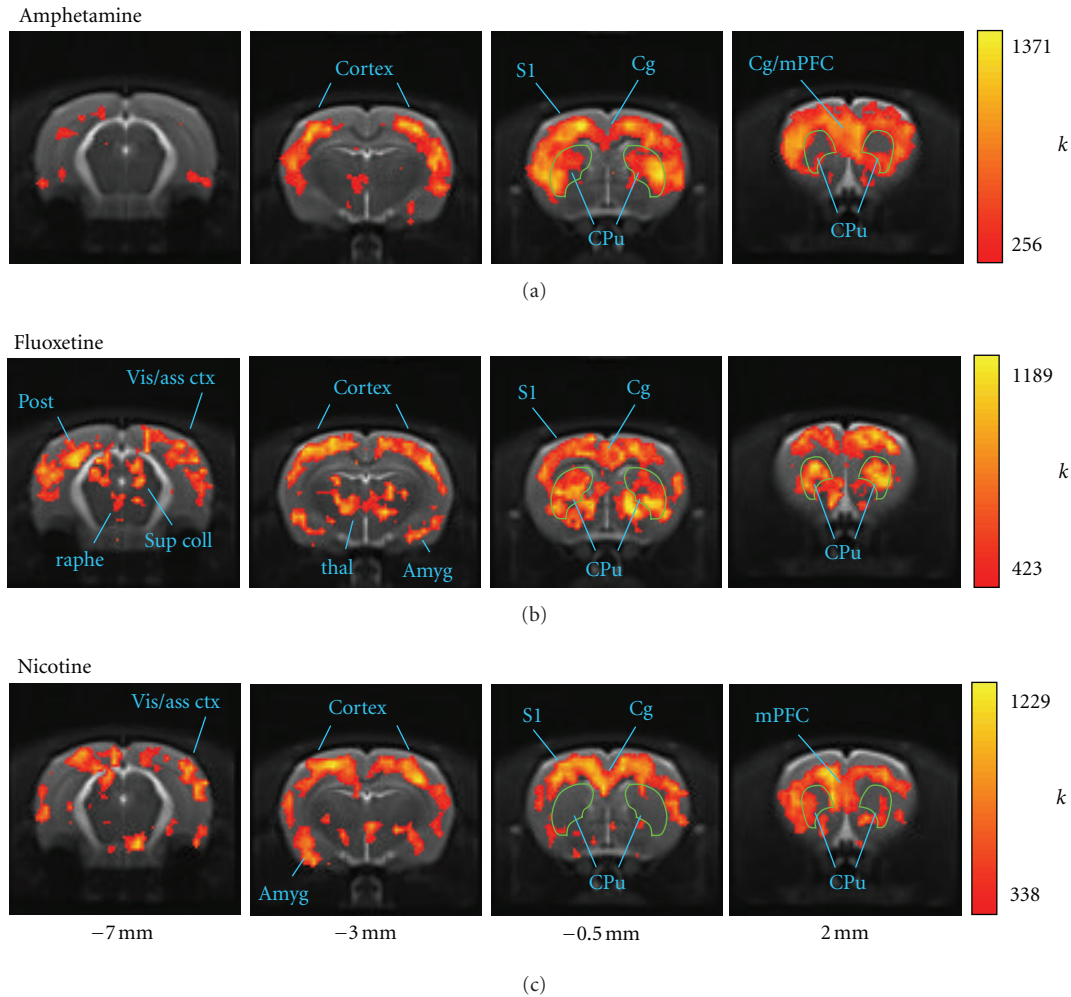


FIGURE 2: Anatomical distributions of node degree  $k$ . (a) amphetamine, (b) fluoxetine, and (c) nicotine pHMRI networks. In order to highlight the neuroanatomical correspondence of the most highly connected nodes, the overlay shows the upper quartile (75%–100%) of the  $k$  distribution for each network (the color scale maxima are compressed slightly to optimize the dynamic range.)

more dorsal sensorimotor cortices and ventral hippocampus/entorhinal cortex are evident (Figure 3(c)). Interestingly, the medial and prefrontal cortices, identified in Figure 2 as high- $k$  regions, are not regions of high  $c$  in this network.

The vehicle network showed few anatomically meaningful regions of high  $c$ , with the exception of the medial prefrontal cortex and entorhinal cortex (Supplemental Data).

**3.4. Differences between Drug and Vehicle Networks by Anatomical Region.** We also examined the anatomical profiles of  $k$  and  $c$  across selected VOIs representing brain structures of interest. Figure 4 illustrates the differences in connectivity structure between the active drug networks and the vehicle network. Consistent with the nodewise maps reported above, the latter was characterized by relatively flat profiles of both parameters with the exception of the mPFC and cingulate cortex (Figure 4(d)). In contrast, the other three networks show clear shifts, as a function of both brain region and drug, in the values of both  $k$  and  $c$  (Figures 4(a), 4(b), and 4(c)). While some brain regions

exhibited an increase in connectivity in the active pharmacological state, in others the values were decreased relative to vehicle.

We further examined these differences in anatomical profile of  $k$  and  $c$  at the VOI level by statistical comparisons between the node parameter values within each brain structure for each psychoactive drug network compared to vehicle (Mann-Whitney tests). Results for the node degree  $k$  are summarized in Table 2. The fluoxetine network had the highest connectivity in thalamic regions, and a differential distribution of  $k$  across different hippocampal regions. In contrast, the amphetamine network exhibited very low connectivity within the thalamic and hippocampal regions and a differential distribution across cortical regions. Profiles of  $c$  by VOI for each of the amphetamine, fluoxetine, and nicotine networks also confirmed the differential anatomical dependence indicated by the parameter maps (Table 3). Common differences from vehicle across all three psychoactive drug networks were increased  $k$  in cingulate, motor and somatosensory cortices, and increased  $c$  in motor and somatosensory cortices. In other brain regions—in

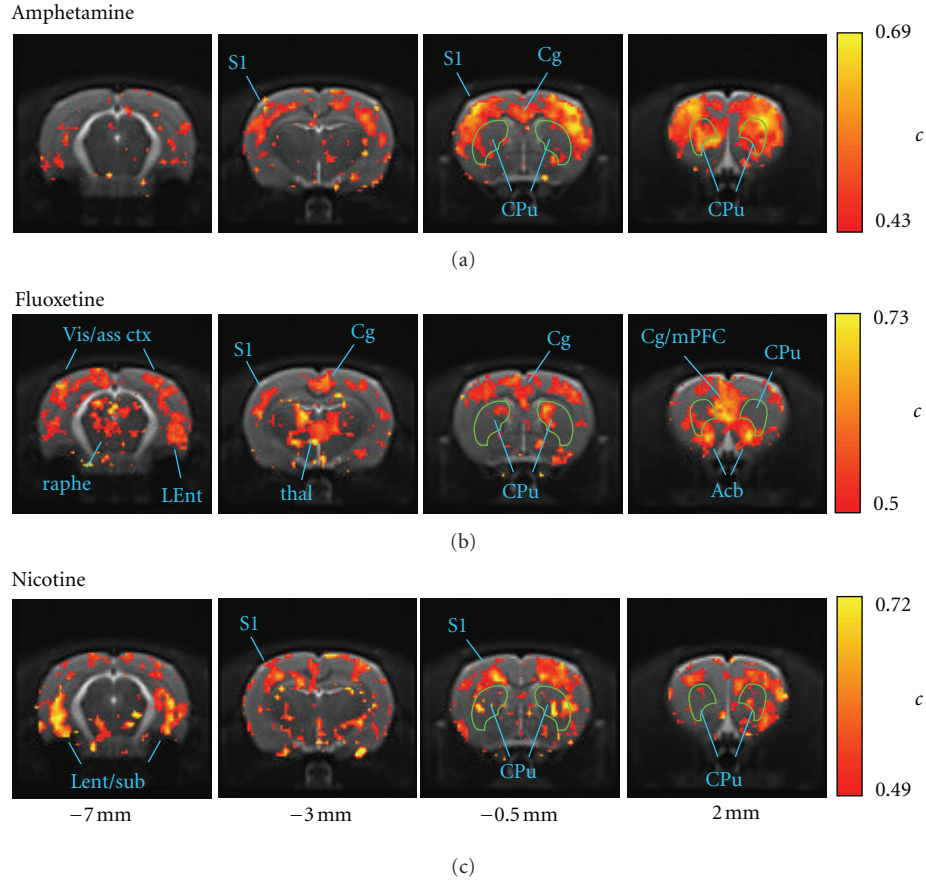


FIGURE 3: Anatomical distributions of node clustering coefficient  $c$ . (a) amphetamine, (b) fluoxetine, and (c) nicotine phMRI networks. In order to highlight the neuroanatomical correspondence of the most “cliquish” nodes, the overlay shows the upper quartile (75%–100%) of the  $c$  distribution for each network (the color scale maxima are compressed slightly to optimize the dynamic range.)

TABLE 2: Differences in degree  $k$  by VOI compared to vehicle network.

Brain region	VOI	Amphetamine	Fluoxetine	Nicotine
Prefrontal cortex	Cg	+	+++	+++
	mPFC	+	—	ns
Somatosensory and motor cortex	M1	+++	+++	+++
	S1BF	+++	+++	+++
	S1FL	+++	+++	+++
	ctxV	—	+++	+++
Other cortex	Ins	+++	ns	ns
	PtA	ns	+	+++
	hcAD	—	—	ns
Hippocampus	hcS	--	ns	ns
	hcV	—	ns	—
Striatum	CPu	ns	+++	—
	thalDL	—	+++	—
Thalamus	thalMD	—	++	ns
	thalVM	ns	ns	ns

“+” signs indicate significantly greater  $k$  compared to vehicle while “—” signs reflect significantly lower  $k$ , determined in each case using Bonferroni-corrected Mann-Whitney tests: + or — indicates  $P_c < 0.05$ , ++ or -- indicates  $P_c < 0.01$ , and +++ or --- indicates  $P_c < 0.001$  (Abbreviations: Cg: cingulate cortex; mPFC: medial prefrontal cortex (prelimbic and infralimbic regions combined); M1: primary motor cortex; S1BF: barrel field of primary somatosensory cortex; S1FL: forelimb field of primary somatosensory cortex, ctxV: visual cortex; Ins: insular cortex; PtA: parietal cortex; hcAD: anterodorsal hippocampus; hcS: subiculum region of hippocampus; hcV: ventral hippocampus; CPu: caudate putamen; thalDL: dorsolateral thalamus; thalMD: mediodorsal thalamus; thalVM: ventromedial thalamus.)

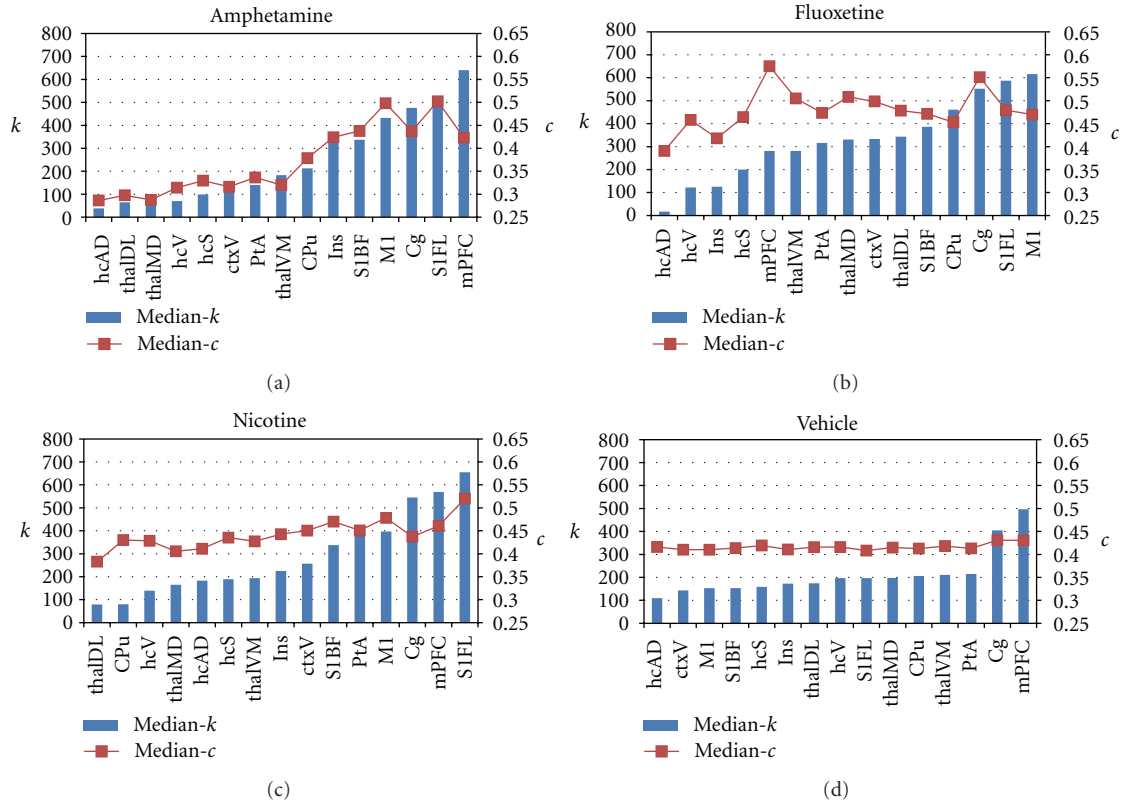


FIGURE 4: VOI profiles of network parameters. Selected VOIs rank ordered by degree (median  $k$  value in each VOI) for each network. Amphetamine, fluoxetine, and nicotine networks (a–c) show both increases and decreases in  $k$  and  $c$  relative to the mainly flat VOI profile of the vehicle network (d). Rank ordering of both parameters is similar for amphetamine and nicotine, but less closely coupled for the fluoxetine network (see Table 2 for VOI abbreviation definitions.)

particular subcortically—the anatomical profiles were drug-dependent.

**3.5. Neuroanatomical Differences between High- $k$  and High- $c$  Foci.** At the scale of individual nodes (voxels), graphs of  $c$  versus  $k$  (Figure 5) revealed that these two parameters were not related by a simple monotonic dependence. For all four networks, there was a far greater range of values of  $c$  at lower values of  $k$ . The vehicle network (Figure 5(d)) was characterized by a spread in  $c$  values between  $\sim 0.1$  and  $0.7$  at low  $k$ , with the range of  $c$  converging to a value  $\sim 0.4$  as  $k$  approached a maximum value  $\sim 1000$ . In contrast, for each of the three active drug networks the distribution extended over a greater range in both  $k$  and  $c$ . Dividing the brain into cortical and sub-cortical nodes revealed that in the amphetamine and nicotine networks, cortical nodes were shifted toward higher  $k$  and  $c$ , whereas in the amphetamine network in particular the sub-cortical nodes were shifted toward lower values of both  $k$  and  $c$  (Figures 5(a) and 5(c)). In contrast, both cortical and sub-cortical nodes in the fluoxetine network were characterized by a greater extent toward higher values of  $k$  and  $c$ , with little decrease in either parameter relative to vehicle (Figure 5(b)). For all networks, nodes of highest degree were not those with highest cliquishness, as represented by the clustering coefficient.

Building on the above observations of differences between active drug and vehicle networks at the VOI scale, we anatomically mapped nodes of altered connectivity at the finer neuroanatomical scale offered by the individual voxel nodes. Using the vehicle network as representing a baseline physiological state, we determined common cutoff values of  $k$  and  $c$  for the three active drug networks. The 95th percentile of the vehicle  $k$  distribution and the 2.5th and 97.5th percentiles of the vehicle  $c$  distribution yielded cutoff values of  $k > 657$ ,  $c < 0.28$ , and  $c > 0.50$ , shown as dashed lines in Figure 5. The con/disjunction maps depicted in Figure 6 highlight the voxels in which the nodes of highest  $k$  and those of highest  $c$  are localized for each network and indicate the presence of heterogeneity on a finer spatial scale than VOI-scale parcellation schemes.

Interestingly, nodes with highest values of  $c$  were, in general, differentially localized from those with the highest values of  $k$ . For all three drug networks, high- $k$  and high- $c$  nodes were identified within the sensorimotor cortex, with the greatest amount of overlap for the amphetamine network. Clear boundaries between high- $k$  and high- $c$  nodes separated the sensorimotor and prefrontal/cingulate cortices in all networks (Figure 6). In the amphetamine network, the mPFC was dominated by high- $k$  nodes, whereas a portion of the cingulate cortex more caudally was a high- $c$  focus. In the fluoxetine network, both mPFC and cingulate contained

TABLE 3: Differences in clustering coefficient  $c$  by VOI compared to vehicle network.

Brain region	VOI	Amphetamine	Fluoxetine	Nicotine
Prefrontal cortex	Cg	ns	+++	ns
	mPFC	ns	+++	++
Somatosensory and motor cortex	M1	+++	+++	+++
	S1BF	+++	+++	+++
	S1FL	+++	+++	+++
	ctxV	—	+++	+++
Other cortex	Ins	++	ns	+++
	PtA	—	+++	+++
	hcAD	—	—	ns
Hippocampus	hcS	—	+++	++
	hcV	—	+++	ns
Striatum	CPu	—	+++	+++
	thalDL	—	+++	+++
Thalamus	thalMD	—	+++	ns
	thalVM	—	+++	ns

“+” signs indicate significantly greater  $k$  compared to vehicle while “—” signs reflect significantly lower  $k$ , determined in each case using Bonferroni-corrected Mann-Whitney tests: + or — indicates  $P_c < 0.05$ , ++ or — indicates  $P_c < 0.01$ , and +++ or — indicates  $P_c < 0.001$ . (See Table 2 for abbreviation definitions.)

high- $c$  foci, whereas in the nicotine network the mPFC and cingulate were high- $k$  regions. The fluoxetine network showed an interesting differential distribution between the dorsal (CPu) and ventral (nucleus accumbens) striatum, with the former dominated by nodes of high degree whereas the latter featured nodes of high clustering coefficient. More caudally, the fluoxetine and nicotine networks had high- $c$  foci in entorhinal cortex/ventral hippocampal regions along with midbrain structures.

The low- $c$  nodes were localized to sub-cortical and midbrain regions in the amphetamine network, consistent with preferential localization of the high- $k$  and high- $c$  regions to frontocortical brain regions (see Supplementary Data). Low- $c$  nodes for the fluoxetine and nicotine networks were few and localized primarily to the brain edge (see Supplementary Data).

#### 4. Discussion

There is increasing interest in using functional imaging techniques to probe connectivity properties of the brain. In this context, it can be intuitive to think of the imaging data—and by extension the brain—as a network, comprising a set of nodes with functional connections defined by links between them. Beyond the conceptual tractability of such a representation, this approach also enables concepts in network theory to be leveraged. The present study extends the application of complex network theory in functional imaging of the rat brain by examining global as well as voxel scale, nodewise, network parameters for data sets characterizing the response to three canonical psychoactive drugs differing in both clinical/behavioral profile and mechanism of action.

Whole-network histograms of connectivity parameters can reveal statistical properties of the network that have deep repercussions for its behavior. Moreover, changes in

connectivity properties may also reflect disease states—for example, the global network-mean clustering coefficient and small-world index have been shown to be reduced in Alzheimer’s Disease relative to normal aging [16, 22]. For all four of the pHMRI networks considered here, whole-brain histograms of  $k$  demonstrated the characteristic scale-free signature up to a high- $k$  cutoff as previously reported for human brain motor task [13] and resting state [14] data. The form of these distributions was robust to the binarization threshold and independent of the challenge drug. A distribution of this type is qualitatively different from that found with random networks, where the degree distribution is strongly unimodal [53]. Heavy-tailed, scale-free degree distributions reflect the presence of a significant number of highly connected nodes, or “hubs,” a characteristic that results in short average distance between any two nodes of the network, and in robustness to random failure of nodes [53]. This is consistent with our observation in the present study of highly-connected brain regions in both cortical and sub-cortical structures in all three active drug networks. Scale-free characteristics have been found in several network analyses of functional imaging data in humans [13, 14]. However, structural studies, based, for example, on diffusion MRI tractography [26], tend to find more exponential distributions (linear on a log-linear scale), consistent with the relatively uniform distribution of neuronal density in grey matter [54]. Hence, it may be argued that the presence of highly connected hubs reflects functional organization of the brain, rather than the structure of the neuronal substrate [10].

In the present study, the anatomical distributions of two key nodewise connectivity parameters—the node degree  $k$  and the clustering coefficient  $c$ —revealed bilaterally symmetric patterns whose features correlated well with known anatomical subdivisions of the brain—including, for

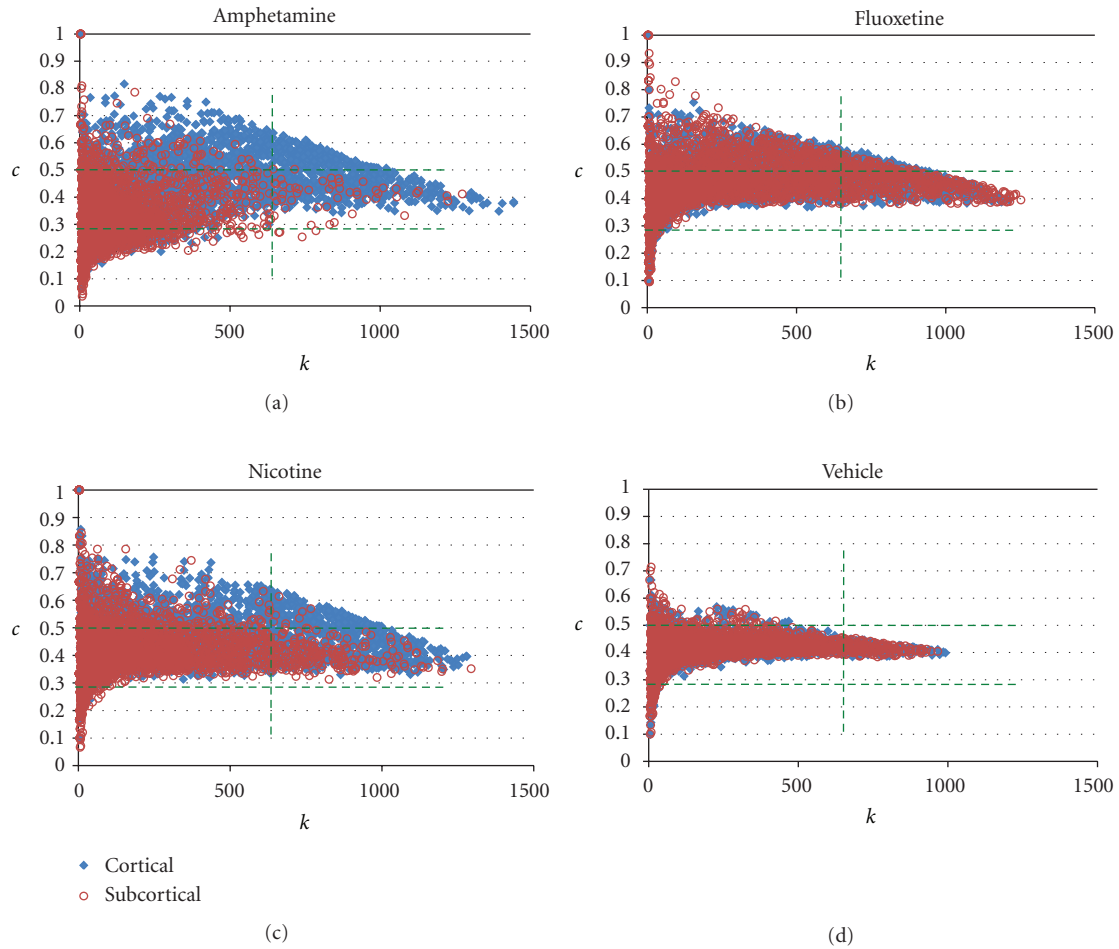


FIGURE 5: Scatter plots of  $c$  versus  $k$  for all nodes, at the voxel scale. Overall, low degree ( $k$ ) nodes were associated with a spread of clustering ( $c$ ) behaviors, whereas the nodes of highest degree had clustering coefficients toward the middle of the range. Compared with vehicle (d), the active-drug networks (a–c) had a greater range in both  $k$  and  $c$ . Amphetamine and nicotine showed a differential shift in the  $k$ - $c$  distributions between cortical and subcortical nodes, whereas for fluoxetine nodes in both brain subdivisions were shifted to higher values. The green lines indicate cutoff values used to identify nodes whose  $k$  and/or  $c$  characteristics were outside the range associated with the vehicle state (see text).

example, sensorimotor, cingulate, and prefrontal cortices (see Figures 2, 3, and 6). These patterns revealed a common increase in connectivity in sensorimotor cortical regions but a dependence on the challenge drug elsewhere in the brain. A statistical analysis of nodes grouped into anatomical VOIs demonstrated significant differences from vehicle in median  $k$  and  $c$  within large-scale brain structures. Interestingly, both increases and decreases in connectivity relative to vehicle were observed (Figures 4 and 5). This is consistent with a preferential functional engagement of certain interregional connections and a suppression of others in the pharmacologically active states. The presence of common features of the anatomical distribution in the sensorimotor cortex for all node-parameters investigated (high  $k$  and high  $c$ ) suggests that these reflect a general functional or structural organization of the rat brain, consistent with the high local connectivity of cortical grey matter.

Regions of high  $k$  reflect voxels that are functionally connected to many others. Studies in which clusters of functional connections in these data were elucidated [6,

42, 43, 55–57] indicate that the voxels in the sensorimotor cortices are likely to be preferentially connected to each other, consistent with the widespread distribution of high- $k$  nodes in the cortex for all three drug networks. However, foci of high node degree were also observed as a function of challenge drug in subcortical structures including the thalamus and striatum, and midbrain regions including the raphe nucleus. The clustering coefficient  $c$  reflects the extent to which the nodes connected to a given node are interconnected within themselves and can be interpreted as an index of local connectivity (where “local” is defined by connections and does not necessarily coincide with anatomical locality) and also representative of local information transfer efficiency [15, 58]. For the *d*-amphetamine network, the anatomical profiles of  $k$  and  $c$  both had a strong cortical localization, consistent with a strong cortical subnetwork [42]. In contrast, for fluoxetine regions of high  $c$  were more localized to prefrontal/cingulate cortices and sub-cortical structures such as the thalamus. This is consistent with the observation of a large sub-network involving these structures

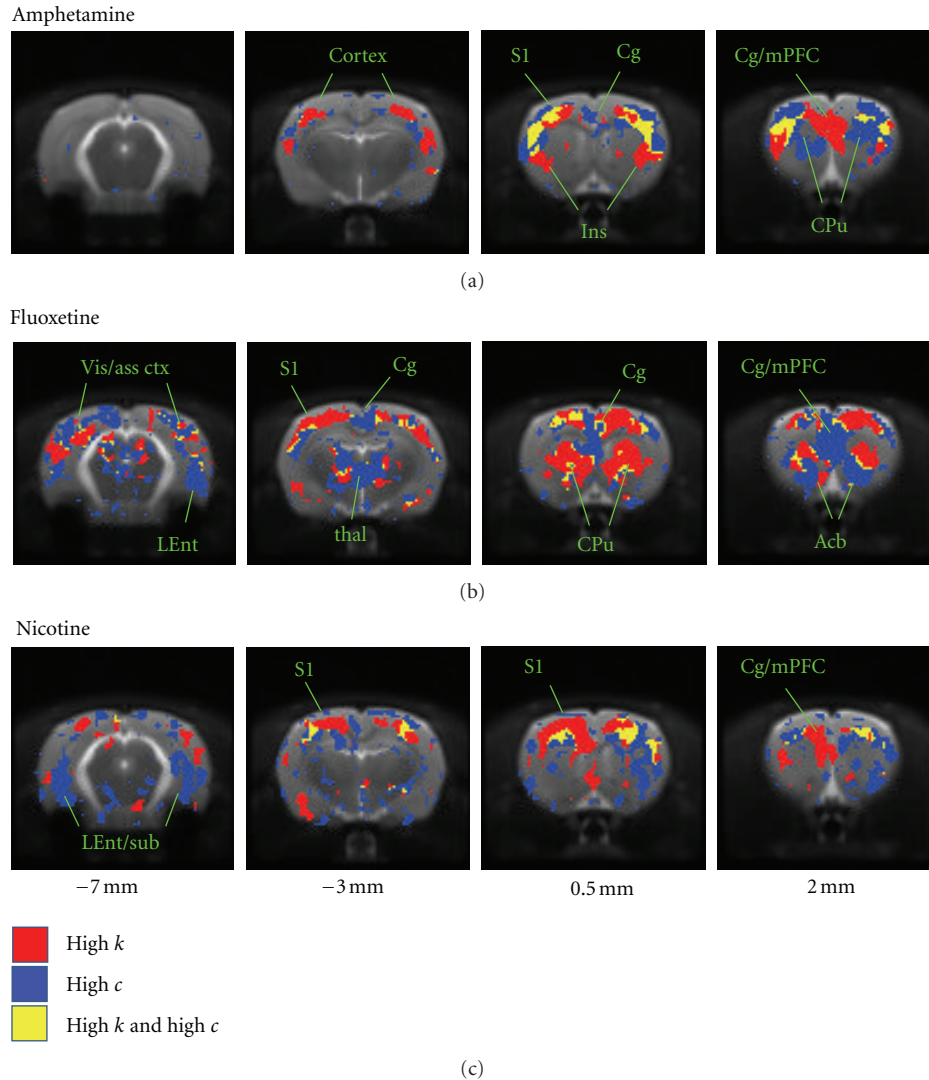


FIGURE 6: Maps of high- $k$  and high- $c$  foci for each drug network. These maps were created using cutoff values of  $k$  and  $c$  based on the vehicle parameter distributions (see Figure 5). The maps illustrate the anatomical disjunction between nodes of highest clustering, compared with those of highest degree. The neuroanatomical dependence of these is a function of the applied pharmacological challenge for prefrontal and subcortical regions, but similar across networks in the sensorimotor cortex.

by both seed region analysis [6] and network partitioning approaches [43, 55]. The nicotine network also showed widespread elevated node degree in cortical regions, but less clear anatomical structure in the maps of the clustering coefficient. Nevertheless, the VOI analysis demonstrated a different anatomical profile of both  $k$  and  $c$  in the response to nicotine, in comparison with the other drug networks. Overall, the high- $k$  and high- $c$  nodes shown in Figure 6 lie within the communities of “core” nodes identified in a network partitioning analysis of the same data [55].

In networks such as those considered here, with connections based on the response to the injection of a pharmacological agent, comparison with a vehicle network is valuable.

Explicit comparison with a vehicle group is standard practice in more traditional group analysis approaches in order to differentiate the effects of the pharmaceutical compound *per se* from those due to the solvent in which it is dissolved. Ideally a benign vehicle, such as physiological

saline in the group analyzed here, is used and expected to elicit minimal response. Nevertheless, in addition to capturing physiological “baseline” variation in the time courses, vehicle injection may itself give rise to weak effects. In the present context, this allows network structure arising from the intravenous injection of the vehicle to be characterized and used as a baseline for determining effects due to the compounds of interest. In the vehicle group analyzed herein, an intravenous injection volume of 1 mL/kg was used, along with a 0.3 mL/kg flush, yielding a total injection volume of 1.3 mL/kg, injected over one minute. For a 300 g rat, assuming a blood volume of 18.77 mL, this equates to  $\sim 7\%$  of the total blood volume. When using blood pool contrast agents as in the CBV method employed in the present study, this results in a slight dilution of the agent which can manifest as a small central signal change post-injection. The injection may also give rise to an autonomic response whose response in particular brain regions may manifest

as correlated signal changes, albeit of small amplitude. The network analysis showed weaker anatomical features of connectivity parameters in the vehicle network than in the other three, with elevated  $k$  and  $c$  observed in prefrontal cortical regions. Indeed, the global degree distribution of the vehicle network had a scale-free structure very similar to the other pHMRI networks, consistent with findings of preserved global topological structure in the presence of cognitively and pharmacologically induced perturbations in (local) functional connectivity in human brain imaging studies [15, 36, 37].

Nevertheless, the connectivity characteristics in the active drug networks were qualitatively different from the vehicle network, as evident from Figures 4–6. Indeed, using the vehicle network as a quantitative reference, regions of both high- $k$  and high- $c$  were clearly identified for all three active drug networks (Figures 5 and 6). These indicated the presence of foci in frontal cortices as a common feature across drugs. Moreover, by considering nodes at the scale of individual voxels, we were able to resolve an anatomical differentiation between the nodes with highest  $k$  and those with highest  $c$  at a finer spatial scale than that of typical VOI parcellations. While the use of more liberal cutoff values in Figure 6 would result in increased overlap between high- $k$  and high- $c$  nodes, the selected values convey that nodes with highest values of  $k$  do not, in general, coincide with nodes of highest  $c$ —a finding implied also in the scatter plots depicted in Figure 5. Furthermore, the maps in Figure 6 also illustrate how the highest- $k$  and highest- $c$  nodes often occupy anatomically adjacent brain structures, particularly in frontal cortical, prefrontal cortical and striatal regions. Sub-cortical foci were also identified, in particular in the fluoxetine network. In contrast, few sub-cortical high- $k$  or high- $c$  nodes were identified for the amphetamine network at the thresholds used here, despite the presence of a sub-network from the VTA projecting forward to the ventral forebrain and the mPFC [6, 42, 55]; this may reflect the smaller size of this module, or potentially a “sequential” nature of connections along this highly localized pathway (see, e.g., Figure 3 in [6]), which would also tend to produce lower  $k$  and  $c$  values.

As in previous studies examining network characteristics of functional imaging networks, we reduced each complete, weighted network (in which all possible links exist and have a variable weight dependent on the correlation in response between its two nodes) to a binary one. The primary reason for this was computational tractability for the relatively large (ca.  $10^4$  nodes) networks that resulted from retaining the spatial scale of functional image voxels. For the main results presented here, we thresholded each network so as to retain the strongest 2% of the edges in the binarized version. The resulting network topology represents a middle ground between two undesirable extremes: as more edges are retained, node connections become increasingly dense and topological distinction is lost; alternatively, as fewer edges are retained, the network becomes disconnected and topological information becomes increasingly suppressed. In fact, the global network properties and the relative anatomical distribution of the network parameters  $k$  and  $c$

are robust to the precise value of the binarization threshold over a range of thresholds in this “intermediate” regime of interest (see Supplementary Data). Furthermore, the 2% networks at the voxel scale satisfy the  $K > \ln(N_{\text{nodes}})$  criteria for estimable topological properties in random comparator networks of the same size [15].

In human studies, brain functional connectivity is typically derived from fMRI series by calculating correlations in the time domain. Recent progress has also been made toward establishing robust and reproducible temporal correlation patterns in rodent fMRI [59–64]. Based on the nature of the present pHMRI data, acquired with a lower temporal resolution than required to resolve temporal correlations, we constructed and characterized networks derived from inter-subject correlations in the response amplitude following drug administration, following a procedure established in 2DG autoradiography [38] and PET [39, 40]. The correlated responses used to determine the links can be interpreted as reflecting a functional coupling in response to the pharmacological challenge in each case [38]. It should be noted that the concept of functional connectivity was first introduced in this context, based on inter-subject correlation analysis and prior to the invention of fMRI. Moreover, this approach has been employed recently to elucidate anatomical networks of grey matter volume from structural MRI data [23, 34]. The use of cross-subject correlations to derive functional connectivity from pHMRI data has been recently demonstrated [6], shown to delineate functional connectivity along different neurotransmitter systems when they were selectively stimulated pharmacologically, and further validated in subsequent work [42, 55].

The images in this study were smoothed before conversion into the network representation, introducing a local correlation between responses in neighboring voxels. A key reason for smoothing is to compensate in part for residual differences in image alignment between different subjects when performing group-level, voxel-wise operations. In the present data, the networks are derived from inter-subject correlations and so spatial normalization of the image data to a common space is critical. To assess the effect of smoothing, we also performed the analyses on networks derived from unsmoothed image data. Smoothing did not greatly affect global characteristics nor anatomical distribution of parameters; a fine anatomical resolution was maintained (Figures 2, 3, and 6). The results in terms of global and anatomical parameter distributions were highly consistent with those obtained from the smoothed image networks—the most noticeable difference was that the parameter maps appeared noisier and less easy to interpret visually in the unsmoothed case. Thus, to depict the neuroanatomical dependence of the network parameters with maximum clarity, we presented data based on the smoothed images.

An important feature of networks generated from functional imaging data is that each node represents a brain region and has a well-defined neuroanatomical location. Here, we investigated the dependence of node degree and clustering coefficient in response to different pharmacological stimulation in the rat. Global degree histograms indicated similar global, scale-free structure in all networks.

However, nodewise maps at the scale of functional image voxels and VOI-level comparisons of these parameters revealed drug- and brain region-dependent modulation of connectivity parameters relative to the physiological baseline state. Increases in both node degree and clustering coefficient in frontal cortices were observed for all active-drug networks, revealing foci of high connectivity independent of the pharmacological challenge. Sub-cortical and pre-frontal features were stimulus-dependent, and showed a disjunct distribution of nodes of highest degree versus those with highest clustering coefficient. These findings suggest that the cortical foci of high connectivity reflect the intrinsic functional organization of the rat brain, with the connectivity properties and node roles in sub-cortical and prefrontal regions being more dependent on the activation of specific neurotransmitter systems, that is, on the specific dynamics of the functional processes elicited by the different pharmacological challenges.

## Summary

The brain's functional architecture is complex, and largely unknown. Recently, correlation analyses of brain activity measured by neuroimaging methods have been shown to resolve patterns of functional connectivity, thus providing a powerful means to unravel its details. Functional connectivity data can be naturally represented in the form of networks, in which the nodes are represented by individual brain regions or image voxels and their interconnections are determined by the correlation strength between each pair of regions. The global topological properties of these networks reveal emergent features of the brain and provide measures of the integration of function within the brain. However, the mammalian brain is not a homogeneous network. For example, the neocortex presents a substantially different functional organization compared with subcortical structures. Here, we applied functional MRI methods to study the anatomical distribution of local network parameters in the rat brain at high spatial resolution ( $\sim 400\mu\text{m}$ ) under different stimulus conditions. We demonstrate that substantial differences in network topology and functional connectivity exist between brain regions that evolved at different times. Some of these statistical properties are independent of the neurotransmitter system activated, indicating that they reflect general features of the underlying anatomical connectivity rather than specific aspects of the functional process elicited by the stimulation paradigm.

## References

- [1] D. Cordes, V. M. Haughton, K. Arfanakis et al., "Frequencies contributing to functional connectivity in the cerebral cortex in "resting-state" data," *American Journal of Neuroradiology*, vol. 22, no. 7, pp. 1326–1333, 2001.
- [2] P. Fransson, "Spontaneous low-frequency BOLD signal fluctuations: an fMRI investigation of the resting-state default mode of brain function hypothesis," *Human Brain Mapping*, vol. 26, no. 1, pp. 15–29, 2005.
- [3] C. F. Beckmann, M. DeLuca, J. T. Devlin, and S. M. Smith, "Investigations into resting-state connectivity using independent component analysis," *Philosophical Transactions of the Royal Society B*, vol. 360, no. 1457, pp. 1001–1013, 2005.
- [4] M. De Luca, C. F. Beckmann, N. De Stefano, P. M. Matthews, and S. M. Smith, "fMRI resting state networks define distinct modes of long-distance interactions in the human brain," *NeuroImage*, vol. 29, no. 4, pp. 1359–1367, 2006.
- [5] J. S. Damoiseaux, S. A. R. B. Rombouts, F. Barkhof et al., "Consistent resting-state networks across healthy subjects," *Proceedings of the National Academy of Sciences of the United States of America*, vol. 103, no. 37, pp. 13848–13853, 2006.
- [6] A. J. Schwarz, A. Gozzi, T. Reese, and A. Bifone, "In vivo mapping of functional connectivity in neurotransmitter systems using pharmacological MRI," *NeuroImage*, vol. 34, no. 4, pp. 1627–1636, 2007.
- [7] R. L. Buckner, J. R. Andrews-Hanna, and D. L. Schacter, "The brain's default network: anatomy, function, and relevance to disease," *Annals of the New York Academy of Sciences*, vol. 1124, pp. 1–38, 2008.
- [8] S. H. Strogatz, "Exploring complex networks," *Nature*, vol. 410, no. 6825, pp. 268–276, 2001.
- [9] E. Bullmore and O. Sporns, "Complex brain networks: graph theoretical analysis of structural and functional systems," *Nature Reviews Neuroscience*, vol. 10, no. 3, pp. 186–198, 2009.
- [10] M. P. van den Heuvel and O. Sporns, "Rich-club organization of the human connectome," *The Journal of Neuroscience*, vol. 31, pp. 15775–15786, 2011.
- [11] O. Sporns, *Networks of the Brain*, MIT Press, 2012.
- [12] R. Salvador, J. Suckling, C. Schwarzbauer, and E. Bullmore, "Undirected graphs of frequency-dependent functional connectivity in whole brain networks," *Philosophical Transactions of the Royal Society B*, vol. 360, no. 1457, pp. 937–946, 2005.
- [13] V. M. Eguíluz, D. R. Chialvo, G. A. Cecchi, M. Baliki, and A. V. Apkarian, "Scale-free brain functional networks," *Physical Review Letters*, vol. 94, no. 1, Article ID 018102, 2005.
- [14] S. Achard, R. Salvador, B. Whitcher, J. Suckling, and E. Bullmore, "A resilient, low-frequency, small-world human brain functional network with highly connected association cortical hubs," *Journal of Neuroscience*, vol. 26, no. 1, pp. 63–72, 2006.
- [15] S. Achard and E. Bullmore, "Efficiency and cost of economical brain functional networks," *PLoS Computational Biology*, vol. 3, no. 2, article e17, 2007.
- [16] K. Supekar, V. Menon, D. Rubin, M. Musen, and M. D. Greicius, "Network analysis of intrinsic functional brain connectivity in Alzheimer's disease," *PLoS Computational Biology*, vol. 4, no. 6, Article ID e1000100, 2008.
- [17] J. C. Reijneveld, S. C. Ponten, H. W. Berendse, and C. J. Stam, "The application of graph theoretical analysis to complex networks in the brain," *Clinical Neurophysiology*, vol. 118, no. 11, pp. 2317–2331, 2007.
- [18] D. J. Watts and S. H. Strogatz, "Collective dynamics of 'small-world' networks," *Nature*, vol. 393, no. 6684, pp. 440–442, 1998.
- [19] M. D. Humphries, K. Gurney, and T. J. Prescott, "The brain-stem reticular formation is a small-world, not scale-free, network," *Proceedings of the Royal Society*, vol. 273, no. 1585, pp. 503–511, 2006.
- [20] D. S. Bassett and E. Bullmore, "Small-world brain networks," *Neuroscientist*, vol. 12, no. 6, pp. 512–523, 2006.
- [21] S. Micheloyannis, E. Pachou, C. J. Stam et al., "Small-world networks and disturbed functional connectivity in schizophrenia," *Schizophrenia Research*, vol. 87, no. 1–3, pp. 60–66, 2006.

- [22] C. J. Stam, B. F. Jones, G. Nolte, M. Breakspear, and P. Scheltens, "Small-world networks and functional connectivity in Alzheimer's disease," *Cerebral Cortex*, vol. 17, no. 1, pp. 92–99, 2007.
- [23] Y. He, Z. J. Chen, and A. C. Evans, "Small-world anatomical networks in the human brain revealed by cortical thickness from MRI," *Cerebral Cortex*, vol. 17, no. 10, pp. 2407–2419, 2007.
- [24] O. Sporns, C. J. Honey, and R. Kötter, "Identification and classification of hubs in brain networks," *PLoS ONE*, vol. 2, no. 10, Article ID e1049, 2007.
- [25] R. L. Buckner, J. Sepulcre, T. Talukdar et al., "Cortical hubs revealed by intrinsic functional connectivity: mapping, assessment of stability, and relation to Alzheimer's disease," *Journal of Neuroscience*, vol. 29, no. 6, pp. 1860–1873, 2009.
- [26] P. Hagmann, L. Cammoun, X. Gigandet et al., "Mapping the structural core of human cerebral cortex," *PLoS Biology*, vol. 6, no. 7, p. e159, 2008.
- [27] C. J. Honey and O. Sporns, "Dynamical consequences of lesions in cortical networks," *Human Brain Mapping*, vol. 29, no. 7, pp. 802–809, 2008.
- [28] M. P. van den Heuvel, C. J. Stam, M. Boersma, and H. E. Hulshoff Pol, "Small-world and scale-free organization of voxel-based resting-state functional connectivity in the human brain," *NeuroImage*, vol. 43, no. 3, pp. 528–539, 2008.
- [29] C. J. Honey, O. Sporns, L. Cammoun et al., "Predicting human resting-state functional connectivity from structural connectivity," *Proceedings of the National Academy of Sciences of the United States of America*, vol. 106, no. 6, pp. 2035–2040, 2009.
- [30] C. H. Park, S. Y. Kim, Y.-H. Kim, and K. Kim, "Comparison of the small-world topology between anatomical and functional connectivity in the human brain," *Physica A*, vol. 387, no. 23, pp. 5958–5962, 2008.
- [31] M. van den Heuvel, R. Mandl, J. Luigjes, and H. H. Pol, "Microstructural organization of the cingulum tract and the level of default mode functional connectivity," *Journal of Neuroscience*, vol. 28, no. 43, pp. 10844–10851, 2008.
- [32] M. P. van den Heuvel, R. C. W. Mandl, R. S. Kahn, and H. E. Hulshoff Pol, "Functionally linked resting-state networks reflect the underlying structural connectivity architecture of the human brain," *Human Brain Mapping*, vol. 30, no. 10, pp. 3127–3141, 2009.
- [33] M. D. Greicius, K. Supekar, V. Menon, and R. F. Dougherty, "Resting-state functional connectivity reflects structural connectivity in the default mode network," *Cerebral Cortex*, vol. 19, no. 1, pp. 72–78, 2009.
- [34] W. W. Seeley, R. K. Crawford, J. Zhou, B. L. Miller, and M. D. Greicius, "Neurodegenerative diseases target large-scale human brain networks," *Neuron*, vol. 62, no. 1, pp. 42–52, 2009.
- [35] L. Deuker, E. T. Bullmore, M. Smith et al., "Reproducibility of graph metrics of human brain functional networks," *NeuroImage*, vol. 47, no. 4, pp. 1460–1468, 2009.
- [36] M. Valencia, J. Martinerie, S. Dupont, and M. Chavez, "Dynamic small-world behavior in functional brain networks unveiled by an event-related networks approach," *Physical Review E*, vol. 77, no. 5, Article ID 050905, 2008.
- [37] D. S. Bassett, A. Meyer-Lindenberg, S. Achard, T. Duke, and E. Bullmore, "Adaptive reconfiguration of fractal small-world human brain functional networks," *Proceedings of the National Academy of Sciences of the United States of America*, vol. 103, no. 51, pp. 19518–19523, 2006.
- [38] T. T. Soncrant, B. Horwitz, H. W. Holloway, and S. I. Rapoport, "The pattern of functional coupling of brain regions in the awake rat," *Brain Research*, vol. 369, no. 1-2, pp. 1–11, 1986.
- [39] B. Horwitz, J. M. Rumsey, and B. C. Donohue, "Functional connectivity of the angular gyrus in normal reading and dyslexia," *Proceedings of the National Academy of Sciences of the United States of America*, vol. 95, no. 15, pp. 8939–8944, 1998.
- [40] A. S. Meyer-Lindenberg, R. K. Olsen, P. D. Kohn et al., "Regionally specific disturbance of dorsolateral prefrontal-hippocampal functional connectivity in schizophrenia," *Archives of General Psychiatry*, vol. 62, no. 4, pp. 379–386, 2005.
- [41] A. J. Schwarz, A. Gozzi, T. Reese, C. A. Heidbreder, and A. Bifone, "Pharmacological modulation of functional connectivity: the correlation structure underlying the phMRI response to d-amphetamine modified by selective dopamine D3 receptor antagonist SB277011A," *Magnetic Resonance Imaging*, vol. 25, no. 6, pp. 811–820, 2007.
- [42] A. J. Schwarz, A. Gozzi, T. Reese, and A. Bifone, "Functional connectivity in the pharmacologically activated brain: resolving networks of correlated responses to d-amphetamine," *Magnetic Resonance in Medicine*, vol. 57, no. 4, pp. 704–713, 2007.
- [43] A. J. Schwarz, A. Gozzi, and A. Bifone, "Community structure and modularity in networks of correlated brain activity," *Magnetic Resonance Imaging*, vol. 26, no. 7, pp. 914–920, 2008.
- [44] A. Gozzi, L. Ceolin, A. Schwarz et al., "A multimodality investigation of cerebral hemodynamics and autoregulation in pharmacological MRI," *Magnetic Resonance Imaging*, vol. 25, no. 6, pp. 826–833, 2007.
- [45] G. Zaharchuk, J. B. Mandeville, A. A. Bogdanov Jr., R. Weissleder, B. R. Rosen, and J. J. A. Marota, "Cerebrovascular dynamics of autoregulation and hypoperfusion: an MRI study of CBF and changes in total and microvascular cerebral blood volume during hemorrhagic hypotension," *Stroke*, vol. 30, no. 10, pp. 2197–2204, 1999.
- [46] A. Gozzi, A. Schwarz, T. Reese, S. Bertani, V. Crestan, and A. Bifone, "Region-specific effects of nicotine on brain activity: a pharmacological MRI study in the drug-naïve rat," *Neuropsychopharmacology*, vol. 31, no. 8, pp. 1690–1703, 2006.
- [47] A. J. Schwarz, T. Reese, A. Gozzi, and A. Bifone, "Functional MRI using intravascular contrast agents: detrending of the relative cerebrovascular (rCBV) time course," *Magnetic Resonance Imaging*, vol. 21, no. 10, pp. 1191–1200, 2003.
- [48] A. J. Schwarz, A. Danckaert, T. Reese et al., "A stereotaxic MRI template set for the rat brain with tissue class distribution maps and co-registered anatomical atlas: application to pharmacological MRI," *NeuroImage*, vol. 32, no. 2, pp. 538–550, 2006.
- [49] A. J. Schwarz, B. Whitcher, A. Gozzi, T. Reese, and A. Bifone, "Study-level wavelet cluster analysis and data-driven signal models in pharmacological MRI," *Journal of Neuroscience Methods*, vol. 159, no. 2, pp. 346–360, 2007.
- [50] B. Whitcher, A. J. Schwarz, H. Barjat, S. C. Smart, R. I. Grundy, and M. F. James, "Wavelet-based cluster analysis: data-driven grouping of voxel time courses with application to perfusion-weighted and pharmacological MRI of the rat brain," *NeuroImage*, vol. 24, no. 2, pp. 281–295, 2005.
- [51] S. Maslov and K. Sneppen, "Specificity and stability in topology of protein networks," *Science*, vol. 296, no. 5569, pp. 910–913, 2002.
- [52] M. Rubinov and O. Sporns, "Complex network measures of brain connectivity: uses and interpretations," *NeuroImage*, vol. 52, no. 3, pp. 1059–1069, 2010.

- [53] A. L. Barabási and Z. N. Oltvai, "Network biology: understanding the cell's functional organization," *Nature Reviews Genetics*, vol. 5, no. 2, pp. 101–113, 2004.
- [54] A. J. Rockel, R. W. Hiorns, and T. P. S. Powell, "The basic uniformity in structure of the neocortex," *Brain*, vol. 103, no. 2, pp. 221–244, 1980.
- [55] A. J. Schwarz, A. Gozzi, and A. Bifone, "Community structure in networks of functional connectivity: resolving functional organization in the rat brain with pharmacological MRI," *NeuroImage*, vol. 47, no. 1, pp. 302–311, 2009.
- [56] M. Chavez, M. Valencia, V. Navarro, V. Latora, and J. Martinerie, "Functional modularity of background activities in normal and epileptic brain networks," *Physical Review Letters*, vol. 104, no. 11, Article ID 118701, 2010.
- [57] S. Fortunato, "Community detection in graphs," *Physics Reports*, vol. 486, no. 3-5, pp. 75–174, 2010.
- [58] V. Latora and M. Marchiori, "Efficient behavior of small-world networks," *Physical Review Letters*, vol. 87, no. 19, Article ID 198701, 2001.
- [59] S. S. Kannurpatti, B. B. Biswal, Y. R. Kim, and B. R. Rosen, "Spatio-temporal characteristics of low-frequency BOLD signal fluctuations in isoflurane-anesthetized rat brain," *NeuroImage*, vol. 40, no. 4, pp. 1738–1747, 2008.
- [60] H. Lu, Y. Zuo, H. Gu et al., "Synchronized delta oscillations correlate with the resting-state functional MRI signal," *Proceedings of the National Academy of Sciences of the United States of America*, vol. 104, no. 46, pp. 18265–18269, 2007.
- [61] C. P. Pawela, B. B. Biswal, Y. R. Cho et al., "Resting-state functional connectivity of the rat brain," *Magnetic Resonance in Medicine*, vol. 59, no. 5, pp. 1021–1029, 2008.
- [62] C. P. Pawela, B. B. Biswal, A. G. Hudetz et al., "A protocol for use of medetomidine anesthesia in rats for extended studies using task-induced BOLD contrast and resting-state functional connectivity," *NeuroImage*, vol. 46, no. 4, pp. 1137–1147, 2009.
- [63] Z. Liang, J. King, and N. Zhang, "Uncovering intrinsic connective architecture of functional networks in awake rat brain," *Journal of Neuroscience*, vol. 31, no. 10, pp. 3776–3783, 2011.
- [64] E. Jonckers, J. van Audekerke, G. de Visscher, A. van der Linden, and M. Verhoye, "Functional connectivity fMRI of the rodent brain: comparison of functional connectivity networks in rat and mouse," *PLoS ONE*, vol. 6, no. 4, Article ID e18876, 2011.